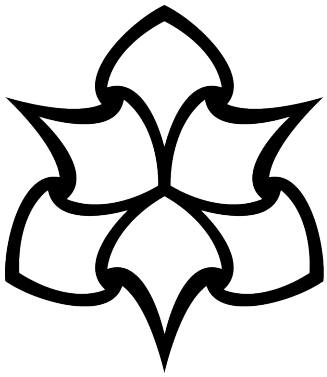

Fundamentals of electrochemistry of graphene and other 2D materials

Alejandro García-Miranda Ferrari

PhD

2019

Fundamentals of electrochemistry of graphene and other 2D materials

Alejandro García-Miranda Ferrari

Submitted in partial fulfilment of the requirements of Manchester Metropolitan University for the degree of Doctor of Philosophy

School of Science and the Environment

Faculty of Science and Engineering

Manchester Metropolitan University

2019

Contents

Abstract 7
Aims and Objectives 10
Acknowledgements 11
List of Tables 12
List of Figures 14
Abbreviations 21
Chapter 1: Fundamentals of electrochemistry 23
1.1 Introduction to Electrochemistry 23
1.1.1 Faradaic processes 24
1.1.2 Mass transport 26
1.1.3 Electrode kinetics 31
1.2 Electrochemical methodologies 35
1.2.1 Cyclic Voltammetry 35
1.2.2 Chronoamperometry 37
1.3 Electrode materials: Graphene and related 2D materials 40
1.3.1 Graphene 41
1.3.2 Other 2D materials: hexagonal boron nitride (hBN) 43
Chapter 2: Experimental Section 45
2.1 Physicochemical characterisation 45
2.1.1 Raman spectroscopy 45
2.1.2 Scanning electron microscopy (SEM) 48
2.1.3 Other techniques 49
2.2 Electrode materials 50
2.2.1 Screen-printed Electrodes 50
2.2.2 Edge-plane pyrolytic carbon and glassy carbon electrodes 50
2.2.3 Chemical Vapour Deposition (CVD) grown mono-layer boron nitride (2D-hBN) 51
2.2.4 Chemical Vapour Deposition (CVD) grown mono-layer graphene electrodes 51
2.2.5 Graphene in-house growth 54
Chapter 3: Determination of electroactive area of electrochemical sensing platforms 61
3.1 Introduction 61
3.2 Results and discussion 63

3.2.1 Determining the electroactive area using cyclic voltammetry.....64
3.2.2 Determining the electroactive area using chronocoulometry 74
3.3 Conclusions.....80
Chapter 4: Exploring the reactivity of distinct electron transfer sites at CVD grown monolayer graphene through the selective electrodeposition of MoO_2 nanowires....81
4.1 Introduction.....81
4.2 Results and discussion 83
4.3 Conclusion 91
4.4 Experimental section.....92
4.5 Supporting Information.....94
4.5.1 Optimising the electrochemical deposition of MoO_2 upon the monolayer graphene sheets.....94
4.5.2 Raman characterisation.....98
4.5.3 AFM characterisation of the selective electrodeposition of MoO_2 upon a monolayer graphene sheet 101
Chapter 5: Investigating the Integrity of Graphene towards the Electrochemical Hydrogen Evolution Reaction (HER) 102
5.1 Introduction.....102
5.2 Results and discussion 104
5.3 Conclusion 119
5.4 Experimental 120
5.5 Supporting Information.....121
Chapter 6: Investigating the Integrity of Graphene towards the Electrochemical Oxygen Evolution Reaction (OER) 124
6.1 Introduction.....124
6.2 Results and discussion 126
6.3 Conclusion 138
6.4 Experimental information 140
Chapter 7: Tailoring the electrochemical properties of 2D-hBN *via* physical linear defects: physicochemical, computational and electrochemical characterisation 141
7.1 Introduction.....141
7.2 Results and discussion 144
7.2.1 Electrochemical and physicochemical characterisation 144
7.2.2 DFT computational characterisation.....152
7.3 Conclusion 161
7.4 Experimental information 163

7.4.1 Density Functional Theory (DFT) 164
7.5 Supporting information 166
Chapter 8: An investigation into the influence of lateral flake size on the electroanalytical performance of graphene/graphite paste electrodes 170
8.1 Introduction 170
8.2 Results and discussion 173
8.3 Conclusions 185
8.4 Experimental information 186
8.5 Supporting information 188
Chapter 9: Tailorable Graphene/Polylactic(acid) thin films, printable filaments and 3D Printable electrodes for electrochemical applications 193
9.1 Introduction 193
9.2. Results and discussion 196
9.2.1 Development and Optimisation of the graphene/PLA polymers 196
9.2.2 Development and Optimisation of the graphene/PLA 3D printed electrodes 202
9.3 Conclusions 208
9.4 Experimental Section 209
Chapter 10: Conclusions and future work 211
10.1 Overall conclusions 211
10.2 Suggestions for future work 211
Publications arising from this Thesis 213
References 215

Abstract

Currently there is a global interest in the application of 2D materials such as graphene, graphene oxide (GO), reduced graphene oxide (rGO), 2D hexagonal boron nitride (2D-hBN), $MoSe_2$, MoS_2, WSe_2, antimonene and phosphorene within electrochemical applications. Some of those applications range from their use as sensors and energy storage/generation devices, including its use as an electrochemical supercapacitor, lithium/sodium ion batteries and as anodes and cathodes within fuel cells, to name just a few. This global interest is due to the unique beneficial properties of the 2D materials over traditional electrochemical materials.

As a result, there is a need to fundamentally understand how these 2D materials behave as electrodes at the single layer scale within electrochemical systems, and develop enhanced 2D materials into useful 3D structures, *e.g.* as 3D printed structures/electrodes. The discovery and/or confirmation of the fundamental electrochemical properties of these 2D materials could enable its application in several areas, such as additive manufacturing, electronics, and energy storage/generation for electrochemical sensor platforms. There is a huge potential for this knowledge to be usefully exploited within sensing and energy sectors and beyond.

This thesis reports the electrochemistry of graphene and other 2D nanomaterials from a fundamental point of view with thorough physicochemical characterisation and resultant electrochemical applicability of using 2D materials as electrodes.

Chapter 1 gives an overview of the fundamental concepts of electrochemistry and 2D materials related to this thesis. Chapter 2 details relevant experimental information used in this thesis.

Chapter 3 compares methods to determine the electroactive area of CVD grown graphene, which is important and novel contribution to those experimentalist using this and other electrode materials in order to benchmark their electrode platform. Chapter 4 demonstrates the origin of electron transfer properties of edge and basal plane sites on *true* graphene (polymer-free transferred and single layer).

Chapters 5 and 6 study, for the first time, the applicability and structural integrity of CVD graphene sheets towards the water splitting reactions depending on the number of layers, scan rate and voltage applied towards energy applications, indicating that mono- and few-layer CVD graphene are *not* suitable electrode materials towards the HER and the OER. Such work is of fundamental importance when graphene surfaces are use either "as is" or as the basis of catalyst as used in the HER/OER (Chapter 5 and 6 respectively).

Chapter 7 explores the introduction of physical linear defects (PLDs) on the surface of monolayer hexagonal-boron nitride films (2D-hBN), in order change from an insulator to a semiconductor material, tailoring its electrochemical properties. Physicochemical, computational and electrochemical characterisation techniques are applied to identify/explain the change in the electrochemical response from the change in surface morphology. 2D-hBN typically is considered an electrochemical insulator, however this thesis reports that through implementation of physical defects (simple surface modifications) the bandgap changes from *ca.* 6.11 eV to *ca*. 2.36 eV, giving rise to electrochemically useful signatures towards RuHex, $Fe^{+2/+3}$ and the HER..

Chapter 8 explores the use of different lateral flake sizes of graphitic powders in paste electrodes, applying the knowledge from Chapter 4, to obtain enhanced sensor devices by using smaller lateral flake sizes graphitic materials.

Lastly, chapter 9 explores the additive manufacturing of Graphene/PLA composites, namely thin films, 3D printable filaments and 3D printed electrodes, demonstrating that useful low cost 3D printable electrode can be manufactured and applied towards electroanalytical applications.

Aims and Objectives

The main focus of this thesis is to investigate the fundamental electrochemical properties of graphene and other 2D nanomaterials with thorough physicochemical characterisation.

Objectives:

1. Contribute to the fundamental understanding of the electrochemistry of CVD graphene and other 2D nanomaterials with physicochemical and electrochemical characterisation. Apply this into future sensing and energy applications.

2. Explore the role of graphene's structure and electrochemical reactivity to understand 2D materials capabilities when incorporated into paste electrodes.

3. Utilise the knowledge gained through the completion of previous objectives to successfully implement, fabricate and evaluate graphene-based 3D printed electrodes for future applications.

Acknowledgements

First of all I would like to express my gratitude to my supervisor Professor Craig Banks, for giving me the opportunity to join this incredibly inspiring journey, with constant guidance, ideas, support and unceasing ambition for research throughout my PhD.

I would also like to thank all the current and previous members of the Banks Research Group, for offering me expertise, advice and motivation, as well as other fellow members of MMU and collaborators who have been present along this project with constant memorable moments, making this period of my life one I will dearly remember.

Finally, I would like to express my infinite gratitude to my family and friends for their unconditional love and support (distance included), and for they values and morals that made me being who I am today, in addition to my girlfriend Joanne who brings me energy.

My father told me many times "*if you are going to do something, do it well",* so here I am.

Thanks also to you, the "reader" for taking the time to read this thesis.

List of Tables

Table 1. Calculated %Real areas for CVD grown mono-layer graphene, GC, EPPG and SPE electrodes using Randles-Ševćik equations. . %Real is the percentage of A_{real} divided by the A_{geo} (averaged using 3 different scan rate studies, each of them averaging 10 different scan rates; N = 3). Note that for dopamine, there is two different estimated values, first calculated using one electrode for the ten scans, and second calculated using ten different electrodes to see the fouling of the electrode due to analyte's adsorption to the surface of the electrode, see Refs[153, 154] (at 19.6 °C). 72
Table 2. Calculated 'areas' for CVD grown mono-layer graphene, GC, EPPG and SPE electrodes using Anson equations. %Real is the percentage of A_{real} divided by the A_{geo} (N = 9) (at 19.6 °C). 78
Table 3. HET kinetics, coverage and electrodeposition times for CVD mono-layer graphene decorations. HET kinetics ($kobs0$) were determined using the near ideal outer-sphere redox probe $[Ru(NH_3)_6]^{3+/2+}$ / 0.1 M KCl, coverage of edge plane (θ_{edge}) and the difference in the percentage of edge coverage upon the surface of the monolayer graphene sheets ($\Delta\theta_{edge}$) followed by the electrochemical decoration of MoO_2 for: 1 (A), 2 (B), 5 (C) and 10 (D) seconds; electrochemical parameters: -0.6 V (vs. Ag/AgCl) using 1 mM Na_2MoO_4 (in 1 M NaCl). Note: each sample (A, B, C and D) is a different CVD monolayer graphene sheet and has a varied initial size and quantity of edge sites, which exhibit distinct electron transfer rates (HET kinetics). 87
Table 4. Determination of the % edge plane sites and % basal plane sites upon the monolayer graphene sheet/electrochemical platform. Cyclic voltammograms were performed within a non-Faradaic region between -0.05 and +0.05 V at different scan rates (0.1, 0.2 and 0.5 V s^{-1} (vs. Ag/AgCl)) and analysed to deduce the average specific capacitance and allow the calculation of the edge and basal plane contributions as described by equation (5.1). Solution composition: 0.5 M H_2SO_4 (degassed using nitrogen). 109
Table 5. Hydrogen bubble size growth generated in-situ while performing chronoamperometry, potential held at -1.4 V (*vs.* Ag/AgCl), using monolayer graphene. Data clearly shows the evolution of a single hydrogen bubble from its initial generation to its explosion. Note that the measurement of the bubble started once it was big enough to be analysed with the optical microscope, therefore it is timed that initial measurement as 'time 0 seconds'. 121
Table 6. Electronic clouds delocalization on Frontier molecular orbitals (HOMO and LUMO) and their corresponding energy gaps for mh-hBN-NR, fh-hBN-NR, fh-hBN-NR (O-N) and fh-hBN-NR (O-B). The shown energy values were obtained by using B3LYP/LANL2DZ method of calculation. The iso value is 0.02. The ELUMO-EHOMO corresponds to the energy gap (i.e. band gap), which is the amount of energy required to transfer one electron from the highest occupied molecular orbital (HOMO) to the lowest unoccupied molecular orbital (LUMO), can indicate the possibility of electron transfer and allow for comparing this property among different structures. Colour code: blue: nitrogen; pink: boron; red: oxygen; white: hydrogen. 154
Table 7. Hydrogen Evolution Reaction (HER) analysis for 2D-hBN and 1 to 6 lines PLD-2D-hBN, including HER onset and current at -1.25 V values. (Scan rate: 5 mV s^{-1}; vs. Ag/AgCl). 159

Table 8. Electrochemical characterisation of graphene/graphite paste electrodes determined from cyclic voltammetry using 1 mM RuHex probe in 0.1 M KCl (N = 3) (k^0 values are the calculated averages of measurements carried out at 15, 50, 100 and 500 mV s^{-1}).....175
Table 9. Comparison of the peak position (Ep; in V) obtained at the various paste electrodes towards the detection of 100 μM of dopamine, uric acid, ascorbic acid, NADH, acetaminophen and p-Benzoquinone in PBS pH 7 (Scan rate 50 mV s^{-1}; vs. Ag/AgCl).....178
Table 10. Comparison of the analytical sensitivities (in M A^{-1}) obtained at the various paste electrodes towards the detection of dopamine, uric acid, ascorbic acid, NADH, acetaminophen and p-Benzoquinone in PBS pH 7 (Calculated from gradient of calibration plots between 0 and 100 μM depicted in Figure 57) (Scan rate 50 mV s^{-1}; vs. Ag/AgCl). 182
Table 11. Comparison of the electrochemical limits of detection (LODs; LOD = 3* σ M^{-1}) (in μM) obtained at the various paste electrodes towards the detection of dopamine, uric acid, ascorbic acid, NADH, acetaminophen and p-Benzoquinone in PBS pH 7 (Calculated from gradient of calibration plots between 0 and 100 μM depicted in Figure 57) (Scan rate 50 mV s^{-1}; *vs.* Ag/AgCl). 183
Table 12. Electrochemical characterisation of FG and KISH graphite paste electrodes determined from cyclic voltammetry using 1 mM RuHex probe in 0.1 M KCl (N = 3) (k^0 values are the calculated averages of measurements carried out at 15, 50, 100 and 500 mV s^{-1}).....189
Table 13. Electrochemical characterisation of graphene/PLA thin film electrodes determined from cyclic voltammetry using 1 mM RuHex probe in 0.1 M KCl (*N* = 7; *vs.* Ag/AgCl). 199
Table 14. Comparison of the analytical voltammetric profiles obtained at the various graphene/PLA thin films electrodes towards the detection of 1 mM dopamine (DA), ascorbic acid (AA), NADH, RuHex and $Fe^{2+/3+}$ determined from cyclic voltammetry (Scan rate 50 mV s^{-1} vs. Ag/AgCl). 201
Table 15. Comparison of the heterogeneous electron transfer (HET; k^0) values obtained at the various graphene/PLA electrodes from 1 mM RuHex scan rate studies (*N* = 7; *vs*. Ag/AgCl). 205
Table 16. Comparison of the analytical voltammetric profiles obtained at the unmodified and polished 20 % wt. 3D printed Graphene/PLA electrode towards the detection of 1 mM dopamine (DA), ascorbic acid (AA), NADH, RuHex and $Fe^{2+/3+}$ determined from cyclic voltammetry (Scan rate 50 mV s^{-1} vs. Ag/AgCl).....207

List of Figures

Figure 1. Schematic of CVD graphene housing 3D printed cell, including a photograph of the mounted cell (A) and schematics from perspective (B). 24
Figure 2. Schematic of the three different mass transport methods: diffusion (left), convection (centre) and migration (right). 26
Figure 3. Fick's second law as a cross section of a known area of a cubic region. Both flux in (x) and flux out (x+ δx) of the cubic region are considered as function of the distance between two opposite faces of the cubic region $(x)^3$. 29
Figure 4. Schematic of the Nernst diffusion layer. 30
Figure 5. Schematic of characteristic cyclic voltammetric profile of hexaammineruthenium (III) chloride (RuHex), showing the typical voltammograms for reversible, quasi-reversible and irreversible electron transfer situations. 34
Figure 6. Schematic of typical cyclic voltammetry as an applied waveform of potential as a function of time. 36
Figure 7. Schematic of typical cyclic voltammetric profile for the reduction of hexaammineruthenium (III) chloride (RuHex), showing the characteristics peak position (Ep) and peak height (Ip) of both anodic and cathodic peaks. 36
Figure 8. Schematic of typical chronoamperometric experiment, where a potential step waveform is applied from a non-faradaic region to a faradaic region, resulting in a change in the current response. 37
Figure 9. Representation of CC (charge vs. $time^{1/2}$) for an adsorbed electrochemical species. 39
Figure 10. Representation of the structures of graphite, graphene, graphene oxide, graphene nanoribbons (GNRs) and carbon nanotubes (CNTs) respectively. 40
Figure 11. Representation of the top down and bottom up graphene synthesis method respectively. 42
Figure 12. 2D chemical structure of the 2D-hBN mono-layer (A) and hBN nanoribbon (B). 44
Figure 13. Schematic of Raman spectrometer platform setup. 46
Figure 14. Schematic of a Scanning Electron Microscope setup. 48
Figure 15. Schematic cross-sectional perspective of the CVD graphene 'housing' 3D printed cell (A) designed using Solidworks and 3D printed using a Form 2 3D UV curable printer. Reference and counter electrodes are incorporated into the three-electrode system in the 3D printed cell. Schematic diagram of the CVD graphene 'housing' 3D printed cell (B). The cell allows the connection of the monolayer graphene sheet to the potentiostat with a copper foil wrapping the graphene chip and allowing its use under a microscope or Raman Spectrometer without dismounting and manipulating the chip. There is a silicon O-ring sealing the graphene chip, keeping the studied area of the WE. 53
Figure 16. Schematic diagram of the cold-wall Chemical Vapour Deposition (CVD) rig used for graphene growth. The arrows indicate the direction of gas flow. 55
Figure 17. Comparison of the Raman profile and optical image respectively of 10 minutes (A and B), 12 minutes (C and D), 15 minutes (E and F), 20 minutes (G and H) and 30 minutes (I and J) of growth time. 56
Figure 18. Graphene 12 minutes growth temperature curve, including H_2, CH_4 and Ar flow rates at every stage. 57

Figure 19. Raman scattering process for graphene Raman bands. First-order G band process, one-phonon second-order double resonance (DR) process for D band (intra-valley process) and two-phonon second-order resonance Raman spectral processes for the DR G process for the triple resonance process for monolayer graphene. For one-phonon, second-order transitions, one of the two scattering events is an inelastic scattering event. Resonance points are shown as circles near the K and K' points respectively. 59
Figure 20. Graphene/copper sample floating at the hexane/etching solution interface. Where A shows that the graphene sheet on copper would be floating between the hexane and the etching solution (0.1 M ammonium persulfate). B shows the process after 5 hours of etching, when the copper is completely removed from the sample. C depicts the cleaning process of the sample when the graphene floats between hexane and DI water in order to clean copper or etchant residues. D shows the graphene sheet being transferred to a Si/SiO_2 wafer or other substrate. 60
Figure 21. Cyclic voltammetry of 1 mM RuHex (A), 1 mM IrCl6 (B), 2 mM Co(phen) (C), 1 mM TMPD (D), 1 mM dopamine (E), 1 mM ascorbic acid (F), 1 mM NADH (G) and 1 mM capsaicin (H) for CVD grown mono-layer graphene, GC, EPPG and SPE electrodes. Scan rate 0.05 V s^{-1} with an arrow pointing at the forward peak selected to calculate the A_{geo} with equations 1 to 3. Results are presented in Table 1. 71
Figure 22. Classification of redox systems by McCreery et al.[20] according to their kinetic sensitivity to particular surface modifications upon carbon electrodes. The figure has been adapted to show clearly outer- and inner- sphere probes. Fc: ferrocene, MV: methyl viologen, CPZ: chlorpromazine and MB: methylene blue. 73
Figure 23. Representation of CC (charge vs. time$^{1/2}$) for a non-adsorbed outer-sphere probe (A) and for an adsorbed inner-sphere probe (B). Note that, in A, the intercept is not truly zero due to the contribution of Q_{dl} (see equation 3.3 and 3.4). 76
Figure 24. Anson plots resulting from using the following redox probes: 1 mM RuHex (A), 1 mM IrCl6 (B), 2 mM Co(phen) (C), 1 mM TMPD (D) 1 mM dopamine (e), 1 mM ascorbic acid (F), 1 mM NADH (G) and 1 mM capsaicin (H) for CVD grown mono-layer graphene, EPPG, GC and SPE electrodes (corresponding estimated areas are shown in Table 2) (at 19.6 °C). 77
Figure 25. SEM images of a monolayer graphene electrode (A), 1 second electrodeposition of MoO_2 at -0.6 V (vs. Ag/AgCl) (C) and 10 second electrodeposition of MoO_2 at -0.6 V (vs. Ag/AgCl) (E). Additionally presented is cyclic voltammetric analyses recorded using 1 mM $[Ru(NH_3 0_6]^{3+/2+}$ / 0.1 M KCl, using a monolayer graphene sheet (B), 1 second electrodeposition of MoO_2 at -0.6 V (vs. Ag/AgCl) (D) and 10 second electrodeposition of MoO_2 at -0.6 V (vs. Ag/AgCl) (F) (Scan rate: 25 mV s^{-1}). Note that the monolayer graphene samples (Fig 4.1A) might contain dust/air impurities due to the manufacturing process explained within the Experimental Section, observed as nanoparticulates. 86
Figure 26. Schematic highlighting the MoO_2 deposition process upon monolayer CVD graphene sheets, where MoO_2 nucleation starts upon the graphene edge plane like- sites/defects. Note that longer deposition times result in the MoO_2 growing from the edge plane like- sites/defects over onto the basal plane sites, until there is a

complete insulating layer covering the entire monolayer graphene sheet, resulting in substantially reduced electrochemical activity. Note, sizes are not to scale. 89
Figure 27. Optical (A) and SEM (B) images of a monolayer graphene sheet deposited upon a SiO_2 wafer covering half of surface in order to expose the edge plane sites/defects of the monolayer graphene before going into the electrochemical cell. Note that the graphene samples may possess air/dust impurities in the form of dots apparent in B. 95
Figure 28. SEM images of a monolayer graphene sheet decorated with MoO_2 through electrodeposition at – 0.6 V (vs. Ag/AgCl, Scan rate: 5mV s^{-1}) for 1 (A), 5 (B), 20 (C) and 100 seconds (D) respectively. Images show how with longer deposition times, deposition is no longer edge plane selective and moves from the edge to the basal planes, covering the entire graphene sheet. 96
Figure 29. SEM images of a monolayer graphene sheet decorated with MoO_2 through electrodeposition at – 1 V (*vs.* Ag/AgCl, Scan rate: 5mV s^{-1}) for 1 (A), 5 (B), 20 (C), 100 (D) and 200 seconds (E) respectively. Images show how with a more negative potential and longer deposition times, deposition is no longer edge plane selective (when is MoO_2 nanowires) and moves from the edge to the basal planes (non-selective deposition, as MoO_2 bulk), covering and breaking the entire graphene sheet. 97
Figure 30. Linear sweep voltammetry recorded with 0.5 (solid line) and 1 mM (dotted line) Na_2MoO_4 solutions depicting the electrodeposition of MoO_2 at a monolayer graphene sheet (vs. Ag/AgCl; Scan rate 5 mV s^{-1}). 98
Figure 31. Schematic of selective MoO_2 deposition process (chronoamperometry at -0.6 V (vs. Ag/AgCl) for 1 second), where the monolayer graphene sheet covers half of the SiO_2 wafer (A). Raman spectra from the edge of the monolayer graphene (B) with a MoO_2 peak at 308 cm^{-1}, the monolayer graphene where MoO_2 has not been electrodeposited yet (C), and an area where there is only SiO_2 wafer (D). 99
Figure 32. Raman spectra from the edge of the monolayer graphene before (A) and after (B) its decoration with MoO_2 (chronoamperometry at -0.6 V (vs. Ag/AgCl) for 1 second). Raman peak at 308 cm^{-1} corresponds to the MoO_2 nanowires on the decorated graphene electrode. 100
Figure 33. AFM analysis of a monolayer graphene sheet following the electrodeposition of MoO2 at -0.6 V for 1 second (vs. Ag/AgCl). Figure 33A shows the topography of the graphene, where most of the surface remains unmodified (basal plane), although some MoO_2 wires can be observed in 33B, C, D and E. 101
Figure 34. Scanning stability experiments using monolayer graphene; linear sweep voltammetry (LSV) from 0 to -1.4 V (scan rate: 25 mV s^{-1}; vs. Ag/AgCl; solution: 0.5 M H_2SO_4). (B) Typical Raman profile of the monolayer graphene sheet described and presented in C, D and E. Optical images of monolayer graphene unused (C), after 5 LSV scans (F), after 10 LSV scans (I) and after 20 LSV scans (L). 2D Raman mapping of the monolayer graphene unused (D), after 5 LSV scans (G), after 10 scans (J) and after 20 LSV scans (M). 3D Raman mapping of the monolayer graphene sheet unused (E), after 5 LSV scans (H), after 10 LSV scans (K) and after 20 LSV scans (N), all in red colour and compared to the unused sheet (yellow overlay). Raman maps show intensity of Graphene's G band (ca. 1590 cm^{-1}) in order to show the presence of graphene. 107

Figure 35. Mono-layer graphene stability schematic under HER consecutive scanning. (A) Monolayer graphene following 20 HER LSV scans. Part (B) depicts the Raman profile near a hole, showing that it is few-layer graphene, with the characteristic ratio of the G/2D peaks near to 1:1. (C) Depicts the Raman profile of a broken area where there is no characteristic graphene peak (or signal) present. (D) Shows the Raman profile of an intact area where there is monolayer graphene including its typical G (1590 cm^{-1}) and 2D (2690 cm^{-1}) peaks. (E) Is a schematic representation of the behaviour identified within this figure (A–D), where the emergence of a bubble on the graphene surface (due to the HER) leads to the creation of some rips when the bubbles move and disperse. The debris created due to the graphene breakdown is stacked in areas near to the holes/rip. When many bubbles explode, there is an incremental rise of the edge sites caused by the broken graphene pieces, which eventually lead to the complete destruction of the graphene sheet. ..111
Figure 36. Scanning stability experiments using few-layer graphene; linear sweep voltammetry (LSV) from 0 to -1.4 V, scan rate: 25 mV s^{-1}; *vs* Ag/AgCl; solution: 0.5 M H_2SO_4. (B) Typical Raman profile of the few-layer graphene described and presented in C, D and E. Optical images of a few-layer graphene unused (C), after 10 LSV scans (F), after 20 LSV scans (I) and after 30 LSV scans (L). 2D Raman mapping of the few-layer graphene unused (D), after 10 LSV scans (G), after 20 LSV scans (J) and after 30 LSV scans (M). 3D Raman mapping of the few-layer graphene unused (E), after 10 LSV scans (H), after 20 LSV scans (K) and after 30 LSV scans (N), all in red colour and compared to the unused sheet (yellow overlay). Raman maps show intensity of Graphene's G band (*ca*. 1590 cm^{-1}) in order to show the presence of graphene. 114
Figure 37. Scanning stability experiments using multilayer graphene; linear sweep voltammetry (LSV) from 0 to -1.4 V, scan rate: 25 mV s^{-1}; *vs* Ag/AgCl; solution: 0.5 M H_2SO_4. (B) Typical Raman profile of the multilayer graphene described and presented in C, D and E. Optical images of a multilayer graphene unused (C), after 30 LSV scans (F), after 50 LSV scans (I), after 70 LSV scans (L) and after 100 LSV scans (L). 2D Raman mapping of the multilayer graphene unused (D), after 30 LSV scans (G), after 50 LSV scans (J), after 70 LSV scans (M) and after 100 LSV scans (P). 3D Raman mapping of the multilayer graphene unused (E), after 30 LSV scans (H), after 50 LSV scans (K), after 70 LSV scans (N) and after 100 LSV scans (Q), all in red colour and compared to the unused sheet (yellow overlay). Raman maps show intensity of Graphene's G band (*ca*. 1590 cm^{-1}) in order to show the presence of graphene. 117
Figure 38. Snapshot from an in-situ video recorded while performing chronoamperometry, (potential held a -1.4 V (vs. Ag/AgCl)) using monolayer graphene clearly showing the evolution of hydrogen bubbles on top of the graphene electrode over the following time periods: 0 (A) (zero as initial measurement time), 1 (B), 4 (C), 14 (D), 45 (E) and 67 (F) seconds. Video recorded from the top of the graphene during the electrochemical experiment. 121
Figure 39. Raman characterisation of mono-, few- and multilayer graphene utilised within this work. Raman is performed with a 532 nm excitation laser at a low power of 3 mW to avoid any heating effects. Spectra were recorded using a 3 seconds exposure time for 3 seconds exposure time for 3 accumulations at each point. 123

Figure 40. Scanning stability experiments of mono- (A), multi- (B) and few-layer graphene (C); linear sweep voltammetry (LSV) from 0 to +1.4 V; Scan rate: 25 mV s^{-1}; vs. Ag/AgCl; Solution: 0.1 M KOH. 127
Figure 41. Scanning OER stability experiments using mono-, few and multi-layer graphene; Mono-layer graphene (A to F) showing an optical image, its Raman profile and 3D Raman map (A, B and C respectively) of the unused mono-layer graphene. Mono-layer graphene after 5 LSV OER scans optical, its Raman profile and 3D Raman map (D to F respectively). Multi-layer graphene (G to L) showing an optical image, its Raman profile and 3D Raman map (G to I) of the unused multi-layer graphene. Multi-layer graphene after 50 LSV OER scans optical, its Raman profile and 3D Raman map (J to L). Few-layer graphene (M to R) showing an optical image, its Raman profile and 3D Raman map (M to O) of the unused few-layer graphene. Few-layer graphene after 5 LSV OER scans optical, its Raman profile and 3D Raman map (P to R). 128
Figure 42. Scan rate OER stability experiments using mono-layer graphene at 2.5 (A), 15 (B), 250 (C) and 2500 (D) mV s^{-1}, showing the Raman mapping characterisation before and after 5 LSV OER scans and optical image of the electrode after the 5 LSV OER scans. (Solution: 0.1 M KOH; *vs.* Ag/AgCl). 131
Figure 43. Chronoamperometry stability experiments using mono-layer graphene, holding a fixed potential at 0.4 V (A to F), 0.8 V (G to L), 1.2 V (M to R) and +1.4 V (S to X), showing optical images and Raman mapping characterisation before and after holding the fixed potential for 280 seconds (Solution: 0.1 M KOH; vs. Ag/AgCl).133
Figure 44. Captions extracted from an *in-situ* video recorded while performing chronoamperometry (potential held a +1.4 V (*vs*. Ag/AgCl)), using mono-layer graphene. Captions show the evolution of hydrogen bubbles over the following time periods: 10 (A), 20 (B), 30 (C) and 40 (D) seconds. Black arrows indicate the movement of the bubbles damaging the surface of the electrode. 135
Figure 45. Monolayer graphene stability schematic under OER consecutive scanning, showing bubbles growing, merging and collapsing inducing structural damage in the surface of the mono-layer graphene electrode. 137
Figure 46. Cyclic voltammetry for 1 mM RuHex /0.1 M KCl (A) and 1 mM $Fe^{2+/3+}$/0.2 M $HClO_4$ (B) using a PLD-SiO_2 wafer as first control (black line), a 2D-hBN electrode (red line) and a PLD-2D-hBN electrode with 1 defective line (violet line) as working electrodes respectively. Scan rate: 50 mV s^{-1}; *vs.* Ag/AgCl. Note that the introduction of PLD gives rise to electrochemically useful signatures. 146
Figure 47. Cyclic voltammetric scan rate study of 1 mM RuHex/0.1 M KCl using a unmodified 2D-hBN (A), 1 line 1PLD-2D-hBN (B) and 6 line 6PLD-2D-hBN (C) as working electrode (vs. Ag/AgCl). Note that in the absence of PLD there is clearly no electrochemical activity (47A) where upon the introduction of PLDs, electrochemically useful signatures are observed (47B and 47C). 147
Figure 48. Optical image of PLD-2D-hBN electrode used for 28 scans for a scan rate study of 1 mM RuHex/0.1 M KCl, decorated with 6 PLD onto it with a growing tree-shape of rips/defects due to its electrochemical application with its overlapped Raman mapping (A). B shows typical Raman peak of 2D-hBN (1365 cm^{-1}), C shows Raman peak of a damaged area caused by the HER scanning and D shows the Raman peak of a physical linear defect. Higher resolution zoom in area with optical image (E), 2D

Raman mapping (F) and 3D Raman mapping (G) of another area of the same PLD-2D-hBN electrode. 149
Figure 49. XPS analysis of 2D-hBN and PLD-2D-hBN's edge of a PLD. XPS map of 2D-hBN and PLD-2D-hBN electrode (A), XPS spectra for both locations (B), high resolution XPS analysis of the B1s components of an 2D-hBN (C) and PLD-2D-hBN (D) electrode and high resolution XPS analysis of the N1s components of an 2D-hBN (E) and PLD-2D-hBN (F) electrode. 151
Figure 50. Total density of states (TDOS) of the investigated 2D-hBN nanoribbons (2D-hBN-NRs). The depicted TDOS values were calculated for the above-mentioned structures optimized at the B3LYP/LANL2DZ method of calculation. 155
Figure 51. Linear Sweep Voltammetry (LSV) of 2D-hBN, 1PLD-2D-hBN and 6PLD-2D-hBN respectively with 0.5 M H_2SO_4, depicting the scanning stability experiments towards the HER, showing an increase in the current when more PLD are created (due to an increase in edge plane-sites/defects) when compared to the bare 2D-hBN electrode (Scan rate: 5 mV s^{-1}; vs. Ag/AgCl). 158
Figure 52. 2D chemical structure of the used 2D-hBN mono-layer (A) and the used hBN nanoribbon (B). 166
Figure 53. Cyclic voltammetry of 1 mM RuHex/0.1 M KCL (A) and 1 mM $Fe^{2+/3+}$/0.2 M $HClO_4$ (B) (Scan rate: 50 mVs^{-1}, *vs.* Ag/AgCl) using a SiO_2 wafer (no 2D-hBN) as an electrode. SEM image of a PLD-SiO_2 wafer (C) and PLD-2D-hBN electrode (D) after being utilised towards voltammetric methods. Raman profiles of a PLD-2D-hBN electrode at its newly physical defects (after utilised towards voltammetric) (E) and diamond scriber tip with a typical diamond Raman peak[288] at 1332 cm^{-1} (F) showing the lack of 2D-hBN or diamond Raman peak in Figure 53E. 167
Figure 54. Voltammetric scan rate study of 1 mM RuHex/0.1 M KCl using a 6PLD-2D-hBN electrode used for 4 (54A) and 28 (54B) consecutive voltammetric scans to test their electrochemical stability towards multiple consecutive potential scanning. Optical image and Raman mapping characterisation (Figure 54C) of the PLD-2D-hBN after used in Figure S54B. Raman spectra is included, showing areas where 2D-hBN is present and its typical Raman peak (red and green colour) and some rips where there is no 2D-hBN peak (blue colour). (vs. Ag/AgCl). 168
Figure 55. Optimized structures of (A) mh-hBN-NR, (B) fh-hBN-NR, (C) fh-hBN-NR with an edge-plane boron atom passivated with an oxygen atom and (D) fh-hBN-NR with an edge-plane nitrogen atom passivated with an oxygen atom. The shown structures were optimized using B3LYP/LANL2DZ functional. Color code: blue: nitrogen; pink: boron; red: oxygen; white: hydrogen. 169
Figure 56. Voltammetric profiles of 100 μM of dopamine (A), uric acid (B), ascorbic acid (C), NADH (D), acetaminophen (E) and p-Benzoquinone (F) in PBS pH 7 at the various paste electrodes (Scan rate 50 mV s^{-1}; vs. Ag/AgCl). 177
Figure 57. Calibration plots of dopamine (A), uric acid (B), ascorbic acid (C), NADH (D), acetaminophen (E) and p-Benzoquinone (F) in PBS pH 7 at the various paste electrodes. Analytical sensitivities of such calibration plots shown in Table 10 (Scan rate 50 mV s^{-1}; *vs.* Ag/AgCl). 181
Figure 58. 1 mM RuHex in 0.1 M KCl voltammetric profiles using the range of graphite and graphene paste electrodes (Scan rate: 15 mV s^{-1}; vs. Ag/AgCl). 188

Figure 59. 1 mM RuHex in 0.1 M KCl voltammetric profiles using the range of FG and KISH paste electrodes (Scan rate: 15 mV s^{-1}; vs. Ag/AgCl). 188
Figure 60. Voltammetric profiles of 100 µM of dopamine (A), uric acid (B), ascorbic acid (C), NADH (D), acetaminophen (E) and p-Benzoquinone (F) in PBS pH 7 using FG and KISH graphite paste electrodes (Scan rate 50 mV s^{-1}; vs. Ag/AgCl). 190
Figure 61. Calibration plots of dopamine (A), uric acid (B), ascorbic acid (C), NADH (D), acetaminophen (E) and p-Benzoquinone (F) in PBS pH 7 using the FG and KISH graphite paste electrodes (Scan rate 50 mV s^{-1}; vs. Ag/AgCl). 191
Figure 62. A schematic shows that the graphite/graphene pastes are mixed with Nujol (60-40 % ratio respectively), are then inserted into a polymeric-composite electrode shell with an inner diameter of 4.5 mm. Electrode material is in contact with copper foil as electrode connector. After polishing treatment, electrodes are ready to be used in conjunction with reference (RE) and counter (CE) electrodes in a three-electrode cell configuration. B Depicts the different working electrodes used in this manuscript. C Shows the different graphene (AO1, AO3, AO4, AO2 and C1) and graphite (HCNG and G250) powders used as electrode material in this manuscript. 192
Figure 63. Thermogravimetric analysis and SEM images of 5-40 % wt. graphene/PLA material. A shows the thermogravimetric analysis (TGA) of 5, 10, 15, 20 and 40 % wt. graphene/PLA material. B to F shows the SEM images of the 5, 10, 15, 20 and 40 % wt. graphene thin films respectively. 197
Figure 64. Optical and RuHex scan rates studies for 5 to 40 % wt. graphene/PLA thin films. A shows the optical images of the graphene/PLA thin films with loading varying from 5 to 40 % wt. respectively. B depicts the respective scan rates studies of 1 mM RuHex from 5 to 500 mV s^{-1} (Scan rate 50 mV s^{-1}; vs. Ag/AgCl). 198
Figure 65. Voltammetric profiles of 1 mM dopamine (A), ascorbic acid (B), β-nicotinamide adenine dinucleotide (NADH) (C), RuHex (D) and $Fe^{2+/3+}$ (F) when using the graphene thin film electrodes (Scan rate 50 mV s^{-1}; vs. Ag/AgCl)..... 201
Figure 66. Optical images of the 20 % wt. graphene/PLA 3D printable filament and 3D printed electrodes (A) with a Raman inset showing the characteristic peaks of graphitic materials. Zoomed in section 20 % wt. 3D printed electrode with its measurements, including an inset showing the 3D printed working electrode, counter and reference electrodes (CE and RE respectively) in the electrolyte. 203
Figure 67. Scan rate studies of 1 mM RuHex using the 20 % wt. graphene electrodes in the following forms: thin film (A), 3D printable filament (B) and 3D printed electrode (C) respectively (Scan rate studies from 5 to 500 mV s^{-1}; vs. Ag/AgCl). 204
Figure 68. Voltammetric profiles of 1 mM dopamine (A), ascorbic acid (B), β-nicotinamide adenine dinucleotide (NADH) (C), RuHex (D) and $Fe^{2+/3+}$ (F) when using the 20 % wt. graphene 3D printed electrodes unmodified and polished respectively (Scan rate 50 mV s^{-1}; vs. Ag/AgCl)..... 207

Abbreviations

- *%Real*: percentage of electrochemical active area compared to geometrical area
- 2D: two-dimensional
- 2D-hBN: hexagonal Boron Nitride
- 3D: three-dimensional
- AA: *L*-Ascorbic Acid
- AFM: Atomic Force Microscopy
- A_{geo}: geometrical area
- Aq: aqueous
- A_{real}: *true* electrochemical active area
- CC: Chronocoulometry
- C_{dl}: Double Layer Capacitance
- CE: Counter electrode
- CV: Cyclic Voltammetry
- CVD Graphene: Chemical Vapour Deposition Graphene
- D: Diffusion coefficient
- DA: Dopamine hydrochloride
- DFT: Density Functional Theory
- DOS: Density of States
- EDX: Energy Dispersive X-ray Spectroscopy
- E_{pa}: Anodic Peak Potential
- E_{pc}: Cathodic Peak Potential
- EPPG: Edge Plane Pyrolytic Graphite
- FWHM: Full Width at Half Maximum
- GC: Glassy Carbon
- GNR: Graphene Nanoribbon
- GQD: Graphene Quantum Dots
- HER: Hydrogen Evolution Reaction
- HET: Heterogeneous electron transfer
- HOMO: Highest occupied molecular orbital
- I_{pa}: Anodic Peak Current

- I_{pc}: Cathodic Peak Potential
- k^0: electrochemical rate constant
- L_a: Lateral Length
- LOD: Limit of Detection
- LSV: Linear Sweep Voltammetry
- LUMO: Lowest Unoccupied molecular orbital
- *n*: Number of Electrons Involved in the Reaction Mechanism
- NADH: β-Nicotinamide adenine dinucleotide
- NR: Nanoribbon
- OER: Oxygen Evolution Reaction
- *p*-Benzo: *p*-Benzoquinone
- PBS: Phosphate buffer solution
- PEM: Proton Exchange Membrane
- QD: Quantum Dot
- RE: Reference electrode
- rGO: reduced graphene oxide
- RSD: Relative Standard Deviation
- SEM: Scanning Electron Microscope
- SPE: Screen-Printed Electrode
- TMPD: N,N,N',N'-tetramethyl-para-phenylenediamine
- UA: Uric Acid
- WE: Working electrode
- XPS: X-ray photoelectron spectroscopy
- ΔEp: Peak to peak separation

Chapter 1: Fundamentals of electrochemistry

This chapter introduces and explains general electrochemistry concepts for general comprehension and interpretation of this topic. The chapters included in this thesis apply and expand those concepts in order to understand the fundamentals of electrochemistry of Graphene and other 2D materials.

1.1 Introduction to Electrochemistry

Electrochemistry is the division of chemistry that focusses on the electrical and chemical reactions, studying the chemical changes triggered by the electric current and electrical energy created by chemical reactions[1]. Electrochemical reactions involve electron exchange processes, measuring current, potential or charge[2], for a wide range of applications including: electrochemical sensing (*e.g.* glucose sensors, heavy metals, pH meters), energy storage (*e.g.* fuel cells, batteries) or synthesis[3].

These electron exchange processes can be involving: species in the same phase (homogeneous electron transfer reactions) or transfer between molecules or between an electronic conductor (electrode) and a molecule (heterogeneous electron transfer reactions). Electrochemistry's main interest is the interaction between the surface of the electrode and the solution[1-3]. The main two types of electroanalytical methods are potentiometric and potentiostatic which need at least two conductors of electrode and a contacting solution (electrolyte). One of the electrodes, the working electrode (WE), responds to the target molecule(s), and the second electrode, or reference electrode (RE), is independent of the properties of the solution (of constant potential). Another option is the introduction of a third electrode, the counter or auxiliary electrode (CE) that allows the current to by-pass the reference electrode, allowing one to observe the energy of the electrons within the working electrode[1]. Figure 1 represents a classic three-electrode system utilised later in this thesis.

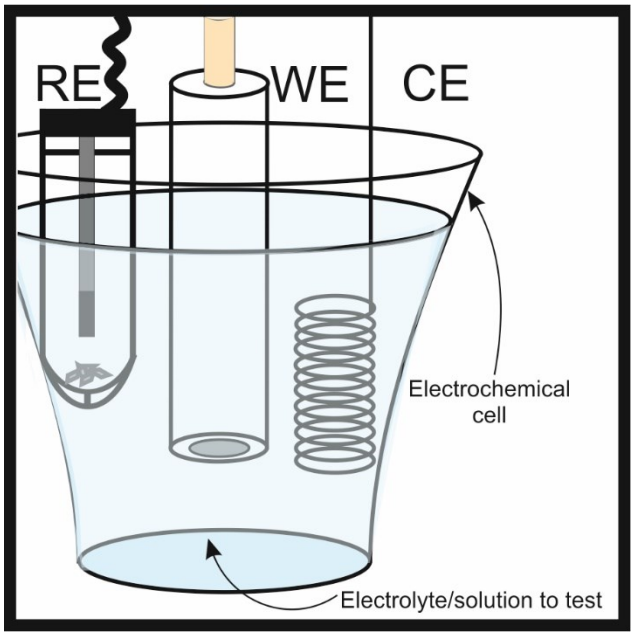

Figure 1. Schematic of classic electrochemical with a three electrode configuration including the reference (RE), working (WE) and counter (CE) electrodes respectively.

Potentiostatic, or potential-controlled techniques, focus on the charge transfer processes at the electrode-solution interface, based on dynamic situations. Potentiostatic techniques measure any electroactive by controlling the potential difference between the WE and the CE so the potential difference between the WE and the RE is accurately measured/defined. Potentiostatic methods have the advantages of high sensitivity and selectivity towards electroactive species, wide linear range, portable and little cost of instrumentation[2].

1.1.1 Faradaic processes

There are two types of processes that can occur at the surface of electrodes, namely Faradaic and non-Faradaic processes. Potentiostatic methods measure the faradaic current that is directly proportional to the concentration of the target analyte[1]. The electrochemical process is expressed in the following equation:

$$O_{(aq)} + ne^-_{(aq)\ k_{ox}} \rightleftharpoons^{k_{red}} R^{ne-}_{(aq)} \quad (1.1)$$

where *O* and *R* are the oxidised and reduced forms of a redox couple respectively. The electrochemical reaction consists in the transfer of charge through the interfacial region of the working electrode that acts as a source/sink of electrons, and a solution phase (aq) or electrolyte. The electron transfer moves towards the equilibrium, developing a charge difference between the electrode and the solution, called potential drop (across the interface), which is the potential difference at the solution-electrode interface. The transfer of electrons will occur in a potential region that makes the electron transfer thermodynamically or kinetically favourable. For systems governed by the laws of thermodynamics, the electrode's potential can be used to calculate the concentration of the electroactive species at its surface, according to the Nernst equation:

$$\mathrm{E} = \mathrm{E}^0 - \frac{\mathrm{RT}}{nF} \ln \frac{C^R}{C^O} \tag{1.2}$$

where E^0 is the standard potential for the redox reaction, R is the universal gas constant, T is the temperature in Kelvin, n is the number of electrons transferred in the reaction, F is Faraday's constant and C is the concentration of the electroactive species (oxidised or reduced respectively). At standard conditions, 298 K of temperature and considering that ln(x) = 2.3 log(x), equation (1.2) can be expressed in the following form[1, 2]:

$$\mathrm{E} = \mathrm{E}^0 - \frac{0.059}{n} \log \frac{C^R}{C^O} \tag{1.3}$$

The resultant recorded current from a change in the oxidation state of the electroactive species is called the faradaic current (as it obeys Faraday's laws), and such faradaic current is directly proportional to the rate of the redox reaction. The resultant current-

potential plot, named voltammogram, displays the current response (y axis) against the excitation potential (x axis).

1.1.2 Mass transport

It is very relevant to emphasise the importance on mass transport due to the transport of electroactive species from the bulk solution to the surface of the electrode and vice versa because of its effect on the overall rate of an electrochemical reaction.

Mass transport generally involves three different phenomena: diffusion, convection and migration-controlled processes.

- Diffusion-controlled process: movement caused by a concentration gradient, from high to lower concentration regions, aimed at reducing the concentration differences.
- Convection-controlled process: movement caused by an external mechanical energy, such as stirring, flowing or rotating the solution (forced-convection). This process can also occur as a result of density of gradients.
- Migration-controlled process: movement caused by an electrical field transporting charged particles along it.

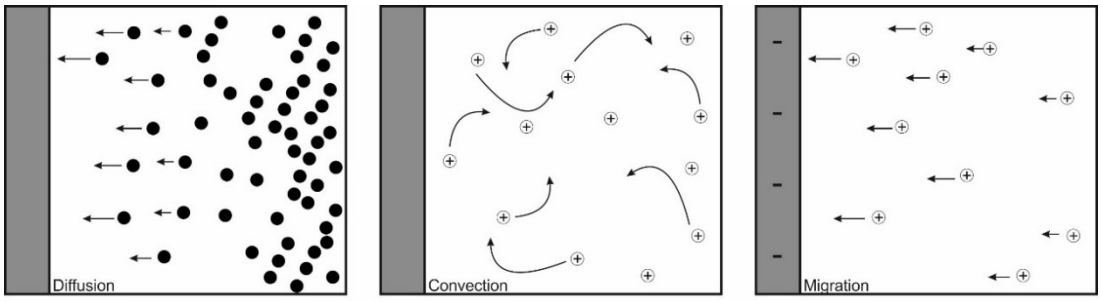

Figure 2. Schematic of the three different mass transport methods: diffusion (left), convection (centre) and migration (right).

When a voltammetric technique is applied, diffusion is being favoured since it ensures the transfer of electroactive species at a reproducible rate (depending on the concentration of the analyte in the bulk solution), but it is important to highlight that all three mass transport modes co-exist in the solution, diffusion being the one with the highest contribution to the overall mass transport. Electrochemical experimentalists usually add a concentrated background electrolyte (such as large concentrations of KCl) to restrict migration effects and limiting the potential drop effects[3]. Lastly, natural convection is classified as negligible too, as long as the scan rate of the experiment is sufficiently fast (50 mV s^{-1} for a voltammetric experiment, the most common one used within this project, is fast enough to nullify the natural convection happening in the reaction). All of the described below make diffusion as the bigger contributor to mass transport, and was described by Fick's laws in 1855[4].

Mass transport within an electrochemical system is governed by the diffusion, molecules moving from a high to a low concentration, and therefore by the flux (j), which is defined by a number of molecules entering a specific area of the electrode over an imaginary plane:

$$j = -D\frac{dC}{dx} \tag{1.4}$$

where j is the diffusive flux in moles cm^2 s^{-1}, D is the diffusion coefficient of the electroactive specie, C is the concentration of the electroactive specie and x is position. The diffusion coefficient is a fundamental term which represents the area in which the electroactive specie will diffuse in a given time.

Diffusion coefficient:

- Two-dimensional:

$$\sqrt{(x^2)} = \sqrt{2Dt} \tag{1.5}$$

- Three-dimensional:

$$\sqrt{(x^2)} = \sqrt{6Dt} \tag{1.6}$$

The Stokes-Einstein equation describes diffusion coefficient as the direct relation between the Boltzmann constant (k) and the temperature (T), being both inversely proportional to the viscosity of the liquid (η) and the hydrodynamic radius (R) of the diffusive specie as described in the following equation:

$$D = \frac{kT}{6\Pi\eta R} \tag{1.7}$$

It is important to note that diffusion coefficients are valid under the presence of an excessive background electrolyte (such as KCl), due to the negation of charge migration[3].

Diffusive flux is also connected to Faradaic current density as follows:

$$I = nFAj \tag{1.8}$$

where n is the number of electrons taking place in the reaction, F is Faraday's constant, A is the electroactive area of the electrode and j is the diffusive flux. Now, if one substitutes diffusive flux from Fick's first low into the above, equation is now:

$$I = nFA - D\,\frac{dC}{dx} \tag{1.9}$$

which is the general equation to represent the current response in relation to the concentration of the electroactive species, being the current directly proportional to the gradient of the concentration of such analyte.

Nevertheless, Fick's first law only considers diffusion at some point adjacent to the surface of the electrode, not taking into account diffusion between two different points. Therefore, Fick's first law is time dependant creating the necessity for another mathematical expression that takes this into account. That is Fick's second law, that explains the diffusion from one point to another in a single direction (applicable for macroelectrodes), considering the molecule's position.

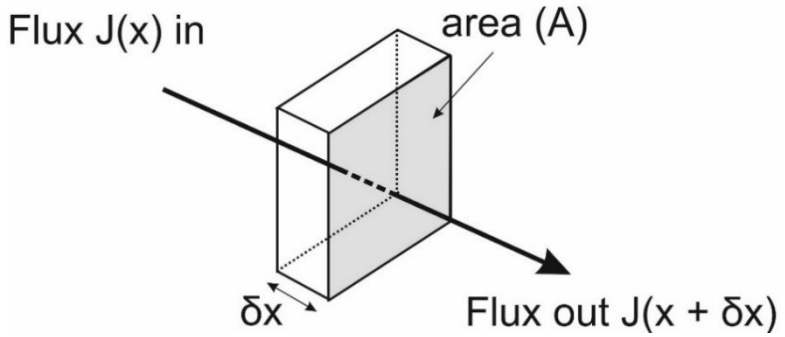

Figure 3. Fick's second law as a cross section of a known area of a cubic region. Both flux in (x) and flux out (x+ δx) of the cubic region are considered as function of the distance between two opposite faces of the cubic region (x).[3]

Fick's second law considers the change of the concentration of the analyte related to the concentration of the bulk, and the separation between these two points as follows:

$$\frac{dC}{dx} = D\frac{d^2C}{dx^2} \tag{1.10}$$

The total diffusive flux is then described as the combination of these components, namely the Nerst-Planck equation for a single dimension:

$$J(x,t) = -D\frac{dC(x,t)}{dx} - \frac{zFDC(x,t)}{RT}\frac{d\phi(x,t)}{dx} + C(x,t)V(x,t) \tag{1.11}$$

Where *dC/dt(x,t)* is the gradient of concentration at distance *x* and time *t*, *dϕ(x,t)/dx* is the potential gradient, *z* is the charge and *C(x,t)* is the concentration of the electroactive species, and *V(x,t)* is the hydrodynamic velocity in aqueous media**.**

According to Nernst, there is a diffusion layer where the physical processes occur, which is at distances around 10 Å from the electrode surface, where the concentration profiles of the analytes change (reactants are being consumed, generating product species). The movement of molecules due to gradient of concentration will occur, mainly, in this region.

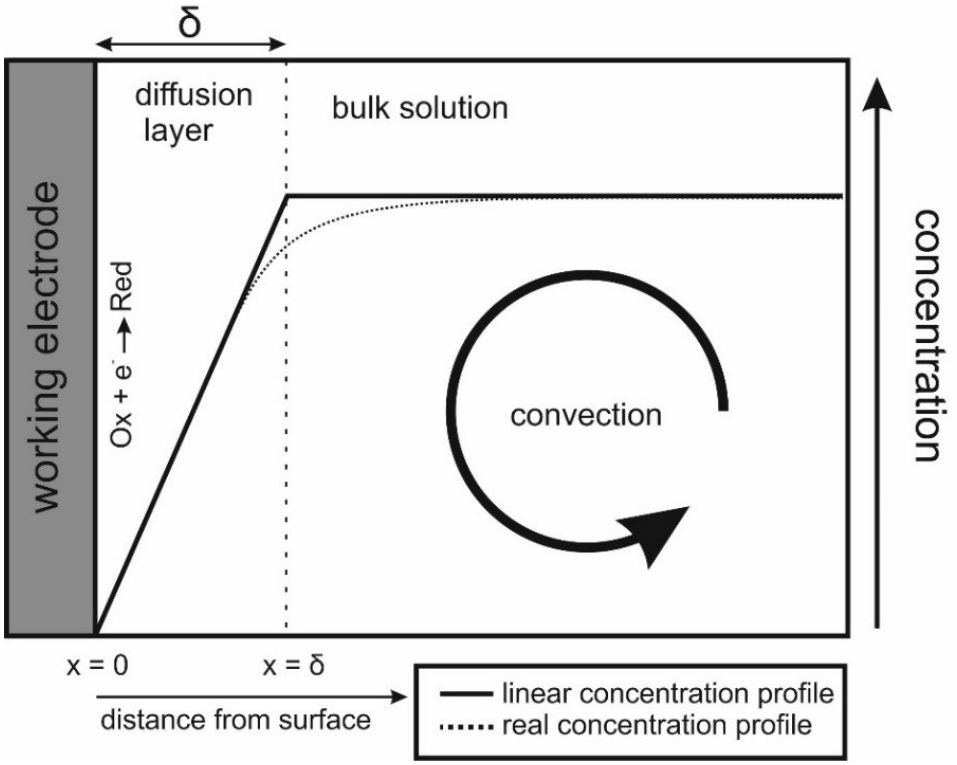

Figure 4. Schematic of the Nernst diffusion layer.

The Nernst model for diffusion layers is used to deduce the mass transport coefficient (*mT*) by experimentalists, by taking into account the flux in this region, therefore:

$$j = \frac{DC^x}{\delta} \tag{1.12}$$

where C^* is the concentration in the bulk solution of the electroactive specie and δ is the diffusion layer thickness. Combining this with Faradaic's current equation:

$$I = nFAD\frac{DC^x}{\delta} \tag{1.13}$$

And the mass transport coefficient is described as:

$$mT = \frac{D}{\delta} \tag{1.14}$$

Combining both, Faradaic current is:

$$I = nFADC^*mT \tag{1.15}$$

Where current is linked to mass transport coefficient when considering electrode kinetics.

1.1.3 Electrode kinetics

Electrochemical reactions, when mass transport is sufficient high, are controlled by the electron transfer kinetics between the electroactive species and the surface of the electrode. Current-potential relation is expressed as described above with equation 1.1, the rate of the forward reaction is given by:

$$k_{for} = k^0\exp(\frac{\alpha F}{RT}[E - E^o_{for}]) \tag{1.16}$$

and the rate of the backwards reaction is:

$$k_{back} = k^0\exp(\frac{-(1-\alpha)F}{RT}[E - E^o_{back}]) \tag{1.17}$$

where E is potential of the cell, k_{back} and k_{for} are the rates of the backward and forward reaction respectively. E^0_{for} and E^0_{back} are the standard potentials of the forward and backward reactions. k^0 is the overall electron transfer rate constant, α is the dimensionless transfer coefficient of the process (usually $\alpha = 0.5$, indicating the

symmetry of the electron transfer energy barrier), R is the universal gas constant and T is temperature.

In the case where in an electrochemical reaction, the forward reaction can be larger than the product of the mass transport coefficient and the rate of the background reaction:

$$k_{for} \gg k_{back} mT \tag{1.18}$$

And the opposite case where the background reaction is greater than the forward reaction:

$$k_{for} \ll k_{back} mT \tag{1.19}$$

However, in the case of mass transport coefficient being larger than the product of both forward and background reaction:

$$mT \gg k_{for} k_{back} \tag{1.20}$$

The system is under control of the electrode kinetics, and the current would be sensitive to the potential applied, leading to three different types of voltammetric systems:

- Reversible, where the electron transfer kinetics constant is so fast that the current response is only limited by the mass transport, with similar intensity for both oxidation and reduction ($I_{p,f} \sim I_{p,b}$) current peaks. Peak to peak separation (ΔEp) around 59 mV and independent of the scan rate. $k^0 \gg mT$
- Irreversible, where the mass transport is so large that the current response is limited exclusively by the rate of electron transfer, ΔEp larger than 212 mV/n, is dependent upon the voltage scan rate and the forward peak is larger than the backward peak. mT $\gg k^0$

- Quasi-reversible system when an intermediate case is happening, *ΔEp* is between 59 and 212 mV/n and $\left(I_{p,f} \sim I_{p,b}\right)$. $k^0 \sim mT$.

In the instance with electrochemical reversible processes with fast electron transfer kinetics, the peak to peak separation is small at the reversible limit (*ΔEp* ≈ 59 mV/n), where can be described as:

$$\Delta Ep = \frac{2.218RT}{nF} \tag{1.21}$$

Also, the intensity of the voltammetric current is ruled by the Randles-Ševćik equations at electrochemical processes as it follows[5-7]:

reversible: $$I_{p,f}^{rev} = \pm\ 0.446\, nFA_{real}C\sqrt{\frac{nFD\nu}{RT}} \tag{1.22}$$

quasi-reversible: $$I_{p,f}^{quasi} = \pm\ 0.436\, nFA_{real}C\sqrt{\frac{nFD\nu}{RT}} \tag{1.23}$$

irreversible: $$I_{p,f}^{irrev} = \pm\ 0.496\sqrt{\alpha n'}\, nFA_{real}C\sqrt{\frac{nFD\nu}{RT}} \tag{1.24}$$

where in all cases, *n* is the number of electrons in the electrochemical reaction, $I_{p,f}$ is the voltammetric current (analytical signal) using the forward peak of the electrochemical process, *F* is the Faraday constant (C mol^{-1}), ν is the applied voltammetric scan rate (V s^{-1}), *R* is the universal gas constant, *T* is the temperature (Kelvin), A_{real} is the electroactive area of the electrode (cm^2) and *D* is the diffusion coefficient (cm^2 s^{-1}), α is the transfer coefficient (usually assumed to be close to 0.5) and *n'* is the number of electrons transferred before the rate determining step.

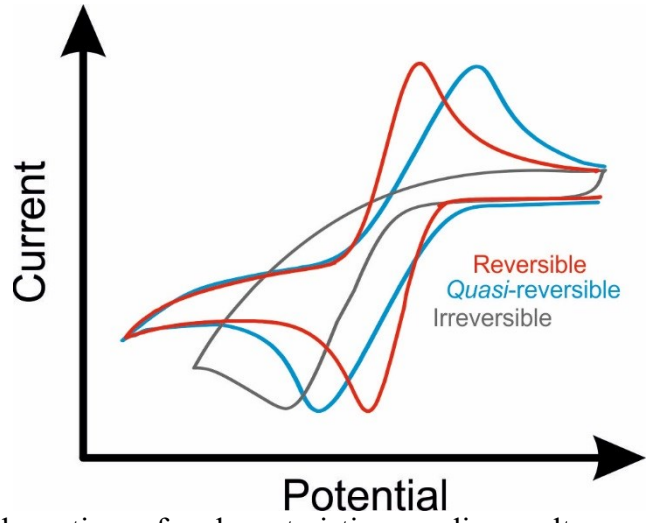

Figure 5. Schematic of characteristic cyclic voltammetric profile of hexaammineruthenium (III) chloride (RuHex), showing the typical voltammograms for reversible, quasi-reversible and irreversible electron transfer situations.

Randles-Ševćik equations can be also used to estimate the electroactive area (A_{real}) *via* a simple cyclic voltammetry experiment. In this method, typically, a reliable redox probe within an aqueous electrolyte is used to determine a plot of the *forward* peak current, $I_{p,f}$, as a function of applied voltammetric scan rate ($\nu^{1/2}$). This is since the Randles-Ševćik equation is derived from assuming that the concentration of the electroactive species (in the bulk solution) is the same as that at the electrode surface, due to the development of the diffusion layer [3].

Finally, the heterogeneous electron transfer (HET) rate constant can be calculated using the Nicholson's equation[8], which for quasi-reversible electrochemical reactions follows [9]:

$$\varphi = k^0_{obs}[\pi DnvF/RT]^{-1/2} \tag{1.25}$$

where φ is a kinetic parameter, D is the diffusion coefficient, n is the number of electrons that are taking part in the process, F is the faraday constant, ν is the scan rate, R is the gas constant and T is the temperature in Kelvin. In order to calculate the

HET rate constant, the peak-to-peak separation (ΔE_p) is used to deduce φ, where ΔE_p is obtained at various voltammetric scan rates[10]. The standard heterogeneous constant (k^0_{obs}) can be calculated *via* the gradient when plotting φ against $[\pi DnvF/RT]^{-1/2}$. In cases where ΔE_p is bigger than 212 mV, the following equation should be implemented:

$$k^0_{obs} = [\,2.18\left(\frac{\alpha Dnv F}{RT}\right)^{-\frac{1}{2}} \exp[-\left(\frac{\alpha \mathrm{nF}}{RT}\right)\Delta \mathrm{Ep}] \qquad (1.26)$$

where α is assumed to be 0.5.

1.2 Electrochemical methodologies

1.2.1 Cyclic Voltammetry

Cyclic voltammetry (CV) is the most commonly employed electrochemical procedure to gain knowledge about electrochemical reactions. CV offers quick identification of redox potentials depending on the electroactive species, displaying information about the kinetics of heterogeneous electron transfer reactions, adsorption processes and thermodynamics. CV is the linear scan of potential of the working electrode utilising a triangular potential wave form.

In CV experiments, the working electrode (WE) measures the current during a potential ramping, which is plotted as a function of time (called cyclic voltammogram). The potential goes from E_1 (starting potential) to E_2 (upper potential), and back to E_1 and a rate called scan rate which is the gradient of the line (scan rate is typically measured in V s^{-1}). If the potential is stopped after E_2, is known as linear sweep voltammetry (LSV).

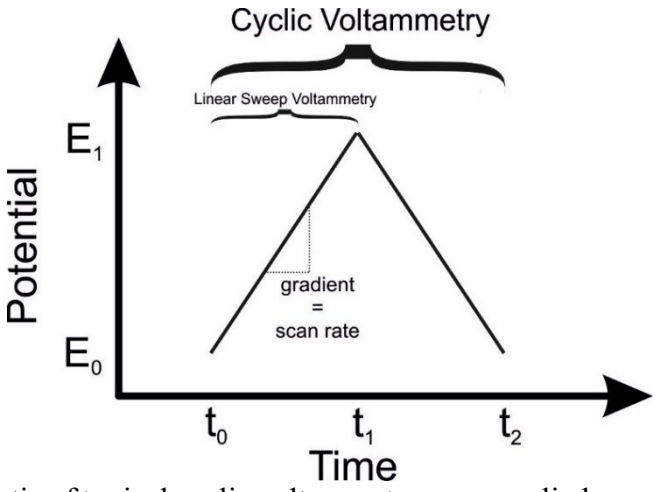

Figure 6. Schematic of typical cyclic voltammetry as an applied waveform of potential as a function of time.

Cyclic voltammograms are usually utilised to quantify an unknown analyte in solution (electroanalysis), and can also give information about the surface of the working electrode such as electroactive area (A_{real}), heterogeneous electron transfer kinetics (k^0) and diffusion coefficients (D).

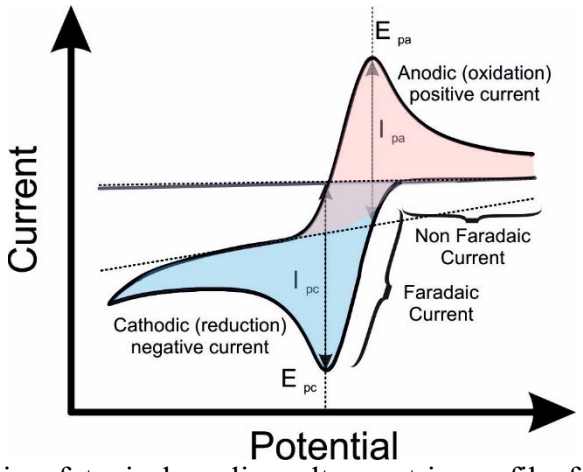

Figure 7. Schematic of typical cyclic voltammetric profile for the reduction of hexaammineruthenium (III) chloride (RuHex), showing the characteristics peak position (Ep) and peak height (Ip) of both anodic and cathodic peaks.

The typical voltammetric peaks are caused by the diffusion layer near the electrode surface, reflecting the constant changes of the concentration gradient with time. The increase in the peak current corresponds to the achievement of diffusion control, while

the current drop is dependent to $t^{-1/2}$ and independent to the applied potential. That is the reason why the forward and the reversal current have the same shape for diffusion control processes[2].

1.2.2 Chronoamperometry

Chronoamperometry (CA) is the experimental technique that consists in applying a fixed potential and measure the current over time. It is a key electroanalytical methodology that allows the distinction and understanding of the diffusional process occurring at the electrode surface. By holding the potential at which there is no Faradaic process happening, and then shifting to a potential where the reaction can proceed spontaneously while measuring the current, there will be a visible change in the peak current directly related to the concentration of the electroactive specie.

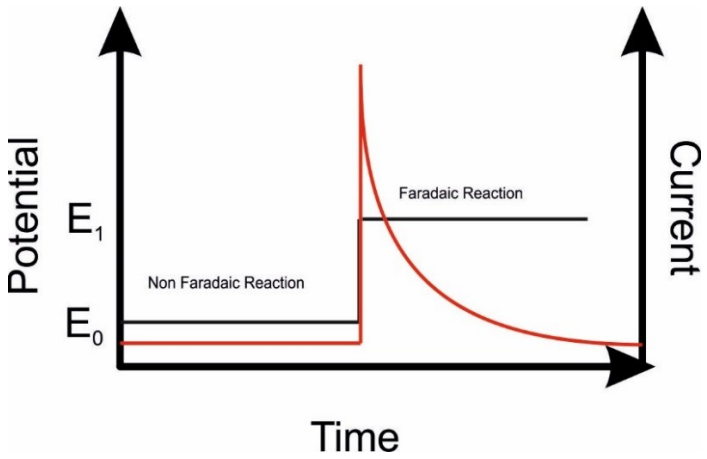

Figure 8. Schematic of typical chronoamperometric experiment, where a potential step waveform is applied from a non-faradaic region to a faradaic region, resulting in a change in the current response.

The mass transport process is only governed by diffusion during this process, therefore the current *vs.* time plot shows the change in the analyte concentration at the surface of the electrode, involving the increase of the diffusion layer that is associated with the decrease of the reactant (its concentration), which is also seen in the plot as time moves forwards.

A decrease in the current is due to the creation of a concentration gradient at the surface of the electrode, in which the flux of the electrochemical species can react rapidly at the surface, being in agreement with Cottrell's equation[1, 3], that describes the current as a function of time (at a planar electrode of infinite size):

$$i(t) = \frac{nFACD^{1/2}}{\pi^{1/2}t^{1/2}} \quad (1.27)$$

Where n is the number of electrons, F is Faraday's constant, A is the electroactive area of the electrode, C is the concentration of the electroactive specie and D is the diffusion coefficient.

It is important to highlight that the current of the double layer also contributes to the overall current, but also decays as a function of time$^{1/2}$ and is only significant at the beginning.

CA is frequently used to estimate the diffusion coefficient of electroactive species or the electroactive surface area of the working electrode. CA can also be applied as double-step methods, where the first potential generates a species and the second one analyses that secondary specie. This potential-step experiment can be used to study the charge *vs.* time relationship, due to the integration of the current recorded from the potential step (and including corrections for the charge due to the double-layer and the adsorbed species)[2]:

$$Q = \frac{2nFA_{real}C\sqrt{Dt}}{\sqrt{\pi}} + Q_{dl} + Q_{ads} \quad (1.28)$$

where Q is the charge, n is the number of electrons in the electrochemical reaction, $Areal$ is the electroactive area, F is Faraday's constant, C is the concentration, D is the diffusion coefficient, Q_{dl} is the double layer capacitance and Q_{ads} is the capacitance from the adsorbed species. Since the adsorbed materials are electrolyzed

instantaneously, the charge is not time-dependant and also the charging of the double layer is instantaneous and independent of time. Q_{ads} can be described as $nFA_{real}\Gamma_0$ where Γ_0 is the coverage of adsorbed reactant (mol cm^{-2}).

The charge measurement method, known as chronocoulometry (CC), is a classical electrochemical technique that has been overlooked over recent years. CC was developed by Anson[11] (see equation 1.28), which involves the measurement of charge *vs.* time response from an applied potential step waveform. CC is a useful technique in electrochemistry allowing one to readily determine the electrochemical active electrode area, as well as their respective diffusion coefficients, the time-window of an electrochemical cell, adsorption of electroactive species and rate constants for chemical reactions coupled to electron transfer reactions; this in summary, is a very useful electrochemical approach.

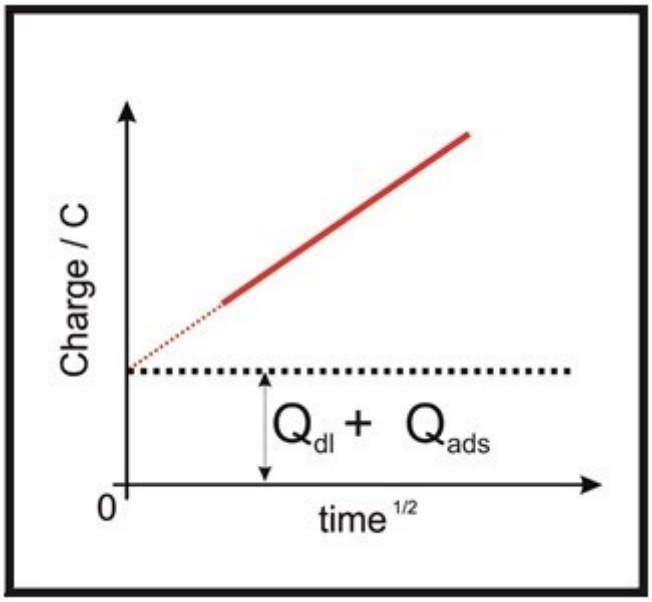

Figure 9. Representation of CC (charge *vs*. time$^{1/2}$) for an adsorbed electrochemical species.

1.3 Electrode materials: Graphene and related 2D materials

Graphitic electrodes have been extensively used in electrochemistry as an attempt to replace precious metals such as gold or platinum. Carbon shapes a variety of materials such as graphite, diamond or charcoal, it also includes a whole family of nanomaterials such as fullerene, graphene, carbon nanotubes (CNTs) and graphene nanoribbons (GNRs). All of these materials show different electrical, optical, thermal and chemical properties depending on their structures[12]. In recent decades, the traditional forms of carbon (e.g. graphite, carbon black or glassy carbon) have lost attention in favour of other novel carbon (see Figure 10) forms with enhanced properties, these are carbon nanotubes, graphene, graphene nanoribbons etc.

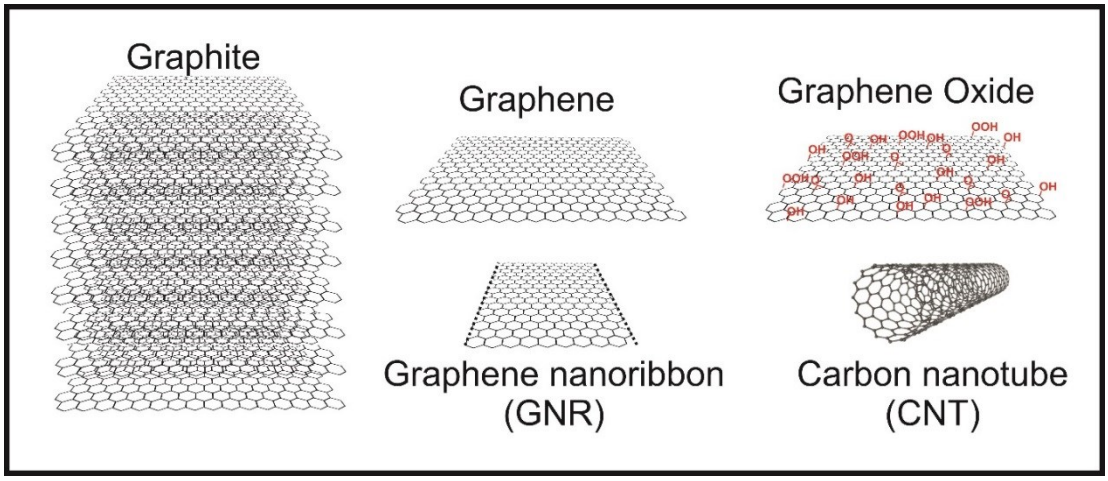

Figure 10. Representation of the structures of graphite, graphene, graphene oxide, graphene nanoribbons (GNRs) and carbon nanotubes (CNTs) respectively.

Carbon nanomaterials such as nanographite, carbon black and nanotubes have long been utilised as electrode materials within electrochemistry, outperforming traditional noble metals[13-15] and even the conventional carbon materials based on graphite or glassy carbon[16-19]. Chemical stability, structural polymorphism, wide operable potential windows, rich surface chemistry and strong C-C bonds present internally and between the carbon material and a surface modifier[20], are some of the reasons why carbon nanomaterials are at the forefront of innovation in

electrochemistry research, as it is fundamentally based on interfacial phenomena[20]. Carbon materials and electrochemistry have been bound to each other since the very beginning of electrochemistry[21], and the appearance of new carbon materials have been connected to research regarding the doping[22, 23], preparation[24], characterisation and application of these materials using electrochemical techniques[10].

1.3.1 Graphene

Graphene is a 2D monolayer lattice of sp^2 hybridised carbon atoms, and it has had the interest of scientists since its isolation as "pristine" graphene (*i.e.* mono-layer graphene without heteroatomic contamination) in 2004[25], which exhibits much greater surface area compared to graphite and even carbon nanotubes. Graphene has already been reported towards the sensing of biologically relevant molecules (such as dopamine[26], glucose[27], hydrazine[28], nitric oxide[29], b-nicotinamide adenine dinucleotide (NADH)[30], uric acid[31], epinephrine[31] or paracetamol[32] among others, allowing to reduce limits of detection[32, 33]. Therefore graphene would seem to be ideally suited for implementation into electrochemical applications[13] as a main component or as a foundation to develop new 2D graphene-based materials. Graphene's electrochemical properties are highly dependent upon its number of layers[34] and by the fabrication process by which it is synthesised as depicted in Figure 11.

Typically, graphene is fabricated *via* one of two routes; a bottom-up (BU) or a top-down (TD) approach. TD methods start from a graphite starting point and modify it to obtain a single layer of graphene. An example of TD methods is chemical/thermal reduction of graphene oxide or using physical/chemical exfoliation can give rise to a large quantity of graphene sheets; however, the fabricated graphene is generally highly defective and abundant with residual C/O groups or other contamination such as

surfactants or metals[35-38]. Bottom-up (BU) fabrication routes directly synthetises the mono-layer graphene from precursors, typically lead to higher quality graphene using carbon sources as methane, benzene and polymers, but in smaller quantities[39]. Chemical Vapour Deposition (CVD) utilises hydrocarbon gases as a precursor to grow graphene over a catalyst. The best effective catalysts so far are transition metal surfaces (namely Cu[40-42] to grow mono- and Ni[43, 44] to grow few-layer graphene). Copper has been recognised as the most appropriate catalyst for carbon formation due to its low affinity towards carbon, but still able to stabilise carbon on their surfaces by forming weak bonds[45].

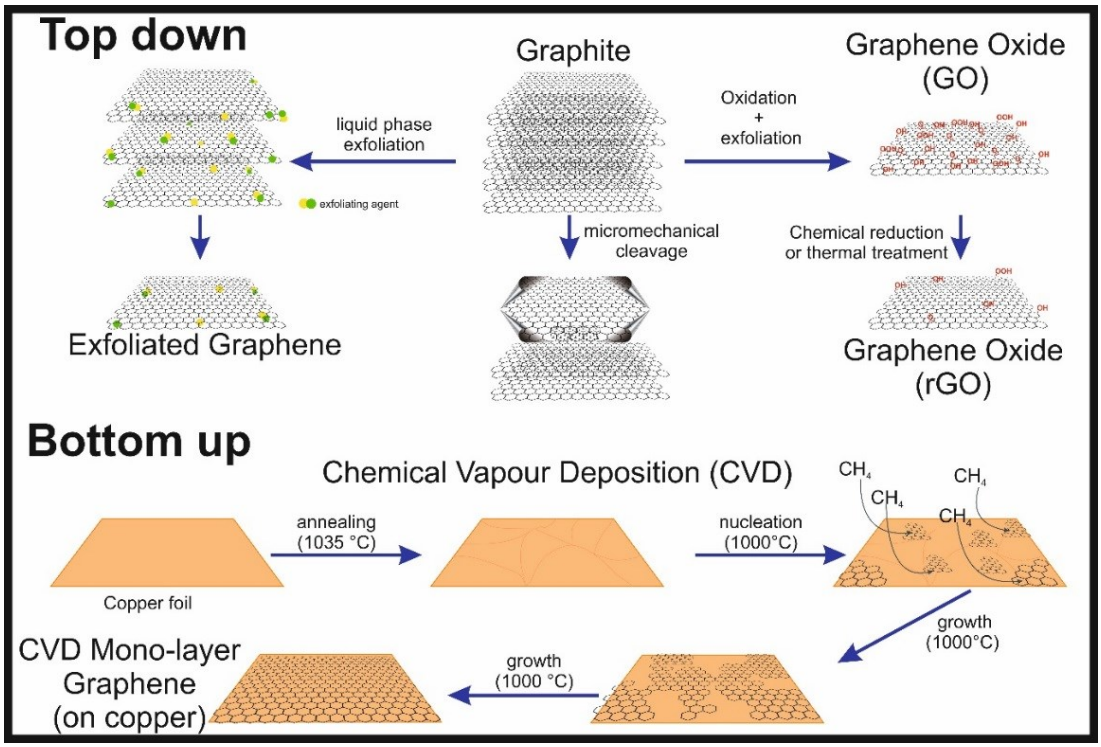

Figure 11. Representation of the top down and bottom up graphene synthesis method respectively.

CVD grown graphene is a BU route that facilitates the study of high quality monolayer graphene[45-47], which can then be transferred after the removal of the copper foil by wet chemical etching. Several transfer techniques have been reported to transfer CVD Graphene onto a suitable substrate, among them the use of Poly(methyl

methacrylate) (PMMA) is the most common one[41, 44, 48]. In this technique, PMMA is first spin coated onto the graphene-copper sample, followed by metal etching. PMMA/Graphene sample would then be scooped onto the substrate, followed by a baking step and finally the PMMA layer would be etched by dissolving it in acetone[49, 50]. PMMA has previously been reported to affect the physical and electrical properties of CVD grown graphene samples transferred *via* this route[51-57].

Fundamental work exploring CVD grown mono-, double- and few-layer graphene electrodes have been reported to exhibit different electron transfer kinetics to each other[34], revealing that the electrochemical response is dependent on the density of edge plane like-sites/defects at graphene-based electrodes. Such performance is due to pristine graphene's fundamental geometry, which contains a small edge plane and large basal plane presence when compared to few- and multi-layer graphene. There is great interest in graphene and graphene-based materials as potential electrodes for energy applications such as supercapacitors[58-61], solar cells[62-65], fuel cells[66-68] and water splitting[69], but further fundamental research needs to be studied.

1.3.2 Other 2D materials: hexagonal boron nitride (hBN)

Boron nitride (BN) is a structural analogue of graphite, in which an equal number of boron and nitrogen atoms form a honeycomb lattice structure[70] of sp^2 bonded layers[71]. This structure is not found naturally and was first synthesised by Balmain[72, 73] in 1842.

Hexagonal boron nitride (2D-hBN) is a structural analogue of graphene and has high thermal conductivity and robustness to oxidation[74], which historically has allowed it to be used as lubricant[75-77]. 2D-hBN has also been reported to improve the mechanical properties of composites, even at low percentages[78-80], when added as few layered nanosheets due to its low density, good thermal and chemical stability[81-83].

According to the literature, pristine 2D-hBN (see Figure 12) has a wide band gap (*ca*. 5.2-5.8 eV)[84, 85] making it an electrical insulator[85], with it being widely applied as a charge leakage barrier-layer in electronic equipment[71, 86]. 2D-hBN has also been used to tailor the bandgap of graphene (creating graphene-hBN interfaces)[86-97]. Another approach to decrease hBN's bandgap is by creating thin strips of single layered 2D-hBN nanosheets, producing nanoribbons (NRs) (see Figure 12), which contain a honeycomb lattice with an armchair or zig-zag edge that possess active dangling bonds[98]. The electronic properties of such nanoribbons are strongly affected by edge termination structures, reconstructions and functionalizations[99, 100] and recently several reports have indicated electrocatalytic behaviour of 2D-hBN[101, 102].

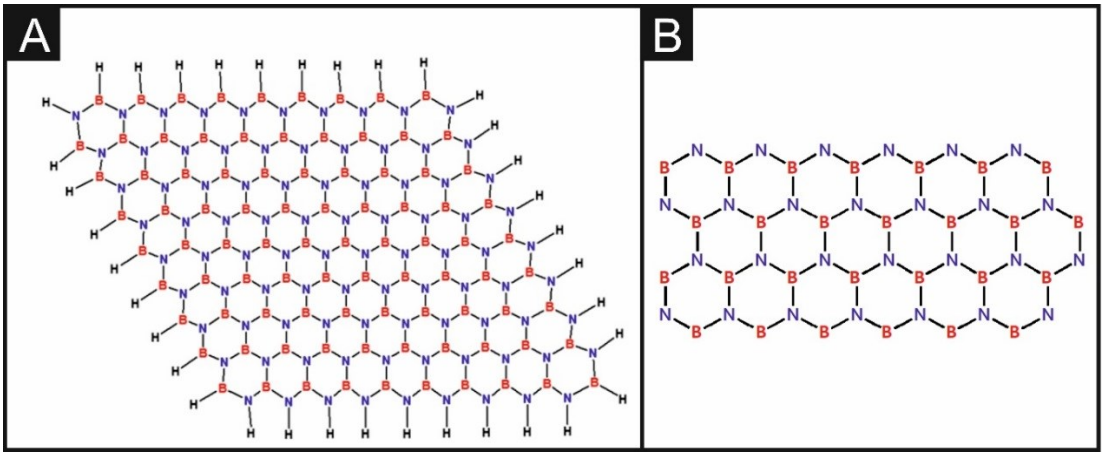

Figure 12. 2D chemical structure of the 2D-hBN mono-layer (A) and hBN nanoribbon (B).

As a summary, this thesis explores the electrochemistry of 2D materials (mainly graphene and 2D-hBN) from the single layer scale (CVD grown) to powder and fully 3D printed structures towards a range of electrochemical applications and considers the effects of the stability and defects upon the observed electrochemistry.

Chapter 2: Experimental Section

This chapter describes the overall experimental settings applicable to the work reported herein, unless specifically said otherwise. In the cases where conditions are different, individual experimental sections included in each chapter of this thesis will be added when relevant.

All chemicals used were analytical grade and were used as received from the manufacturer without any further purification. All solutions were prepared with deionised (DI) water of resistivity no less than 18.2 MΩ cm and were vigorously degassed prior to electrochemical measurements with high purity, oxygen free nitrogen.

Electrochemical measurements were carried out using an Autolab PGSTAT204 potentiostat (Metrohm Autolab, The Netherlands). All measurements were conducted using a three electrode system. Working electrodes were variable, and unless differently stated, a platinum counter/auxiliary electrode and an Ag/AgCl reference electrode completed the circuit.

2.1 Physicochemical characterisation

2.1.1 Raman spectroscopy

Raman spectroscopy is a non-destructive technique that analyses the inelastically scattered light produced by the interaction of the light with the atomic vibrations (as shown in Figure 13). In Raman spectroscopy, a beam of light interacts with a sample, where the main measurement recorded is the shift in energy between the incoming and the inelastically scattered light[103]. Majority of the light is reflected and a small fraction of the incoming light is scattered due to the inhomogeneities inside the sample. Those inhomogeneities can be static as crystal dislocations, generating

elastic scattering (when there is no change in wavelength), or dynamic scattering such as atomic vibrations (when there are changes in the wavelength). Raman spectroscopy has historically been a powerful tool for the fundamental understanding and characterisation of graphitic materials[104-108], and has also become the most common spectroscopy used to study and characterise graphene[109-111].

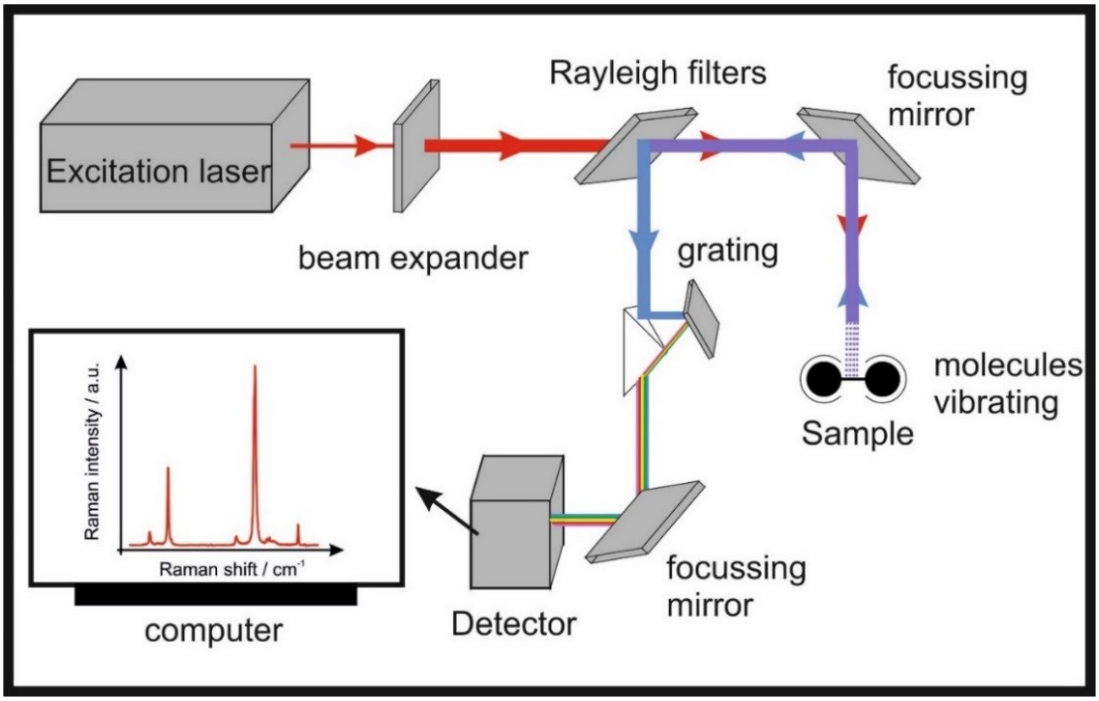

Figure 13. Schematic of Raman spectrometer platform setup.

Raman mapping spectroscopy data from chapters 4, 5 and 8 was recorded using a Thermo Scientific DXR Raman microscope fitted with a 532 nm excitation laser at a low power of 3 mW to avoid any heating effects. In chapters 4 and 5, spectra were recorded using a 3 seconds exposure time for 3 accumulations in each point. To collect the map we used a step size of 75 x 75 µm, to collect a Raman profile between the region of 1050 and 3300 cm^{-1}. In chapter 8 spectra were recorded using a 10 seconds exposure time for 10 accumulations in each point. To collect the map a step size of 10 x 10 µm was used, to collect a Raman profile in the region of 1100 and 2000 cm^{-1}. Raman Mapping Spectroscopy data included in chapter 6 was collected using XploRA PLUS (Horiba, UK) fitted with a 638 nm excitation laser at a low power of 3 mW to

avoid any heating effects. Spectra were recorded using a 5 seconds exposure time for 1 accumulations at each point. To collect the map a step size of 40 x 40 μm and a Raman profile between the region of 1300 and 3200 cm^{-1} was employed, mapping a circular-shaped area of 2.6 mm of diameter.

2.1.2 Scanning electron microscopy (SEM)

Scanning electron microscope (SEM) is a type of electron microscope that produces an image by focussing a beam of high-energy electrons that hits the surface of the sample as shown in Figure 14. When the electrons hit the sample, they produce secondary electrons (that produce SEM images) and other signals such as backscattered electrons, X-rays, photons, visible light and heat. These signals are detected by their respective detectors. When the electron beam hits the sample, it penetrates a few microns and produces secondary and backscattered electrons, depending on their accelerating voltage and the sample itself, secondary and backscattered electrons are the most common ones used for imaging.

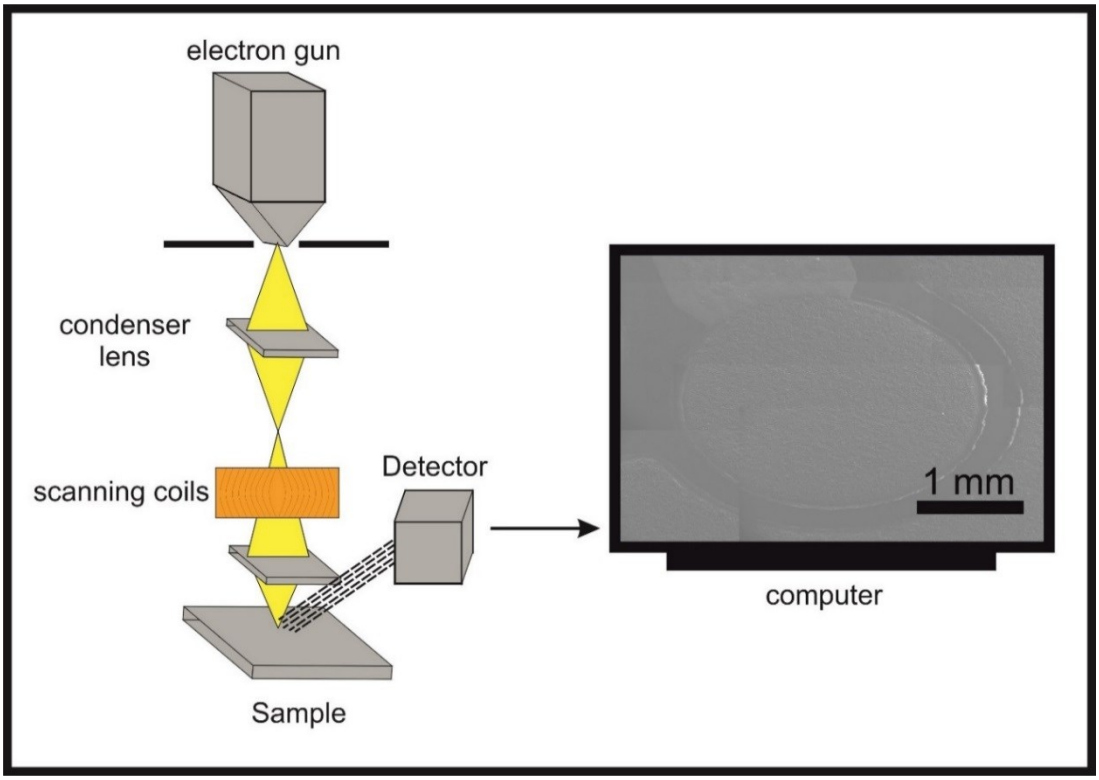

Figure 14. Schematic of a Scanning Electron Microscope setup.

SEM images and surface element analysis were obtained using a JEOL JSM-5600LV model SEM equipped with an energy-dispersive X-ray microanalysis (EDS) package.

2.1.3 Other techniques

2.1.3.1 Atomic Force Microscopy (AFM)

Atomic Force Microscopy (AFM) data was collected using a DualScope C26 (DME, Germany), carried out using AC mode using DS 95 AC probes with a spring constant of 42 N m^{-1} (DME, Germany). Scans were carried out at 40 µm s^{-1} with a force set point of 6 nN. Samples were attached to glass microscope slides using double sided tape.

Unless stated otherwise, AFM data was collected by Dr. Kathryn A. Whitehead.

2.1.3.2 X-Ray Photoelectron Spectroscopy (XPS)

X-Ray Photoelectron Spectroscopy (XPS) data was acquired using an AXIS Supra (Kratos, UK), which was equipped with an Al X-ray source (1486.6 eV) operating at 300 W in order to perform survey scans and 450 W for narrow scans. All X-rays were mono-chromated using a 500 mm Rowland circle quartz crystal X-ray mirror. The angle between X-ray source and analyser was 54.7°. With an electron energy analyser: 165 mm mean radius hemispherical sector analyser operating in fixed analyser transmission mode, pass energy 160 eV for survey scans and 40 eV narrow scans. A detector with a delay line detector with multichannel plate was utilised.

Unless stated otherwise, XPS data was collected by Dr. Samuel J. Rowley-Neale and Dr. Christopher W. Foster.

2.1.3.3 Density-Functional Theory (DFT)

Density Functional Theory (DFT) calculations were performed to unravel the reasons underlying the enhanced electron-transfer properties of 2D-hBN after making line defects and edge plane sites. All DFT computations were performed using B3LYP/LANL2DZ functional implemented in Gaussian 09 package. GaussView Version 05 package was used for visualization of the optimized structures, highest

occupied molecular orbital (HOMO) and the lowest unoccupied molecular orbital (LUMO).

Unless stated otherwise, DFT characterisation was collected by Dr. Ahmed S. Abo Dena.

2.2 Electrode materials

2.2.1 Screen-printed Electrodes

The Screen-printed electrodes (SPEs) were manufactured in-house with appropriate stencil designs to achieve a 3.1 mm diameter working electrode, using a carbon-graphite ink (Product ink: C2000802P2; Gwent Electronic Materials Ltd, UK) printed using a DEK 248 screen printer machine (DEK, Weymouth, UK) onto a polyester (Autostat, 250 micron thickness) flexible film. This layer was cured in a fan oven at 60 °C for 30 minutes and finally, a dielectric paste (Product Code: D2070423D5; Gwent Electronic Materials, UK) was then printed onto the polyester substrate to cover the connections. After a second curing process at 60 °C for 30 minutes, the SPEs are ready to be used. The in-house fabricated SPEs have been previously reported and characterised[112, 113]. Unless stated otherwise, SPE were fabricated by Dr. Christopher W. Foster and Dr. Samuel J. Rowley-Neale.

2.2.2 Edge-plane pyrolytic carbon and glassy carbon electrodes

The edge plane-pyrolytic graphite (EPPG) working electrode (4.9 mm diameter, Le Carbone, Ltd. Sussex, UK fabricated from highly ordered pyrolytic graphite) and the glassy carbon (GC) working electrode (3 mm diameter, BAS, Indiana, USA) were used without any further modifications from the manufacturer. EPPG and GC electrodes were polished before the start of each experimental using two diamond suspensions (1 and 0.25 μm; Kemet international Ltd., Kent, United Kingdom[114]) in a spray format. After carrying out each polishing step, the electrode

was washed and sonicated in DI water in order to remove diamond particles.

2.2.3 Chemical Vapour Deposition (CVD) grown mono-layer boron nitride (2D-hBN)

CVD grown mono-layer boron nitride (2D-hBN) on SiO_2 wafer were commercially obtained from Graphene Supermarket[115] (Reading, MA, USA)[116], which is grown on copper foil under low pressure (LPCVD) using borazane as precursor at a fixed temperature of 1000 °C. First, borazane is heated up to 130 °C to generate borazane vapour from its solid and to diffuse to the growth chamber while being carried out by hydrogen gas. Borazane is decomposing producing hydrogen, monomeric aminoborane (BH_2NH_2) and borazine (HBNH). Monomeric aminoborane is very active and it forms polymeric aminoborane, which is a white non-crystalline solid and stable at room temperature. Following growth, the 2D-hBN is transferred onto an oxidised silicon wafer (electrochemically inert supporting substrate) *via* a poly-methyl methacrylate (PMMA) assisted transfer method, the exact details are proprietary information[116].

2.2.4 Chemical Vapour Deposition (CVD) grown mono-layer graphene electrodes

The commercially available CVD synthesised graphene films were obtained from 'Graphene Supermarket' (Reading, MA, USA)[116] and is known as 'graphene on 285 nm SiO_2 Wafer'. The single layer continuous graphene film (*ca*. 97% graphene coverage (95% monolayer) with occasional holes, cracks and small multi-layer islands) comprises graphene grains of different crystallographic orientations (polycrystalline in nature) and is grown utilising a copper foil (0.025 mm thick) catalyst *via* a CVD synthesis method (*ca*. 1000 °C (cooling rate 40–300 °C min^{-1}) with H_2/CH_4 precursor (0.06 sccm and partial pressure 66.66 Pa) for less than 3 minutes growth time[47]). Following growth, the graphene is transferred onto an oxidised silicon

wafer (electrochemically inert supporting substrate) *via* a poly-methyl methacrylate (PMMA) assisted transfer method, as previously reported and characterised[47, 117-119], the exact details are proprietary information[116].

The commercially available CVD synthesised double-layer graphene film was obtained from 'Graphene Supermarket' (Reading, MA, USA)[116] and is known as 'Single/Double Layer graphene on 285 nm SiO_2 Wafer'. The mono-/bi-layer continuous graphene film (*ca*. 95% graphene coverage (up to *ca*. 30% coverage is double-layer graphene islands) with occasional holes and cracks) comprising graphene grains of different crystallographic orientations (polycrystalline in nature) is grown utilising a modified method of the aforementioned CVD process. An example of this CVD method would be, a copper foil (206 nm thick) catalyst is utilised *via* a CVD synthesis method (*ca*. 800 °C (cooling rate 40– 300 °C min^{-1}) with H_2/CH_4 precursor (5 sccm and partial pressure 52 Pa) for *ca*. 10 minutes growth time)[47, 117], after which the graphene film is transferred onto an oxidised silicon wafer *via* the PMMA assisted transfer method, as previously reported and characterised[47, 117-119]. The exact details are proprietary information[116].

The CVD graphene working electrodes were secured into a 3D printed electrochemistry cell described in Figure 15, connected with copper foil to a crocodile connector which leads to the potentiostat and external reference and counter electrodes. In this work, 0.025 mm copper foils (99.99+%) purity from Goodfellow were used to grow graphene. A polymer-free graphene transfer method, 0.1 M $(NH_4)_2S_2O_8$ 98% from Sigma-Aldrich in DI water and hexane 97% from Sigma-Aldrich, were used.

Autodesk software has been used to design the 3D printed electrochemistry cell, which has been printed using a UV curable proprietary polymer and a Form 2 3D printer

from Formlabs, USA. The use of a bespoke electrochemistry cell configuration (Figure 15) allows us to carry out electrochemistry experiments with a solution and analyse the sample (1 x 1 cm graphene sample) with the DXR Raman without needing external manipulation, keeping the electrode area constant and having extra space to allocate reference and counter electrodes.

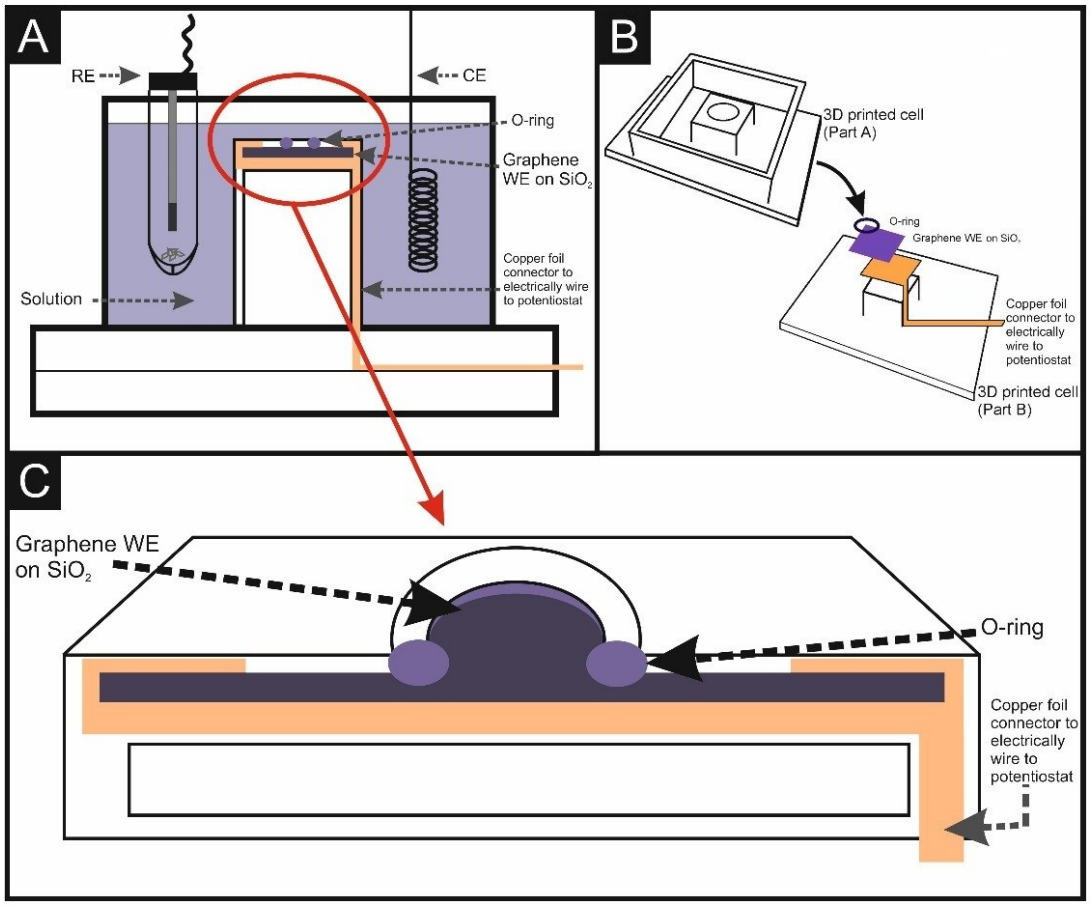

Figure 15. Schematic cross-sectional perspective of the CVD graphene 'housing' 3D printed cell (A) designed using Solidworks and 3D printed using a Form 2 3D UV curable printer. Reference and counter electrodes are incorporated into the three-electrode system in the 3D printed cell. Schematic diagram of the CVD graphene 'housing' 3D printed cell (B). The cell allows the connection of the monolayer graphene sheet to the potentiostat with a copper foil wrapping the graphene chip and allowing its use under a microscope or Raman Spectrometer without dismounting and manipulating the chip. There is a silicon O-ring sealing the graphene chip, keeping the studied area of the WE.

2.2.5 Graphene in-house growth

The graphene in-house growth has taken placed in a nanoCVD-8G rig from Moorfield, which uses a cold-wall variant of the chemical vapour deposition. Chemical Vapour Deposition (CVD) of monolayer graphene on copper has been proven to be one of the most competitive graphene growth method. In this project a cold wall variant of the CVD process is used, where the Cu foils are selectively heated at temperatures ≈ 1000 °C in a quartz tube furnace, in which the hydrocarbon gas flows as precursor gas. This method, as other cold wall CVD systems, allows faster and more efficient temperature ramps, shorter growth times and less gas consumption. This leads to a more uniform heating of the copper foils acting as a substrate, reducing the contaminants that might happen due to chemical reactions that can take place in the gas phase at high temperature, and allows the quality of the graphene sheets grown by CVD on copper foil to be enhanced, due to very fast cooling rates[120].

2.2.5.1 Growth procedure for graphene sheets

Using a CVD-8G rig from Moorfield (schematic shown in Figure 16), our own monolayer graphene has been grown in the lab following an in-house recipe based on the one developed by Bointon[120]. Copper foils (25 μm, 99.99+%) were placed in the stage (1 cm by 1 cm square sample), followed by heating up the CVD system from room temperature to 1035 °C (growth temperature) with H_2 gas flowing at a rate of 0.4 sccm at 1.33 Pa. Following this, the annealing step was performed for 300 seconds at 1035 °C in a H_2 atmosphere, keeping a constant 0.4 sccm H_2 flow at 1.33 Pa. This is followed by a nucleation and growth process at 1000 °C, with the first 120 seconds with a flow of 1.4 sccm of CH_4 and then 600 seconds (also compared to 720, 900, 1200 and 1800 seconds) at 7 sccm of CH_4, keeping constant the 0.4 sccm of H_2. Next there is a cooling down process, based on a flow of H_2 at 0.4 sccm and Ar at 100 sccm,

which reduces the temperature from 1000 °C to 190 °C for 600 seconds at 1.33 Pa. Finally, the sample is left cooling down at atmospheric pressure, and no gas flow until a temperature below 40 °C is reached to avoid any copper oxidation.

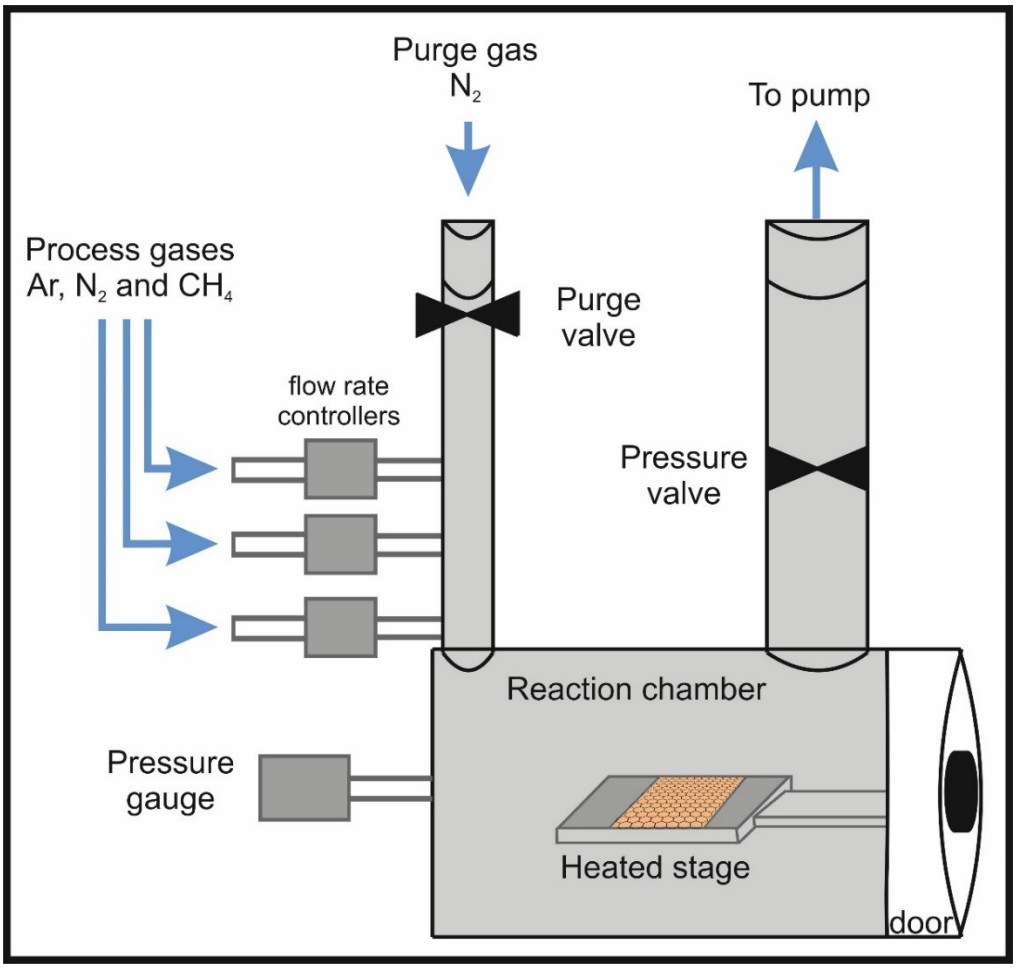

Figure 16. Schematic diagram of the cold-wall Chemical Vapour Deposition (CVD) rig used for graphene growth. The arrows indicate the direction of gas flow.

The number of layers and the quality of the graphene was compared depending upon their nucleation and growth time with Raman Spectroscopy from Figure 17, including its typical D (≈1335 cm^{-1}), G (≈1590 cm^{-1}) and 2D (≈2690 cm^{-1}) bands, showing that the 12 minutes variant (described in Figure 18) was the one which gives rise to the best monolayer graphene coverage and high quality due to the shape, position and relative intensity of the G and 2D peaks ($I_{G/2D}$) similar to 0.25.

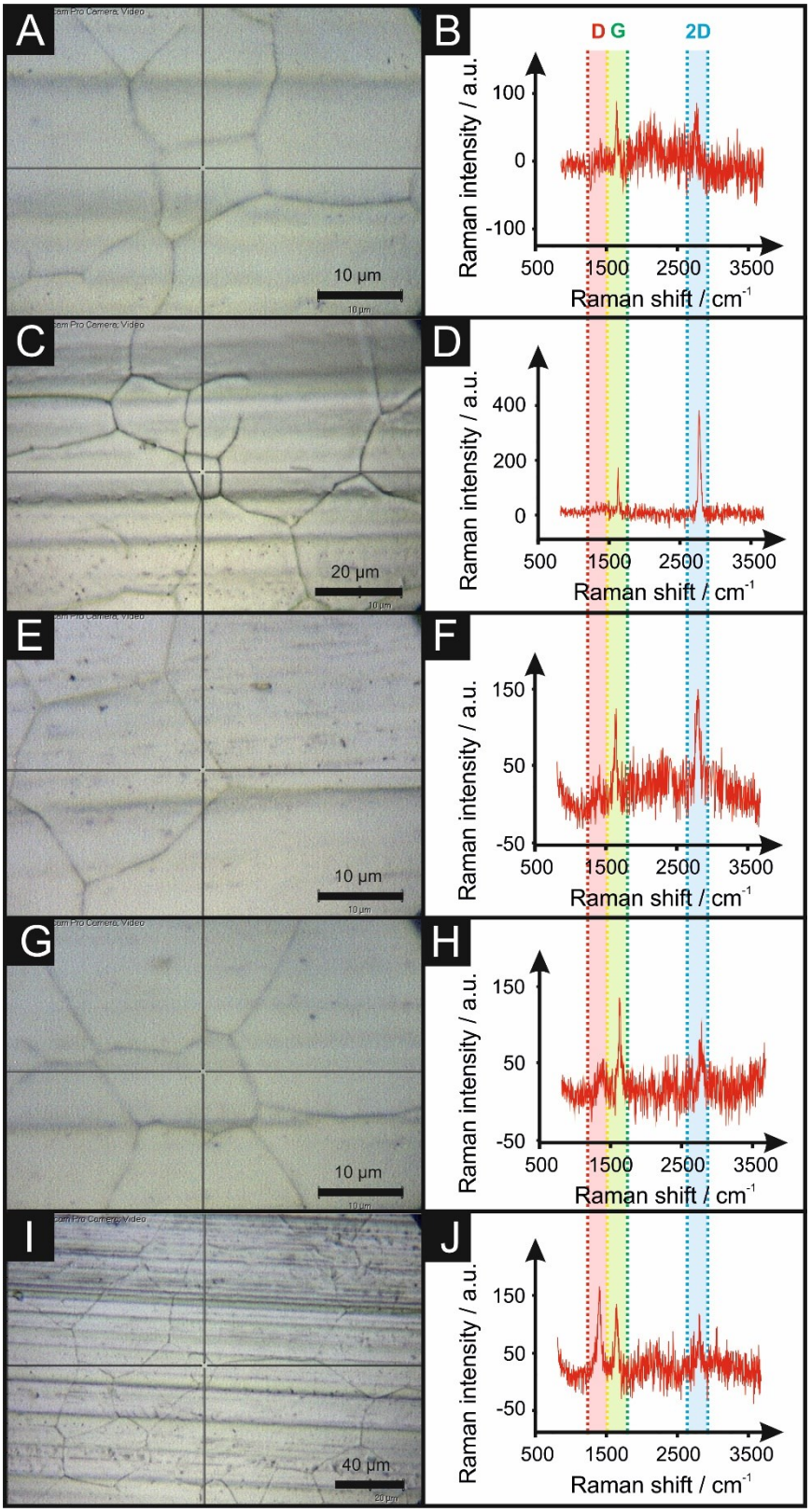

Figure 17. Comparison of the Raman profile and optical image respectively of 10 minutes (A and B), 12 minutes (C and D), 15 minutes (E and F), 20 minutes (G and H) and 30 minutes (I and J) of growth time.

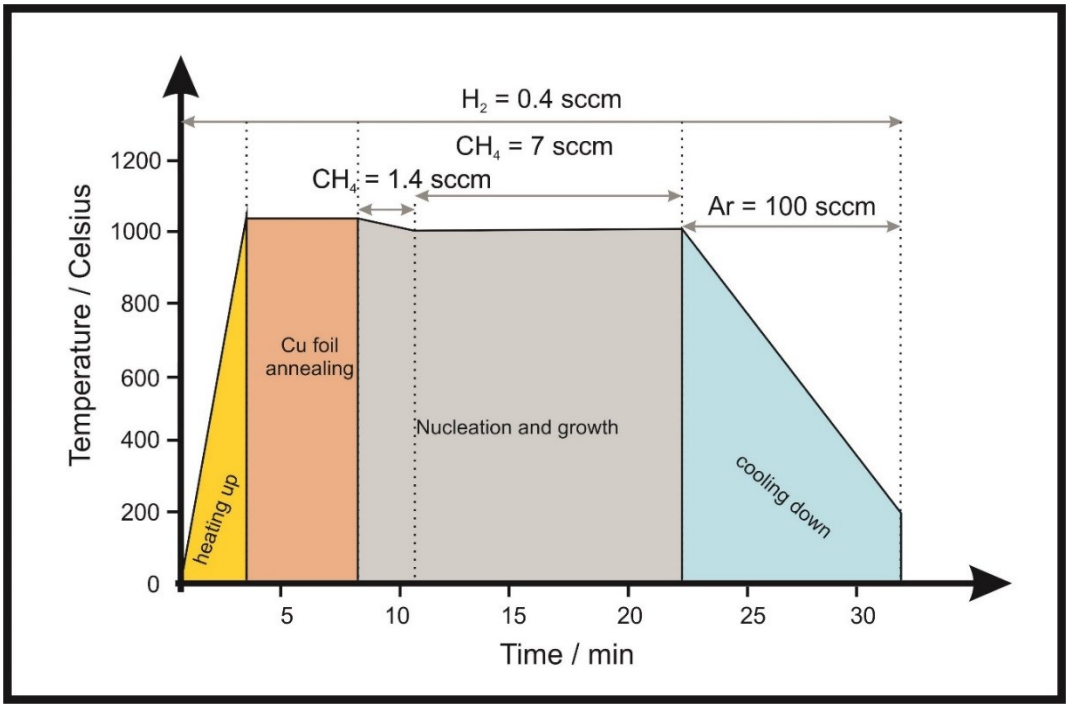

Figure 18. Graphene 12 minutes growth temperature curve, including H_2, CH_4 and Ar flow rates at every stage.

Phonon dispersion of graphitic materials is an important topic interpreting their Raman spectra. Phonons are atomic vibrations, being a phonon the unit of vibrational energy that come from atoms that are oscillating within a crystal. In graphene, the optical phonons in the central zone (Γ) and in the edges (K and K') have great interest, due to their accessibility using Raman spectroscopy. The Γ point optical phonons are generated with symmetry (for pristine graphene). The vibrations correspond to rigid displacements of two sub-lattices. This phonon is Raman active, and generates the Raman G band in graphene[111].

The 2D band (double or triple resonance) begins with an electron of wave-vector k around K absorbing a photon. That electron is in-elastically scattered by a phonon or a defect of wavevector q to a point belonging to a circle around the K point (with a wavevector $k+q$). The electron is then scattered back to a k state, emitting a photon by recombining with a hole at a k state. In case of the D band, one scattering

process is elastic (defect) and the other one is inelastic (emitting or absorbing a phonon). In the case of the 2D band, both processes are inelastic, with two phonons involved. The triple resonance process can happen by both scattering of electrons and holes, added to the recombination at the inequivalent *K'* point with respect to *K* point generating a photon. The G and 2D bands represent the two-dimensional hexagonal lattice is due to the bond stretching of all pairs of sp^2 atoms in rings and chains[109, 110, 121].

The designation of the Raman band for Graphene is depicted in Figure 19. The G band is related to the first-order Raman band of all sp^2 hybridized carbons. The D band is usually associated with defects and disorders due to the breathing modes of sp^2 atoms in rings within graphite atoms in rings within graphite layers[110, 122-124]. There is tangential stretching of the σ bonds along the plane that gives rise to the G band, which is a one phonon intra-valley scattering process at the Γ point. The in-plane transverse optical (iTO) phonon around the edges is accessible by a two-phonon Raman process, giving rise to the 2D band (also called G') of graphene.

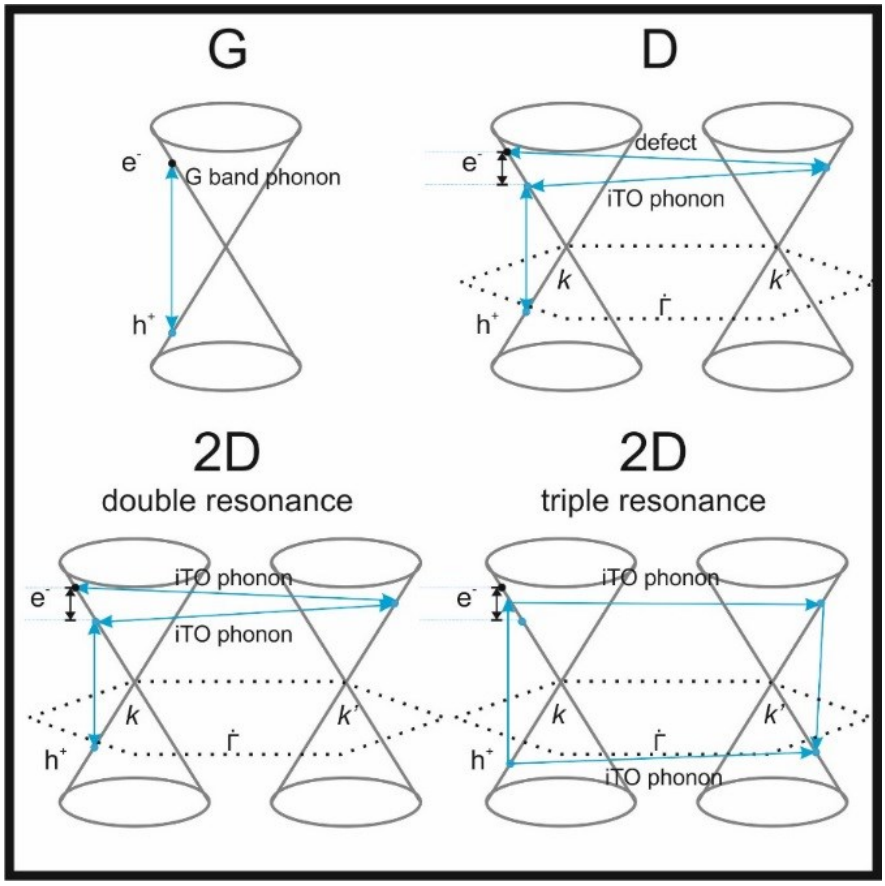

Figure 19. Raman scattering process for graphene Raman bands. First-order G band process, one-phonon second-order double resonance (DR) process for D band (intra-valley process) and two-phonon second-order resonance Raman spectral processes for the DR G process for the triple resonance process for monolayer graphene. For one-phonon, second-order transitions, one of the two scattering events is an inelastic scattering event. Resonance points are shown as circles near the K and K' points respectively.

2.2.5.2 Transfer procedure of graphene sheets from Cu foil onto other substrates

A modified version of the polymer free transfer method is utilised in this work adapted from Zhang[125], that makes use of an organic/aqueous biphasic configuration made from hexane/ammonium persulfate. The ammonium persulfate acts as an etching solution to remove the copper avoiding the use of any polymers that can contaminate graphene[48, 53], as depicted in Figure 20. After etching all the copper below

the graphene, the sheets are transferred into a DI water/hexane interface to clean any etching product that might still be in solution. To transfer the free-floating graphene sheet onto another substrate or solution, the sheet is scooped out with a Si/SiO_2 wafer or the desired final transfer to be used as an electrode for further studies.

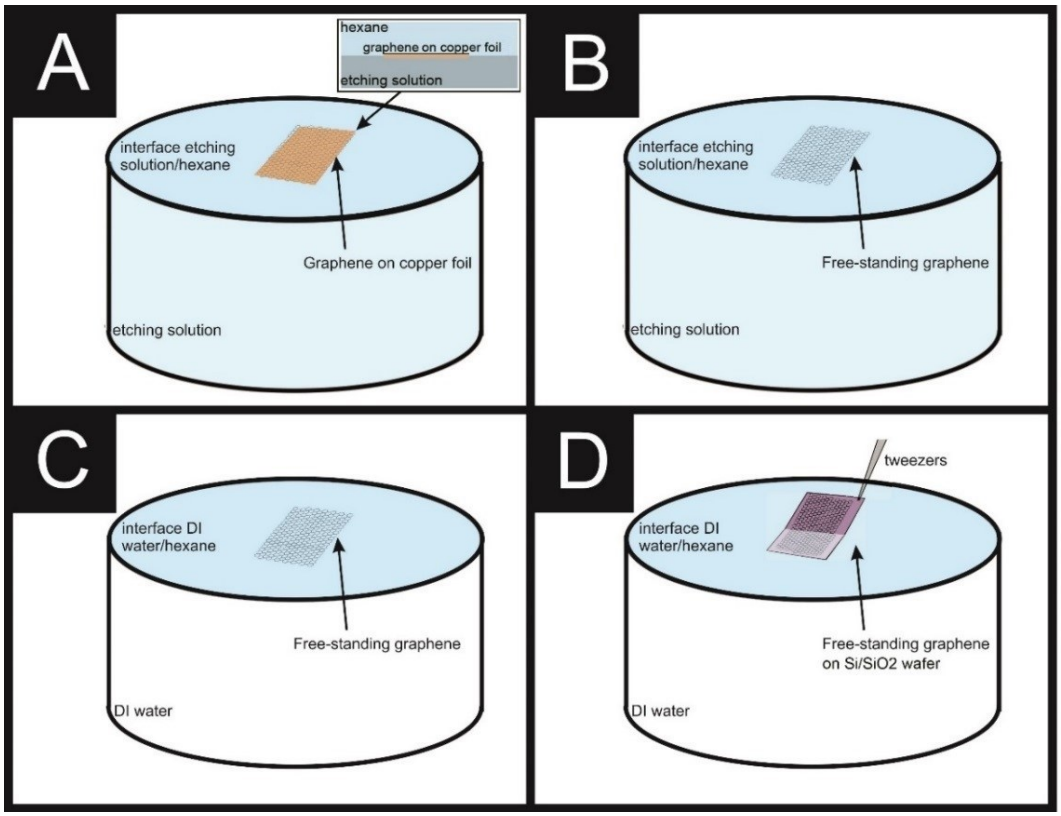

Figure 20. Graphene/copper sample floating at the hexane/etching solution interface. Where A shows that the graphene sheet on copper would be floating between the hexane and the etching solution (0.1 M ammonium persulfate). B shows the process after 5 hours of etching, when the copper is completely removed from the sample. C depicts the cleaning process of the sample when the graphene floats between hexane and DI water in order to clean copper or etchant residues. D shows the graphene sheet being transferred to a Si/SiO_2 wafer or other substrate.

Chapter 3: Determination of electroactive area of electrochemical sensing platforms

This chapter investigates determination of the electroactive area of polymer-free CVD grown mono-layer graphene electrodes using a range of outer- and inner- sphere redox probes and various experimental approaches. There is a clear need to standardise mono-layer graphene samples fabricated and used globally in electrochemical applications. In order to achieve this, two approaches are explored: cyclic voltammetry (CV) in conjunction with the appropriate Randles-Ševćik equation and chronocoulometry (CC) with the implementation of the Anson plot. Herein, the importance of redox probe selection is highlighted and shows that for CVD grown mono-layer graphene, the use of an outer-sphere redox appears to be the optimal approach to be used in order to report the electroactive area of the given mono-layer graphene electrode/surface. Conversely, when employing an inner-sphere redox probe, electrochemists should take into account the fouling of the electrode surface when this is used multiple times (*i.e* scan rate study).

3.1 Introduction

An important factor when utilising electrochemical platforms (such as glassy carbon, edge-plane pyrolytic carbon, screen printed electrodes (SPEs) etc.) is the determination of their electrochemical active surface area, which allows for the benchmarking of these SPEs and is an important parameter in Quality Control. In this chapter, it is considered the use of cyclic voltammetry (CV) and chronocoulometry (CC) to allow for the determination of the electrochemical area of screen-printed and mono-layer graphene electrochemical sensing platforms, comparing them to classic electrodes such as glassy carbon (GC) and edge-plane pyrolytic carbon, highlighting to experimentalist the various parameters that need to be diligently considered and controlled in order to obtain useful measurements of the electroactive area.

Screen-printed electrochemical platforms form the basis of translating industry 'in-the-field' and are fabricated on a large scale resulting in low cost, yet highly reproducible sensors which can be used as either single-use (disposable) or can be readily modified *via* surface modification with enzymes, nanostructures or even the bulk of the sensor can be adapted to allow bespoke applicability in a multitude of applications [126, 127]. For example, Banks *et al* [128, 129] have shown that metal oxide (bismuth, antimony and tin) bulk modified screen-printed electrodes can offer a suitable platform for the sensing of heavy metals. Additionally, screen-printed platforms have been utilised, both as-is (unmodified) and modified, within many sensing applications, for example, towards the detection of biomolecules (such as lactate[130] or l-cysteine[131]), gases (such as O_2[132] or CO[133]) and metals (such as Sb and Sn[134]); with particular success within the food industry a key indication of their quality and versatility, with respect to capsaicin [135] and garlic [136] which have been successfully analysed with SPEs. An important parameter to consider when utilising electrochemical sensors is the electroactive area, especially within fundamental calculations of electrochemical processes, as well as providing a methodology for their benchmarking with respect to the quality control of SPEs.

Jarzabek and Borkowska [137] have reported upon determining the electrochemical area of gold polycrystalline electrodes using the mass transport and adsorption process of different species (namely $HClO_4$ and $LiClO_4$). While Czervinski *et al* [138] have provided a thorough overview of the various approaches to determine the electroactive area of noble metal electrodes, reporting that each method implemented to measure the electroactive area of an electrode is based upon very specific theory and assumptions, thus not providing a standardised method for the determination of these

metal based electrodes, and in particular there is a lack of research in the determination of the electroactive area of mono-layer 2D materials as electrode materials.

The determination of the electroactive surface area of SPEs has also been investigated using the redox probe N,N,N',N'-tetramethylphenyl-diamine (TMPD)[139], through the popular methodologies of cyclic voltammetry (CV) and chronocoulometry (CC). Interestingly, the approach *via* chronocoulometry has been used to determine the electroactive area of nitrogen-doped graphene modified electrodes, with $Ru(NH_3)_6^{3+/2+}$ used as the redox probe[140]. Other groups have also used CC to measure the area of gold nanostructures[141], CNT/NiO microfluidic electrode[142], and Ag@Pt nanorods[143] using ferrocyanide/ferricyanide redox probes. Additionally, alternative electrochemically irreversible probes such as NAD^+ and ascorbic acid have been used to measure the surface area of commercial SPEs using CV[144]. Moreover, Terranova *et al.* have utilised diluted H_2SO_4 determining the area of a MWCNT-PtNP modified electrode using a both CV and CC methods[145].

In the literature, in the above reported methodologies, such measurements are undertaken with little understanding or consideration for the redox probe utilised or experimental parameters and this same literature does not properly explain this to novices.

3.2 Results and discussion

The electrode area of screen-printed electrodes (SPEs) and CVD grown mono-layer graphene can be physically/visually determined with techniques such as scanning electron microscopy. In this case, the geometrical area, A_{geo}, is determined through its physical dimensions, but there is no resemblance to the true electroactive area and there is no way of knowing which parts of the electrode surface are

electrochemically active or indeed inactive. The most appropriate way is to use an interfacial technique such as electrochemistry; it is this approach that is considered herein.

3.2.1 Determining the electroactive area using cyclic voltammetry

Firstly, one must consider the respective Randles-Ševćik equations (at non-standard conditions)[1, 5-7] for reversible, *quasi*-reversible and irreversible electrochemical processes[5-7] :

$$I_{p,f}^{rev} = \pm\ 0.446\, nFA_{real}C\sqrt{\frac{nFD\nu}{RT}} \tag{1.22}$$

$$I_{p,f}^{quasi} = \pm\ 0.436\, nFA_{real}C\sqrt{\frac{nFD\nu}{RT}} \tag{1.23}$$

$$I_{p,f}^{irrev} = \pm\ 0.496\sqrt{\alpha n'}\, nFA_{real}C\sqrt{\frac{nFD\nu}{RT}} \tag{1.24}$$

where in all cases, n is the number of electrons in the electrochemical reaction, $I_{p,f}$ is the voltammetric current (analytical signal) using the forward peak of the electrochemical process, F is the Faraday constant (C mol^{-1}), ν is the applied voltammetric scan rate (V s^{-1}), R is the universal gas constant, T is the temperature (Kelvin), A_{real} is the electroactive area of the electrode (cm^2) and D is the diffusion coefficient (cm^2 s^{-1}), α is the transfer coefficient (usually assumed to be close to 0.5) and n' is the number of electrons transferred before the rate determining step. Equations (1.22, 1.23 and 1.24) can be used to determine the electroactive area (A_{real}) through a simple cyclic voltammetry experiment. In this approach, typically, a reliable redox probe within an aqueous electrolyte is used to determine a plot of the *forward* peak current, $I_{p,f}$, as a function of applied voltammetric scan rate ($\nu^{1/2}$). This is since the Randles-Ševćik equation is derived from assuming that the concentration of the

electroactive species (in the bulk solution) is the same as that at the electrode surface, due to the development of the diffusion layer[3].

There are important factors to consider when utilising the aforementioned Randles-Ševćik equations:

1) Which equation should be used for each redox probe utilised? *I.e.* which equation from 1.22, 1.23 and 1.24 is the most suitable to use? Analysis of the peak-to-peak separation (*ΔEp)* of the recorded voltammogram is useful, where in the *reversible* limit the $\Delta Ep \text{ is } \sim 59mV$ and is independent of scan rate. In the case of *quasi*- and *irreversible* conditions the *ΔEp* is larger and is dependent upon the voltage scan rate. The wave-shape of the forward peak allows one to determine between reversible and irreversible conditions; a full analysis is given in reference[3].
2) These should only be used for the forward scan[3], this is due to the fact that on the forward wave, the product is electrochemically produced and diffusion occurs, giving, as a result, a concentration of zero product within the bulk solution compared to that at the electrode surface. Consequently on the return scan, reducing the electrochemically formed product back to its starting material, a decrease in the concentration of the product has occurred, resulting in a less intense backward peak than the forward one. The Randles-Ševćik equations are only an approximation, and therefore *do not* represent an exact value, as is, for example, in the case of chronocoulometry.
3) The Randles-Ševćik equations are more suitable for macroelectrodes, therefore which size of electrode can be utilised to satisfy the Randles-Ševćik equation? *I.e.* how big does the electrode need to be in order to give rise to the mass transport dominated by planar diffusion? Compton has undertaken experiments inferring that working electrodes of not less than 4 mm radius should be employed for

investigations in aqueous solutions [146]. Their work demonstrates that for a simple electron transfer process, the ΔEp is reduced from 60.6 mV using a radius of 0.5 mm to 57.5 mV in the case of a radius of 4 mm and larger; the quantitative change is due to the geometric electrode size increasing such radial diffusion [146].

4) One must consider, is the electrode relatively flat and non-porous? In order for equations (1-3) to hold, this should be the case. In the case of a SPE, the electrode is heterogeneous, comprising a range of different carbons (graphite, carbon black) and also binder(s). It should be noted that the surface roughness of a SPE is typically 0.078 μm. In the case of CVD grown mono-layer graphene, its surface is virtually flat, being reported to be the origin of electrochemical activity at its edges and defect sites across its basal surface (see Chapter 4[147]), the electroactive area is an important parameter to calculate and compare. Over the timescale of the voltammetric experiment, as determined by Compton[148, 149], the diffusion layer is larger than the SPE and graphene micro-features such that the electrode kinetics is heterogeneous and dominated by the faster electrode material, *i.e* the edge plane features of the graphite(s)/carbon black(s). In this case, equations (1.22-24) hold; see references 20 and 10 for the categorisation of electrochemically heterogeneous surfaces that may be encountered.
5) The potential window is not reversed too early, and the analysis of the forward peak is used on the first scan[3].
6) The scan rate is not too fast to make the cyclic voltammetric response become non-reversible. This is since the Randles-Ševćik equations are derived from assuming the concentration of the electroactive species in the bulk is the same as that at the surface of the electrode, which as highlighted above is due to a diffusion layer developing[3].

7) In the case of determining the electrode area, a reliable diffusion coefficient (*D*) value needs to be utilised. A useful approach is the Wilke-Chang[150] equation to determine the diffusion coefficient:

$$D = 7.4 \times 10^{-8} \frac{T\sqrt{xMs}}{\eta V^{0.6}} \quad (3.1)$$

where *x* is the association parameter to define the effective molecular weight of the solvent with respect to the diffusion process (where x = 2.6 for water and x = 1 for non-associated solvents[150]), *Ms* is the molecular weight of the solvent (g mol^{-1}), η is the viscosity of the solution (g cm^{-1} s^{-1}) and *V* is the molar volume of solute at normal boiling point (cm^3 g^{-1} mol^{-1}). This equation predicts the *D* value with an exponential error of ±13%. As highlighted by Sitaraman *et al*[151], finding the association parameter (*x*) becomes an issue for unknown systems, therefore the following correction has been proposed:

$$D = 5.4 \times 10^{-8} \left(\frac{TLs^{\frac{1}{3}}\sqrt{xMs}}{\eta V^{0.6}\sqrt{Vm}Ls^{0.3}}\right)^{0.93} \quad (3.2)$$

where *Ls* is the latent heat of vaporization of solute at normal boiling point (cal g^{-1}). This methodology still has an error of ±13%, but is simpler when used by experimentalists. Clearly, temperature is critical in determining the electrochemical area. Changes and fluctuations in temperature will affect the information obtained from equations (1.22-24 and 3.1-2). Consequently, the temperature at the time of the experiment should be measured and factored into these equations.

8) The Randles-Ševćik equations are useful for single electron transfer processes that feature a 1:1 reaction stoichiometry, inversely however, for example, the reduction of protons to hydrogen (hydrogen evolution reaction, HER) has a 2:1 stoichiometry and experimental results deviate from theory.[152] The diffusion

coefficients used here are either from the academic literature or deduced using equation (3.2).

Returning to the case of determining the electrode area, electrochemical experiments were performed using redox probes with a range of voltammetric scan rates utilised (see experimental section). The appropriate Randles-Ševćik equations were utilised to determine the electrode area (A_{real}). The estimated areas for the different electrodes are shown in Table 1, with their calculated A_{real} and its percentage compared to the A_{geo} ($\%Real = (A_{real} / A_{geo}) \times 100$); examples from their CVs are depicted in Figure 21. (Note: in case of capsaicin, the second electron of the reaction was utilised and in case of the TMPD, the first oxidation peak was chosen).

It is readily evident that a range of $\%Real$ values for SPEs are obtained alternating from 65.5 to 145.7%. Using SPEs, one can realise that this value will likely deviate from 100% due to the binder holding the graphite and carbon black components together comprising the electrode surface. So what value of *%Real* is the one to be utilised? One needs to not only consider the limitations of the Randles-Ševćik equations, as identified above, but also the redox probe used is of importance.

Hexaammineruthenium (III) chloride (RuHex) is a near-ideal outer-sphere redox couple which does not show changes in electron transfer rates upon varying surface chemistry and is dependent *only* on the electrode's electronic structure (DOS and Fermi level)[20]. In order to calculate the areas for the range of electrodes, an average of three sets (each set calculated as an average of ten different scan rates each (5 to 500 mV s^{-1})) were performed for each electrode and redox probe, in order to collect strong and reliable data. The estimated areas for the CVD grown mono-layer graphene, SPE, glassy carbon and EPPG electrodes are shown in Table 1 and examples from their CVs are depicted in Figure 21. Areas were calculated as 0.057, 0.056, 0.052

and 0.023 cm^2 for RuHex, Co(phen), TMPD and $IrCl_6$ respectively for CVD graphene, which correspond to 72.4, 70.7, 42.4 and 29.5% of the geometrical area of the electrode respectively. In comparison, RuHex estimates an A_{real} percentage in comparison to the geometrical one (*%Real* = (A_{real}*100/A_{geo})) of 90.4, 100.8 and 82.8 % for the GC, EPPG and SPE electrodes respectively. Using TMPD, another outer-sphere redox probe, the calculated *%Real* is 154.1, 167.0, 75.6 and 65.7 % for GC, EPPG, SPE and CVD mono-layer graphene. Co(phen) measurements give a *%Real* of 104.1, 103.3, 112.3 and 70.9 % for GC, EPPG, SPE and CVD mono-layer graphene electrodes respectively. Lastly, $IrCl_6$ estimates a *%Real* of 108.7, 99.3, 84.1 and 29.5 % for GC, EPPG, SPE and CVD grown mono-layer graphene.

Interestingly, in the case of inner-sphere electron transfer probes (which show deviations due to the surface chemistry, physical structure and electronic structure since the redox probe requires contact with the electrode surface or through a bridging ligands) such as dopamine, a value of 0.056 cm^2 is predicted for the CVD graphene electrode when a new electrode is used for each scan rate. If the same electrode is used for the ten scan rates, the estimated area is 0.011 cm^2; corresponding to 71.0 and 13.4% of the geometrical area of the electrode respectively. This blockage/fouling of the electrode is due to the dopamine adsorption onto the surface of the electrode, and therefore decreasing the analytical response from the second scan [153, 154]. Same process seem to happen when using any of the inner-sphere redox probes such as NADH, capsaicin or ascorbic acid that only estimate 13.4, 12.3 and 41.2 % of the geometrical area of the working electrode.

Dopamine and NADH, according to McCreery[20], need to adsorb onto the surface prior to electro-oxidation occurring and furthermore, capsaicin's oxidation product has been reported to adsorb on to the surface of the electrode[155-157]. The

oxidation of ascorbic acid is reported to be controlled by kinetics of adsorption together with diffusion, whereas the reaction probably occurs at the less active sites of Pt electrodes, while the more active sites are covered by the adsorbed ascorbic acid[158]. A new electrode should be used after oxidation to prevent polymerized products being analysed.

Dopamine, NADH and capsaicin employed as redox probes results in similar estimates of the electrode area when using the Randles-Ševćik equation (at identical electrodes and when using the entire scan rate study (10 different scans)), this is likely be due to the adsorption processes of the three molecules. While dopamine is a small molecule, NADH's size is larger and it has been reported that two different adsorption mechanisms may occur. Planar adsorption of the molecule happens rapidly but occupies a large area with a few number of molecules. On the other hand, perpendicular adsorption happens more slowly, in which each molecule occupies less overall area, giving an optimal condition for reproducibility[159].

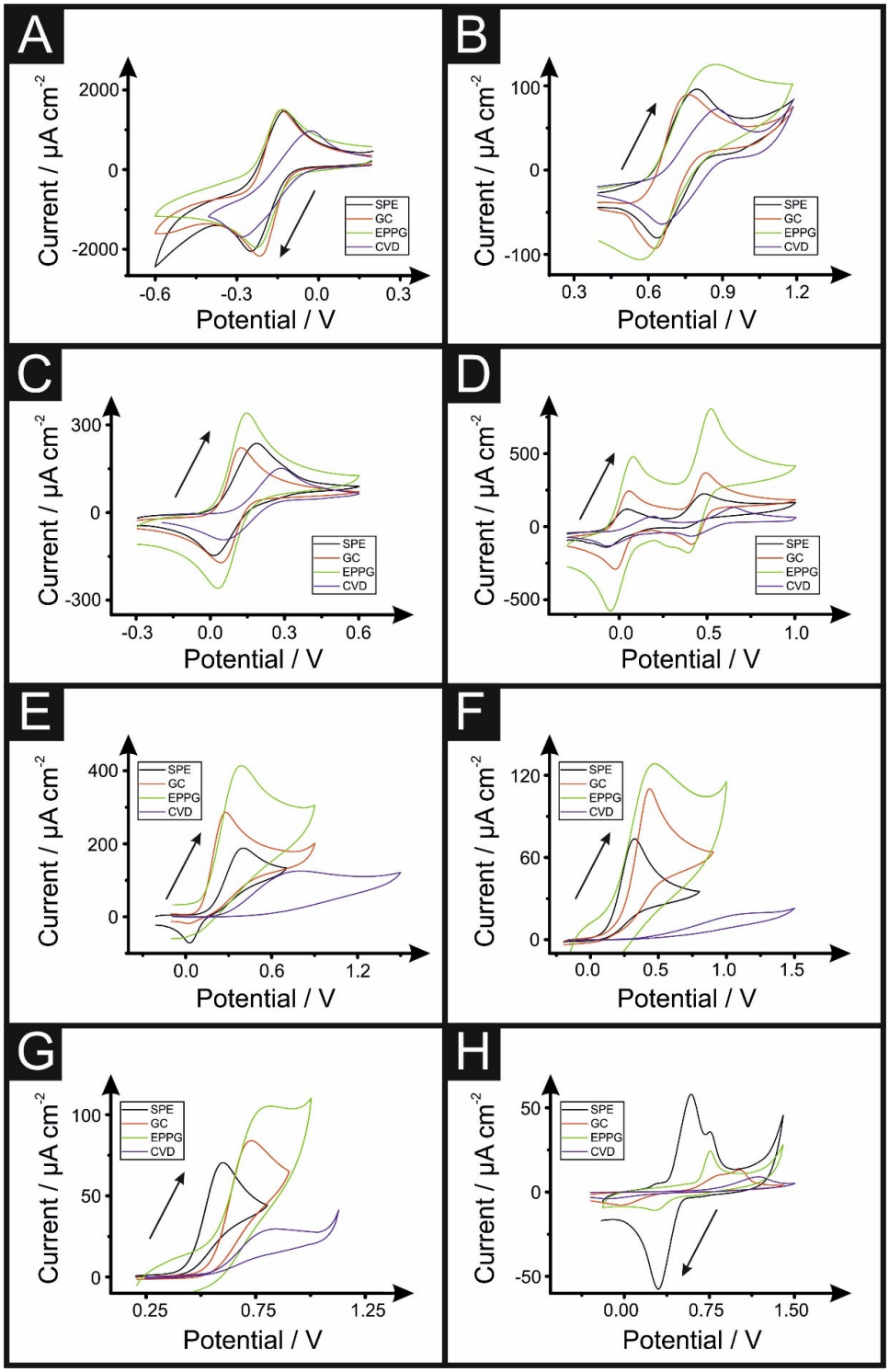

Figure 21. Cyclic voltammetry of 1 mM RuHex (A), 1 mM IrCl6 (B), 2 mM Co(phen) (C), 1 mM TMPD (D), 1 mM dopamine (E), 1 mM ascorbic acid (F), 1 mM NADH (G) and 1 mM capsaicin (H) for CVD grown mono-layer graphene, GC, EPPG and SPE electrodes. Scan rate 0.05 V s^{-1} with an arrow pointing at the forward peak selected to calculate the A_{geo} with equations 1 to 3. Results are presented in Table 1.

Electroactive Probe	*%Real GC / %*	*%Real EPPG / %*	*%Real SPE / %*	*%Real CVD mono-graphene / %*
RuHex	90.4 ± 1.6	100.8 ± 8.9	82.8 ± 3.4	72.4 ± 2.1
$IrCl_6$	108.7 ± 1.5	99.3 ± 4.3	84.1 ± 2.0	29.5 ± 0.7
Co(phen)	104.1 ± 1.6	103.3 ± 2.0	112.3 ± 9.7	70.9 ± 1.6
TMPD	154.1 ± 3.6	167.0 ± 7.0	75.6 ± 2.4	65.7 ± 3.2
Dopamine	187.5 ± 6.5	169.7 ± 9.1	120.2 ± 4.6	13.4/71.1 ± 4.5
Ascorbic acid	136.4 ± 9.5	78.5 ± 7.2	145.7 ± 3.6	53.1 ± 2.9
NADH	63.6 ± 3.0	52.6 ± 4.3	65.5 ± 7.3	11.81 ± 1.6
Capsaicin	13.4 ± 1.0	11.6 ± 2.2	123.7 ± 6.2	12.3 ± 0.5

Table 1. Calculated *%Real* areas for CVD grown mono-layer graphene, GC, EPPG and SPE electrodes using Randles-Ševćik equations. *%Real* is the percentage of A_{real} divided by the A_{geo} (averaged using 3 different scan rate studies, each of them averaging 10 different scan rates; N = 3). Note that for dopamine, there are two different estimated values, first calculated using one electrode for the ten scans, and second calculated using ten different electrodes to see the fouling of the electrode due to analyte's adsorption to the surface of the electrode, see Refs[153, 154] (at 19.6 °C).

Figure 22 shows McCreery's elegant flow chart depicting the electrochemical processes of redox complexes, classifying each redox probe as either inner and outer-sphere probes depending on how the electron transfer processes occur on the surface of the electrode. Randles-Ševćik equations are only an approximation and also strictly apply for diffusion controlled redox processes[3]. Redox processes (see Figure 21) are classed into outer-sphere where electron transfer is fast where the redox probes comes close to the electrode surface for electrons to tunnel/hop across a monolayer of solvent but do not directly interact with the electrode surface. Such redox probes are influenced by the electronic structure of the electrode surface only. On the other hand, inner-sphere probes are influenced not only by the electronic structure but also the electrode surface (either reactant, product), *i.e.* surface functional groups (adsorption sites)/surface chemistry [160]. Thus in the redox probes utilised, RuHex is a near ideal

outer-sphere redox couple which does not show any changes in its electron transfer rates due to varying surface chemistry and is only dependent upon the electrodes electronic structure (Density of States (DOS) and the Fermi level), thus allowing its use to give rise to the closest estimations of the electroactive area (A_{real}).

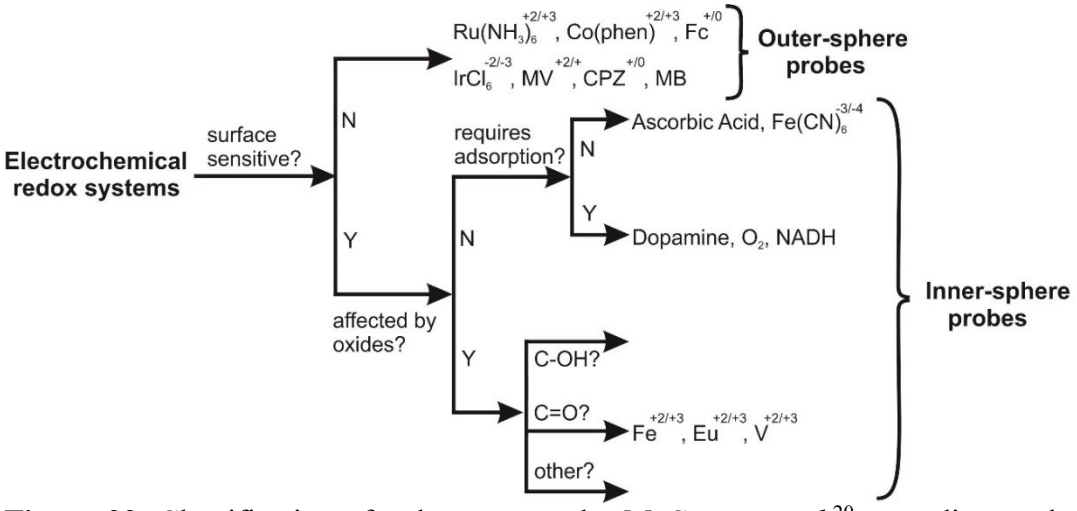

Figure 22. Classification of redox systems by McCreery *et al*.[20] according to their kinetic sensitivity to particular surface modifications upon carbon electrodes. The figure has been adapted to show clearly outer- and inner- sphere probes. Fc: ferrocene, MV: methyl viologen, CPZ: chlorpromazine and MB: methylene blue.

3.2.2 Determining the electroactive area using chronocoulometry

Chronocoulometry (CC) is a classical electrochemical technique that has been overlooked over recent years. CC was developed by Anson[11] (see equations 3.3 and 3.4), which involves the measurement of charge *vs.* time response from an applied potential step waveform. The shape of the resulting chronocoulogram, is summarised within Figure 23. CC is a useful technique in electrochemistry allowing one to readily determine the electrochemical active electrode area, as well as their respective diffusion coefficients, the time-window of an electrochemical cell, adsorption of electroactive species and rate constants for chemical reactions coupled to electron transfer reactions; this in summary, is a very useful electrochemical approach.

The Anson equation for diffusion only processes (see equation 3.3) defines the charge-time dependence for linear diffusion control, using a CC method, which is the measure of charge (Coulombs) as a function of time, and can be applied to the measurement of the electroactive area of electrodes[139]. In the case of adsorption, for electrochemical processes (such as the case of inner-sphere probes, see equation 3.4) where the reactants is adsorbed, the charge is due to the electrolysis of the adsorbed species which can be distinguished from the charge that is occurring from the electrolysis of the solution based species. The adsorbed materials upon the electrode surface are electrolyzed immediately upon application of the potential step, while the solution based species obviously have to diffuse to the electrode surface to react. In this case, the total charge is the contribution of the double layer, the electrolysis of the adsorbed species and the electrolysis of the solution.

Anson equations:

- *for diffusion processes*

$$Q = \frac{2nFA_{real}C\sqrt{Dt}}{\sqrt{\pi}} + Q_{dl} \quad (3.3)$$

- *for adsorption processes*

$$Q = \frac{2nFA_{real}C\sqrt{Dt}}{\sqrt{\pi}} + \mathrm{nFA}_{real}\Gamma_0 + Q_{dl} \quad (3.4)$$

where Q is the charge, n is the number of electrons in the electrochemical reaction, A_{real} is the electroactive area, F is Faraday's constant, C is the concentration, D is the diffusion coefficient, Q_{dl} is the double layer capacitance and Γ_0 is the coverage of adsorbed reactant (mol cm^{-2}). The electrolysis of the diffusion species shows a dependence upon $time^{1/2}$. Since the adsorbed materials are electrolyzed instantaneously, the charge is not time-dependent and also the charging of the double layer is instantaneous and independent of time. Thus, as shown in Figure 23 the difference in the charge due to the $Q_{dl} + \mathrm{nFA}_{real}\Gamma_0$ is readily evident but the gradient is the same, due to the reaction cited above. Therefore, CC is the most accurate when considering near-ideal outer-sphere probes or highly adsorbed analytes.

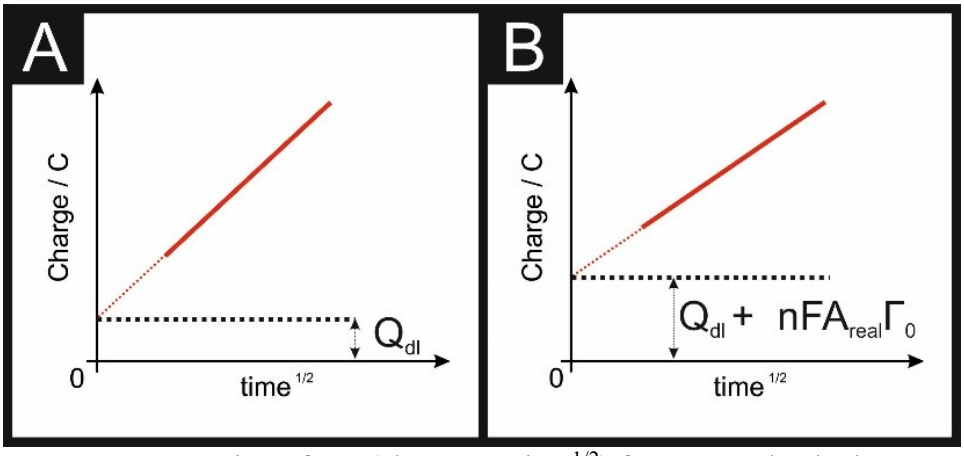

Figure 23. Representation of CC (charge *vs.* time$^{1/2}$) for a non-adsorbed outer-sphere probe (A) and for an adsorbed inner-sphere probe (B). Note that, in A, the intercept is not truly zero due to the contribution of Q_{dl} (see equation 3.3 and 3.4).

CC was described by Anson as a method to determine quantities of adsorbed reactants, as such, this equation cannot be reliably used to determine A_{real}. It is because of the contributions of "$nFA_{real}\Gamma_0$" in the aforementioned equations (*i.e.* having two different terms in the equations representing the area) that the electroactive area cannot be directly calculated. A range of redox probes was used to calculate the electroactive area of the different electrodes using the Anson plot (equation 3.3 and 3.4), applying first a potential pulse to reduce all of the analyte and a second pulse to oxidise (or reduce in the case of RuHex and TMPD, thus the first step was inversed also) with the results depicted in Figure 24, and their calculated A_{real} and *%Real* reported in Table 2.

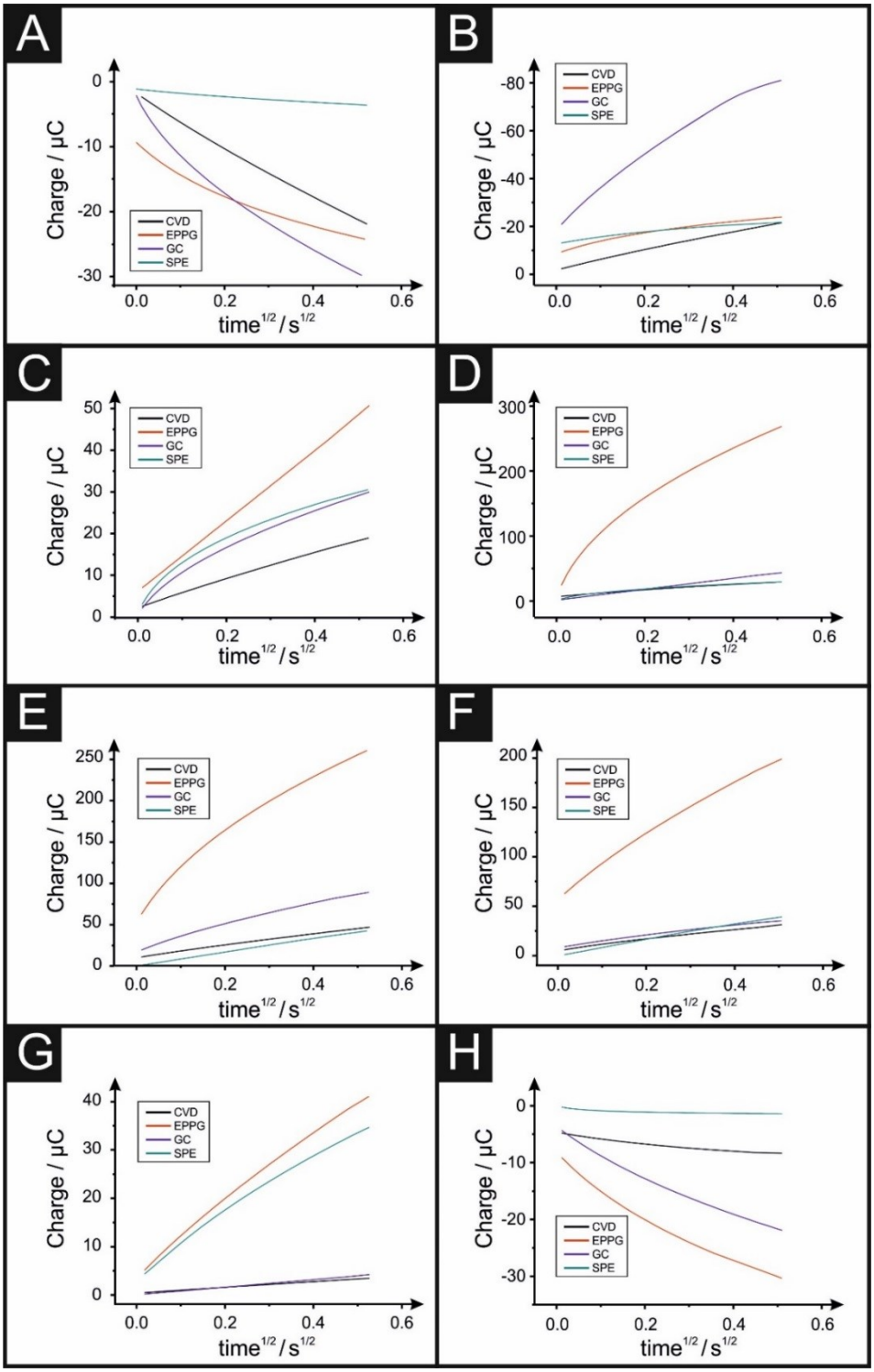

Figure 24. Anson plots resulting from using the following redox probes: 1 mM RuHex (A), 1 mM IrCl6 (B), 2 mM Co(phen) (C), 1 mM TMPD (D) 1 mM dopamine (e), 1 mM ascorbic acid (F), 1 mM NADH (G) and 1 mM capsaicin (H) for CVD grown mono-layer graphene, EPPG, GC and SPE electrodes (corresponding estimated areas are shown in Table 2) (at 19.6 °C).

Electroactive Probe	*%Real GC / %*	*%Real EPPG / %*	*%Real SPE / %*	*%Real CVD mono-graphene / %*
RuHex	62.1 ± 2.1	137.1 ± 7.8	73.3 ± 6.0	128.2 ± 5.2
$IrCl_6$	101.9 ± 7.3	178.2 ± 6.1	132.8 ± 1.6	92.2 ± 5.7
Co(phen)	234.4 ± 1.4	147.1 ± 0.5	220.2 ± 3.2	106.1 ± 3.8
TMPD	395.4 ± 0.3	741.6 ± 5.5	70.5 ± 5.2	123.7 ± 5.5
Dopamine	502.4 ± 9.4	522.3 ± 6.5	102.5 ± 5.0	324.5 ± 4.0
Ascorbic acid	246.5 ±10.3	160.7 ± 6.2	161.2 ± 0.6	558.1 ± 2.8
NADH	25.0 ± 1.4	194.7 ± 8.1	103.3 ± 5.2	50.5 ± 9.8
Capsaicin	110.9 ± 6.6	118.4 ± 3.0	75.9 ± 1.4	69.9 ± 9.5

Table 2. Calculated 'areas' for CVD grown mono-layer graphene, GC, EPPG and SPE electrodes using Anson equations. *%Real* is the percentage of A_{real} divided by the A_{geo} ($N = 9$) (at 19.6 °C).

In the case of CVD grown mono-layer graphene and, as a comparison, GC, EPPG and SPE electrodes as depicted in Figure 24 and Table 2. Displayed data is the average of three sets of data from three different electrodes, each data made by three repetitions. Each CC method was made by a first potential applied at a low voltage where no electrochemical Faradaic reaction occurred, and the second potential was applied in order detect the corresponding Faradaic process, with the total charge passed *versus* time was recorded for 6 seconds. It can be readily observed in Figure 24 that the linearity of the Anson plots change depending on the electrode utilised. For example, in Figure 24A-D, which corresponds to the Anson plot for the outer-sphere redox probes, CVD grown mono-layer graphene shows a linear response of charge *vs.* $time^{1/2}$. Inversely, Figure 24E-H shows the Anson plot for the inner-sphere redox probes that adsorb onto the surface of the different electrodes in different degrees.

The *%Real* for the CVD grown mono-layer graphene electrode using the Anson plots are shown in Table 2. The estimated electroactive areas for the CVD grown mono-layer graphene are 0.10, 0.084, 0.084 and 0.098 cm^2 using RuHex, Co(phen), TMPD and $IrCl_6$ respectively, which correspond to 128.2, 106.1, 123.7 and 92.2 % of

the geometrical area respectively. In comparison, RuHex estimates a *%Real* of 62.1, 50.9 and 73.3 % for GC, EPPG and SPE electrodes respectively. Using TMPD, another outer-sphere redox probe, the calculated *%Real* is 392.4, 741.6, 70.5 and 123.7 % for GC, EPPG, SPE and CVD mono-layer graphene. Co(phen) measurements give a *%Real* of 234.4, 147.1, 220.2 and 106.1 % for GC, EPPG, SPE and CVD mono-layer graphene electrodes respectively. Lastly, $IrCl_6$ estimates a *%Real* of 101.9, 178.2, 132.8 and 92.2 % for GC, EPPG, SPE and CVD grown mono-layer graphene.

Last, note that when comparing the use of the outer- and inner-sphere redox probes, it is suggested to always use an outer-sphere redox probe (such as RuHex, $IrCl_6$, Co(phen) or TMPD) that are only sensitive to the density of states (DOS). Contrarily, the use of an inner-sphere redox probe to estimate the area depend on the electronic structure and the surface of the electrode (such as surface functional groups) and also can foul the electrode surface when is used multiple times, therefore electrochemists should consider these factors. In order to compare between the different electrochemical techniques: Randles–Ševćik *vs.* the Anson plot to estimate the area of CVD graphene electrodes, given that the Anson plot (with CC) minimises the effect of adsorption processes and needs less experiments, it is recommended to use CC to calculate the electroactive area. It is important to note that the parameters described herein are applicable for the stated experimental conditions; in cases where working electrodes have high roughness factors, porosity, capacitance and/or presence of inactive materials the equations might not be applicable.

3.3 Conclusions

In summary, this works compares for the first time, methods to determine the electroactive area (A_{real}) of screen-printed and mono-layer graphene electrodes *via* CV and CC. Details are given to allow novices to utilise these approaches to understand the various parameters that need to be taken into consideration to determine a robust value for the electroactive area. Outer-sphere electron transfer redox probes, are the optimal choice of analyte to employ when one needs to obtain the most accurate and reliable indication of the electroactive surface. For classic electrode platforms the Randles-Ševćik equation is considered the most accurate one. SPE's active area results are less than 100% due to the presence of inactive binders; for GC and EPPG it is expected values close to 100% due to their flat and fully reactive surfaces using the Randles-Ševćik equation. For CVD grown mono-layer graphene, given that mono-layer graphene structure comprises a large coverage of low electro-catalytic activity (namely its basal plane) and a low coverage of active edge plane like-sites/defects, the estimated A_{real} calculated using the appropriate Randles–Ševćik equation with outer-sphere redox probes correspond to between 42.4 and 70% of the geometrical area of the given electrode. In contrast, the use of the Randles-Ševćik equation might introduce newly created defects/rips/damage as it is explored in Chapters 5 and 6, therefore it is recommended herein the use of the Randles-Ševćik equation with an outer-sphere redox probe.

This work is an important and fundamental contribution to those experimentalist who use and benchmark the electroactive area of different electrode platforms, independently to their roughness, since it provides the first comparison of inner and outer-sphere redox probes, highlighting the various parameters that need to be considered in order to obtain useful estimations of the electroactive area.

Chapter 4: Exploring the reactivity of distinct electron transfer sites at CVD grown monolayer graphene through the selective electrodeposition of MoO_2 nanowires

This chapter investigates electron transfer at Chemical Vapour Deposition (CVD) grown monolayer graphene using a polymer-free transfer methodology through the selective electrodeposition of Molybdenum (di)oxide (MoO_2). This work demonstrates the distinct electron transfer properties of edge and basal plane sites on CVD grown monolayer graphene, inferring favourable electrochemical reactivity at edge plane like- sites/defects and clarifying the origin of graphene electro-activity. The confirmation of monolayer graphene's electrochemical properties could enable enhanced application in several areas, by tailoring devices the utilised graphene exposing its edges such as additive manufacturing, electronics, energy storage/generation and for electrochemical sensor platforms.

4.1 Introduction

Graphene is extensively studied due to its reported unique electronic, mechanical and optical properties[161-165] which translate into abundant research interest in energy applications such as supercapacitors[58-61], solar cells[62-65], fuel cells[66-68], water splitting[69] and for electrochemical sensors[166-168] when utilised as an electrode material.

In terms of understanding the electrochemical response of CVD grown monolayer graphene (*via* a BU approach), the reactivity of such electrodes is *commonly assigned* to the graphene edge planes, which are reported to exhibit *ca*. 4 orders of magnitude greater specific capacitance, faster electron transfer rates and higher electrocatalytic activity when compared to the graphene basal planes[169]. Recent work involving the electrochemical behaviour of CVD grown pristine graphene has shown a correlation in the structure of graphene, in terms of a dependence upon its number of layers and the macroscopic electrochemical response/performance[34, 170].

Moreover, an identical relationship in terms of graphene's geometric structure (the quantity of edge plane *vs*. basal plane coverage) has recently been reported with respect to the lateral flake size, in which smaller graphitic flake sizes (comprising a large edge plane like- site/defect density and a respectively small basal plane geometric contribution) exhibited improved electrochemical properties when compared to the inverse[171]. Indeed, there have been numerous other studies reporting that, in comparison to the edge plane like- sites/defects[172, 173], the basal planes of graphitic and carbon-based materials are effectively inert[34, 169, 174, 175]. However, regardless of the vast number of recent reports concerning graphene-based electrodes, researchers still debate the *real* contributions of edge and basal plane like- sites/defects at the macroscopic scale, in the future researchers should clarify the experimental configuration of their studies, *i.e*. macro- *vs* microscopic voltammetry[176] with respect to their observed heterogeneous electron transfer (HET) kinetics[10, 175, 177-179]; further work is required to explore this edge *vs*. basal argument for carbon surfaces[176]. It is these aforementioned research considerations that are investigated herein, through the utilisation of a MoO_2 deposition technique decorating CVD grown monolayer graphene using a polymer-free transfer method, so that one can determine the *true electrochemical contributions* arising from its structure.

Molybdenum oxide(s) and other metal oxides have been shown to electrochemically nucleate specifically onto the edge plane like- sites/defects of highly oriented pyrolytic graphite (HOPG)[180-184]. Davies *et al.*[185] reported that edge plane like- sites/defects on basal plane orientated HOPG (SPI-1 grade) are responsible for the voltammetric signal, and Rowley-Neale *et al.*[9] extended these insights with screen-printed graphitic electrodes (SPEs) with similar results. In these approaches, the selective deposition of metals and metal oxides onto graphite is called 'step edge

decoration'[180-183], and has been utilised to demonstrate that electrochemical reactions at edge plane graphite are "anomalously fast" in comparison to the basal plane, which is effectively inert[184-186]. Through the selective coating and blockage method of the edge plane like- sites/defects with MoO_2 nanowires (that are electrochemically insulating), a reduction in the electrochemical response towards $[Ru(NH_3)_6]^{3+/2+}$ [34, 175] was reported; clearly demonstrating that the electrochemical reactivity of the HOPG is due to edge plane like- sites/defects. To the best of our knowledge, the above elegant approach has not previously been applied towards CVD grown monolayer graphene sheets (in addition to the polymer-free transfer method utilised herein) contributing to the understanding of graphene and *all akin* carbon-based electrode materials.

4.2 Results and discussion

Previously reported methodologies have utilised the electrochemical decoration of MoO_2 onto HOPG and SPEs[185,9], where MoO_2 selectively deposits upon the available edge plane like- site/defects, allowing their electrochemical contributions to be deduced. In consideration of these approaches, herein this method is adapted to CVD grown monolayer graphene sheets. Presented within the Experimental Section and Supporting Information are details of the fabrication process, optimisation and physicochemical characterisation of the CVD grown monolayer graphene sheets and their MoO_2 decorated counterparts. Briefly, Figure 32 depicts the full Raman spectra of a MoO_2 decorated monolayer graphene, displaying the typical monolayer graphene D (1350 cm^{-1}), G (1580 cm^{-1}), 2D (2700 cm^{-1}) and 2D' (3250 cm^{-1}) peaks, the presence of MoO_2 (308 cm^{-1})[187] and the presence of the underlying Si (514 and 985 cm^{-1}) wafer (which usually are not shown in the literature and generally ignored / not-presented even though they will be observed). Additionally, AFM images were collected in order to characterise the MoO_2 nucleation upon the edge plane like- sites/defects as depicted

in Figure 33, where the length and width of the wires is 1-2 μm and 30-75 nm respectively, which corroborates with the *selective* nucleation characterised by Rowley-Neale *et al*.[9]

Figure 25A depicts an SEM image of the edge of an unmodified monolayer graphene sheet and Figure 25B presents the corresponding cyclic voltammetric response, using the near-ideal outer-sphere redox probe, $[Ru(NH_3)_6]^{3+/2+}$, which exhibits a peak-to-peak separation (ΔE_p) of 160 mV (at 50 mV s^{-1} *vs.* Ag/AgCl) and a HET (k^0_{obs}) rate of 1.91×10^{-3} cm s^{-1} (see Experimental Section). Note that this value is similar but slightly faster than other CVD monolayer graphene sheets previously reported by our research group[34], which is due to a higher exposure of the edge plane like- sites/defects upon the graphene sheet. Furthermore, it is worth noting at this stage that each individual graphene sheet is unique in terms of its level of edge plane like-site/defects, so there is natural variation in the reported HET rates throughout the literature; thus, it is important to characterise each monolayer graphene sample[16] prior to modification with MoO_2. Figure 25C depicts an SEM image of the MoO_2 electrochemically decorated monolayer graphene sheet following applying chronoamperometry at a set voltage (-0.6 V *vs.* Ag/AgCl) for 1 second, where it is readily observed that the MoO_2 nucleates upon the edge plane like-sites/defects/wrinkles of the monolayer graphene surface.

Figure 25D represents the voltammetric responses using the near-ideal redox probe, $[Ru(NH_3)_6]^{3+/2+}$, which exhibits a ΔE_p of 200 mV (at 50 mV s^{-1} *vs.* Ag/AgCl) and a k^0_{obs} of 8.80×10^{-4} cm s^{-1}. Such decreased voltammetric behaviour implies that the insulating MoO_2 nanowires have coated some of the available edge plane like- sites/defects, with some edge sites remaining unmodified. Figure 25D compares the voltammetric profiles and Table 3 shows (with respect to

the HET kinetics (k^0_{obs}) and the percentage of edge plane coverage ($\%\theta_{edge}$) values) the changes observed as one electrodeposits MoO_2 onto the graphene electrode's surface. Such voltammetric profiles, show that the decorated electrode (dashed line) still exhibits relatively fast HET kinetics when compared to the unmodified electrode (solid line), but presents a lower current intensity due to the limited availability of edge plane like- sites/defects on the electrode surface. This is corroborated with the SEM presented within Figure 25C.

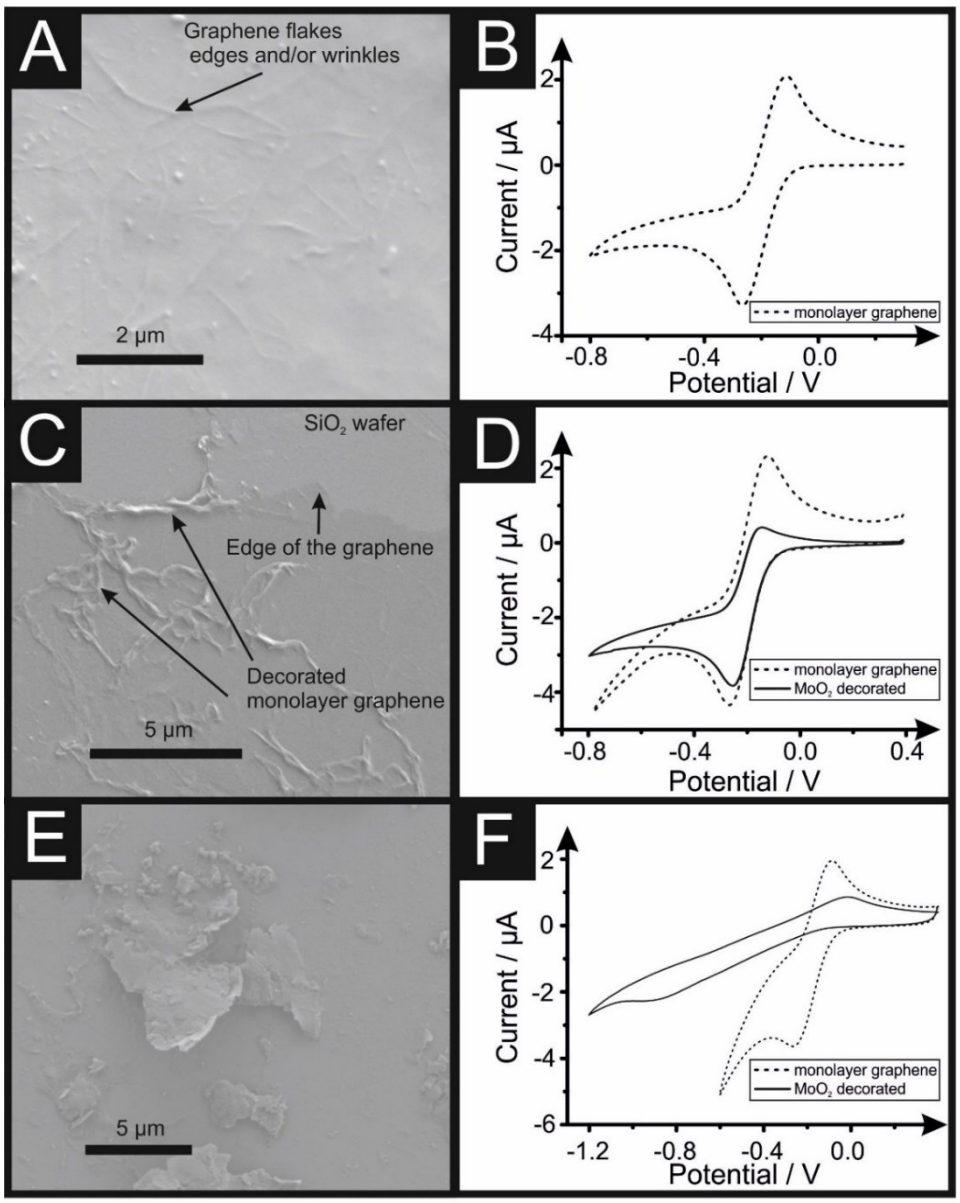

Figure 25. SEM images of a monolayer graphene electrode (A), 1 second electrodeposition of MoO_2 at -0.6 V (*vs.* Ag/AgCl) (C) and 10 second electrodeposition of MoO_2 at -0.6 V (*vs.* Ag/AgCl) (E). Additionally presented is cyclic voltammetric analyses recorded using 1 mM $[Ru(NH_30_6]^{3+/2+}$ / 0.1 M KCl, using a monolayer graphene sheet (B), 1 second electrodeposition of MoO_2 at -0.6 V (*vs.* Ag/AgCl) (D) and 10 second electrodeposition of MoO_2 at -0.6 V (*vs*. Ag/AgCl) (F) (Scan rate: 25 mV s^{-1}). Note that the monolayer graphene samples (Fig 4.1A) might contain dust/air impurities due to the manufacturing process explained within the Experimental Section, observed as nanoparticulates.

Graphene Sample	*Prior to electrodeposition*		*Electro-deposition Time / s*	*Post electrodeposition*		$\Delta\%\theta_{edge}$
	k^0_{obs} *(cm s^{-1})*	$\%\theta_{edge}$		k^0_{obs} *(cm s^{-1})*	$\%\theta_{edge}$	
A	1.64×10^{-3}	0.4	1	9.65×10^{-4}	0.24	-41.5
B	4.26×10^{-4}	0.1	2	3.44×10^{-4}	0.09	-18.2
C	2.32×10^{-3}	0.6	5	8.75×10^{-4}	0.22	-62.1
D	2.83×10^{-3}	0.7	10	2.18×10^{-6}	0.0005	-99.9

Table 3. HET kinetics, coverage and electrodeposition times for CVD mono-layer graphene decorations. HET kinetics (k^0_{obs}) were determined using the near ideal outer-sphere redox probe $[Ru(NH_3)_6]^{3+/2+}$ / 0.1 M KCl, coverage of edge plane (θ_{edge}) and the difference in the percentage of edge coverage upon the surface of the monolayer graphene sheets ($\Delta\theta_{edge}$) followed by the electrochemical decoration of MoO_2 for: 1 (A), 2 (B), 5 (C) and 10 (D) seconds; electrochemical parameters: -0.6 V (*vs*. Ag/AgCl) using 1 mM Na_2MoO_4 (in 1 M NaCl). Note: each sample (A, B, C and D) is a different CVD monolayer graphene sheet and has a varied initial size and quantity of edge sites, which exhibit distinct electron transfer rates (HET kinetics).

Next, the effect of increased deposition times at -0.6 V (*vs*. Ag/AgCl) is investigated. Presented within Figure 25E is an SEM image of the MoO_2 electrochemically decorated monolayer graphene sheet that has been applied at -0.6 V (*vs*. Ag/AgCl) for 10 seconds *via* chronoamperometry, where it is clear that electrodeposition is no longer isolated upon the edge plane like- sites/defects. Instead, the MoO_2 has coated/blocked the entire electroactive surface. Upon electrodeposition at more electrochemically negative potentials (*ca*. –1.0 V) or longer deposition times, a large MoO_2 film is created/deposited on the graphene sheet, originating and expanding from the original edge plane like- sites/defects (non-selective deposition), as shown in Figures 29. Figure 25F corroborates with this topographical analysis as

the corresponding cyclic voltammetric analysis utilising the same near-ideal redox probe, $[Ru(NH_3)_6]^{3+/2+}$, exhibits a ΔE_p of 820 mV and a k^0_{obs} of 2.18×10^{-6} cm s^{-1}. As expected, the monolayer graphene sheets coated with insulating MoO_2 (upon the edge plane like- sites/defects), gives rise to an electrochemical response with a larger ΔE_p (slower electron transfer) than the unmodified monolayer graphene. The aforementioned MoO_2 coverage dependant electrochemical behaviour has been illustrated within the schematic presented within Figure 26. Figure 26 represents the selective nucleation process of MoO_2 wires that nucleate onto the graphene's edge plane (and or defect/wrinkle) sites when a electrodeposition for 1 second at -0.6 V is performed, resulting in a decrease in the reversibility of the $[Ru(NH_3)_6]^{3+/2+}$ redox peaks. Longer deposition times will increase the nucleation of the MoO_2 onto remaining edge sites and towards the basal plane of the graphene sheet (deposition of 5 seconds at -0.6 V). Eventually, a complete coverage of the surface of the graphene is confirmed by the absence of cyclic voltammetric redox peaks of $[Ru(NH_3)_6]^{3+/2+}$, for example, when an electrodeposition of 10 total seconds at -0.6 V is performed.

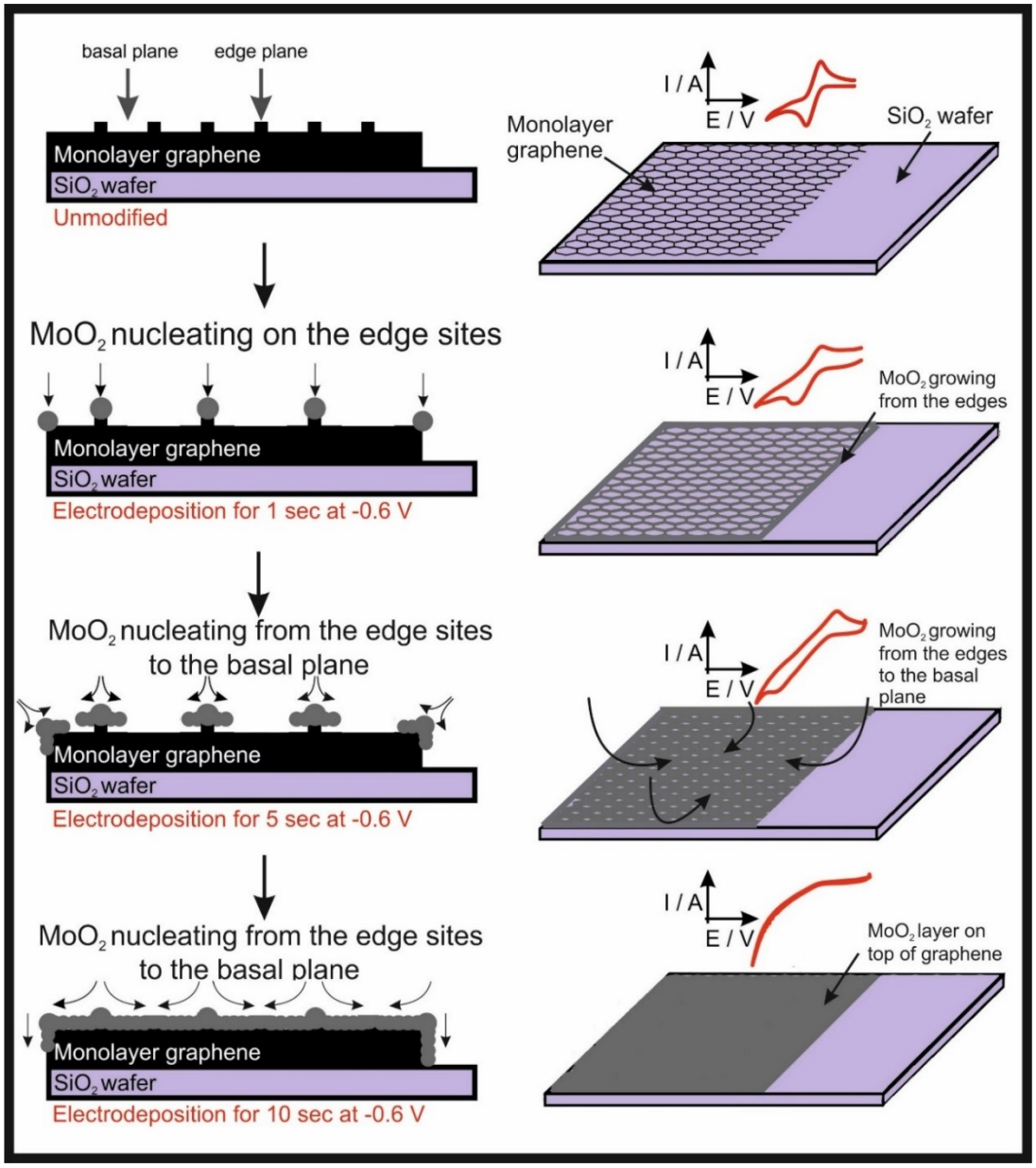

Figure 26. Schematic highlighting the MoO_2 deposition process upon monolayer CVD graphene sheets, where MoO_2 nucleation starts upon the graphene edge plane like- sites/defects. Note that longer deposition times result in the MoO_2 growing from the edge plane like- sites/defects over onto the basal plane sites, until there is a complete insulating layer covering the entire monolayer graphene sheet, resulting in substantially reduced electrochemical activity. Note, sizes are not to scale.

The experiments performed above confirm that the MoO_2 wires are indeed being electrodeposited selectively onto the graphene edge plane like- sites/defects, at a set potential of -0.6 V (*vs.* Ag/AgCl) for 1 second and this results in a decrease in the k^0_{obs} by 41.5% (shown in Figure 25 and Table 3). Note that the electrochemical activity of the monolayer graphene sheet is reduced since the MoO_2 selectively electrodeposits upon the edge plane like- sites/defects, which is confirmed by physicochemical characterisation indicating that these are the active sites for electron transfer. If no changes in the voltammetry were observed, this would indicate that basal planes sites are the origin of electron transfer, as this is not the case, our work provides convincing evidence that it is the edge plane like- sites/defects of the CVD grown monolayer graphene that are the origin. When utilising an electrodeposition of 10 seconds, an insulating film is created, which largely decreases the amount of available edge plane like- sites/defects by 99.9%. Note that in the case of sample B, however, in this instance due to the initial low θ_{edge} and hence k^0_{obs}, the deposition of MoO_2 has fewer edge plane like- sites/defects to deposit upon. This demonstrates again that each individually grown CVD graphene sheet is unique in terms of edge plane like- sites/defects and k^0_{obs}; therefore emphasising the importance of their characterisation (both physicochemical and electrochemical) upon fabrication and prior to application. Last, note that if incorrect deposition parameters are utilised, *i.e.* too long deposition times and high deposition potentials, physicochemical characterisation would indicate a large film is created, which would give the *false impression* that the basal plane of monolayer graphene is as *equally* electrochemically active as the edge plane sites, *which is not the case*. However, there has been a great deal of elegant work published on the micro scale response of electron transfer at carbon materials using novel nanoscale techniques[188, 189], therefore it is intended that the data reported herein be

considered in-conjunction with such other studies for the electrochemical community to better understand this phenomena as a whole.

4.3 Conclusion

MoO_2 nanowire arrays have been electrodeposited onto the edge plane like-sites/defects of CVD grown monolayer graphene using a polymer-free transfer method, which have been confirmed *via* physicochemical characterisation. The electrochemical activity *pre* and *post* MoO_2 electrochemical deposition has been assessed using a near-ideal redox probe and in the latter case indicates that the HET kinetics (k_{obs}^0) are significantly reduced, providing convincing evidence that the edge plane like- sites/defects/wrinkles of the CVD grown monolayer graphene are the predominant origin of electron transfer. The confirmation of the origin of monolayer graphene's electrochemical properties could enable its application in several areas, such as additive manufacturing, electronics, energy storage/generation and for electrochemical sensor platforms.

4.4 Experimental section

Test solutions were: 1 mM $[Ru(NH_3)_6]^{3+/2+}$ (in 0.1 M KCl), 0.5 M H_2SO_4 and 1 mM Na_2MoO_4 (in 1 M NaCl). Working electrodes were in-house fabricated CVD synthesised monolayer graphene films supported on an oxidised silicon wafer. A nickel wire counter/auxiliary electrode and a silver/silver chloride electrode (Ag/AgCl) reference electrode completed the circuit.

The in-house graphene growth took place within a nanoCVD-8G rig (Moorfield, UK), which uses a cold-wall variant of the CVD process, using the method described in Chapter 2.

The HET rate constants, k^0_{obs}, were calculated using the near ideal outer-sphere redox probe $[Ru(NH_3)_6]^{3+/2+}$ (in 0.1 M KCl) using the well-known[190] and utilised Nicholson method[8], for electrochemical reactions *via* the equation 1.25 and 1.26[9] described in Chapter 1.

The observed electron transfer rate, k^0_{obs}, of graphite electrodes has been shown to be a contribution of edge plane like- sites/defects (k^0_{edge}) and basal planes (k^0_{basal}), allowing one to calculate the specific contributions with the following equation:

$$k^0_{obs} = k^0_{edge}\left(\theta_{edge}\right) + k^0_{basal}\left(1 - \theta_{edge}\right) \quad (4.1)$$

where θ_{edge} is the coverage of edge plane like- sites/defects on the surface of the electrode, and k^0_{edge} has been shown as anomalously fast over that of k^0_{basal} on graphite, allowing one to write:

$$k^0_{edge} \gg k^0_{basal} \quad (4.2)$$

Such that equation (4.1) now becomes:

$$k^0_{obs} = k^0_{edge}\left(\theta_{edge}\right) \quad (4.3)$$

allowing the coverage of edge plane like- sites/defects upon the graphite electrode to be deduce; it is used and adapted this to the voltammetry observed at the CVD grown monolayer graphene sheets. $\%\theta_{edge}$ is the percentage representation of the edge plane coverage in comparison to the total coverage, being the sum of $\%\theta_{edge}$ and $\%\theta_{basal}$ always equalling 100%. In the above analysis, the assumption is that the electron transfer rate for edge plane like- sites/defects (k^0_{edge}) for the near ideal outer-sphere redox probe, $[Ru(NH_3)_6]^{3+/2+}$, has been widely determined with a commercial simulation package providing a value of 0.4 cm s^{-1} for HOPG electrodes[185].

Note that the area studied is in the macroscale range which is not considered too large (*ca.* 6 mm^2 of full exposed graphene area), because indeed it averages the actual phenomena occurring locally (which it is studied in terms of physicochemical characterisation on the nanoscale too). Such that this makes this study applicable for real applications. It is reported herein on the average response of the macro electrode with varying contributions of the two micro features (edge and basal planes), which is relevant because the likely end use/application of such systems will be on that of the macro scale.

4.5 Supporting Information

4.5.1 Optimising the electrochemical deposition of MoO_2 upon the monolayer graphene sheets

A monolayer graphene sheet covering half of the SiO_2 wafer surface, was used to highlight the edge plane sites/defects of the monolayer graphene, creating a single step of one carbon atom as depicted in Figure 27. The monolayer graphene electrode was immersed in solutions of 0.5 and 1 mM Na_2MoO_4 (in 1 M NaCl and 1M NH_4Cl adjusted to pH 8.5 with liquid NH_3). Linear sweep voltammetry was performed from 0.5 to -1.5 V (*vs.* Ag/AgCl) as depicted in Figure 30, where the electrochemical deposition of MoO_2 onto the electrode surface is detected *via* the electrochemical reduction peak at -0.6 V (*vs.* Ag/AgCl). In this electrochemical process, the reduction of Mo^{6+} to Mo^{4+} occurs through the following reaction mechanism: $MoO_4^{2-} + 2H_2O + 2e^- \rightarrow MoO_2 + 4OH^-$, producing MoO_2 deposited on the monolayer graphene. Note that in the experiments performed herein, the potential at which the MoO_2 electrodeposition occurs is shifted to a less negative potential compared to -1.0 V as reported previously when using HOPG[183, 185] and graphitic SPEs[9], which is likely due to the use of inert binders in the SPEs, and that we have exposed the edge plane of the monolayer graphene making it more readily available. Inspection of the voltammetric signals shown in Figure 30 reveal deposition potentials of -0.6 V (*vs.* Ag/AgCl), which corresponds to the onset of MoO_2 deposition, and resultantly the required chronoamperometry was subsequently performed at this potential.

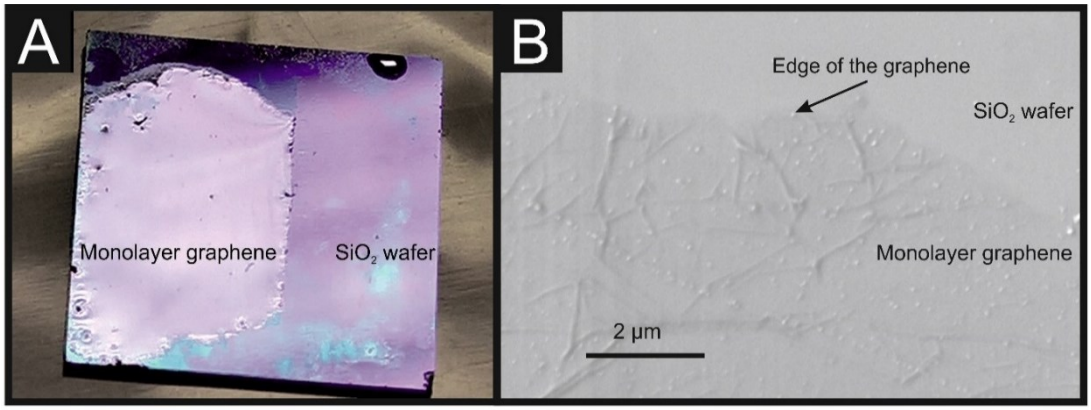

Figure 27. Optical (A) and SEM (B) images of a monolayer graphene sheet deposited upon a SiO_2 wafer covering half of surface in order to expose the edge plane sites/defects of the monolayer graphene before going into the electrochemical cell. Note that the graphene samples may possess air/dust impurities in the form of dots apparent in B.

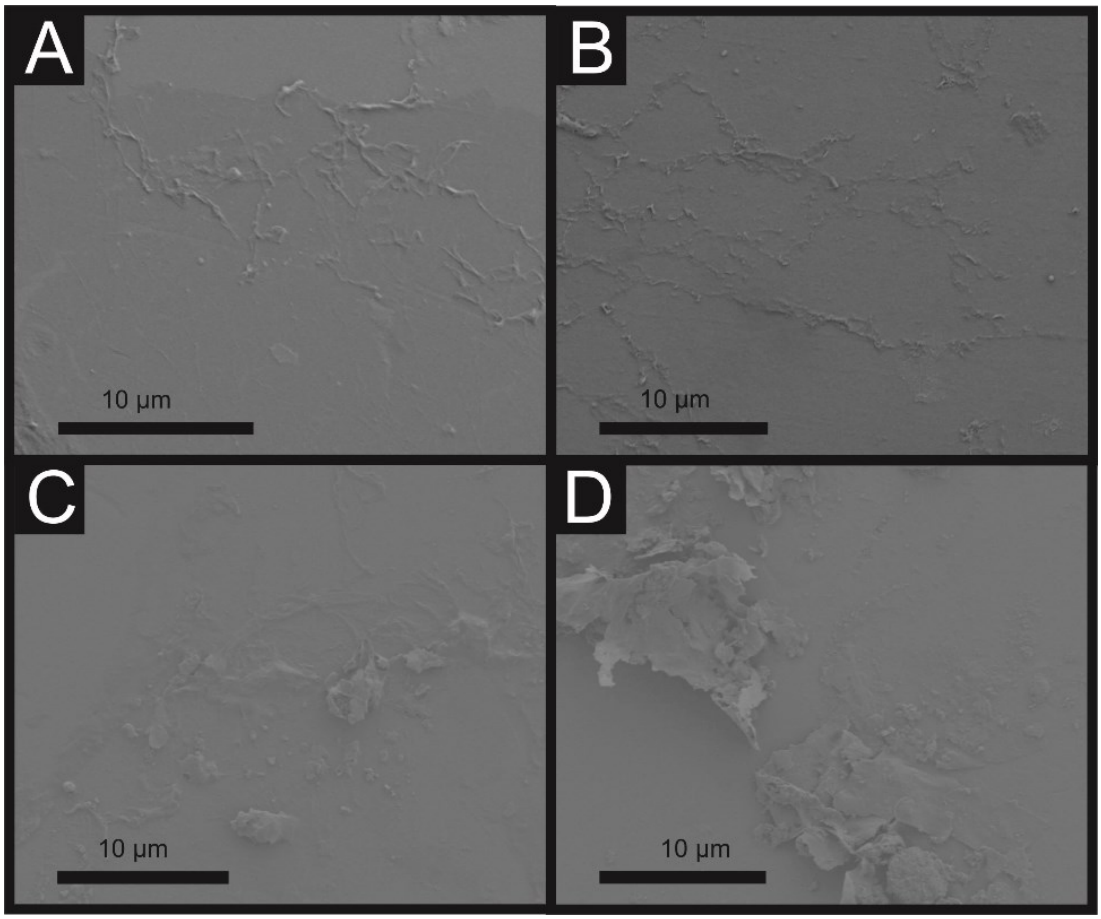

Figure 28. SEM images of a monolayer graphene sheet decorated with MoO_2 through electrodeposition at – 0.6 V (*vs.* Ag/AgCl, Scan rate: 5 mV s^{-1}) for 1 (A), 5 (B), 20 (C) and 100 seconds (D) respectively. Images show how with longer deposition times, deposition is no longer edge plane selective and moves from the edge to the basal planes, covering the entire graphene sheet.

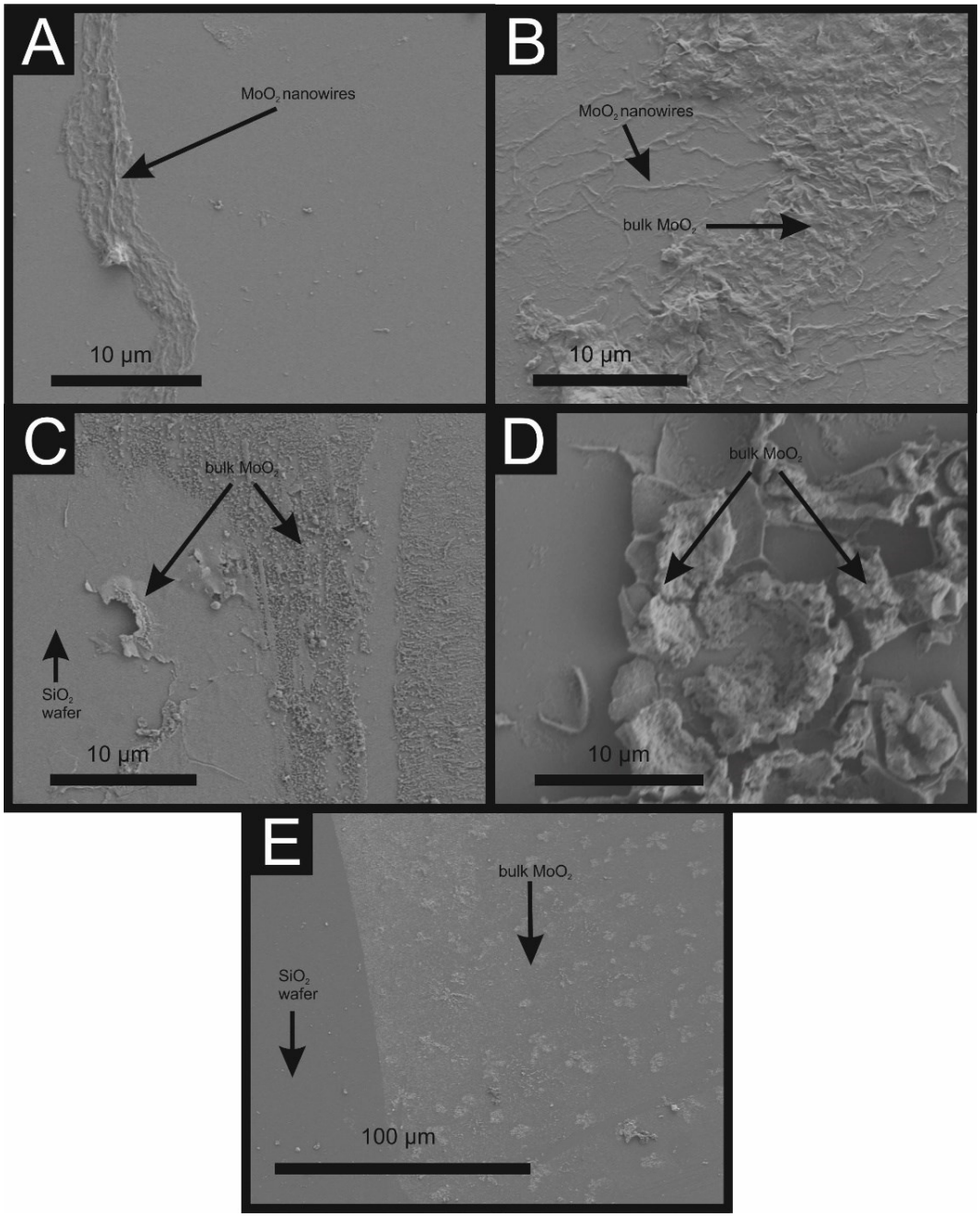

Figure 29. SEM images of a monolayer graphene sheet decorated with MoO_2 through electrodeposition at – 1 V (*vs.* Ag/AgCl, Scan rate: 5 mV s^{-1}) for 1 (A), 5 (B), 20 (C), 100 (D) and 200 seconds (E) respectively. Images show how with a more negative potential and longer deposition times, deposition is no longer edge plane selective (when is MoO_2 nanowires) and moves from the edge to the basal planes (non-selective deposition, as MoO_2 bulk), covering and breaking the entire graphene sheet.

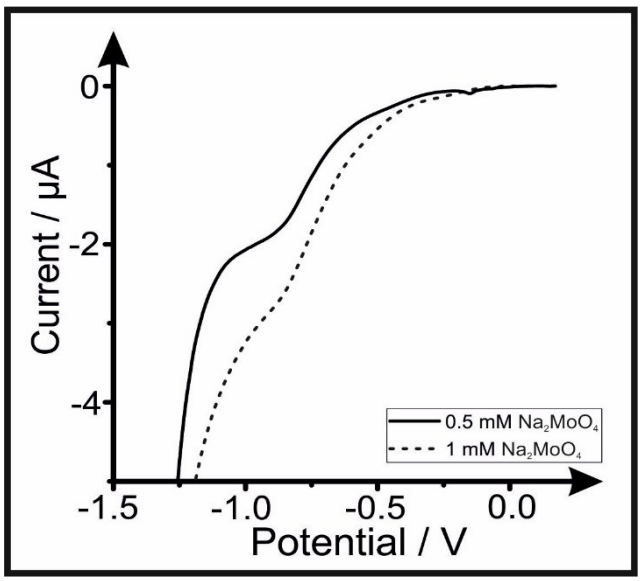

Figure 30. Linear sweep voltammetry recorded with 0.5 (solid line) and 1 mM (dotted line) Na_2MoO_4 solutions depicting the electrodeposition of MoO_2 at a monolayer graphene sheet (*vs.* Ag/AgCl; Scan rate 5 mV s^{-1}).

4.5.2 Raman characterisation

Raman characterisation of the MoO_2 decorated monolayer graphene is recorded over the range: 20–3300 cm^{-1}. The schematic presented in Figure 31A depicts the electrodeposition process of MoO_2 nucleating onto the monolayer graphene edge plane like- sites/defects, when the electrochemical decoration is held -0.6 V (*vs.* Ag/AgCl) for 1 second. Figure 31B shows the full Raman spectra of a MoO_2 decorated monolayer graphene, displaying the typical monolayer graphene D (1350 cm^{-1}), G (1580 cm^{-1}), 2D (2700 cm^{-1}) and 2D' (3250 cm^{-1}) peaks, the presence of MoO_2 (308 cm^{-1})[187] and the presence of the Si (514 and 985 cm^{-1}) wafer (which usually are not shown in the literature). Figure 31C depicts the Raman analysis of an area where MoO_2 has not grown yet, indicating the presence of monolayer graphene and the Si wafer. Figure 31D shows the Raman spectra of an area of the chip where there

is no monolayer graphene and therefore there is no presence of MoO_2, showing only the presence of the Si wafer.

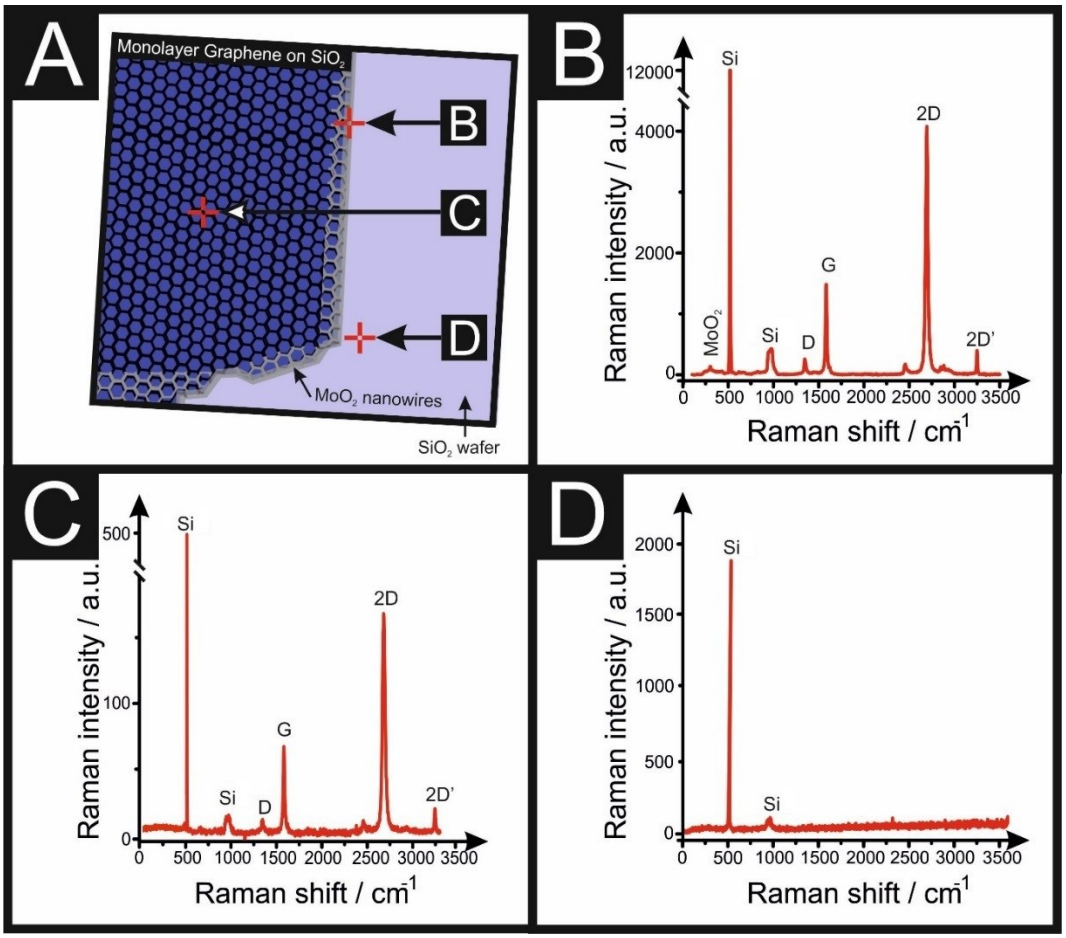

Figure 31. Schematic of selective MoO_2 deposition process (chronoamperometry at -0.6 V (*vs.* Ag/AgCl) for 1 second), where the monolayer graphene sheet covers half of the SiO_2 wafer (A). Raman spectra from the edge of the monolayer graphene (B) with a MoO_2 peak at 308 cm^{-1}, the monolayer graphene where MoO_2 has not been electrodeposited yet (C), and an area where there is only SiO_2 wafer (D).

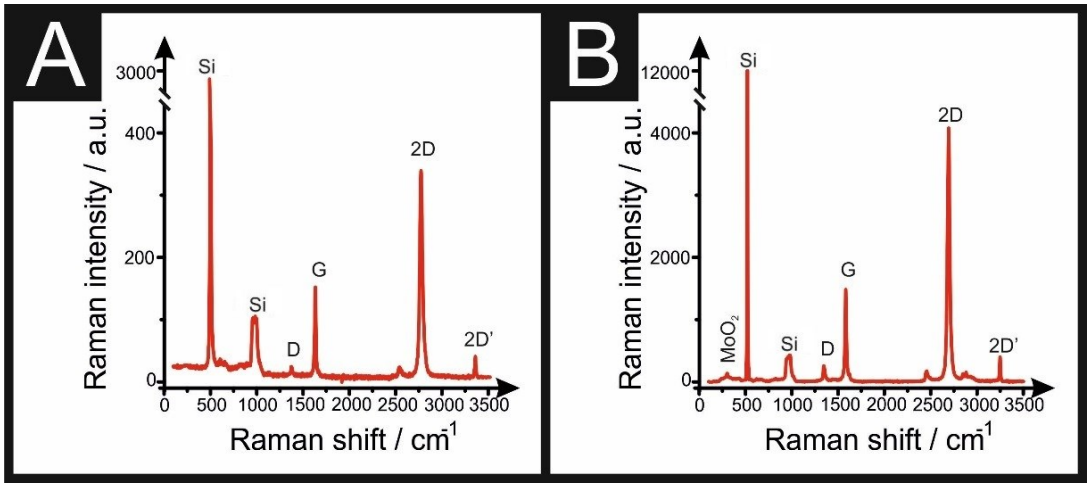

Figure 32. Raman spectra from the edge of the monolayer graphene before (A) and after (B) its decoration with MoO_2 (chronoamperometry at -0.6 V (*vs*. Ag/AgCl) for 1 second). Raman peak at 308 cm^{-1} corresponds to the MoO_2 nanowires on the decorated graphene electrode.

4.5.3 AFM characterisation of the selective electrodeposition of MoO_2 upon a monolayer graphene sheet

AFM images were collected in order to characterise the MoO_2 nucleation upon the edge plane like- sites/defects as depicted in Figure 33, where the length and width of the wires is 1-2 μm and 30-75 nm respectively, which corroborates with the *selective* nucleation characterised by Rowley-Neale *et al.*[9].

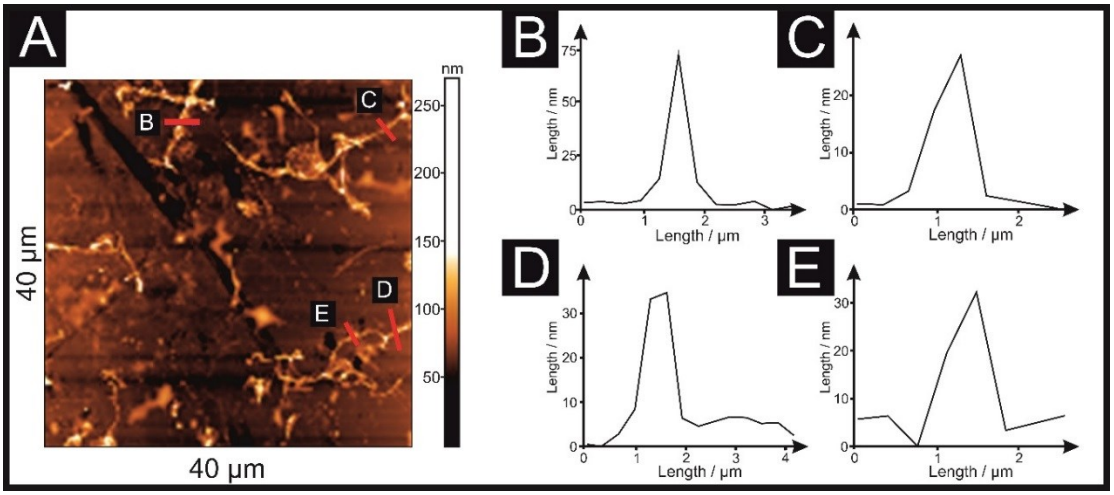

Figure 33. AFM analysis of a monolayer graphene sheet following the electrodeposition of MoO2 at -0.6 V for 1 second (*vs.* Ag/AgCl). Figure 33A shows the topography of the graphene, where most of the surface remains unmodified (basal plane), although some MoO_2 wires can be observed in 33B, C, D and E.

Chapter 5: Investigating the Integrity of Graphene towards the Electrochemical Hydrogen Evolution Reaction (HER)

This chapter investigates mono-, few- and multi- layer graphene towards the electrochemical Hydrogen Evolution Reaction (HER). This chapter indicates the importance of benchmarking and studying the structural integrity stability of CVD graphene electrodes towards electrochemical applications and how can the creation of rips increase the coverage of edge plane like-sites/defects, having a direct effect on the electrochemical results. This chapter also indicates that multilayer graphene has more potential as an electrochemical platform for the HER, rather than that of mono- and few-layer graphene. Electrochemical perturbation, in the form of electrochemical potential scanning (linear sweep voltammetry), as induced when exploring the HER using mono-/few-layer graphene, creates defects upon the basal plane surface that increases the coverage of edge plane sites/defects resulting in an increase in the electrochemical reversibility of the HER process. This process of improved HER performance occurs up to a threshold, where substantial break-up of the basal sheet occurs, after which the electrochemical response decreases; this is due to the destruction of the sheet integrity and lack of electrical conductive pathways.

5.1 Introduction

The electrocatalytic splitting of water is considered a promising strategy for the production of hydrogen, which is a clean and carbon neutral fuel with potential applicability in a range of commercial, industrial and transportation sectors[191-193]. The production of molecular hydrogen due to the electrocatalytic splitting of water *via* the Hydrogen Evolution Reaction (HER; $2H^+ + 2e^- \rightarrow H_2$) is well-known and improving the overall process, output and costs can give rise to a desirable future source of sustainable energy[194].

Currently, platinum (Pt) is considered the most active catalyst towards the HER given that it has a small binding energy for the reaction to occur, resulting in the reaction proceeding instead at low over-potential values close to zero[195-197]. However, Pt is a precious metal with a low natural abundance in the Earth's crust and has a prohibitive cost for wide-spread implementation in water electrolysers[198], meaning that for this technology to prevail, an alternative cheaper yet still efficient catalyst is required. As a result of their beneficial properties (in comparison to other, more traditional materials)[175, 199-202], there is interest in the application of 2D materials, such as graphene[67, 203-205], graphene oxide[206], and other (non)carbon nanomaterials[207], to be explored as Pt alternatives.

For example, Qu *et al*[208] have reviewed the use of pristine, doped and hybrid graphene materials for the electrocatalytic splitting of water, indicating that graphene has been subjected to substantial investigation and thus implemented to undertake multiple roles within this area, such as being the electrochemical platform and/or as a functionalizable support[208-217] for use within a multitude of distinct carbon-based hybrid catalyst. That said, there is a lack of research and understanding with respect to the application of graphene towards the HER in terms of the graphene structure and how the surface changes as a function of electrochemical perturbation.

This chapter fully characterises, for the first time, the electrochemical performance of mono-, few- and multilayer graphene electrodes towards the HER, with the purpose of correlating the observed electrochemical behaviour to the change in the physical structure of the graphene surfaces using electrochemical perturbation in the form of electrochemical scanning (linear sweep voltammetry) and Raman analysis.

5.2 Results and discussion

Attention was first turned to benchmarking monolayer graphene, without any further modification from the manufacturer, as an electrochemical platform towards the HER within acidic media (0.5 M H_2SO_4) as is common within the literature[218, 219], which is the cathode in polymer electrolyte membrane (PEM) electrolysers. The physiochemical characterisation of the graphene sample and others are presented in the Supporting Information, confirming a true monolayer graphene surface. Figure 34A depicts scanning stability experiments using monolayer graphene towards the HER using linear sweep voltammetry (LSV). The initial voltammetric response indicates the HER reaction occurs with an onset value of *ca.* -0.669 V, a current density of -7.39 mA cm^{-2} and a Tafel Slope of 234 mV dec^{-1} (onset and Tafel slope calculated at an overpotential of 10 mA cm^{-2}; *vs.* RHE). The HER is less electrochemically reversible than conventional Pt systems (30 mV dec^{-1}), which is as expected due to Pt being a pure metal that has a very small binding energy for H^+[195, 220]; whereas pristine graphene's surface is mostly comprised of basal planes, that are reported to have *limited* electrochemical activity[3, 10, 147, 176].

Critically, the effect of electrochemical perturbation, in terms of electrochemical reversibility, stability and cyclability was explored *via* driving the electrochemical potential back and forth multiple times from +0.21 to -1.2 V (*vs.* RHE), the region in which the HER occurs; this stability studies are often overlooked with the academic literature. Additionally after each scan, the graphene sample was interrogated with Raman spectroscopy to allow the direct comparison of electrochemical perturbation upon the graphene's physical structure. Surprisingly, after five successive LSV scans, the current density was -1.60 mA cm^{-2} (at -0.65 V) with an onset potential of *ca.* -0.859 V and a Tafel slope of 280.5 mV dec^{-1} (*vs.* RHE), showing a decrease in the

electrochemical HER performance. Interestingly, after electrochemical perturbation of ten voltammetric scans, an onset value of *ca.* -0.59 V and a current density at -0.65 V of -15.11 mA cm^{-2} is evident, indicating an improvement in the onset potential, however the Tafel slope had changed to 292.0 mV dec^{-1}. Furthermore, after a further ten LSV scans, meaning that a total of twenty voltammetric scans had been performed, an onset value of *ca.* -0.099 V and a limited current density at -0.85 V of -0.0014 mA cm^{-2} was exhibited, with a Tafel slope of 141.1 mV dec^{-1} describing poor electrochemical activity throughout the HER experiments, indicating an overall significant drop in the electrochemical current and reduced electrochemical activity. These changing electrochemical observations clearly suggest a physical change of the monolayer graphene and in the conductive pathways. In summary, the monolayer graphene initially gives rise to a useful electroactive graphene surface, which upon electrochemical perturbation and potential cycling ultimately reduces to a worse electrochemical response towards the HER.

In order to understand this phenomenon, Raman mapping of the monolayer graphene surface was explored *after each* LSV scan. Figure 34 B to 34N depicts Raman mapping of monolayer graphene following electrochemical perturbation towards the HER, showing how the graphene surfaces changes in-line with the electrochemical data presented in Figure 34A. Figure 34B represents the typical Raman profile of monolayer graphene. Figures 34C, D and E depict an unused monolayer graphene surface, indicating that it is a good quality monolayer graphene surface, as demonstrated by the characteristic G and 2D Raman peaks (see Figure 34B and Supplementary Information for the full characterisation). Five LSV scans were performed and a decrease in the electrochemical performance was observed, followed by a mapping with Raman spectroscopy to study the surface of the electrode. Figure

34F, G and H show the graphene monolayer following after five voltammetric scans, where it is evident that the graphene sheet starts to fracture. When more scans are undertaken, it is apparent that one observes the presence of more rips, which correlates to the decreased performance. This phenomena is explored further, with a total of ten voltammetric scans (as depicted in Figure 34I, J and K) undertaken. The Raman mapping shows the increased prevalence of holes, with the presence of few and/or multilayer graphene areas (confirmed with Raman spectroscopy as shown in Figure 35B and D) at the edges of the rips and surrounding the damaged areas. The manifestation of few- and multilayer areas is likely responsible for the improved HER performance (formation of H_2) reported above. Notably, after twenty LSV scans, there is no electrochemical response and as depicted in Figure 34L, M and N, the electrode is completely ripped, such that there is a lack of electrical conductive pathways.

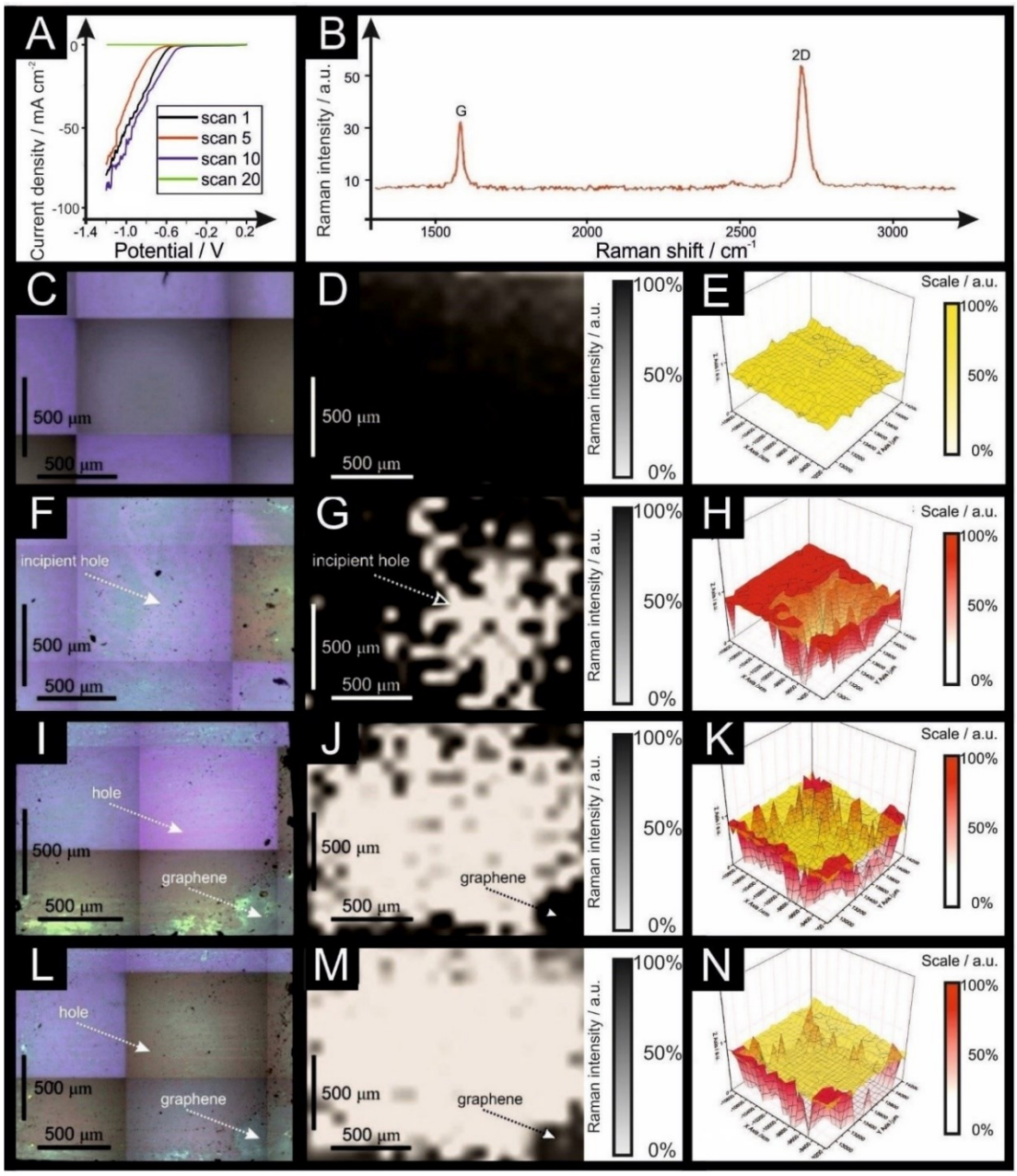

Figure 34. Scanning stability experiments using monolayer graphene; linear sweep voltammetry (LSV) (scan rate: 25 mV s^{-1}; vs. RHE; solution: 0.5 M H_2SO_4). (B) Typical Raman profile of the monolayer graphene sheet described and presented in C, D and E. Optical images of monolayer graphene unused (C), after 5 LSV scans (F), after 10 LSV scans (I) and after 20 LSV scans (L). 2D Raman mapping of the monolayer graphene unused (D), after 5 LSV scans (G), after 10 scans (J) and after 20 LSV scans (M). 3D Raman mapping of the monolayer graphene sheet unused (E), after 5 LSV scans (H), after 10 LSV scans (K) and after 20 LSV scans (N), all in red

colour and compared to the unused sheet (yellow overlay). Raman maps show intensity of Graphene's G band (ca. 1590 cm^{-1}) in order to show the presence of graphene.

Given the apparent degradation of mono-layer graphene observed above and the presence of few- and multilayer graphene surrounding the damaged areas, total specific capacitance (C^0) calculations are now explored in order to estimate the edge and basal plane coverages of respective 'pristine' and 'damaged' graphene samples. Total specific capacitance is calculated as described by equation 5.1, which is a weighted average of the edge (C_e) and basal plane (C_b) contributions comprising the graphene surface[186]:

$$C^0 = C^0_{edge}\, f_{edge} + C^0_{basal}\, (1 - f_{edge}) \quad (5.1)$$

where C^0_{edge} and C^0_{basal} (in μF cm^{-2}) are the specific weighted capacitance averages for edge and basal plane surfaces respectively and f_{edge} is the fraction of edge plane on the graphene surface. Previous studies using the *basal plane* of highly ordered pyrolytic graphite (HOPG)[221] have reported specific capacitance values of *ca*. 1 - 2 μF cm^{-2}, while the specific capacitance of *edge plane* orientated HOPG is *ca*. 70 μF cm^{-2}, allowing one to estimate *via* equation (5.1) the relative edge and basal sites of the graphene electrodes utilised herein. Note that previously, the specific capacitance values of graphene (fabricated identically to that used in this study) for 1 to 5 layers have been reported, with values independent to the number of layers but similar in range to that of basal plane HOPG[222].

Analysis of the edge and basal plane % contribution as a function of electrochemical perturbation (number of scans) is presented in Table 4 which indicates that initially (prior to the first voltammetric scan) the % edge and basal plane is 0.15

and 99.85% respectively. This is in agreement with the voltammetry observed in Figure 34, where electrochemically irreversible processes are observed due to the low percentage of edge plane coverage and lack of electron transfer sites. Following the fifth LSV scan, the surface changes to 1.24% edge plane and 98.76% basal plane, again correlating with the observed HER performance and Raman mapping experiments. A dramatic change is then observed following ten scans, where the % edge changes to 19.81% and the basal plane to 80.19% respectively, indicating that the graphene surface has a substantial edge plane coverage and thus substantial increase in sites available for fast electron transfer to occur. This agrees with the LSV presented within Figure 34, where the voltammetric signature becomes more electrochemically reversible. After 20 LSV scans, the % edge plane changes to 8.29 % and the % basal plane to 91.71 %. Note that adhesively cleaved HOPG has 1-10 % edge plane surface coverage[20, 149, 223] suggesting that the mono-layer graphene becomes similar akin to defect free HOPG. The deduced relative edge and basal plane values support the data observed *via* LSV and Raman mapping, demonstrating how

the mono-layer graphene dramatically changes over the course of the HER process, which has not been reported before.

Scan Number	***Average specific capacitance / µF***	***Relative edge plane %***	***Relative edge basal %***
1	0.90	0.15 %	99.85 %
5	1.86	1.24 %	98.76 %
10	12.67	19.81 %	80.19 %
20	6.72	8.29 %	91.71 %

Table 4. Determination of the % edge plane sites and % basal plane sites upon the monolayer graphene sheet/electrochemical platform. Cyclic voltammograms were performed within a non-Faradaic region between -0.16 and +0.26 V at different scan rates (0.1, 0.2 and 0.5 V s^{-1} (*vs.* RHE)) and analysed to deduce the average specific

capacitance and allow the calculation of the edge and basal plane contributions as described by equation (5.1). Solution composition: 0.5 M H_2SO_4 (degassed using nitrogen).

A schematic representing the observed changes to the physical surface of monolayer graphene when applied towards the HER is summarised within Figure 35. As the monolayer graphene rips *via* electrochemical use it is evident that the edges of the holes sometimes fold upon themselves, as is shown in Figure 35A and 35B. In these instances the graphene is then present as double layer (as evident in the Raman spectra; note, such spectra is not present prior to electrochemical testing), giving rise to increased edge plane content[34]. Figure 35C shows the Raman profile of the damaged graphene sheet, where there is no presence of the typical G and 2D peaks of the pristine graphene, which usually occur at *ca.* 1590 cm^{-1} and 2690 cm^{-1} respectively[110], instead only background noise is present due to the SiO_2/Si wafer onto which the graphene was suspended. Given the above insights, the observed initial improvement in the electrochemical performance of monolayer graphene is most likely due to an increase in the planar edge density when a hole is created and the surface is ripped (as depicted schematically in Figure 35E), after which and with continued ripping the hole becomes too extensive such that there is a loss of the electrical conductive pathways and effectively the graphene sheet 'disintegrates' with no further recordable electrochemical signal.

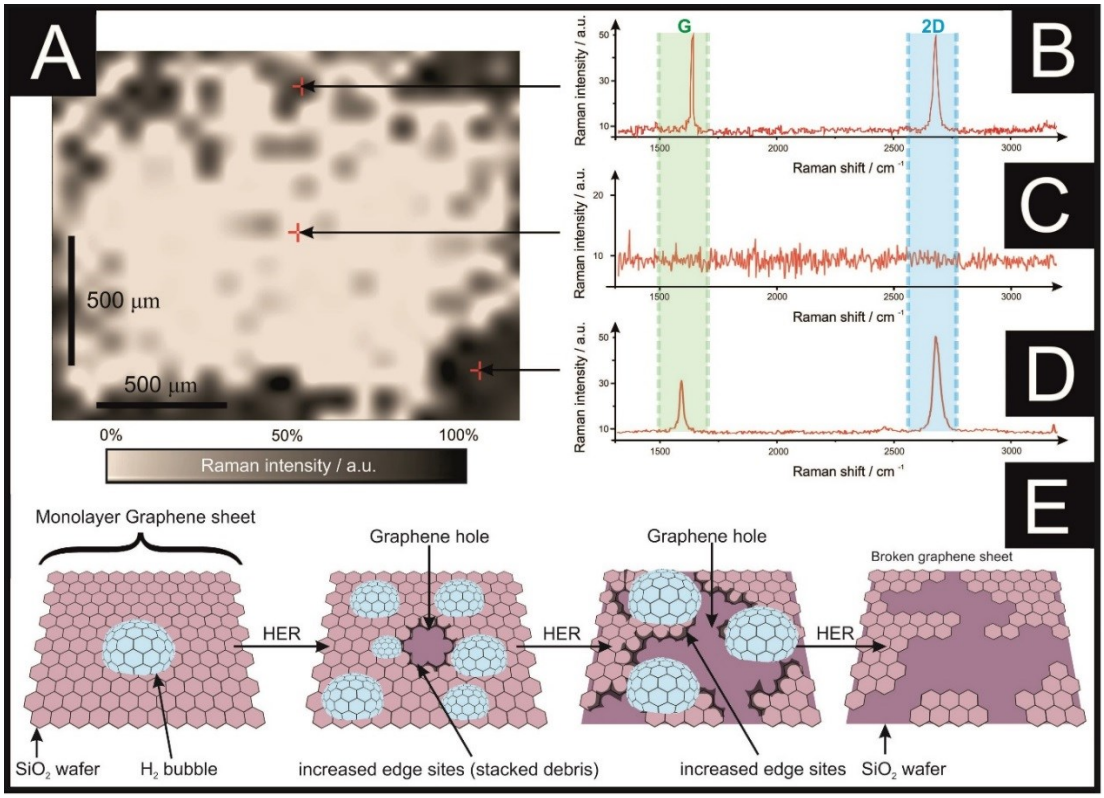

Figure 35. Mono-layer graphene stability schematic under HER consecutive scanning. (A) Monolayer graphene following 20 HER LSV scans. Part (B) depicts the Raman profile near a hole, showing that it is few-layer graphene, with the characteristic ratio of the G/2D peaks near to 1:1. (C) Depicts the Raman profile of a broken area where there is no characteristic graphene peak (or signal) present. (D) Shows the Raman profile of an intact area where there is monolayer graphene including its typical G (1590 cm^{-1}) and 2D (2690 cm^{-1}) peaks. (E) Is a schematic representation of the behaviour identified within this figure (A–D), where the emergence of a bubble on the graphene surface (due to the HER) leads to the creation of some rips when the bubbles move and disperse. The debris created due to the graphene breakdown is stacked in areas near to the holes/rip. When many bubbles explode, there is an incremental rise of the edge sites caused by the broken graphene pieces, which eventually lead to the complete destruction of the graphene sheet.

The behaviour observed in Figures 34 and 35, and in Table 4 and Figure 38 depict the evolution of a graphene monolayer during the HER, where holes are created due to interfacial friction forces caused by H_2 bubbles growing on top of the graphene, with an estimated value of 4.8 x 10^{-7} mm^3 to 1.1 x 10^{-3} mm^3 (supported by Figure 38 and Table 5 in the supplementary information), after which such bubbles exploded, inducing a cavitational collapse upon the graphene surface, which is likely asymmetric in nature upon the graphene surface, contributing to its physical degradation. This is akin to that observed in sonoelectrochemistry. The broken graphene debris likely folds onto itself due to Van der Waals forces, creating a *quasi*[224] or multilayer graphene area surrounding the edges of the hole (supported with Raman spectroscopy), which leads to an increase in electrochemical behaviour at first (as shown in Figure 34A). Following that, when the hole is enlarged due to further scanning of the electrode, *via* LSV, the breakdown of the basal layer leads to the creation of more edge plane sites (supported by capacitance tests), hence there is a reduction in the overall electrochemical behaviour or even the full destruction of the graphene monolayer. Note that it has been previously reported that Chemical Vapour Deposition (CVD) graphene and SiO_2 substrates have different wettability properties, although underlying substrates do not seem to affect the wettability of such graphene[225]; in the presence of graphene with rips and holes as this chapter reports, is likely that the different areas might have different wettability, such effect needs further explorations and will be investigated in the future.

In order to gain further insights, it is interesting to compare the above results with few- and multilayered graphene, applying the same analysis of stability and cyclability experiments towards the HER. Thus, it is next investigated if the

thickness/number of layers of the graphene layers has an impact on the structural integrity.

Few- and multilayer graphene electrodes were explored towards the HER (as shown in Figures 36A and 37A respectively). Few-layer graphene was tested for a maximum of thirty voltammetric scans, showing a change in the current density (at -0.85 V) from –0.065 mA cm^{-2} to -0.0042 mA cm^{-2}. In contrast, the multilayer graphene sheet increased its current density from -0.028 mA cm^{-2} to -0.41 mA cm^{-2} when scanned for *one hundred times*. Evidently, the surface of few-layer graphene is susceptible to similar surface changes as observed with monolayer graphene (but to a less significant degree than the latter), whereas multilayered graphene remains unaltered and stable throughout experiments (with an intrinsic resistance to such surface changes apparent).

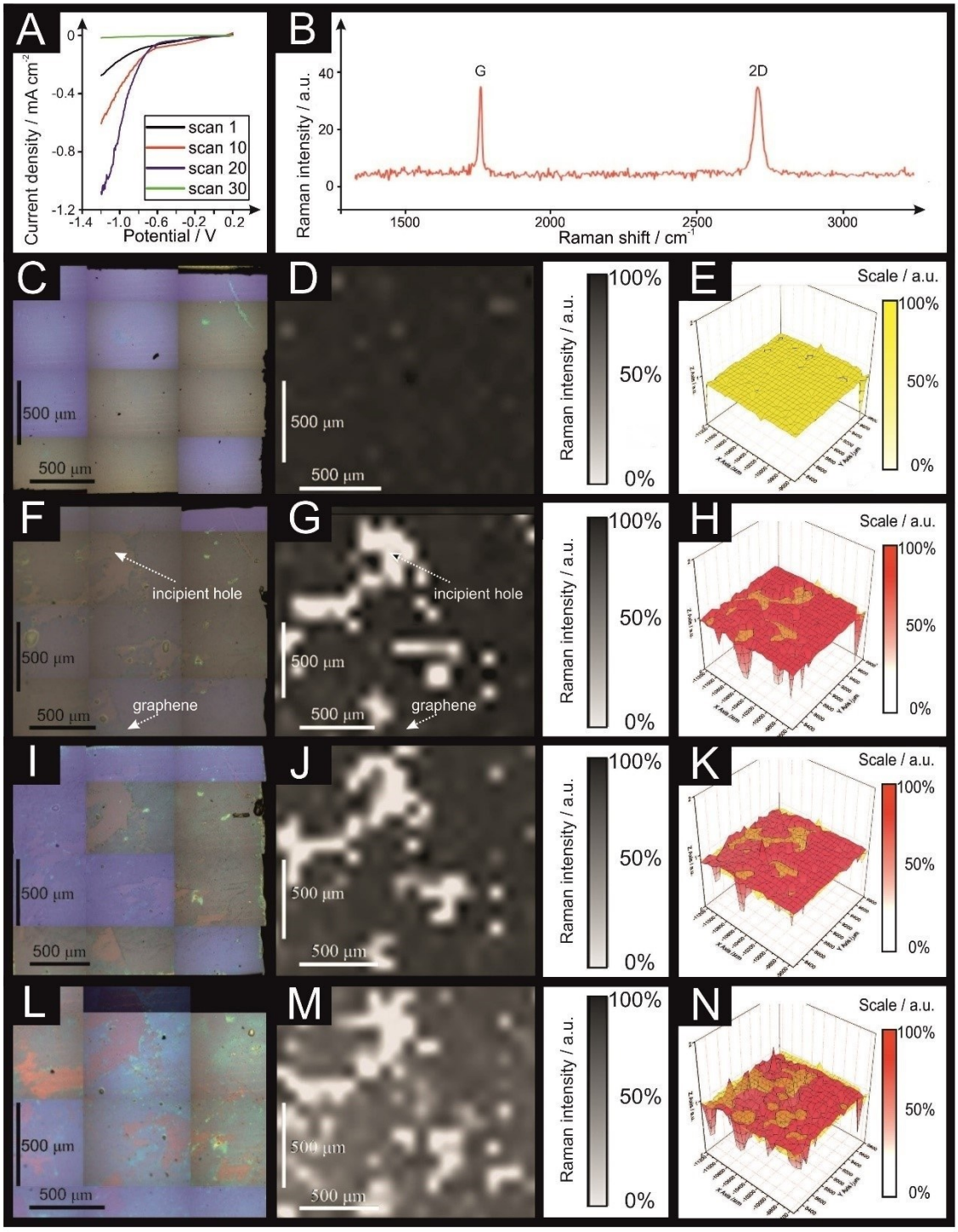

Figure 36. Scanning stability experiments using few-layer graphene; linear sweep voltammetry (LSV), scan rate: 25 mV s^{-1}; *vs.* RHE; solution: 0.5 M H_2SO_4. (B) Typical Raman profile of the few-layer graphene described and presented in C, D and E. Optical images of a few-layer graphene unused (C), after 10 LSV scans (F), after 20 LSV scans (I) and after 30 LSV scans (L). 2D Raman mapping of the few-layer

graphene unused (D), after 10 LSV scans (G), after 20 LSV scans (J) and after 30 LSV scans (M). 3D Raman mapping of the few-layer graphene unused (E), after 10 LSV scans (H), after 20 LSV scans (K) and after 30 LSV scans (N), all in red colour and compared to the unused sheet (yellow overlay). Raman maps show intensity of Graphene's G band (*ca*. 1590 cm^{-1}) in order to show the presence of graphene.

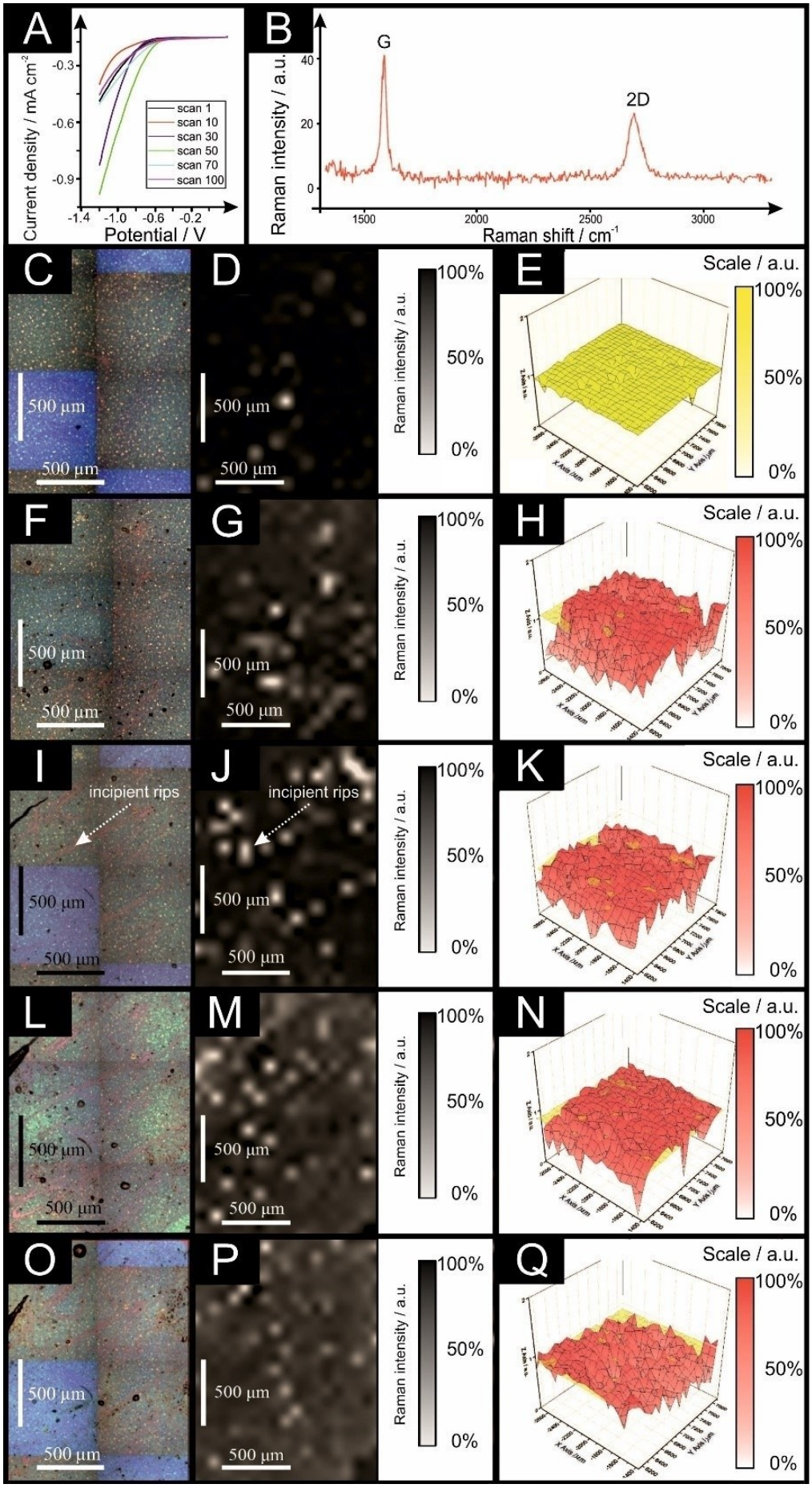
A
Current density / mA cm^{-2}
-0.3
-0.6
-0.9
-1.4 -1.0 -0.6 -0.2
Potential / V
scan 1
scan 10
scan 30
scan 50
scan 70
scan 100
B
Raman intensity / a.u.
40
20
0
G
2D
1500 2000 2500 3000
Raman shift / cm^{-1}
C
D
E
F
G
H
I
J
K
L
M
N
O
P
Q
500 µm
incipient rips
Raman intensity / a.u.
100%
50%
0%
Scale / a.u.

Figure 37. Scanning stability experiments using multilayer graphene; linear sweep voltammetry (LSV), scan rate: 25 mV s^{-1}; *vs.* RHE; solution: 0.5 M H_2SO_4. (B) Typical Raman profile of the multilayer graphene described and presented in C, D and E. Optical images of a multilayer graphene unused (C), after 30 LSV scans (F), after 50 LSV scans (I), after 70 LSV scans (L) and after 100 LSV scans (L). 2D Raman mapping of the multilayer graphene unused (D), after 30 LSV scans (G), after 50 LSV scans (J), after 70 LSV scans (M) and after 100 LSV scans (P). 3D Raman mapping of the multilayer graphene unused (E), after 30 LSV scans (H), after 50 LSV scans (K), after 70 LSV scans (N) and after 100 LSV scans (Q), all in red colour and compared to the unused sheet (yellow overlay). Raman maps show intensity of Graphene's G band (*ca*. 1590 cm^{-1}) in order to show the presence of graphene.

It is now turn to analyse the surface of the few- and multilayer graphene electrodes with Raman mapping spectroscopy. In order to study how the number of layers affects the integrity of the graphene sheet when utilised in electrochemistry, as depicted in Figure 36 and 37 respectively.

The few-layer graphene electrode is confirmed to be a continuous good quality sheet *via* the Raman and optical images that are presented. Electrochemical scanning the HER potential window ten times evidently creates holes in the sheet, as shown in Figure 36F, G and H. Following an additional twenty scans, a major damaged area is evident on the electrode surface, which is confirmed with Raman spectroscopy in Figure 36L, M and N; however, one must be aware that the disruption to the electrode surface is not to the same extent as that observed previously with monolayer graphene as it is likely that underlying layers dissipate the effect of lost layers and hence a loss in electrical conductivity.

Finally, multilayer graphene was analysed *via* Raman mapping and shown to be approaching the structural configuration of graphite (see Figure 37B), as confirmed in Figure 37C, D and E. Note that although minor changes to the electrode surface are observable following fifty LSV scans of the HER potential window, this remains unchanged up to one hundred scans (Figure 37F to 37Q). Clearly however, the Raman maps remain unaltered and there is little change in the HER performance observed, such that with the multilayered graphene electrode there appears to protect against the increase of holes. The origin of this maintained integrity is likely that of the underlying graphene layers (when exposed due to the failure of the upper most layers) reacting identically to the first layer and thus maintaining the observed response.

5.3 Conclusion

In summary, this chapter indicates that mono- and few-layer graphene, when used as electrodes toward the HER break-up when an electrical current is applied to them during electrochemical HER experiments performed within aqueous solution. The mechanism of which is first ripping of the film due to the evolution of H_2 (*i.e.* bubbles), creating surface defects due to frictional forces and a larger edge plane % (*i.e.* causing an observed improved response), after which ultimately the integrity of the graphene film as a whole is not viable and the electrical conductive pathways are disrupted and result in a loss of electrochemical signal. This response is mirrored with few-layered graphene structures, but not to the same extent. Conversely, multilayered graphene structures do not present this phenomena and remain stable (HER values and film integrity) after HER scanning for an extensive number of scans. These findings are of high importance to those working in the graphene energy field, particularly for those designing and implementing graphene electrical components given that the sheet integrity is questioned herein and this report shows that pristine graphene is not a beneficial electrode material towards the HER.

5.4 Experimental

The tested solutions were 0.5 M H_2SO_4. Working electrodes were: commercially obtained chemical vapour deposition (CVD) synthesised mono-layer, a few-layer (*quasi*-graphene) and multilayer-graphene films supported on an oxidised silicon wafer. A Pt wire counter/auxiliary electrode and a silver/silver chloride (saturated Ag/AgCl; +0.210 V *vs.* RHE) reference electrode completed the circuit.

The commercially available CVD synthesised graphene films, that have been used in our previous work[16, 34, 226], were obtained from 'Graphene Supermarket' (Reading, MA, USA)[227] and are known as 'graphene on 285 nm SiO_2 Wafer' and have been previously reported and characterised in the literature[47, 118, 119, 226]; the exact details are proprietary information[227]. Note that full physicochemical characterisation (Raman spectroscopy and X-ray photoelectron spectroscopy (XPS)) of the various graphene samples utilised within this work is reported in the Supplementary Information.

Raman Mapping Spectroscopy data was performed using a DXR Raman Microscope (Thermo Scientific, UK) fitted with a 532 nm excitation laser at a low power of 3 mW to avoid any heating effects. Spectra were recorded using a 3 seconds exposure time for 3 accumulations at each point. To collect the map a step size of 75×75 μm and a Raman profile between the region of 1050 and 3300 cm^{-1} was employed. Raman maps show intensity of Graphene's G band (*ca*. 1590 cm^{-1}) in order to show the presence of graphene.

5.5 Supporting Information

Time / s	*Diameter of bubble / µm*	*Volume of bubble / mm³*
0.0	9.7	4.8×10^{-7}
1.0	36.4	2.5×10^{-5}
3.0	54.9	8.7×10^{-5}
5.0	77.1	2.4×10^{-4}
20.0	151.8	1.8×10^{-3}
45.0	219.9	5.6×10^{-3}
72.5	272.8	1.1×10^{-2}

Table 5. Hydrogen bubble size growth generated in-situ while performing chronoamperometry, potential held at -1.2 V (*vs.* RHE), using monolayer graphene. Data clearly shows the evolution of a single hydrogen bubble from its initial generation to its explosion. Note that the measurement of the bubble started once it was big enough to be analysed with the optical microscope, therefore it is timed that initial measurement as 'time 0 seconds'.

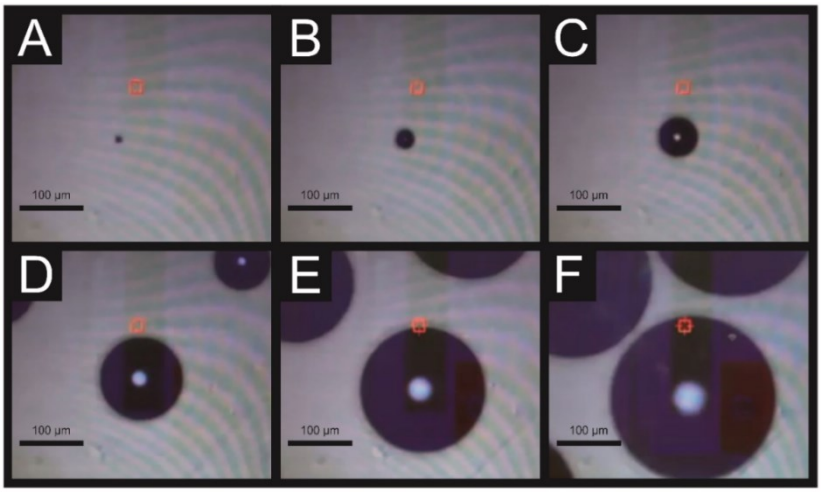

Figure 38. Snapshot from an in-situ video recorded while performing chronoamperometry, (potential held a -1.2 V (*vs*. RHE)) using monolayer graphene clearly showing the evolution of hydrogen bubbles on top of the graphene electrode over the following time periods: 0 (A) (zero as initial measurement time), 1 (B), 4 (C), 14 (D), 45 (E) and 67 (F) seconds. Video recorded from the top of the graphene during the electrochemical experiment.

The physicochemical characterisation of the batch graphene samples used in this work and their characterisation is reported below.

Atomic force microscopy (AFM) characterisation of the batch graphene samples used in this work including the monolayer and multilayer graphene have been reported previously by Brownson *et al.*[34]. Furthermore, X-ray photoelectron spectroscopy (XPS) has previously been performed on these batch samples revealing the monolayer graphene to comprise of an O/C ratio of *ca*. 0.05, which is consistent with that of a low oxygen content of the graphene domain and thus is indicative of being pristine (*aka* pristine graphene)[186]. In the case of the multilayer graphene samples, XPS reveals a O/C ratio of *ca*. 0.07, that is again consistent with inferences gained through Raman spectroscopy (see later) and indicates that the this material is comprised of pristine graphene.

Raman characterisation of the batch mono-, few- and multilayer graphene electrode normalised to the G peak were performed and are as depicted in Figure 39. The Raman spectra of the graphene films confirms the G (*ca.* 1550 cm^{-1}) and 2D (*ca.* 2680 cm^{-1}) characteristic peaks that allow us to quantify the number of graphene layers. The Raman spectra of the monolayer graphene sheets reveals that the full width at half-maximum (FWHM) of the 2D band corresponds to 34.72 cm^{-1}, which upon exploring the literature[110, 228] indicates that our batch samples are comprised of single layer of graphene; additionally the intensity ratio G/2D of 0.72 suggests that the graphene samples are comprised of monolayer due to the lower intensity of the G band in relation to the 2D peak. The Raman spectrum of the few-layer graphene films reveals an intensity ratio of G/2D of 1.00 suggesting that the electrode is comprised of dual-layer graphene, but as there are occasional multilayer islands; it is therefore named herein as “few-layer” graphene. The Raman spectrum of the multilayer graphene

reveals an intensity ratio of G/2D of 1.76 suggesting that such electrode is comprised of multilayer graphene.

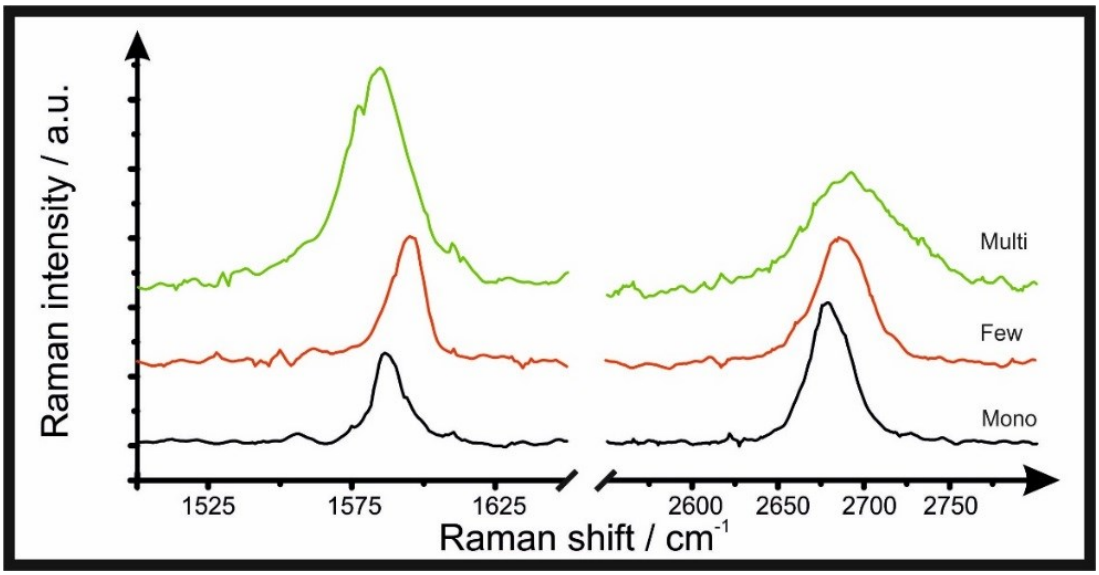

Figure 39. Raman characterisation of mono-, few- and multilayer graphene utilised within this work. Raman is performed with a 532 nm excitation laser at a low power of 3 mW to avoid any heating effects. Spectra were recorded using a 3 seconds exposure time for 3 seconds exposure time for 3 accumulations at each point.

Chapter 6: Investigating the Integrity of Graphene towards the Electrochemical Oxygen Evolution Reaction (OER)

This chapter investigates mono-, few- and multi- layer graphene towards the electrochemical Oxygen Evolution Reaction (OER). This work indicates the importance of the scan rate and potential limits applied to graphene electrodes in addition to the relationship between the number of layers and structural integrity. Raman mapping characterisation is performed, revealing that the structure of graphene is damaged due to the electrochemical perturbation of the OER. The performance of mono- and few- layer graphene electrodes gradually decrease with consecutive OER scans, with the process damaging the graphene sheet, after which there is a loss in the electrochemical signal and the electrically conductive pathways. Importantly, the severity of these changes is dependent on the potential and chosen scan rate that is applied to the graphene electrode. Contrary however, multilayer graphene's initial performance towards the OER process improves after the first few scans, which is likely due to an increase in the coverage of edge plane sites/defects and underlying layers maintaining electrical contact. This work highlights the impact of establishing the correct experimental conditions when applying CVD graphene towards electrochemical applications, and how parameters such as gas formation, potential limits, scan rate and surface characterisation are important parameters to take into account when one is applying CVD graphene towards electrochemical/energy applications.

6.1 Introduction

Water oxidation, namely the oxygen evolution reaction (OER), is part of the water splitting reaction and involves a complex process with a solid catalyst, electrolyte, and both gas-/liquid-phase reactants and products[229, 230]. The OER is recognized as a very sluggish reaction in water electrolysis for clean hydrogen energy,

due to not being kinetically favored and usually requires precious iridium- or ruthenium-based catalysts to reduce the overpotential[231]. Water splitting consists of the reaction of water molecules to form molecular hydrogen and molecular oxygen, usually described as two half reactions: at the cathode, protons are reduced to hydrogen (hydrogen evolution reaction; HER); and at the anode, water is oxidized to oxygen (oxygen evolution reaction; OER). The OER involves four proton-coupled electron transfers and oxygen-oxygen bond formation in *acidic* conditions: $2H_2O \rightarrow O_2 + 4H^+ + 4e^-$. In *alkaline* conditions the OER involves four hydroxyl groups (OH^-) being transformed into H_2O and O_2 molecules with four electrons involved $4OH^- \rightarrow O_2 + 2H_2O + 4e^-$.

Currently, there is significant research interest into studying the fundamentals of the OER in order to obtain more active catalysts[232-236]. At the same time, the key to developing mass-producible and economical fuel cells is realizing the use of nonprecious metals as highly active catalysts[237-241]. Recently, carbon-based materials have been reported to be a viable source for durable and affordable OER catalysts[242]. A promising alternative is the combination of carbon-nitrogen with the high activity of earth-abundant transition metals (such as Co, Ni, Mn, Fe *etc*.)[243-247]. It is also important to consider that thick carbon shells have been reported to obstruct the electron transfer from metals to carbon, reducing the catalytic activity of the catalyst[248, 249]. As a result, there is interest in developing graphene-based catalysts using innovative strategies including surface functionalization[250], geometric arranging[251] and heteroatom doping[252]. There is therefore a need to fundamentally understand the intrinsic relationship of the graphene structure (mono-, few- and multilayer) correlated to electrochemical performance.

Herein, it is explored and fully characterise the electrochemical stability of mono-, few- and multi-layer Chemical Vapour Deposition (CVD) grown graphene electrodes towards the OER, with the purpose of finding the origin of physical/structural changes in pristine graphene and with importance to future graphene-based OER catalysts.

6.2 Results and discussion

Attention was first turned to benchmarking mono-, few- and multi-layer (basal plane) graphene as an electrode platform towards the OER within alkaline media (0.1 M KOH), as is common within the literature[253]. Figure 40 shows electrochemical scanning stability experiments using mono-, few- and multi-layer graphene electrodes towards the OER after five OER linear sweep voltammetry (LSV) scans (from +0.21 to +1.61 V; Scan rate: 25 mV s^{-1}, *vs.* RHE). As one can see in Figure 40A, the electrochemical performance of mono-layer graphene towards the OER decays when successive scans are completed; note also that the electrochemical signal of the first scan is affected by bubbles being formed upon the graphene electrode's surface, which are oxygen bubbles being formed as a result of the OER occurring at edge plane sites/defects upon the basal plane graphene surface.

The first OER scan using the mono-layer graphene has a current of 3.13 μA cm^{-2} (at +1.61 V, vs. RHE), after which there is a significant decrease to 2.24, 1.78, 1.58 and 0.29 μA cm^{-2} (at +1.61 V) for the successive five scans respectively, indicating a decay in the electrochemical current and reduced electrochemical activity. These changing electrochemical observations clearly suggest a physical change of the mono-layer basal plane electrode and in the conductive electron pathways. In the case of few-layer graphene towards the OER, as depicted in Figure 40B, shows a gradual decrease in the electrochemical performance during 5 individual LSV scans (from 11.3 μA cm^{-2}

at the first scan down to 0.852 μA cm^{-2} (at +1.61 V) at the fifth scan), similar to the case observed with mono-layer graphene. Finally the electrochemical response of multi-layer graphene, as shown in Figure 40C, the current increases when further scans are performed from 108 μA cm^{-2} to 3234 μA cm^{-2} (at +1.61 V; vs. RHE) at the fifth scan, having a similar LSV profile and values between the 30th and 50th consecutive scans, where the electrochemical performance stabilises.

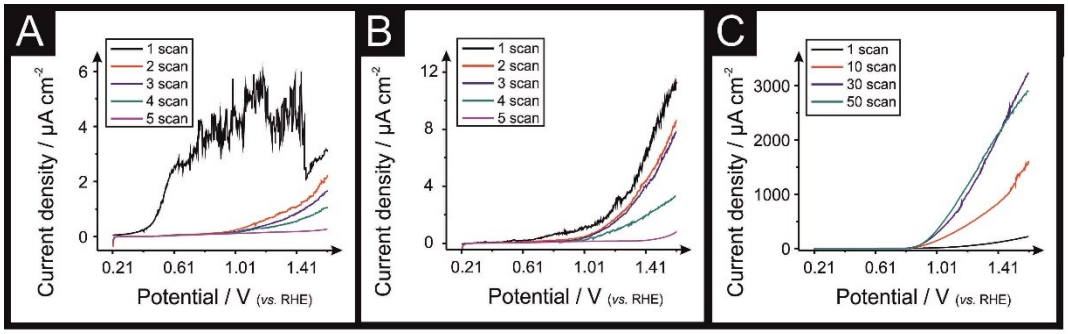

Figure 40. Scanning stability experiments of mono- (A), few- (B) and multi-layer graphene (C); linear sweep voltammetry (LSV) from 0 to +1.61 V; Scan rate: 25 mV s^{-1}; *vs.* RHE; Solution: 0.1 M KOH.

In Figure 41 the Raman mapping characterisation and optical images from the graphene samples/electrodes in Figure 40 can be observed. It is clear that the mono- and few-layer basal plane graphene surfaces are mostly damaged and show the lack of characteristic Raman peaks, which usually occur at *ca*. 1590 cm^{-1} and 2690 cm^{-1} respectively; such peaks *are* evident *prior* to experimental probing[110] after 5 LSV scans. Conversely, the multi-layer graphene electrode remains mostly unaltered across its surface throughout experiments, evidenced by to the optical and Raman mapping characterisation (showing an inherent resistance to such surface changes).

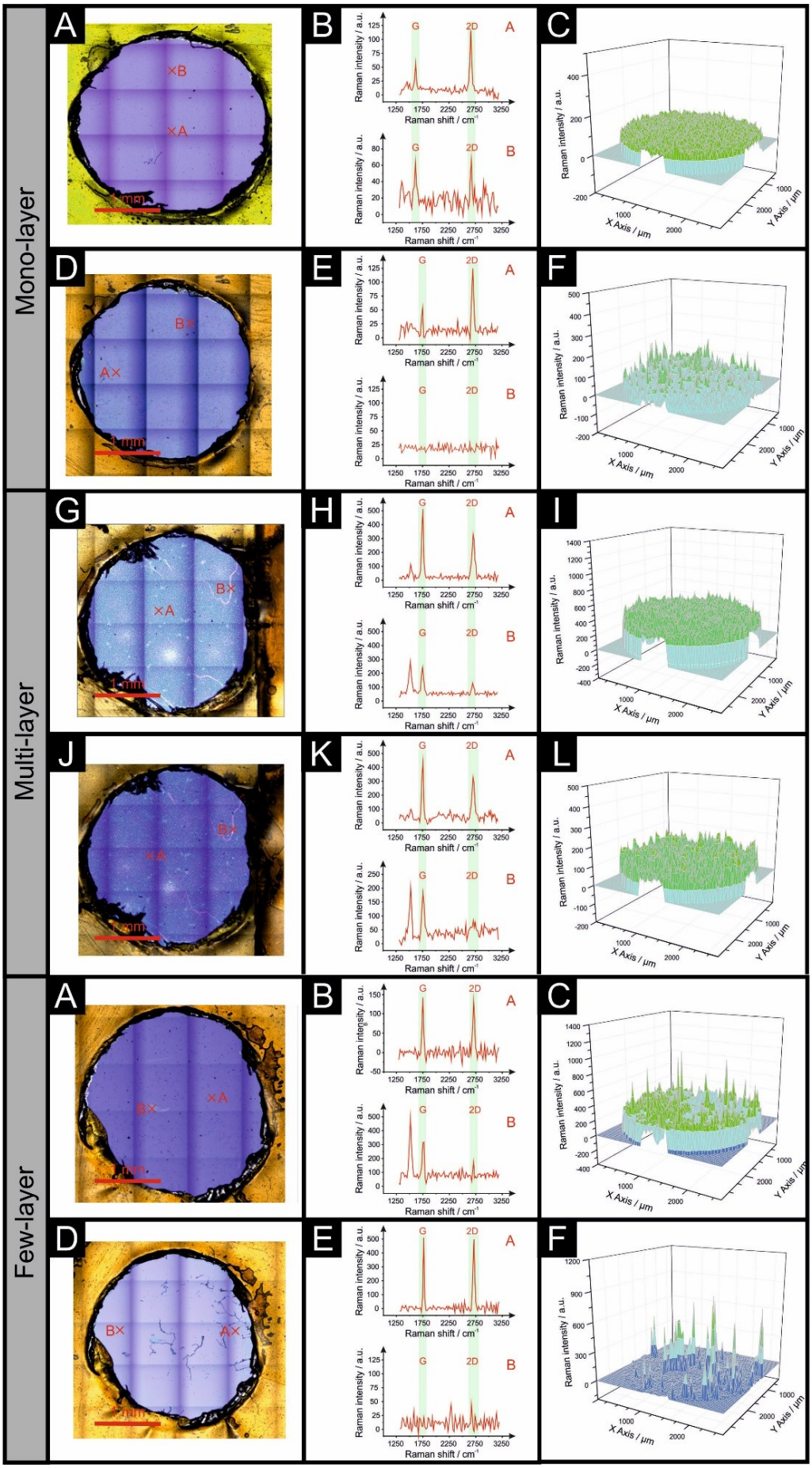
Mono-layer
Multi-layer
Few-layer
A
B
C
D
E
F
G
H
I
J
K
L
×A
×B
1mm
G
2D
Raman intensity / a.u.
Raman shift / cm⁻¹
X Axis / μm
Y Axis / μm

Figure 41. Scanning OER stability experiments using mono-, few and multi-layer graphene; Mono-layer graphene (A to F) showing an optical image, its Raman profile and 3D Raman map (A, B and C respectively) of the unused mono-layer graphene. Mono-layer graphene after 5 LSV OER scans optical, its Raman profile and 3D Raman map (D to F respectively). Few-layer graphene (G to L) showing an optical image, its Raman profile and 3D Raman map (G to I) of the unused few-layer graphene. Few-layer graphene after 50 LSV OER scans optical, its Raman profile and 3D Raman map (J to L). Multi-layer graphene (M to R) showing an optical image, its Raman profile and 3D Raman map (M to O) of the unused multi-layer graphene. Multi-layer graphene after 5 LSV OER scans optical, its Raman profile and 3D Raman map (P to R).

Attention was then turned to considering how the different scan rates applied to the electrode surface can affect the structural integrity of the mono-layer graphene. Note that this is a common approach to characterize the electrochemical performance of an electrode material (voltammetric scan rate study) to determine the heterogeneous electron transfer kinetics, providing an electrochemical benchmarking of the graphene electrode under investigation. Figure 42 shows the optical images and Raman maps of both 'unused' and 'used' (following 5 LSV OER scans) electrodes, after being used at different scan rates (2.5, 25, 250 and 2500 mV s^{-1}). The damage created on graphene surfaces is evident, the degree of damage is related to the scan rate applied. It is clear that faster scan rates create extended damage on the surface of the electrode, having a more focused or confined damage pattern than when slower scan rates are applied. Interestingly, similar microstructural and compositional surface fragmentation have been previously reported in graphite electrodes, due to prolonged and variable scan rates potential cycling when exploring Li-ion storage applications[254-256]. This could suggest, that *in-situ* generated gas bubbles and Li-ion intercalation move along the surface of graphitic films creating similar defects/damage to the surface of the electrode.

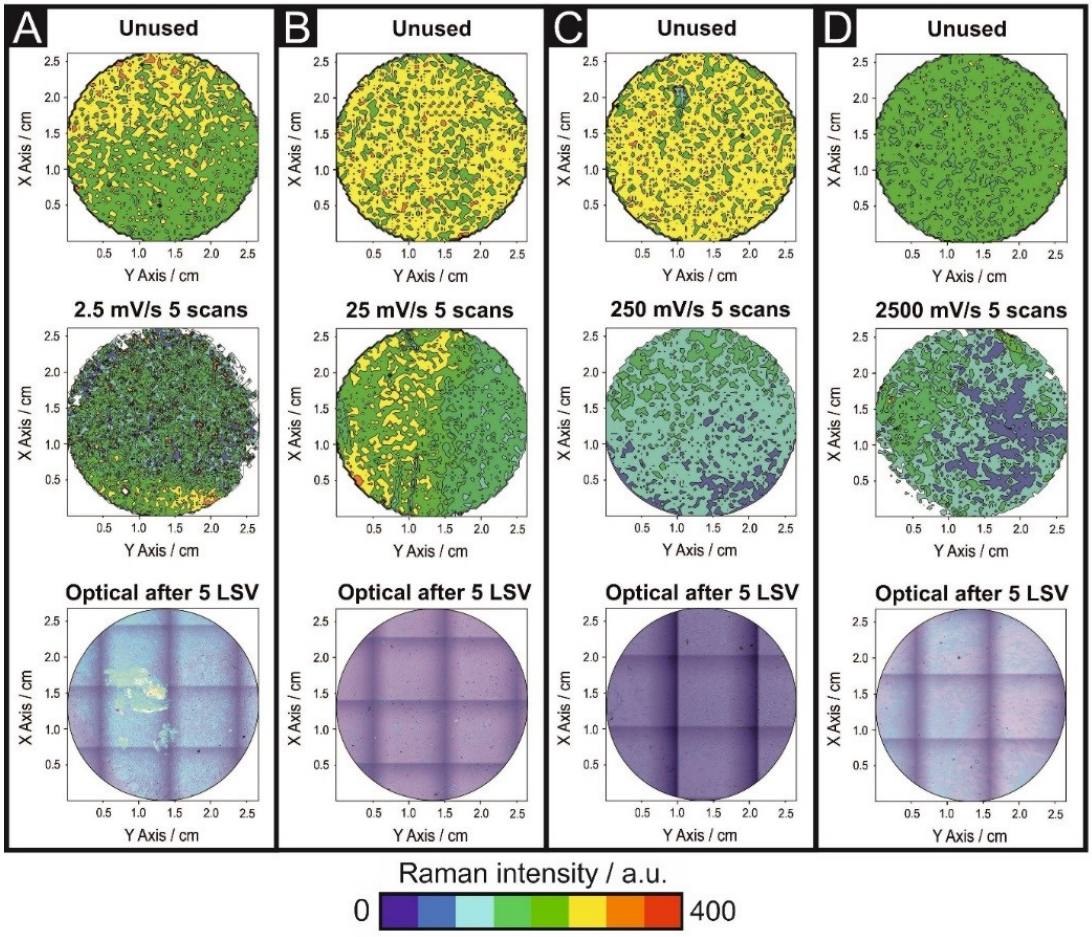

Figure 42. Scan rate OER stability experiments using mono-layer graphene at 2.5 (A), 15 (B), 250 (C) and 2500 (D) mV s^{-1}, showing the Raman mapping characterisation before and after 5 LSV OER scans and optical image of the electrode after the 5 LSV OER scans. (Solution: 0.1 M KOH; *vs.* RHE).

Next, chronoamperometry (CA) was utilised in order to analyse the origin of the breakup of graphene's structure when applied towards the OER. Herein, a fixed potential was held for 280 seconds, which corresponds to the same amount of time as the electrode using in the scanning stability studies at 25 mV s^{-1} (Figures 41 and 42). In Figure 43, CA studies are performed at +0.61, +1.01 +1.41 and +1.61 V (*vs.* RHE) for samples named 1 to 4 of mono-layer graphene respectively, showing optical images, Raman profiles and Raman mapping characterisation for each sample 'before' and 'after' applying the fixed potential. Sample 1 and 2 (Figure 43A to F and 43G to

L respectively) have the typical Raman peaks in their profiles both before and after being used; although some localized damage can be seen. Sample 3 (Figure 43M to R) shows the presence of a continuous graphene sheet after being used for 280 seconds at +1.41 V, however upon inspection of the Raman profile one can observe the presence of a graphene D band (*ca*. 1350 cm^{-1}) that corresponds to defects in the lattice structure, similar to that observed in graphene quantum dots[257-260] (GQD; sometimes also called nanographene[261]) or ozonolyzed CVD graphene[262]. Sample 4 (Figure 43S to X) shows a large damaged area after holding +1.61 V (*vs.* RHE) for 280 seconds, in addition to the presence of the characteristic D band/peak (*ca*. 1350 cm^{-1}) previously described in Sample 3.

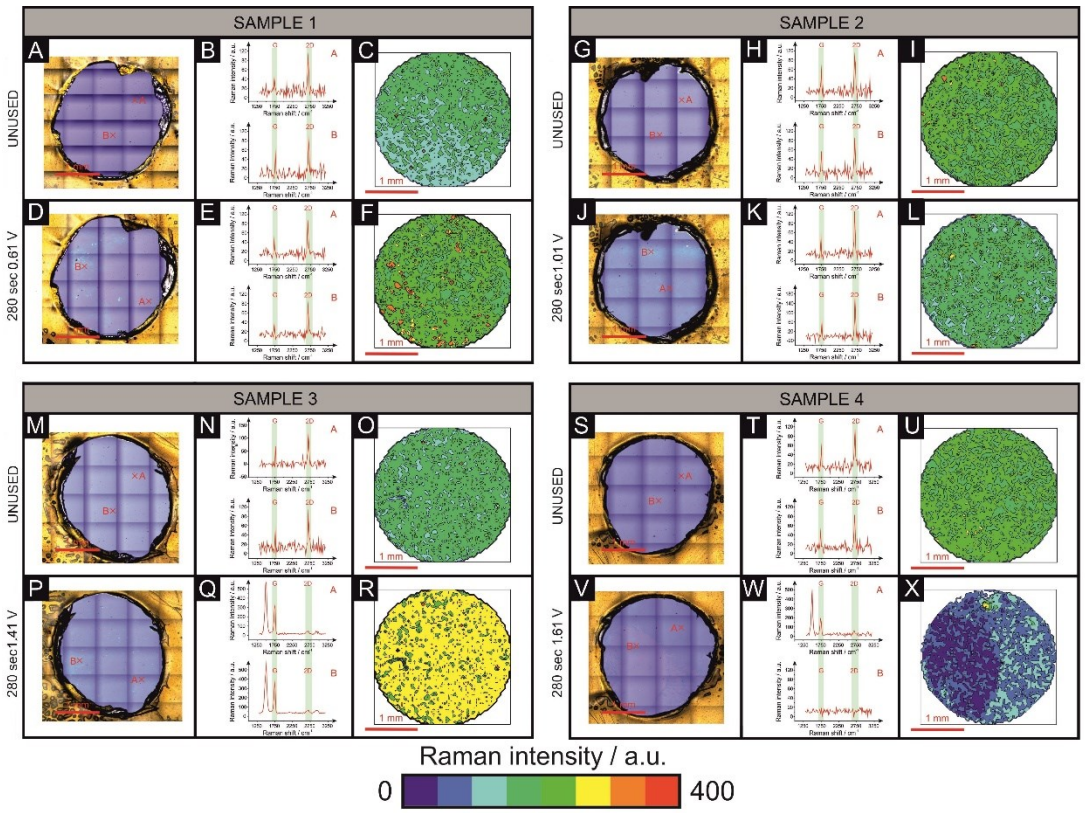

Figure 43. Chronoamperometry stability experiments using mono-layer graphene, holding a fixed potential at 0.61 V (A to F), 1.21 V (G to L), 1.41 V (M to R) and +1.61 V (S to X), showing optical images and Raman mapping characterisation before and after holding the fixed potential for 280 seconds (Solution: 0.1 M KOH; *vs.* RHE).

As shown above, clearly, an important factor to consider in terms of material integrity in the OER in the degradation of the graphene sheet is the physical movement of the generated oxygen bubbles themselves, which are generated at edge plane sites/defects. Electrochemical systems have been reported to suffer poor management of evolving gas bubbles[263]. Gas formation can be divided in four stages that occur simultaneously on the surface of the electrode: nucleation, growth, detachment and rise[264, 265]. In order to capture the graphene damage due to O_2 evolution, as a result of the OER occurring at the various graphene electrodes/surfaces, as it takes place, an *in-situ* video was captured, showing a mono-layer graphene electrode while a CA was

applied (at +1.61 V, *vs.* RHE). Figure 44 depicts screen captures taken from the aforementioned video, showing the graphene surface and the nucleation, growth and detachment of O_2 at ten, twenty, thirty and forty seconds (Figures 44A, B, C and D respectively) since the fixed potential is applied. One can see the direct damage created to the surface of the mono-layer graphene when a bubble is nucleating, growing and coalescing with other bubbles and while moving across the electrode. Large bubbles act as collectors, attracting smaller growing bubbles, inducing mechanical forces, heat transfer and mass diffusion due to supersaturation of surrounding liquid solution[266] and are likely the reason of the collapse of the graphene integrity.

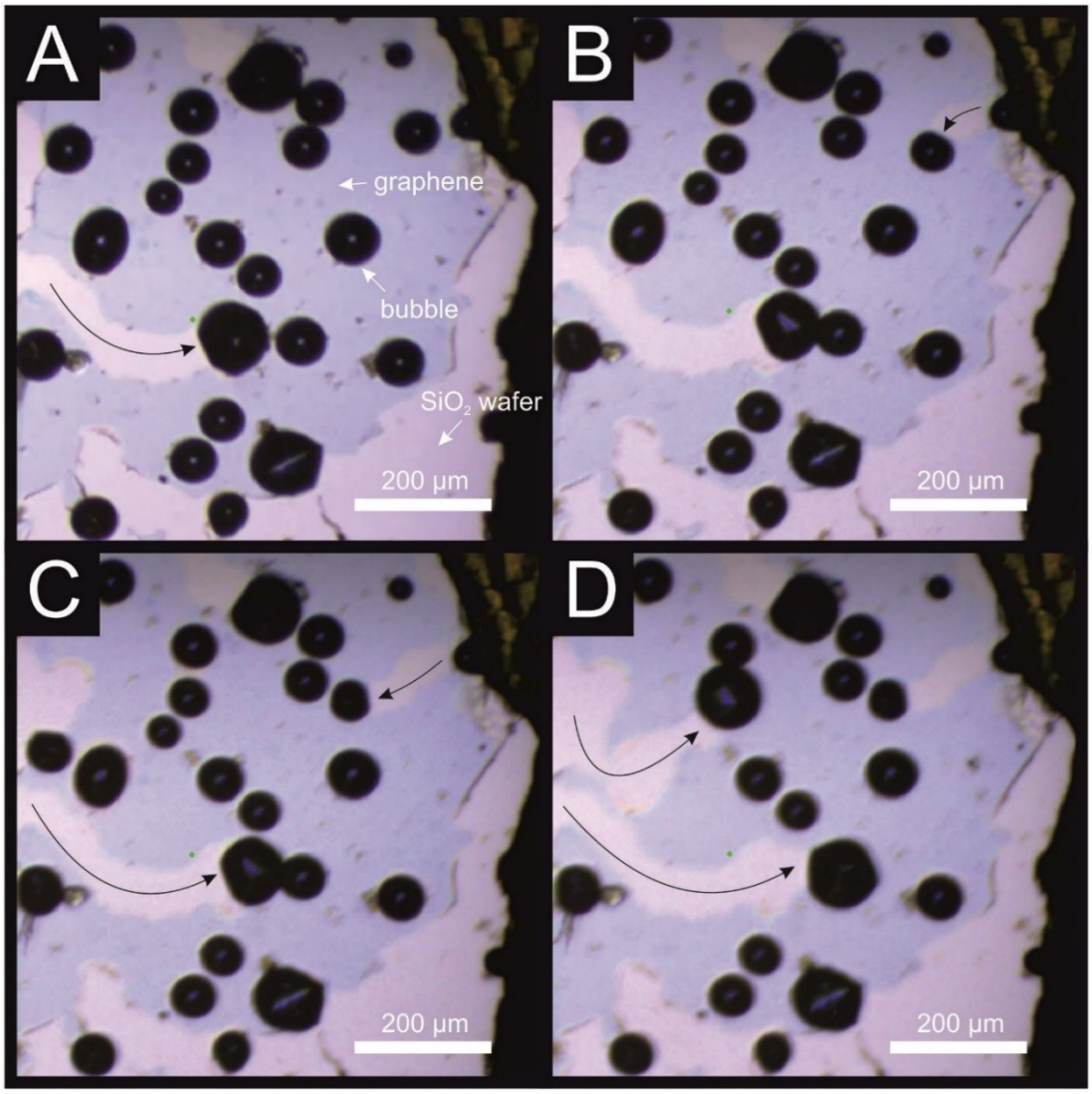

Figure 44. Captions extracted from an *in-situ* video recorded while performing chronoamperometry (potential held a +1.61 V (*vs*. RHE)), using mono-layer graphene. Captions show the evolution of hydrogen bubbles over the following time periods: 10 (A), 20 (B), 30 (C) and 40 (D) seconds. Black arrows indicate the movement of the bubbles damaging the surface of the electrode.

Figure 45 presents a schematic overview of the proposed mechanism of degradation of the mono- and few-layer graphene electrode, which shows that the detachment or departure of bubbles from the electrode's surface can also cause damage to the electrode. Once a bubble grows, fuelled at the edge plane sites/defects *via* the OER reaction, large enough to reach a critical volume, at which the flotation force surpasses the interfacial tension between the oxygen filled gas bubble and the electrode surface, the bubble will detach or collapse from the surface of the electrode into the bulk solution. The collapse of the bubble can lead to surface cleaning, *via* frictional forces as it is "filled" at active edge plane sites/defects, or in addition, to surface cavitation, ablation and/or fracture[267]. It is inferred herein that this is the mechanism that results in the degradation of graphene surfaces, rather than graphene not being able to support such large over-potentials. It is likely that the mechanism for breakup of the graphene sheet occurs due to three contributing factors: *i*) given that the graphene structure is too thin/fragile on the macro-scale, it cannot accommodate the charge/current passed through it; *ii*) bubbles are formed on the surface of the graphene sheet and break it *via* frictional forces and when the bubbles collapse (as described above); and *iii*) bubbles evolve from underneath the graphene sheet (which is unlikely). Currently, there is no way to de-convolute the degradation process from that of bubbles generation/surface motion from that of charge instability, but we inferred the former based upon observations (Figure 44) and note that the predominant mechanism is likely that of (*ii*) the bubbles formed upon the graphene surface and the resultant physical forces induced.

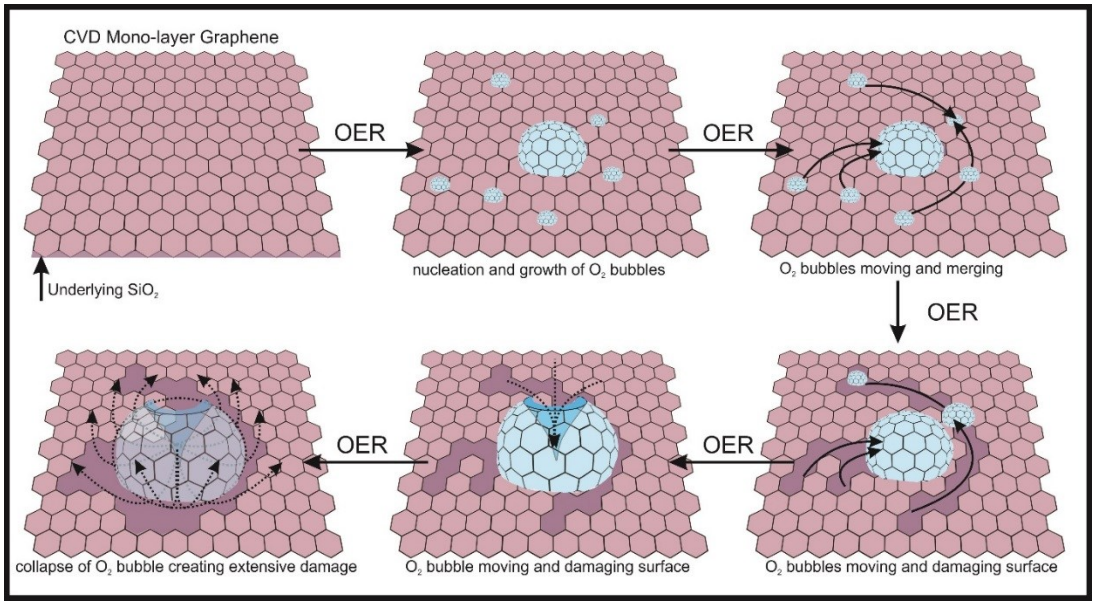

Figure 45. Monolayer graphene stability schematic under OER consecutive scanning, showing bubbles growing, merging and collapsing inducing structural damage in the surface of the mono-layer graphene electrode.

The data presented herein has shown the damage sustained to a graphene structure when applied as an electrode material towards the OER. This damage is directly dependent on the number of layers comprising the graphene electrode, the applied voltage (voltages higher than +1.41V, *vs.* RHE, in this case) and scan rate applied (faster scan rates create more extensive damage). This behaviour indicates that the generation and movement of O_2 bubbles results in the graphene surface first becoming defective (according to the presence of a D band in its Raman profile) and later collapsing/breaking-up completely. Note that it has been reported previously that mono- and few-layer CVD graphene is not a beneficial electrode material towards the HER due to the generation of H_2 bubbles (see Chapter 5 of this thesis); although at first its response improves the electrochemical reversibility of the reaction due to an increase in the edge-site/defect coverage prior to electrochemical cycling damaging the electric pathway. In this case of this chapter, the application of CVD graphene towards the OER induces the creation of defects on/across the electrode's surface, likely due to the generation and movement of O_2 bubbles, creating rips, holes and defect-dense graphene domains akin to nano-ribbon like structures, which finally disrupt the conductive pathway, ultimately resulting in a loss of electrochemical signal.

6.3 Conclusion

The behavior described in this chapter shows, for the first time, that mono- and few-layer CVD graphene electrodes break-up when utilised towards the OER. The mechanism in which the graphene structure rips occurs when potentials more positive than +1.41 V (*vs.* RHE) are reached. Evidence of small fragments of graphene/nano-ribbon like structures were found, according to the Raman characterisation, when a potential of +1.41 V is held for prolonged time. More positive potentials fixed for the

same period of time (as per cycling potential exposures) created extended damage on the mono-layer graphene sheet. The scan rate applied on the electrode surface also has an effect on the stability of the reaction, creating more damage when faster scan rates are applied. This reported response (or instability) is evident at both CVD mono- and few-layer graphene electrodes, what is important however, is that multi-layer graphene *does not* present the same inherent limitations, with this material remaining stable after OER scanning for a larger number of consecutive scans. These findings are relevant to those working with CVD graphene at high potentials, given that the integrity of the material's structure is compromised, it is evident that CVD mono-and few-layer graphene are *not* suitable electrode materials towards the OER. Such work is of fundamental importance when graphene surfaces are use either "as is" or as the basis of catalyst as used in the OER.

6.4 Experimental information

The tested solutions were 0.1 M KOH. Working electrodes were: commercially obtained Chemical Vapour Deposition (CVD) synthesised mono-layer, a few-layer (*quasi*-graphene) and multilayer-graphene films supported on an oxidised silicon wafer. A Pt wire counter/auxiliary electrode and a silver/silver chloride (saturated Ag/AgCl; converted to *vs*. RHE using the factor +0.210V *vs.* RHE) reference electrode completed the circuit.

The commercially available CVD grown graphene films, that have been used in our previous work[16, 34, 226, 268], were obtained from 'Graphene Supermarket' (Reading, MA, USA)[227] and are known as 'graphene on 285 nm SiO_2 Wafer' and have been previously reported and characterised in the literature[47, 118, 119, 226, 268]; the exact details are proprietary information[227]. Note that full physicochemical of the various graphene samples utilised within this work have been previously reported and characterised[268].

Raman Mapping Spectroscopy data was performed using XploRA PLUS (Horiba, UK) fitted with a 638 nm excitation laser at a low power of 3 mW to avoid any heating effects. Spectra were recorded using a 5 seconds exposure time for 1 accumulations at each point. To collect the map a step size of 40×40 μm and a Raman profile between the region of 1300 and 3200 cm^{-1} was employed, mapping a circular-shaped area of 2.6 mm of diameter. 3D Raman map figures depict the intensity of the characteristic Raman G band for graphene (*ca*. 1590 cm^{-1}) recorded from their full Raman spectra.

Graphene Raman characterisation

Raman characterisation of the batch mono-, few- and multilayer graphene electrode normalised to the G peak were performed and are as depicted in Chapter 5, Figure 39.

Chapter 7: Tailoring the electrochemical properties of 2D-hBN *via* physical linear defects: physicochemical, computational and electrochemical characterisation

This chapter considers physicochemical, computational and electrochemical characterisation techniques towards identifying the electrochemical activity of monolayer hexagonal-boron nitride films (2D-hBN). 2D-hBN films are typically reported within the literature to be electrochemically insulating due to their considerable band gap; however this chapter shows that the formation of physical linear defects (PLD) on the basal plane surface can lead to the full hydrogenation of the 2D-hBN sheets, which can also lead to oxygen passivation of the boron and/or nitrogen at its edge sites; this in turn causes a decrease in the band gap (from *ca*. 6.11 to 2.36/2.84 eV, calculated Density Functional Theory (DFT) values). 2D-hBN films with such defects are shown to be electrochemically active, this behaviour is dependent directly upon the coverage of edge plane-sites/defects and this is correlated with the electrocatalytic activity towards Hexaammineruthenium (III) chloride (RuHex), $Fe^{2+/3+}$ and the Hydrogen Evolution Reaction (HER). This chapter de-convolutes, for the first time, the fundamental electron transfer properties of 2D-hBN, demonstrating that through implementation of physical defects one can tailor the properties of this material. It is also shown in this chapter how other 2D materials such as 2D-hBN can be tailored and applied for electrochemical applications by simple surface modifications.

7.1 Introduction

Two-dimensional (2D) nanomaterials came into the spotlight after Novoselov and Geim first isolated a mono-layer of the carbon honeycomb lattice structure, 'graphene' in 2004[25], and have since gained more traction following the award of their Nobel prize in 2010.

Boron nitride (BN) is a structural analogue of graphite, in which an equal number of boron and nitrogen atoms form a honeycomb lattice structure[70] of sp^2 bonded layers[71]. This structure is not found naturally and was first synthesised by Balmain[72, 73] in 1842. Hexagonal boron nitride (2D-hBN) is a structural analogue of graphene and has high thermal conductivity and robustness to oxidation[74], which historically has allowed it to be used as a lubricant[75-77]. 2D-hBN has also been utilised to improve the mechanical properties of composites, even at low percentages[78-80], when added as few layered nanosheets due to its low density and good thermal/chemical stability[81-83].

As reported within the literature, electrically, 2D-hBN (see Figure 52A) has a wide band gap (*ca*. 5.2-5.8 eV)[84, 85], which makes it classed as an electrical insulator[85], thus it is widely applied as a charge leakage barrier-layer in electronic equipment[71, 86]. Interestingly, 2D-hBN has also been used to tailor the band gap of graphene (creating graphene-hBN interfaces)[86-97] and another approach to decreasing/modifying 2D-hBN's band gap is creating thin strips of single layered 2D-hBN nanosheets; thus producing nanoribbons (NRs) (see Figure 52B), which contain a honeycomb lattice with either armchair or zig-zag edges that possess active dangling bonds[98]. The electronic properties of such nanoribbons are strongly affected by edge termination structures, reconstructions and functionalization[99, 100] and recently several reports have indicated the inherent electrocatalytic behaviour of 2D-hBN[101, 102]. Moreover, Golberg *et al.*[269] reported that 2D-hBN-NRs become semiconductors due to doping-like conducting edge states and vacancy defects. Furthermore, by controlling the hydrogenation ratio, the electronic and magnetic properties of zig-zag–terminated 2D-hBN-NRs can be precisely tailored, modulating their band gap[270]. Most recently in electrochemistry however, 2D-hBN has been explored computationally as a potential

electrocatalyst towards the Oxygen Reduction Reaction (ORR) (when computationally supported upon Co, Ni or Cu substrates), where it was shown that the underlying metal support highly influences the electrochemical behaviour of the 2D-hBN[271]. In other work, Uosaki *et al.* reported 2D-hBN powder immobilised upon gold electrodes showing activity towards the ORR[272], proving previous theoretical predictions, and Khan *et al.* have reported 2D-hBN powder to be sensitive to the substrate roughness[102] and surfactant content[101] towards the ORR. In terms of electrochemical properties, Li recently developed a nano-flake hBN supported on a glassy carbon electrode (hBN/GCE) towards the detection of ascorbic acid, dopamine and uric acid, which exhibited wide linear ranges, a low limit of detection and outstanding anti-interference ability, making it a potential candidate for sensor devices[273].

In order to de-convolute and understand the electrochemical properties of 2D-hBN, this chapter utilises CVD grown 2D-hBN (supported upon SiO_2), in comparison to 2D-hBN in powder form used in all the above, allowing full control of the surface morphology which is studied with physicochemical, computational supported and electrochemical characterisation. It is demonstrated herein, that the electrochemical response of 2D-hBN can be tailored through the introduction of physical linear defects (PLDs) upon the surface of the 2D-hBN, which transforms this previously electrochemically inert material into one that gives rise to electrochemically useful signatures/activity. Importantly, given that the current accepted model of 2D-hBN is that of being an insulator/inert material within electrochemical applications, this chapter shows that its behaviour is more complex than initially reported.

7.2 Results and discussion

7.2.1 Electrochemical and physicochemical characterisation

The electrochemical properties of CVD grown 2D-hBN (supported on SiO_2) are first characterised with cyclic voltammetry (CV), using $Ru(NH_3)_6^{3+/2+}$ (RuHex) which is a near ideal[190] outer-sphere probe (exclusively sensitive to the electronic structure of the electrode's surface), and additionally $(NH_4)_2Fe(SO_4)_2$ ($Fe^{2+/3+}$) is selected as an inner-sphere redox probe due to its sensitivity to oxide groups on the electrode's surface only[190]. Figure 46 shows that the 2D-hBN electrodes exhibit no observable electrochemical activity towards RuHex and $Fe^{2+/3+}$. These results confirm the literature assertion that 2D-hBN is indeed an inert/insulating material.

Previous work on 2D materials has asserted that active edge plane-sites/defects are the origin of electron transfer[9, 147, 171], and consequently, attention was turned to try and introduce such sites, through investigating the creation of physical linear defects (PLD) upon the surface of the 2D-hBN (now termed: PLD-2D-hBN). In order to explore this, a *ca.* 1 mm (length) by 60 μm (width) physical linear defect (PLD) was physically created, with a diamond knife, on the surface of the electrode (as described within the Supporting Information; 0.8 x 0.8 cm of exposed area) to create defective edges on the surface. The PLD-2D-hBN sample was then applied towards the electrochemical detection of RuHex and $Fe^{2+/3+}$ as depicted in Figure 46. Figure 46A depicts the absence of voltammetric peaks associated to RuHex when a 2D-hBN electrode was utilised. For controls, a PLD-SiO_2 wafer was utilised (no 2D-hBN), and just a SiO_2 wafer which also yielded no electrochemically measurable/observable responses. However, in the case of the PLD-2D-hBN there is a clearly evident electrochemical response, which is associated to the electrochemical reduction and oxidation of RuHex. It is interesting to note that the electrochemical signature (*viz*

Figure 46A) is sigmoidal in nature and is due to the fact that the PLD is akin to that of a nanoband; while the PLD is fabricated with a 1 mm length and 60 micron width, it creates a morphology that has no material in the middle and that we have 2 x 1mm lengths and two 60 micron width and as the edges are only active, and due to diffusional interaction, the overall response becomes that of a nanoband. This is consistent with the magnitude of the current observed in Figure 46. In the case of the other redox probe, Figure 46B shows the CVs of $Fe^{+2/+3}$ which again exhibits no measurable electrochemical activity at the PLD-SiO_2 wafer and SiO^2 wafer, but again, for the case of the PLD-2D-hBN there is clearly an electrochemical oxidation peak associated with the redox probe. In summary it is clear that upon the introduction of physical linear defects upon a 2D-hBN film/electrode, an electrochemical signal output is observed that is not present with the pristine 2D-hBN working electrode (and controls). Note that we infer that the PLDs are acting as electroactive sites. CVs of RuHex and $Fe^{+2/+3}$ using a PLD-SiO_2 wafer (*i.e.* a substrate control with no 2D-hBN) are depicted in Figure 53, showing the absence of a voltammetric profile when no 2D-hBN is present; also the lack of diamond contamination is shown from observing the Raman profile of both SiO2 and PLD-2D-hBN (shown in Figure 53), thus there is confidence that the PLDs are the origin of the observed electron transfer.

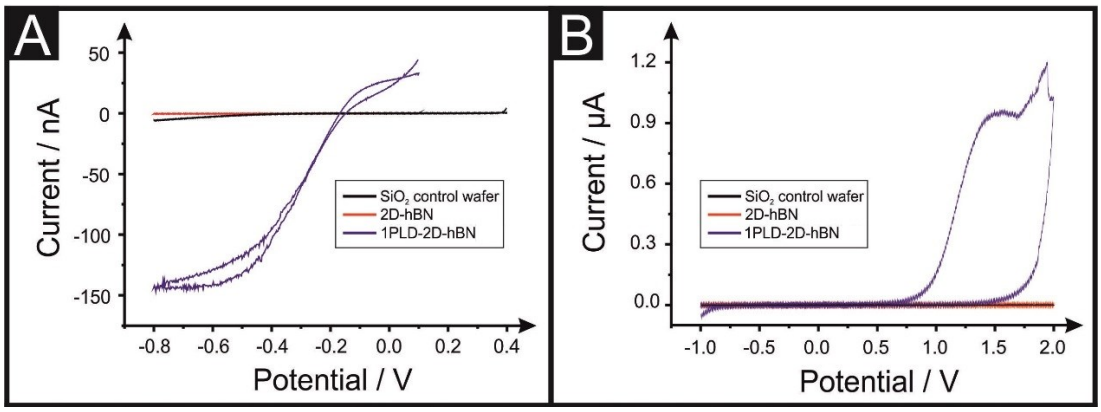

Figure 46. Cyclic voltammetry for 1 mM RuHex /0.1 M KCl (A) and 1 mM $Fe^{2+/3+}$/0.2 M $HClO_4$ (B) using a PLD-SiO_2 wafer as first control (black line), a 2D-hBN electrode (red line) and a PLD-2D-hBN electrode with 1 defective line (violet line) as working electrodes respectively. Scan rate: 50 mV s^{-1}; *vs.* Ag/AgCl. Note that the introduction of PLD gives rise to electrochemically useful signatures.

In the above approach, a microband electrode is fabricated, this approach, historically, has the electrochemical advantages of fast mass transport, high signal to noise ratio, short time to reach the steady state and gives rise to enhancements in electroanalytical and kinetic measurement. However, due to the size (*i.e.* nano) the current output is nano-amperes and can be plagued with noise such as from the mains. To overcome this, an array of many nanobands wired in parallel can offer the same enhanced sensitivity of a single microband but with the advantage of a higher total current output. We sought to introduce multiple PLDs onto the 2D-hBN electrode surface. It is explored next, the response of 1 PLD through to a total of 6 PLDs using RuHex as shown in Figure 47. It was found that additional PLDs created on the surface result in further improvement in the electrochemical response, but the current doesn't readily scale with the increasing number of PLDs since there are diffusional inactions between the PLDs due to physical constrains upon the electrode surface. Nevertheless, this demonstrates that the current can be increased from the nano-ampere region to

that in the micro-ampere range. It is attempted to undertake a voltammetric scan rate study, that is, the scan rate is changed from slow (15 mV s^{-1}) to fast (250 mV s^{-1}) to provide further electrochemical insights. It is observed that the voltammetric current started to fade upon excessive scan rates, it is this what is next explored.

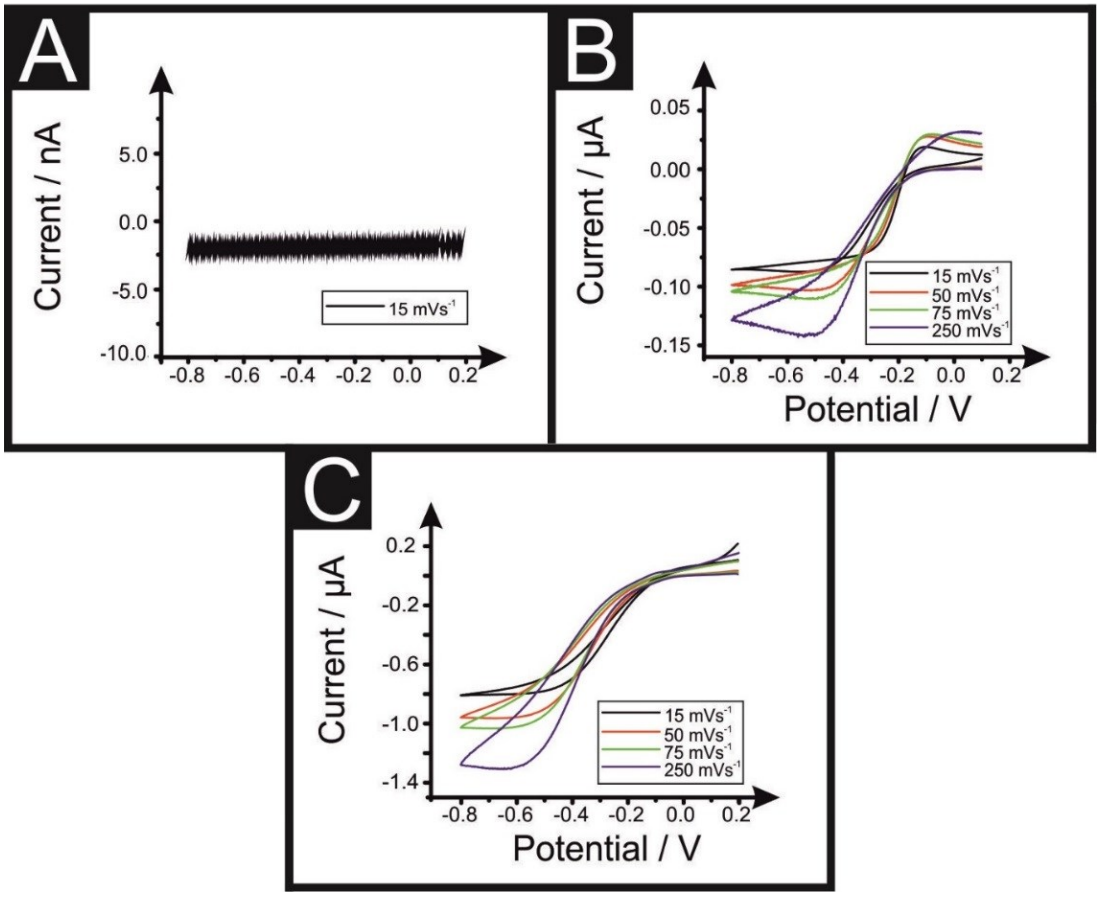

Figure 47. Cyclic voltammetric scan rate study of 1 mM RuHex/0.1 M KCl using a unmodified 2D-hBN (A), 1 line 1PLD-2D-hBN (B) and 6 line 6PLD-2D-hBN (C) as working electrode (*vs.* Ag/AgCl). Note that in the absence of PLD there is clearly no electrochemical activity (47A) where upon the introduction of PLDs, electrochemically useful signatures are observed (47B and 47C).

Raman mapping characterisation was performed as depicted in Figure 48, where it can be observed that cracks/defects have formed across the surface from the PLD upon the 2D-hBN surface. Figure 48 shows damage on the surface of the 2D-hBN caused during electrochemical perturbation (in the form of CV), resulting in less 2D-hBN coverage, as confirmed by Raman mapping characterisation and optical images.

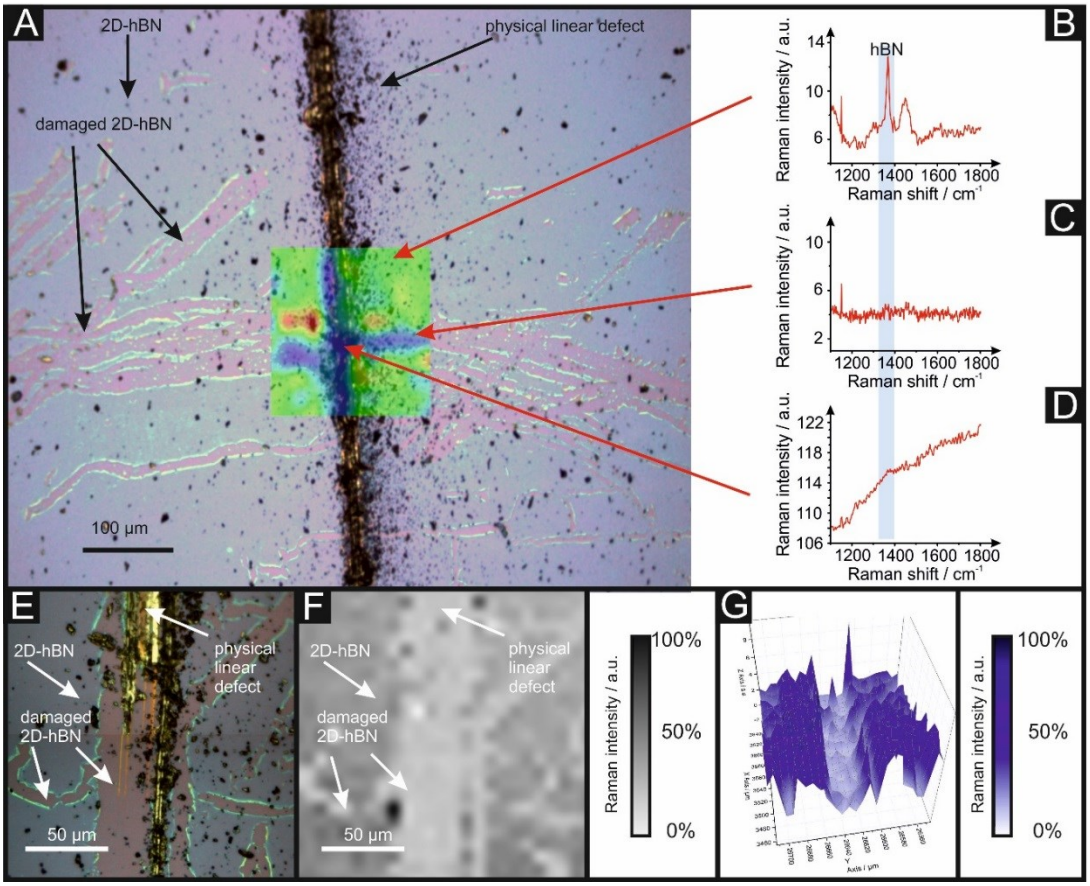

Figure 48. Optical image of PLD-2D-hBN electrode used for 28 scans for a scan rate study of 1 mM RuHex/0.1 M KCl, decorated with 6 PLD onto it with a growing tree-shape of rips/defects due to its electrochemical application with its overlapped Raman mapping (A). B shows typical Raman peak of 2D-hBN (1365 cm^{-1}), C shows Raman peak of a damaged area caused by the HER scanning and D shows the Raman peak of a physical linear defect. Higher resolution zoom in area with optical image (E), 2D Raman mapping (F) and 3D Raman mapping (G) of another area of the same PLD-2D-hBN electrode.

To explore the elemental change upon the surface of the 2D-hBN, X-ray photoelectron spectroscopy (XPS) was also performed, confirming the commercially sourced sample to be 2D-hBN. Figure 49 depicts a XPS map of both unmodified and PLD-2D-hBN samples with the coverage of Si highlighted. It is clear that the physical linear defect (PLD) has penetrated the 2D-hBN sheet and exposed the underlying Si wafer (PLD-Si wafer was confirmed in Figure 53 not to be electrochemically active towards RuHex and $Fe^{2+/3+}$). Spot XPS analysis was next performed on the two 2D-hBN sheets and as shown in Figure 49B, the first sample was an undamaged basal plane (2D-hBN) and the second was at the edge of the induced defect of a PLD-2D-hBN sample. XPS spectra for both locations are shown, B1s in Figure 49C and 49D for unmodified and PLD-2D-hBN samples respectively, and N1s in Figure 49E and 49F for unmodified and PLD-2D-hBN samples respectively. Components are seen at *ca*. 190.8 eV and 398.5 eV, respectively with roughly a 1:1 stoichiometry. The observed binding energy of these photoelectron peaks strongly correlate to those expected for 2D-hBN[274, 275]. There is a significant amount of carbon and oxygen present on the surface at both sample sites, due to typical adventitious carbon contamination[276] and from the manufacturing process. During synthesis the 2D sheet, it is commonly transferred onto the desired substrate using a PMMA polymer[48, 118, 277] (which has been previously reported to affect physical and electrical properties of CVD grown graphene transferred samples[51, 52]). High resolution XPS analysis of the B1s and N1s components at the basal and edge sites are reported in Figure 49C and 49D, and 49E and 49F, respectively. There is no observed alteration in the B component, however interestingly a minor peak signal is observed at 400.3 eV for the edge site N1s component, which is not observed at the basal site. This additional minor

peak at the edge site may be related to protonated amine groups[274, 278, 279], which represents the hydrogenation of the nitrogen at these edge sites.

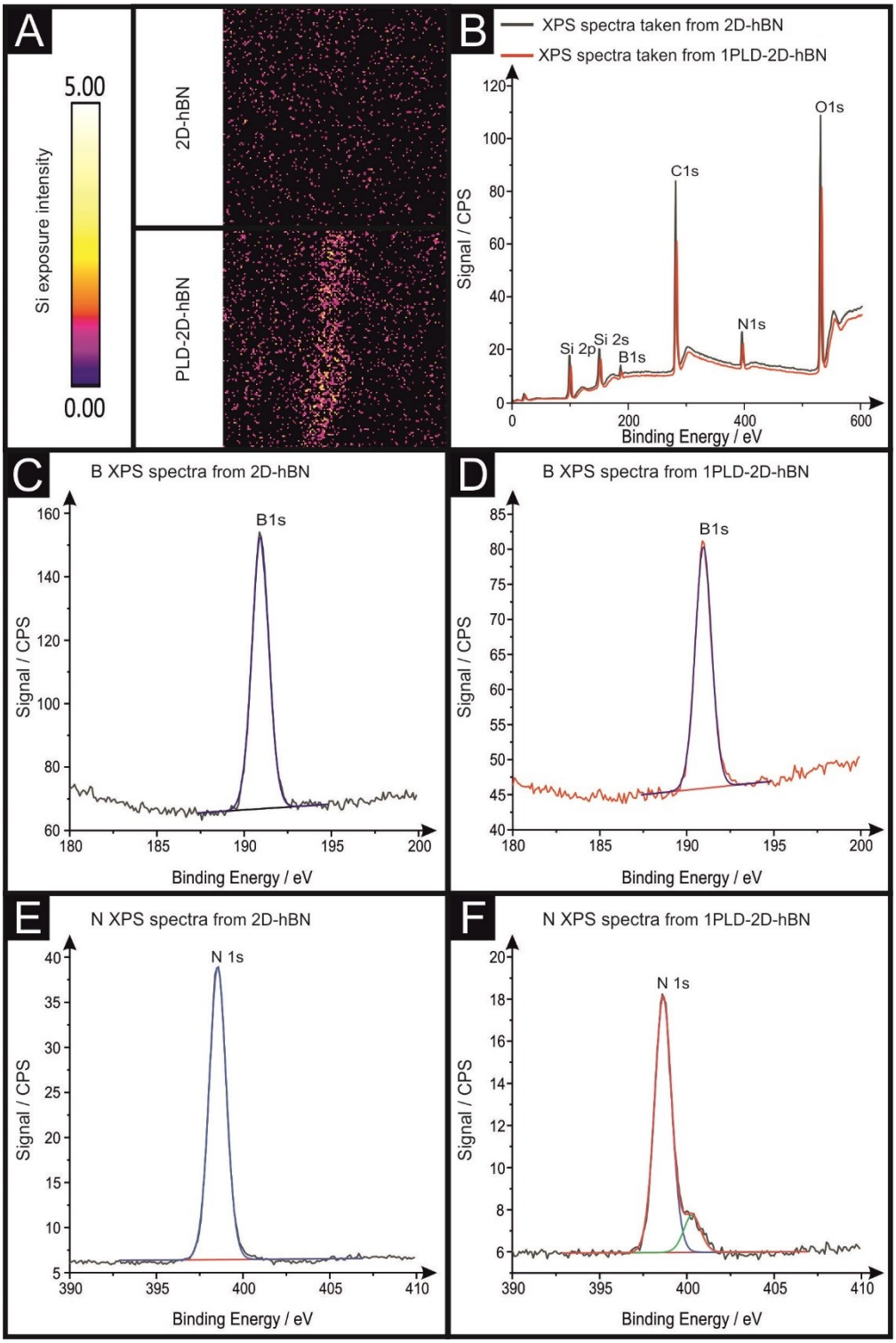

Figure 49. XPS analysis of 2D-hBN and PLD-2D-hBN's edge of a PLD. XPS map of 2D-hBN and PLD-2D-hBN electrode (A), XPS spectra for both locations (B), high

resolution XPS analysis of the B1s components of an 2D-hBN (C) and PLD-2D-hBN (D) electrode and high resolution XPS analysis of the N1s components of an 2D-hBN (E) and PLD-2D-hBN (F) electrode.

7.2.2 DFT computational characterisation

Density Functional Theory (DFT) was used in order to explain the observed beneficial electrochemical response when PLDs are introduced to the 2D-hBN electrode surface.

7.2.2.1 Percent of hydrogenation

According to the literature, an increase in the hydrogenation ratio of the edge-plane atoms can turn the 2D-hBN from an insulator to a semiconductor, having a noticeable enhancement of the electrical conductivity of 2D-hBN-NRs[270]. As PLDs are effectively nanobands akin to NRs, Density Functional Theory (DFT) calculations are performed, as an attempt to find an interpretation for the increased rate of electron transfer and electrical conductivity in the modified 2D-hBN nanosheets; DFT optimisations are described in full in the Supporting Information.

As previously mentioned[98], this chapter focuses on the nanoribbon structures of 2D-hBN because they were proved to have an enhanced conductivity/electron transfer rates. Through investigating pristine basal plane sheets of 2D-hBN such as those depicted in Figure 46, unsatisfactory results were obtained where no significant changes in the electrochemical properties could be observed prior to inducing physical PLDs upon the basal plane atoms (PLD-2D-hBN). On the other hand, the amount of hydrogen atoms in the nanoribbons was changed so as to investigate the influence of varying the hydrogenation ratio of 2D-hBN-NRs on their electrical and electronic properties. Therefore, mono- (mh-hBN-NR) and fully hydrogenated (fh-hBN-NR) edge-planes were simulated in the computational study. DFT calculations were explored to investigate the highest occupied molecular orbital (HOMO) to the lowest

unoccupied molecular orbital (LUMO) and the total density of states (TDOS) with mh-hBN-NRs and fh-hBN-NRs edge planes, and oxygen-passivated structures investigated due to the presence of oxygen peaks in the XPS results.

7.2.2.2 Molecular orbitals and electron transfer

The electron-transfer process takes place mainly on the edge planes of the 2D-hBN-NRs, where the edge-plane boron atoms are the ones that participate more, as depicted by the HOMO and LUMO molecular orbitals in Table 6. This is clearly from the delocalization of the HOMO molecular orbital on the edge-plane nitrogen atoms; however, the LUMO is delocalized on the edge-plane boron atoms. Interestingly in fh-hBN-NR (O-N) and fh-hBN-NR (O-B), the LUMO molecular orbitals are delocalized on the oxygen atoms indicating that also oxygen passivation has a crucial role in enhancing electron-transfer through the 2D-hBN-NR structure. In addition, the energy gap involved in the process of electron transfer decrease significantly by adding hydrogen atoms to the edge planes of the nanoribbon. The narrowest energy gap was obtained in the fh-hBN (O-B). The energy gaps are in the order: mh-hBN-NR > fh-hBN-NR > fh-hBN-NR (O-N) > fh-hBN-NR (O-B). This information explains the higher electrical conductivity (due to enhanced electron transfer) in the case of fh-hBN-NR which contains a large number of edge-plane boron atoms passivated with oxygen. Consequently, increasing the number of oxygen-passivated edge-plane boron atoms results in the following transformation: insulator-semiconductor-metallic. Interestingly, the electrical resistivity of 2D-hBN-NR can reach zero in some cases where the degrees of passivation and hydrogenation are at the *maxima*.

Nanoribbon	HOMO	LUMO	$E_{HOMO-LUMO}$ /eV
mh-hBN-NR	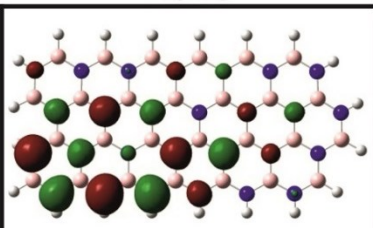	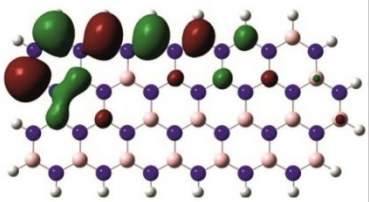	6.11
fh-hBN-NR	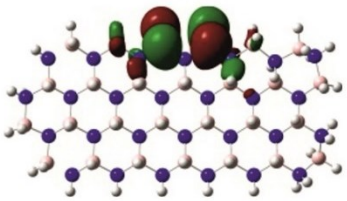	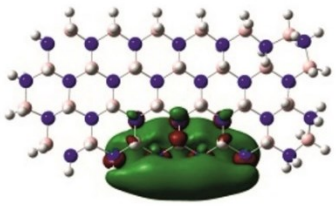	3.35
fh-hBN-NR (O-N)	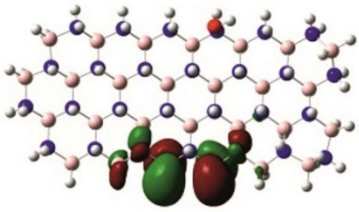	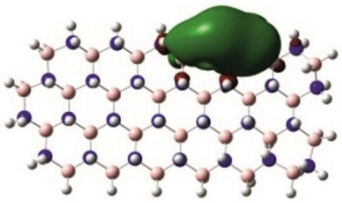	2.84
fh-hBN-NR (O-B)	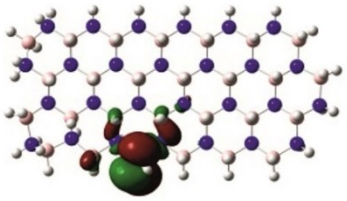	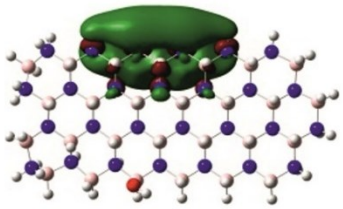	2.36

Table 6. Electronic clouds delocalization on Frontier molecular orbitals (HOMO and LUMO) and their corresponding energy gaps for mh-hBN-NR, fh-hBN-NR, fh-hBN-NR (O-N) and fh-hBN-NR (O-B). The shown energy values were obtained by using B3LYP/LANL2DZ method of calculation. The iso value is 0.02. The ELUMO-EHOMO corresponds to the energy gap (i.e. band gap), which is the amount of energy required to transfer one electron from the highest occupied molecular orbital (HOMO) to the lowest unoccupied molecular orbital (LUMO), can indicate the possibility of electron transfer and allow for comparing this property among different structures. Colour code: blue: nitrogen; pink: boron; red: oxygen; white: hydrogen.

7.2.2.3 Total density of states (TDOS)

In the studied 2D-hBN-NRs, the conduction bands are almost below -5 eV while the valence bands are at 2.5 eV for mh-hBN-NR and at 5 eV for the remaining nanoribbons. It is obvious from the depicted results (Figure 50) that the band gap in case of mh-hBN-NR is larger than its counterparts were in fh-hBN-NRs. Moreover, it is notable that some electronic states are added to the conduction band upon oxygen passivation (in other words, increasing the number of oxygen atoms will increase the number of electronic states in the conduction band). This elevation in the conduction band's number of electronic states will increase the electrical conductivity of the nanoribbon; acquiring a semiconductor then a metallic character. Interestingly, passivation of edge-plane boron atoms increases the number of electronic states in the conduction band more significantly than the case where edge-plane nitrogen atoms are passivated instead.

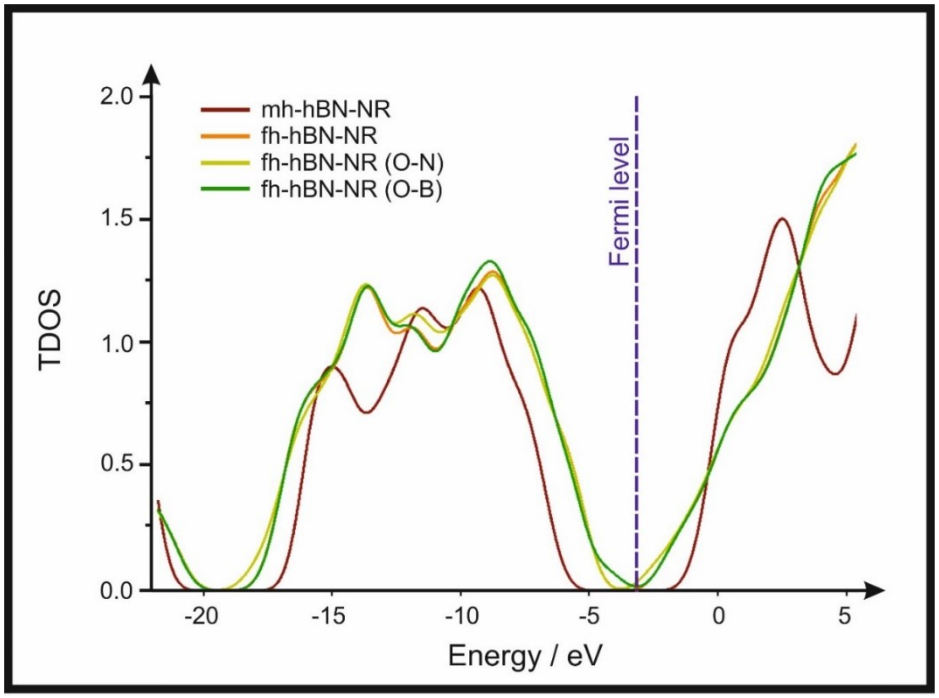

Figure 50. Total density of states (TDOS) of the investigated 2D-hBN nanoribbons (2D-hBN-NRs). The depicted TDOS values were calculated for the

above-mentioned structures optimized at the B3LYP/LANL2DZ method of calculation.

The above confirms the conclusion that, fully hydrogenation and oxygen passivation (presence of N1s in the XPS results) at the edge-plane boron atoms may be an acceptable interpretation of the enhanced electron transfer and/or electrical conductivity of fh-hBN-NRs with larger number of edge planes (*i.e.* with induced line defects). In addition, it was found that the total energy of fh-hBN-NR (O-B) and fh-hBN-NR (O-N) are -61787.2 and -61784.3 eV, respectively. This finding suggests that oxygen atoms attach favourably to edge-plane boron atoms on account of their neighbouring nitrogen atoms. Therefore, it is expected that, when line defects are induced, fh-hBN-NR (O-B) is formed in a larger amount compared to the fh-hBN-NR (O-N) counterpart (see Figure 55 for the respective structures).

7.2.2 Electrochemical application

2D-hBN, has been previously reported as a promising material when incorporated into PEM fuel cells, such as when protecting the membrane from degradation[280-282]. The production of molecular hydrogen due to the electrocatalytic reduction of water *via* the Hydrogen Evolution Reaction (HER) ($2H^+ + 2e^- \rightarrow H_2$) is a widely studied mechanism and a potential source of sustainable energy supply for the future. With this in mind, in order to test the electrochemical stability of PLD-2D-hBN when applied to electrochemical applications, it is explored herein the HER using a 2D-hBN electrode, and a PLD-2D-hBN (with 1 to 6 PLDs on its surface as described previously herein); this is shown in Table 7 and in Figure 51 (HER stability test are explored only to study if the 2D-hBN sample might have electrochemical responses too when modified). Table 7 shows scanning stability experiments of PLD-2D-hBN towards the HER, which is an approach used to benchmark the system against literature reports. As is common practise within the literature, 0.5 M H_2SO_4 was used for the HER[218, 219]. Figure 51 shows the Linear Sweep Voltammogram (LSV) of the 2D-hBN, 1 line 1PLD-2D-hBN and 6 lines 6PLD-2D-hBN respectively, depicting the evolution of the HET kinetics when defects upon the basal plane surface are created; leading to an increase in its edge plane-sites/defects when compared to the bare 2D-hBN electrode. As it is evident in Table 7 and Figure 51, the electrode's performance shifts from a 'not possible' (NP) HER reaction when unmodified to an onset potential occurring at *ca.* -1.19, -1.15, -1.1, -1.08, -0.99 and -0.98 V when 1 to 6 lines are drawn onto the surface respectively. A change in the current is also observed at -1.25 V from -5.23×10^{-2} μA when 1 line is drawn through to -6.56×10^{-1} μA when 6 PLD are drawn, due to the presence of newly generated electroactive sites, *i.e.* more PLD result in a larger electroactive area.

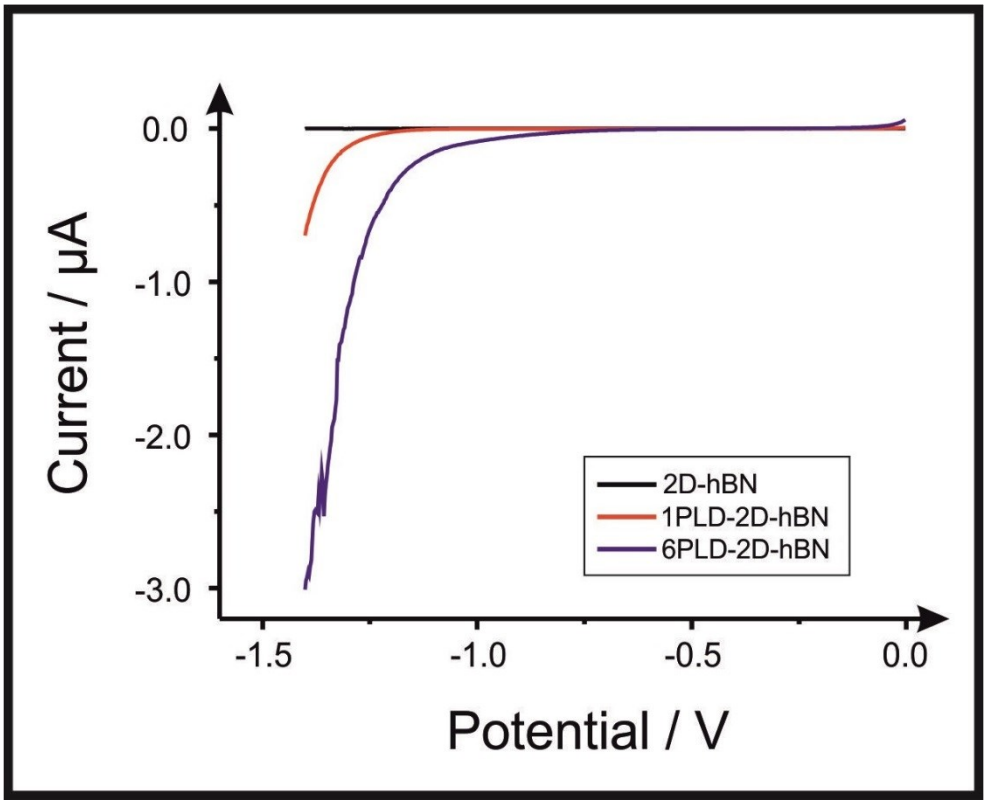

Figure 51. Linear Sweep Voltammetry (LSV) of 2D-hBN, 1PLD-2D-hBN and 6PLD-2D-hBN respectively with 0.5 M H_2SO_4, depicting the scanning stability experiments towards the HER, showing an increase in the current when more PLD are created (due to an increase in edge plane-sites/defects) when compared to the bare 2D-hBN electrode (Scan rate: 5 mV s^{-1}; *vs.* Ag/AgCl).

PLDs	*Onset / V*	*Current at -1.25 V / μA*
0	NP	-2.53×10^{-5}
1	-1.19	-5.23×10^{-2}
2	-1.15	-2.14×10^{-1}
4	-1.10	-3.15×10^{-1}
5	-1.08	-4.97×10^{-1}
6	-0.99	-5.03×10^{-1}

Table 7. Hydrogen Evolution Reaction (HER) analysis for 2D-hBN and 1 to 6 lines PLD-2D-hBN, including HER onset and current at -1.25 V values. (Scan rate: 5 mV s^{-1}; *vs*. Ag/AgCl).

In order to compare the stability of the 2D-hBN sheet towards consecutive electrochemical perturbation (in the form of scanning applications), Figure 54 compares the electrochemical stability of a 6 lines 6PLD-2D-hBN electrode used for 4 and 28 RuHex scans respectively. As is clearly depicted in Figure 54A, the PLD-2D-hBN electrode used for 4 scans has an increased current and increased electrochemical reversibility than the one used for 28 times (Figure 54B). Following this, physicochemical characterisation shows that the passing current clearly disrupts the nature of the film by creating rips and holes, as confirmed by Raman spectroscopy mapping (shown in Figure 54C) (by the presence/absence of the typical hBN Raman peak at *ca*. 1365 cm^{-1} (red-green areas)[283-286]). Similar damage has been previously reported for CVD grown mono- and few-layer graphene when applied towards the Hydrogen Evolution Reaction (HER)(See Chapter 5 of this thesis[287]).

This confirms a drop in the electrochemical activity upon multiple scanning cycles (28 CV scans), which can be attributed to the damage/destruction of the electrode. This fact is likely due to the dissemination of rips across the surface of the electrode, leading to a lack of conductive pathway, and therefore, to a decrease of its electrochemical performance.

7.3 Conclusion

It is shown for the first time, that the introduction of PLDs upon the surface of 2D-hBN transforms it from electrochemically inert to that exhibiting electrochemically useful signatures. Tailoring the number of PLDs results in a change in the magnitude of the voltammetric current output. A thorough physicochemical (X-ray photoelectron spectroscopy, Raman spectroscopy and Scanning Electron Microscopy), electrochemical (RuHex, $Fe^{2+/3+}$ probes and application towards the Hydrogen Evolution Reaction) and computational (Density Functional Theory) characterisation of the 2D-hBN, both pre- and post- defect creation (*i.e.* PLDs) revealed the fully hydrogenated amine groups and edge-plane boron atoms passivated with oxygen at the newly created edge plane-sites/defects give rise to recordable/beneficial electrochemical reactivity. Physicochemical and computational characterisation demonstrate that mono hydrogenated 2D-hBN-NRs change from an insulating material with a band gap of 6.11 eV to semi-conducting material when fully hydrogenated with a band gap of 2.84 eV for oxygen-passivated boron and 2.36 eV for oxygen-passivated nitrogen. This transition from an insulator to a semiconductor explains the electrochemical observations when using 2D-hBN electrodes for voltammetric studies. It is important for further studies to note that it is observed, and documented within this chapter, that the repeated use of the 2D-hBN in voltammetric studies creates increasing numbers of defect sites on the nano-sheet electrode; and that these eventually decrease the electrode's performance, likely due to a decrease in the number of electron pathways.

The results described above help to de-convolute the electrochemical properties and responses expected when using 2D-hBN within electrochemical systems. Future studies can apply this or other modifications to 2D-hBN and other

2D materials (and their derivatives, such as nanoribbons), which will help one take advantage of their unique electrochemical properties.

7.4 Experimental information

The tested solutions were 0.5 M H_2SO_4, 1 mM $(NH_4)_2Fe(SO_4)_2$ ($Fe^{2+/3+}$) in 0.2 M $HClO_4$ and outer-sphere 1 mM $Ru(NH_3)_6Cl_3^{3+/2+}$ (RuHex) in 0.1 M KCl. Working electrodes were CVD grown mono-layer 2D-hBN (hBN) on a SiO_2 wafer from Graphene Supermarket completing the circuit. 2D-hBN sample in contact with electrolyte was *ca.* 0.8 x 0.8 cm.

Raman Mapping Spectroscopic analysis was performed using a Thermo Scientific DXR Raman Microscope fitted with a 532 nm excitation laser at a low power of 6 mW to avoid any heating effects. Spectra were recorded using a 10 seconds exposure time for 10 accumulations in each point. To collect the map we used a step size of 10 x 10 μm, to collect a Raman profile between the region of 1100 and 2000 cm^{-1}. Scanning electron microscope (SEM) images were obtained using a JSM-5600LV (JEOL, Japan) model. 3D Raman map figures depict the intensity of the characteristic Raman for 2D (*ca*. 1365 cm^{-1}) recorded from their full Raman spectra.

The purposeful modification or deliberate creation of defects upon the mono-layer films consisted of drawing/etching *ca*. 1 mm long-line across the surface of the electrode using a fine diamond scriber from Lattice Gear. Figure 53 presents Scanning Electron Microscope (SEM) images of the modification after and before running electrochemical experiments. Figure 53F depicts the Raman spectra of the diamond scriber tip, showing that there is no contamination on the samples from it.

The X-ray photoelectron spectroscopy (XPS) data was acquired using an AXIS Supra (Kratos, UK), which was equipped with an Al X-ray source (1486.6 eV) operating at 300 W in order to perform survey scans and 450 W for narrow scans. All X-rays were mono-chromated using a 500 mm Rowland circle quartz crystal X-ray mirror. The angle between X-ray source and analyser was 54.7°. With an electron

energy analyser: 165 mm mean radius hemispherical sector analyser operating in fixed analyser transmission mode, pass energy 160 eV for survey scans and 40 eV narrow scans. A detector with a delay line detector with multichannel plate was utilised.

7.4.1 Density Functional Theory (DFT)

Density Functional Theory (DFT) calculations were performed to unravel the reasons underlying the enhanced electron-transfer properties of 2D-hBN after making line defects and edge plane sites. All DFT computations were performed using B3LYP/LANL2DZ functional implemented in Gaussian 09 package. GaussView Version 05 package was used for visualization of the optimized structures, highest occupied molecular orbital (HOMO) and the lowest unoccupied molecular orbital (LUMO). A 6 × 3 (ring × raw) structure of 2D-hBN which was used to simulate 2D-hBN nanoribbons (hBN-NR) as shown in Figure 52. The studied structure of hBN-NR were either mono- (mh-hBN-NR) or fully hydrogenated (fh-hBN-NR).

The molecular geometry of hBN-NRs with fully-hydrogenated edge planes (fh-hBN-NRs) were optimized using the B3LYP/LANL2DZ functional and the results were compared with the mono-hydrogenated structure (mh-hBN-NR) (Figure 55). As oxygen presence was detected in the XPS results, oxygen-passivation was also explored, bonding an oxygen atom to either an edge-plane nitrogen or boron in order to study both possibilities. It is worth to mention that, in this study the effect of only one atom of oxygen is investigated which means that the obtained results can be maximized by increasing the number of oxygen atoms used for passivating the edge plane nitrogen and/or boron atoms of the nanoribbon. Frequency calculations did not result in any imaginary frequencies indicating the stability of the proposed 2D-hBN-NR structures.

Investigation of the HOMO and LUMO molecular orbitals can give valuable information about the electron-transfer properties through 2D sheets such as graphene and hBN materials[171]. The so called energy gap (*i.e.* band gap), is the amount of energy required to transfer one electron from the highest occupied molecular orbital (HOMO) to the lowest unoccupied molecular orbital (LUMO), can indicate the possibility of electron transfer and allow for comparing this property among different structures. This parameter is referred to as E_{LUMO}-E_{HOMO}.

The total density of electronic states (TDOS) can give an insight on the electrical properties of materials. Density of states is a concept in solid-state physics, which represents the number of electronic states per unit energy interval. The DOS of a given quantum system/material is an important gadget in order to understand the electrical conductivity and other electronic parameters[171].

7.5 Supporting information

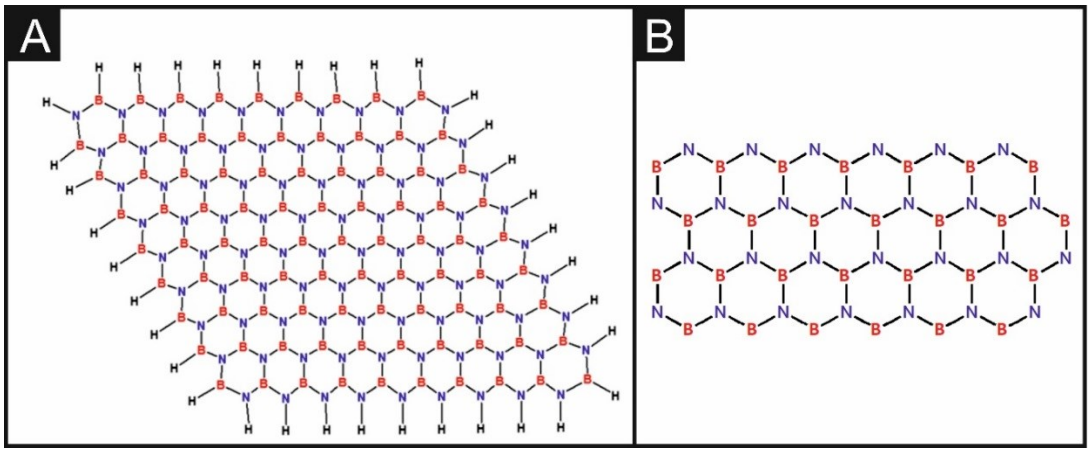

Figure 52. 2D chemical structure of the used 2D-hBN mono-layer (A) and the used hBN nanoribbon (B).

Creation of edges:

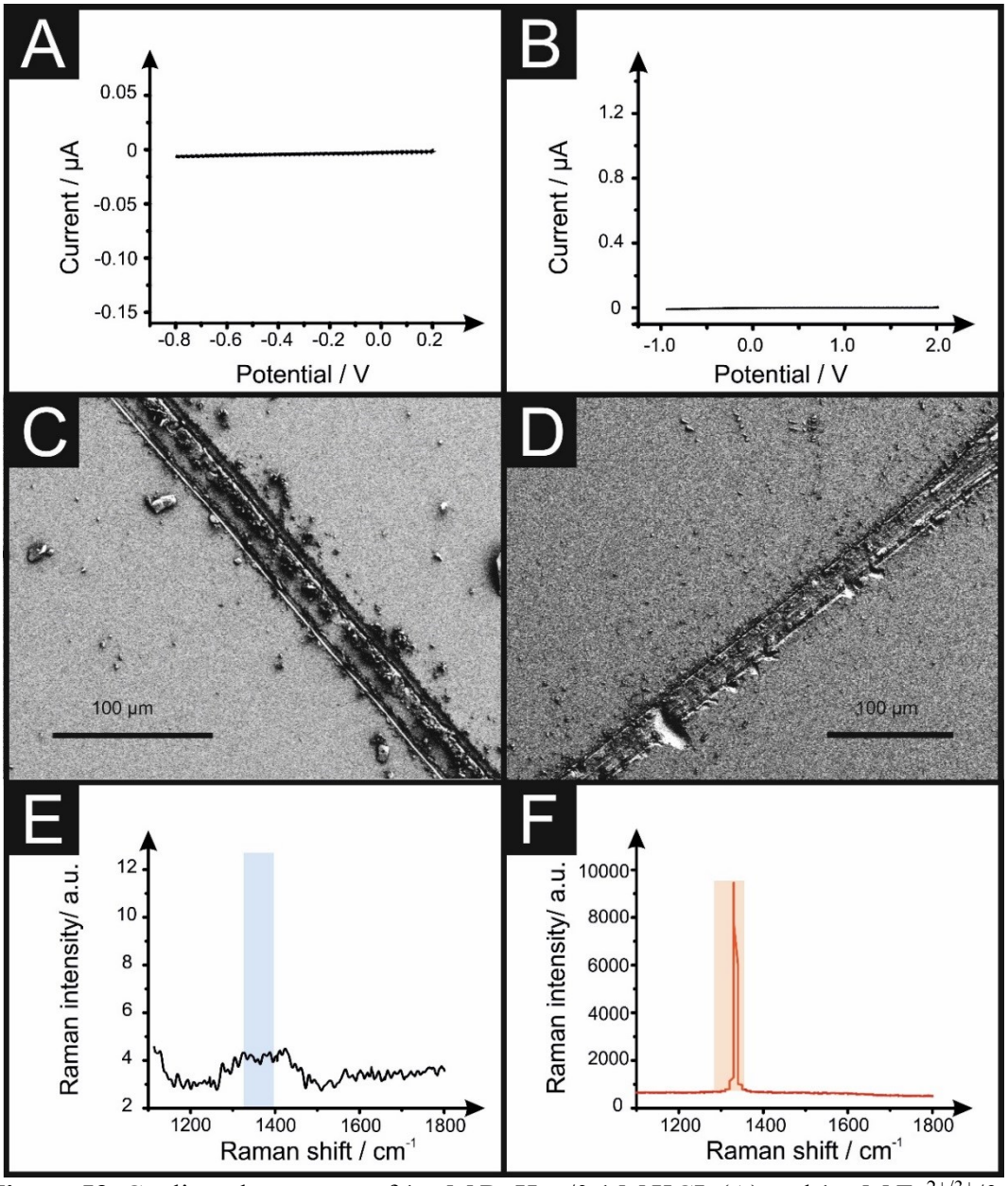

Figure 53. Cyclic voltammetry of 1 mM RuHex/0.1 M KCL (A) and 1 mM $Fe^{2+/3+}$/0.2 M $HClO_4$ (B) (Scan rate: 50 mVs^{-1}, *vs.* Ag/AgCl) using a SiO_2 wafer (no 2D-hBN) as an electrode. SEM image of a PLD-SiO_2 wafer (C) and PLD-2D-hBN electrode (D) after being utilised towards voltammetric methods. Raman profiles of a PLD-2D-hBN electrode at its newly physical defects (after utilised towards voltammetric) (E) and diamond scriber tip with a typical diamond Raman peak[288] at 1332 cm^{-1} (F) showing the lack of 2D-hBN or diamond Raman peak in Figure 53E.

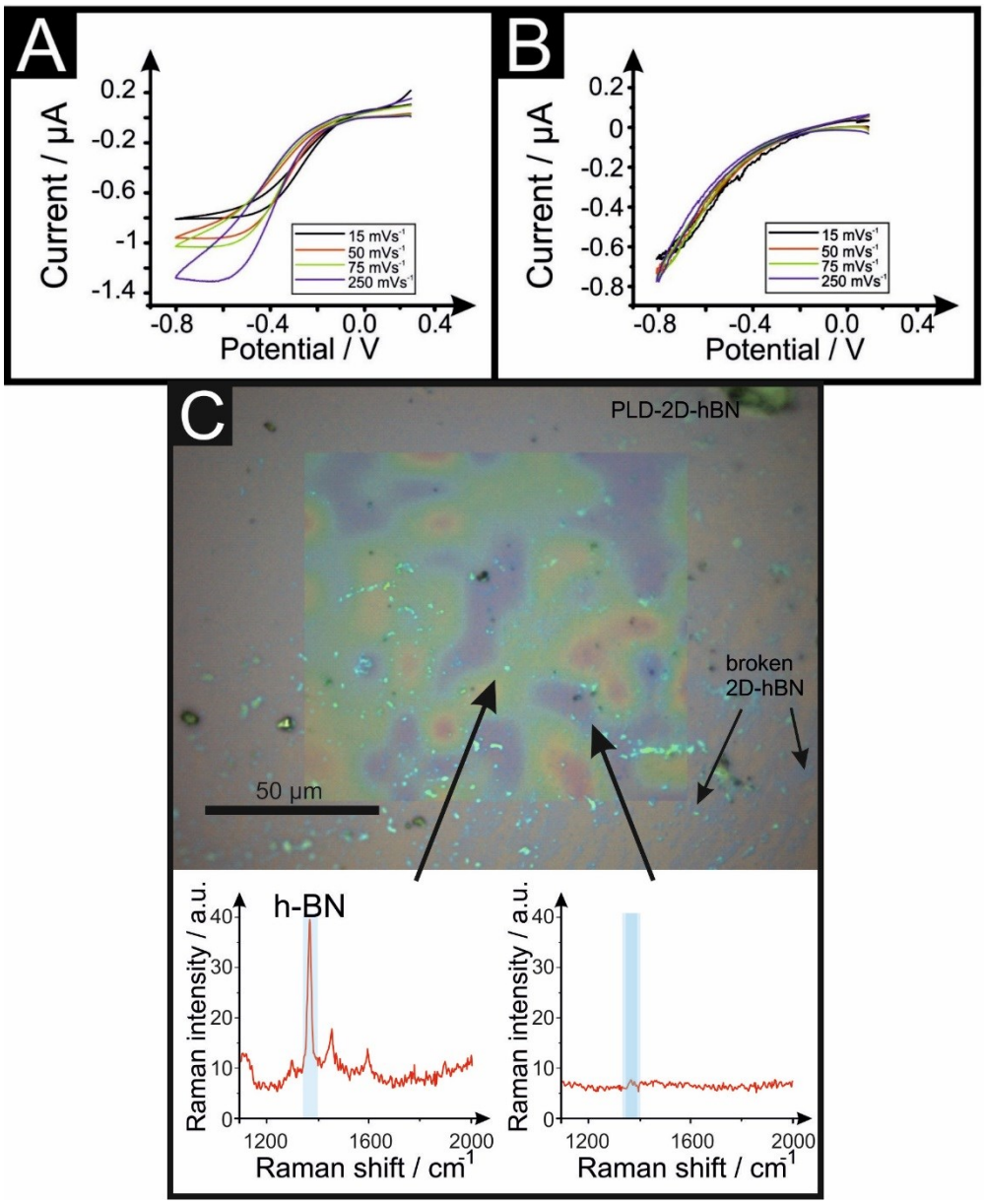

Figure 54. Voltammetric scan rate study of 1 mM RuHex/0.1 M KCl using a 6PLD-2D-hBN electrode used for 4 (54A) and 28 (54B) consecutive voltammetric scans to test their electrochemical stability towards multiple consecutive potential scanning. Optical image and Raman mapping characterisation (Figure 54C) of the PLD-2D-hBN after used in Figure S54B. Raman spectra is included, showing areas where 2D-hBN is present and its typical Raman peak (red and green colour) and some rips where there is no 2D-hBN peak (blue colour). (*vs.* Ag/AgCl).

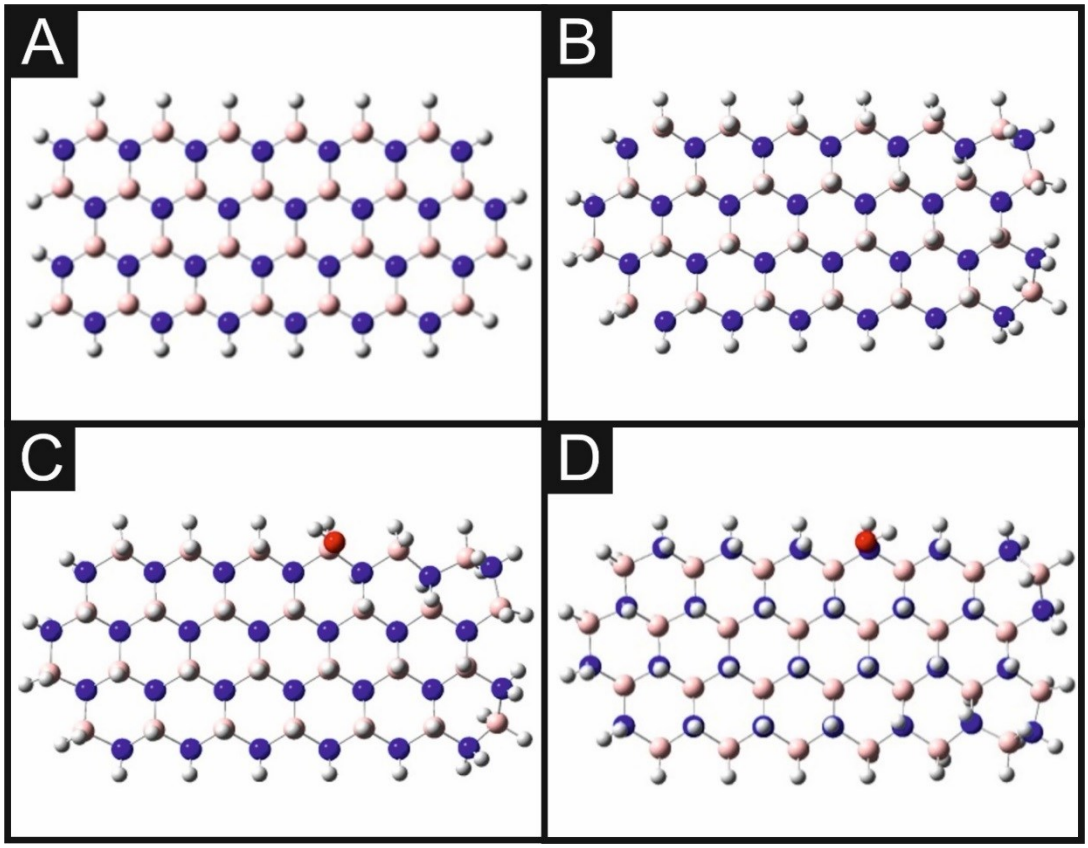

Figure 55. Optimized structures of (A) mh-hBN-NR, (B) fh-hBN-NR, (C) fh-hBN-NR with an edge-plane boron atom passivated with an oxygen atom and (D) fh-hBN-NR with an edge-plane nitrogen atom passivated with an oxygen atom. The shown structures were optimized using B3LYP/LANL2DZ functional. Color code: blue: nitrogen; pink: boron; red: oxygen; white: hydrogen.

Chapter 8: An investigation into the influence of lateral flake size on the electroanalytical performance of graphene/graphite paste electrodes

This chapter explores the electrochemical and electroanalytical properties of graphene and graphite paste electrodes comprising varying lateral flake sizes. This work demonstrates the sensing capabilities of varying lateral flake sizes at graphene and graphite paste electrodes. As seen that the edge plane like-sites/defects in monolayer graphene are the origin of electrochemical properties, this chapter applies that to paste electrodes and infers that higher electroanalytical responses can be obtained at smaller lateral flake sizes. Its application as sensor devices may lead to the improvement of future graphite and graphene-based electrodes, however this inference likely has wider implications in the energy sector too.

8.1 Introduction

Currently there is a global interest in the application of 2D materials such as graphene, graphene oxide, reduced graphene oxide, 2D-hBN, $MoSe_2$, MoS_2, WSe_2, antimonene and phosphorene[289-292] within electrochemical applications. Some of those application range from their use as basics of biosensors and also in electrochemical energy storage/generation, to name just a few. This global interest is due to the unique enhanced/beneficial properties of the 2D materials over traditional electrochemical materials, such as having higher surface areas and high absorption capacities over planar geometries than those traditionally used, high mechanical strength, wide potential windows, good electro-catalytic activities, thermal conductivity and tunable band gap to name a few, which will give benefits in a plethora of electrochemical applications[293-297]. 2D nanomaterials are able to assemble themselves into heterostructures due to van der Walls forces, producing structures that can combine properties of those materials that are present in the

different layers, offering the possibility of materials with numerous beneficial properties contained in a small volume[289, 298].

Multiple carbon nanostructures (such as fullerenes[299], carbon nanotubes (CNTs)[300, 301], carbon nanodots (C-dots)[302, 303], carbon nanofibers (CNFs)[304] or 2D materials[305, 306]) have been applied towards biosensing applications. Electrochemical approaches offer a simple method, low instrumental cost, and ability in real-time and *in vivo* measurements[307]. Graphene electrochemical sensors, due to their high surface area to volume ratio in a layered material[308], have already been reported towards the detection of biologically relevant molecules such as dopamine[26], glucose[27], hydrazine[28], nitric oxide[29], b-nicotinamide adenine dinucleotide (NADH)[30], uric acid[31], epinephrine[31] or acetaminophen[32] among others, allowing to reduce limits of detection[32, 33].

In terms of understanding the electrochemical properties of carbon-based electrodes, carbon paste electrodes (CPEs) are an easy, well-known, quick and low cost solution to prototype and benchmark different carbonaceous materials[309]. CPEs are mixtures prepared from graphitic powders with various non-electrolytic binders, packed into an inert holder with an electrical connection at the back[310, 311]. Suitable graphitic materials should follow these criteria: micrometric particle size, uniform distribution of particles, high chemical purity and low adsorption capabilities[312]. It is important to note that it has been reported the lack of observable differences in the electrochemical capabilities between graphene and graphite paste electrodes (when comparing similar sizes, due to the presence of multiple layers of graphene turns it into graphite)[313]. In terms of the electrochemical properties, it should be noted the reported distinction between two different structural contributions in graphitic materials, that is basal and edge planes[20], where basal is considered almost

electrochemically inert[169, 174, 175, 314], and edge plane like- sites/defects are considered to have "*anomalously fast*" heterogeneous electron transfer (HET) kinetics[34, 169, 175, 184-186]. Regarding the electrochemical capabilities of edge plane like- sites/defects in graphitic materials, recent work involving the heterogeneous electron transfer (HET) kinetics of graphitic paste electrodes has shown a trend demonstrating that as lateral flake size (F_s) decreases, the edge plane to basal plane ratio shifts, leading to an increase in the amount of edge planes found on the electrode surface, increasing the electrochemical activity of such electrode[171]. However, there is an ongoing debate regarding the *true* contributions of edge and basal plane like- sites/defects at the macroscopic scale[10, 175-179] with respect to their observed heterogeneous electron transfer (HET) kinetics. Recent work by Slate *et al.* suggests the presence of a lateral size threshold around 2 μm, below which the improvement of HET is negligible due to the proximity to the reversibility limit of the electrochemical process[171].

Given the above insights, in this chapter it is reported the fabrication and electrochemical performance of a range of graphene nano-powders (AO1, AO2, AO3, AO4 and C1) and graphite (high crystalline natural graphite (HCNG) and nanostructured graphite-250 (G250)) paste electrodes with varying lateral flake sizes towards the detection of several relevant biological molecules. Seen that the differences between graphene and graphite capabilities do not enhance the electrochemical performance of paste electrodes, and in order to elucidate the presence (or not) of the F_s threshold, all our flake sizes are the variable factor under controlled investigation. Therefore investigations on graphite and graphene powders with lateral flake sizes from 0.5 μm to 12.2 μm to be tested in order to establish a correlation between F_s, their HET kinetics, and their sensitivity and LODs to detect and benchmark relevant biomolecules.

8.2 Results and discussion

First, it is important to characterise and benchmark our electrochemical system to correlate the performance with reported literature to ensure is reliable/accurate. Herein, the electrochemical systems were benchmarked against the near-ideal outer sphere redox probe Hexaammineruthenium (III) chloride (RuHex) in order to calculate the Heterogeneous Electron Transfer (HET) rate constant (k^0), *real* electroactive area (A_{real}) and its $\%Real_{Area}$ (percentage comparison from A_{real} to geometrical area) for the range of graphitic-paste electrodes. The aforementioned values are calculated as described in the Experimental section, and are shown in Table 8 (see voltammetric profiles at 15 mV s^{-1} in Figure 56).

Table 8 shows the averaged lateral flake sizes, percentage of oxygen (EDX), averaged heterogeneous electron transfer kinetics (k^0), peak-to-peak separation (ΔEp), electroactive area (A_{real}) and the percentage difference between A_{real} and geometrical area $\%Real_{Area}$). ΔEp values indicate a trend that, the use of smaller lateral flake size impacts the peak-to-peak separation by decreasing it. This indicates that electrochemical process becomes more reversible when the lateral flake size is decreased, and therefore, the averaged HET (k^0) improves. This is likely to be due to the edge-to-basal plane ratio changing depending on the lateral flake size, as the amount of available edge sites increases when the lateral flake size decreases (and the 'un-reactive'[169] basal plane sites decreases in comparison to larger flake sizes). Resultantly, it was electrochemically estimated that graphite HCNG, with an average lateral flake size of 12.2 µm and a ΔEp of 68.36 mV (at 15 mV s^{-1}), has an avg. HET value of 1.15 x 10^{-3} ± 2.62 x 10^{-4} cm s^{-1}. The graphene AO1, with an estimated lateral flake size of 9.4 µm and a ΔEp of 86.67 mV (at 15 mV s^{-1}), has an averaged HET value of 1.20 x 10^{-3} ± 2.39 x 10^{-4} cm s^{-1} and the graphene C1, with a lateral flake size

of 1.3 μm and a ΔEp of 68.36 mV (at 15 mV s^{-1}), has a HET value of 1.21 x 10^{-3} ± 3.31 x 10^{-4} cm s^{-1}. Lastly, the graphite G250 with an avg. lateral flake size of 0.5 μm and ΔEp of 59 mV (at 15 mV s^{-1}), has an avg. HET value of 1.21 x 10^{-3} ± 6.33 x 10^{-4} cm s^{-1}. The values/trend as discussed above correspond well with that previously reported[171], confirming that our system is working and now the implication of this towards electrochemical sensing applications can be explored.

Attention is turned now to estimate the real electroactive area of the different range of paste electrodes using the Randles–Ševćik equation[1] (see equations 1.22, 1.23 and 1.24). The electroactive area of the graphene and graphite electrodes is included in Table 8, with results that vary from 0.12 cm^2 for graphene AO1 to a range between *ca.* 0.19-0.22 cm^2 for the rest of the electrode materials. Overall, the above results indicate that as the reversibility of the electrochemical reaction increases (and therefore its HET), the lateral flake size of the carbon material comprised in the electrode decreases. An increase in the peak-to-peak separation is observed when larger lateral flakes are used, representing a lower k^0 and therefore a less reversible process, however this does not appear to result in a clear trend to relate to the $A_{real}/\%Real.$ It is assumed from these observations the relationship between the edge plane contribution (assumed to be higher in smaller flake sizes) with the reversibility of the RuHex process, which is known to be independent on the oxygenated species on the electrode's surface and therefore only related to the electronic density of states[315].

		Size / µm (N = 20)	*Oxygen average* / %	*Avg.* k^0 / cm s^{-1}	*ΔEp* (at 15 mV s^{-1})	*Avg.* A_{real} / cm^{-2}	*%Real*
GRAPHITE	HCNG	12.2 (± 0.7)	2.88	$1.15 \times 10^{-3} \pm 2.62 \times 10^{-4}$	0.063	0.195	122.48
GRAPHENE	AO1	9.4 (± 0.7)	4.56	$1.20 \times 10^{-3} \pm 2.39 \times 10^{-4}$	0.087	0.120	75.45
	AO3	5.0 (± 0.3)	4.27	$1.12 \times 10^{-3} \pm 2.2 \times 10^{-4}$	0.059	0.219	138.01
	AO4	4.0 (± 0.3)	3.18	$1.23 \times 10^{-3} \pm 3.40 \times 10^{-4}$	0.061	0.214	134.67
	AO2	2.3 (± 0.5)	3.01	$1.22 \times 10^{-3} \pm 2.23 \times 10^{-4}$	0.061	0.203	127.82
	C1	1.3 (± 0.1)	3.03	$1.21 \times 10^{-3} \pm 3.31 \times 10^{-4}$	0.068	0.207	132.22
GRAPHITE	G250	0.5 (± 0.1)	3.56	$1.21 \times 10^{-3} \pm 3.16 \times 10^{-4}$	0.059	0.192	120.83

Table 8. Electrochemical characterisation of graphene/graphite paste electrodes determined from cyclic voltammetry using 1 mM RuHex probe in 0.1 M KCl (N = 3)

(k^0 values are the calculated averages of measurements carried out at 15, 50, 100 and 500 mV s^{-1}).

Considering such results, next it is explored the electroanalytical performance of these graphitic paste electrodes towards the electrochemical detection of relevant biological analytes such as dopamine (DA) and uric acid (UA), ascorbic acid (AA), NADH, paracetamol (APAP) and p-Benzoquinone (p-Benzo) and will correlate the responses based upon the lateral flake size. Cyclic voltammetries (CV) can be observed in Figure 56 and peak position for each CV and electrode materials are reported in Table 9. In order to see the bigger picture from the recorded data, it is time to compare the overpotential for the analytical detection of the analytes (E_p^{ox} for all of the molecules, except E_p^{red} for RuHex and p-benzoquinone) when using graphite HCNG (9.4 μm), graphene AO4 (4.0 μm) and graphite G250 (0.5 μm) electrodes as representative sizes.

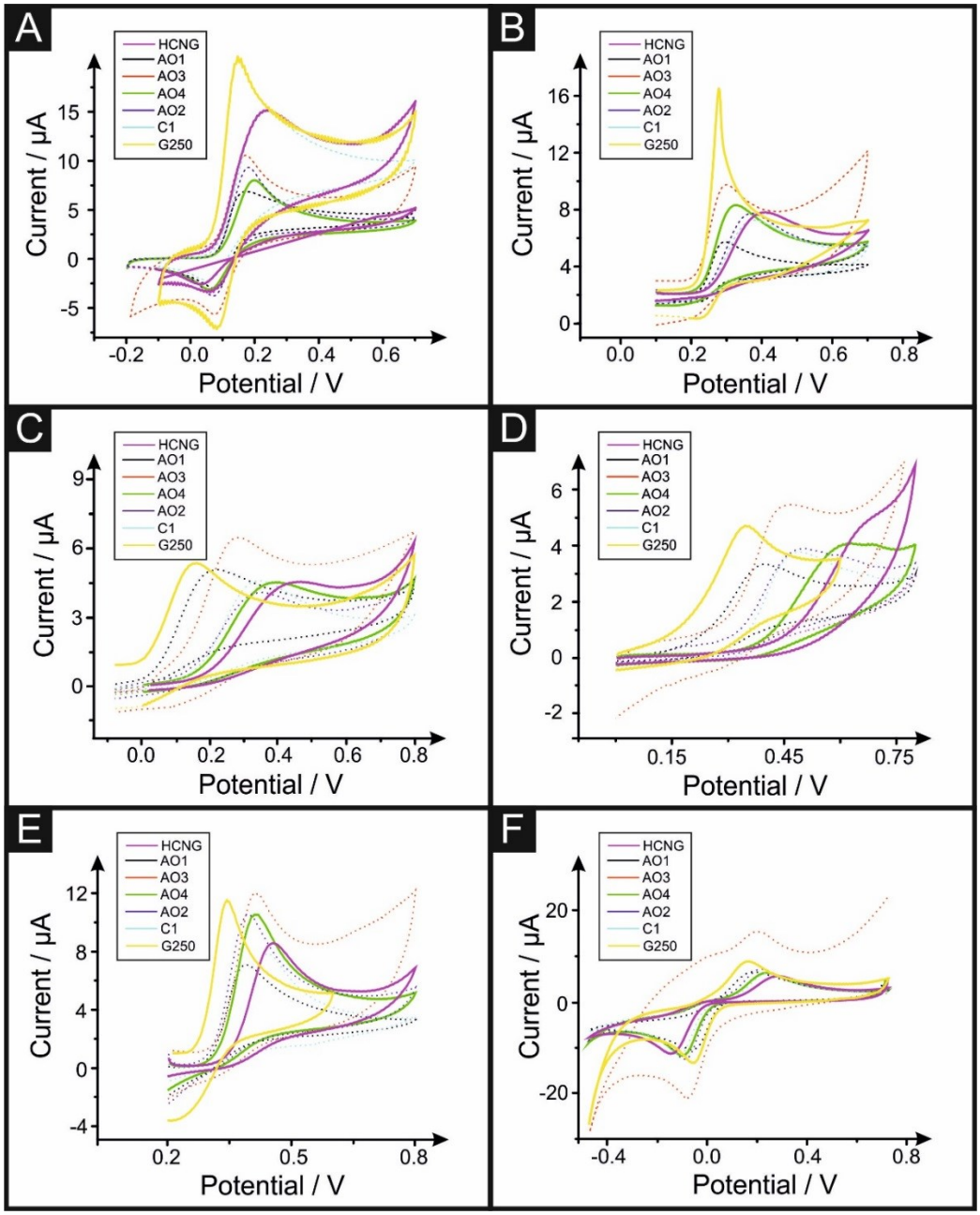

Figure 56. Voltammetric profiles of 100 µM of dopamine (A), uric acid (B), ascorbic acid (C), NADH (D), acetaminophen (E) and p-Benzoquinone (F) in PBS pH 7 at the various paste electrodes (Scan rate 50 mV s^{-1}; *vs.* Ag/AgCl).

		DA / V	UA / V	AA / V	NADH / V	APAP / V	P-BENZO / V
GRAPHITE	HCNG	0.220	0.442	0.447	0.664	0.458	-0.164
GRAPHENE	AO1	0.162	0.296	0.195	0.397	0.373	-0.089
	AO3	0.170	0.293	0.266	0.446	0.408	-0.106
	AO4	0.178	0.315	0.310	0.489	0.393	-0.112
	AO2	0.195	0.337	0.373	0.588	0.414	-0.122
	C1	0.219	0.359	0.359	0.495	0.436	-0.133
GRAPHITE	G250	0.147	0.283	0.163	0.354	0.347	-0.071

Table 9. Comparison of the peak position (Ep; in V) obtained at the various paste electrodes towards the detection of 100 μM of dopamine, uric acid, ascorbic acid, NADH, acetaminophen and p-Benzoquinone in PBS pH 7 (Scan rate 50 mV s^{-1}; *vs*. Ag/AgCl).

Dopamine (DA) is a well-known neurotransmitter that plays an important role in the hormonal, renal and central nervous systems[316]. Figure 56A depicts typical dopamine cyclic voltammetric (CV) responses obtained using the range of graphitic electrodes described above and exhibits voltammetric peaks (E_p^{ox}) decreasing from 0.220 V to 0.178 V and 0.147 V when using HCNG, AO4 and G250 respectively.

Uric acid (UA), the primary end compound of purine metabolism, is a neurochemical commonly encountered in biological samples[317]. Unusual levels of uric acid can indicate illnesses such as hyperuricaemia and gout[317]. Figure 56B depicts typical uric acid CV responses recorded using the different graphitic paste electrodes described herein, exhibiting E_p^{ox} values decreasing from 0.442 V to 0.315 V and 0.283 V when using HCNG, AO4 and G250 respectively.

Ascorbic Acid (AA), also known as Vitamin C, is an antioxidant and a co-substrate of many important dioxygenases and its high presence in urine can interfere with other target molecules such as dopamine or uric acid[26, 318, 319]. Figure 56C depicts the CV responses recoded, exhibiting E_p^{ox} shifts from 0.447 V to 0.310 V and 0.163 V when using HCNG, AO4 and G250 respectively.

β-Nicotinamide adenine dinucleotide (NADH) is part of the NAD^+/NADH redox reaction, which is used in many cellular processes, mainly NAD^+ acts as a substrate of enzymes that add or remove chemical groups from proteins, making NAD^+ metabolism a target for drug discovery[320]. Figure 56D depicts the CV responses recoded, exhibiting E_p^{ox} from 0.664 V to 0.489 V and 0.354 V when using HCNG, AO4 and G250 respectively.

Lastly, acetaminophen and *p*-benzoquinone detection are depicted as Figure 56E and F respectively. Acetaminophen, also known as paracetamol or APAP, is a widely used analgesic/antipyretic drug which requires routine monitoring in many biofluids and in quality assurance but is also associated to hepatic toxicity and renal failure[32, 321]. Figure 56D depicts the typical acetaminophen CV responses recorded using the different graphitic paste electrodes described above, exhibiting E_p^{red} from 0.458 V to 0.393 V and 0.347 V when using HCNG, AO4 and G250 respectively. *p*-Benzoquinone is a toxic metabolite of benzene that can be found in human blood, urine and adipose tissue and can be utilised to monitor the exposure to compounds containing benzene[322-325]. Figure 56E depicts the typical *p*-Benzoquinone CV responses recorded using the different graphitic paste electrodes described above, exhibiting E_p^{red} from -0.164 V to -0.112 V and -0.071 V when using HCNG, AO4 and G250 respectively.

It is clearly evident that the use of smaller lateral flake sizes deeply reduces the overpotential needed for the analytical detection of the molecules, due to a higher electron transfer kinetics and promoting charge transfer.

Figure 57 depicts the calibration plot studies for DA, UA, AA, NADH, APAP and *p*-Benzo respectively, using the different graphitic pastes within a range of 5 to

100 μM in Phosphate Buffer Solution (PBS) pH 7. The sensitivity of such analytes is calculated from the slope of their respective calibration plots (in A M^{-1}). Table 10 shows the sensitivities of all analytes obtained from the slope of each calibration plot depicted in Figure 57.

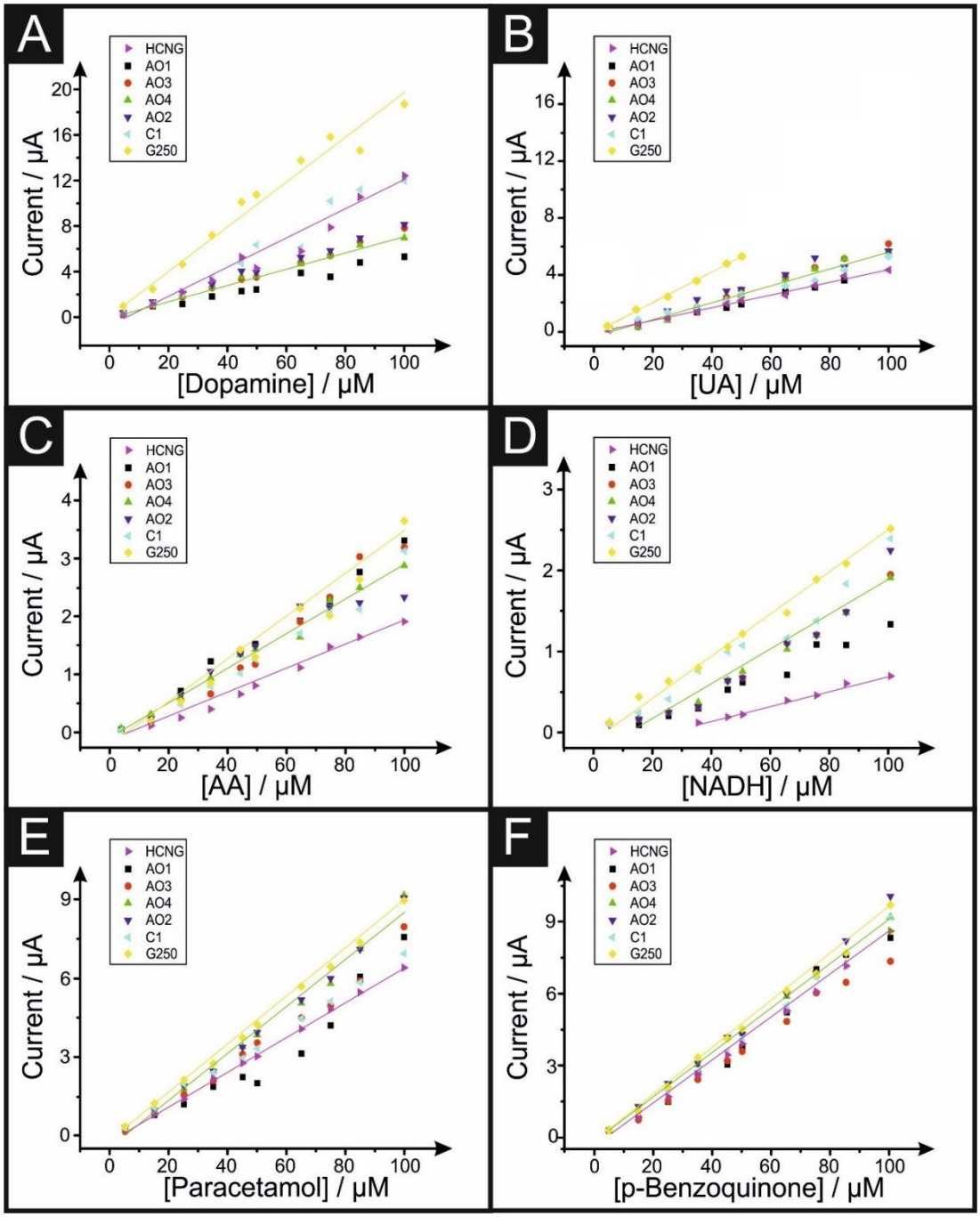

Figure 57. Calibration plots of dopamine (A), uric acid (B), ascorbic acid (C), NADH (D), acetaminophen (E) and p-Benzoquinone (F) in PBS pH 7 at the various paste electrodes. Analytical sensitivities of such calibration plots shown in Table 10 (Scan rate 50 mV s^{-1}; *vs.* Ag/AgCl).

		DA / A M^{-1}	UA / A M^{-1}	AA / A M^{-1}	NADH / A M^{-1}	APAP /A M^{-1}	*p*-BENZO / A M^{-1}
GRAPHITE	HCNG	0.126	0.046	0.023	0.009	0.066	0.090
GRAPHENE	AO1	0.054	0.044	0.034	0.015	0.073	0.092
	AO3	0.079	0.069	0.037	0.021	0.077	0.081
	AO4	0.071	0.064	0.030	0.020	0.090	0.091
	AO2	0.080	0.059	0.026	0.021	0.089	0.101
	C1	0.133	0.049	0.031	0.023	0.069	0.092
GRAPHITE	G250	0.190	0.168	0.038	0.025	0.090	0.097

Table 10. Comparison of the analytical sensitivities (in A M^{-1}) obtained at the various paste electrodes towards the detection of dopamine, uric acid, ascorbic acid, NADH, acetaminophen and p-Benzoquinone in PBS pH 7 (Calculated from gradient of calibration plots between 0 and 100 μM depicted in Figure 57) (Scan rate 50 mV s^{-1}; *vs.* Ag/AgCl).

The electrochemical sensitivity of dopamine using these electrodes goes from a value of 0.126 A M^{-1} to 0.071 A M^{-1} and 0.190 A M^{-1} when using HCNG, AO4 and G250 respectively. In the case of uric acid, its sensitivity increases from a value 0.046 A M^{-1}, 0.064 A M^{-1} and 0.107 A M^{-1} for HCNG, AO4 and G250 electrodes respectively. The electrochemical sensitivity of ascorbic acid shifts from 0.023 A M^{-1} to 0.030 A M^{-1} and 0.038 A M^{-1} for the electrodes made with HCNG, AO4 and G250 respectively. Sensitivity studies for NADH go from a value of 0.009 A M^{-1} to 0.020 A M^{-1} and to 0.025 A M^{-1} for the HCNG, AO4 and G250 electrodes respectively. In the case of acetaminophen, electrochemical sensitivity varies from 0.066 A M^{-1} to 0.090 A M^{-1} and to 0.090 A M^{-1} for the HCNG, AO4 and G250 electrodes respectively. In the case of *p*-Benzoquinone, its sensitivity changes from a value of 0.090 A M^{-1}, to 0.091 A M^{-1} and 0.097 A M^{-1} for HCNG, AO4 and G250 respectively. It is clear the increase of the electroanalytical sensitivities when smaller lateral flakes sizes are used within the paste electrodes.

The electrochemical Limit of Detection (LODs; LOD = 3*σ M^{-1}), presented in full in Table 11, were obtained from the data depicted in Figure 49. One can easily see from the data presented in Table 11 that for most of the analytes, there is a trend where the LOD decreases, as the lateral flake size decreases. As an example, in the case of the detection of UA, the calculated LOD decreases from 1.42 to 1.06 and 0.85 μM for the HCNG, AO4 and G250 electrodes respectively. In the case of AA, similar results are observed, with calculated LOD of 0.7, 0.5 and 0.19 μM, for HCNG, AO4 and G250 respectively. LODs for NADH also show similar trend, with LODs of 3.43, 1.57 and 1.3 μM, for HCNG, AO4 and G250 respectively.

		DA / μM	**UA / μM**	**AA / μM**	**NADH / μM**	**APAP / μM**	***p*-BENZO / μM**
GRAPHITE	HCNG	0.25	1.42	0.70	3.43	0.48	0.35
GRAPHENE	AO1	0.59	0.94	0.73	2.11	0.44	0.35
	AO3	0.41	0.85	0.46	1.50	0.41	0.40
	AO4	0.45	1.06	0.50	1.57	0.35	0.35
	AO2	0.40	1.24	0.54	1.49	0.36	0.33
	C1	0.24	1.03	0.65	1.42	0.47	0.35
GRAPHITE	G250	0.17	0.85	0.19	1.30	0.48	0.32

Table 11. Comparison of the electrochemical limits of detection (LODs; LOD = 3* σ M^{-1}) (in μM) obtained at the various paste electrodes towards the detection of dopamine, uric acid, ascorbic acid, NADH, acetaminophen and p-Benzoquinone in PBS pH 7 (Calculated from gradient of calibration plots between 0 and 100 μM depicted in Figure 57) (Scan rate 50 mV s^{-1}; *vs.* Ag/AgCl).

Flake graphite and Kish graphite (FG and KISH respectively from now on), with lateral flake sizes of 608.0 (±40) μm and 1389.9 (±148) μm respectively were also explored and are presented in the Supporting Information for comparison purposes. Table 12 shows the averaged lateral flake sizes, percentage of oxygen (EDX), averaged heterogeneous electron transfer kinetics (k^0), peak-to-peak separation, electroactive area and the percentage difference between A_{real} and

geometrical area $\%Real_{Area}$) for FG and KISH electrodes. Figure 59 depicts the voltammetric profiles for RuHex using FG and KISH. Figure 60 shows the CVs of DA, UA, AA, NADH, APAP and *p*-Benzo using FG and KISH respectively. Figure 61 depicts the calibration plot studies for those same molecules using FG and KISH. As one can see, these much larger lateral flake size graphite powders exhibit a larger peak-to-peak separation resulting in slower HET k^0 values. Additionally, the electroanalytical detection (*via* CVs) for the group of relevant biomolecules occurs, generally, at higher potentials and higher calibration ranges. All of these results make it not clear and/or appropriate to compare FG and KISH with the rest of the graphitic powders due to the *major* differences in lateral flake size and electrochemical performance.

Considering the observations using a wide range of relevant biomolecules and the outer-sphere redox probe RuHex, it is observed that nanostructured graphite G250 with the smallest lateral flake sizes, offer the best overall electrochemical performance from the studied in this chapter. These results indicate that smaller lateral flake (with improved HET kinetics) give an improved electrochemical sensitivity and lower limits of detection, in contrast to larger flake sizes. Depending on the electrode material, the presence of oxygen or other chemical species could also affect the performance (as it has been already reported in the literature for Dopamine or Ascorbic acid respectively). In the case of sensing applications, electrochemical processes that undergo through complex adsorption routes might lead to ambiguous results.

This work shows the importance of lateral flake size when graphitic materials are considered as electrodes with improved/enhanced electrochemical sensitivities and LODs. Given the results showed above, one should choose higher edge plane

density materials in order to obtain higher sensitivity and LODs. Further attention needs to be put in which graphitic materials are used for applications such as energy storage and sensors.

8.3 Conclusions

It is shown herein that in the case of the analytes studied here, namely dopamine hydrochloride, uric acid, acetaminophen and *p*-benzoquinone, that the sensitivity of graphite and graphene based paste electrode with varying lateral flake sizes depends directly on its structural composition. Decreasing the lateral flake sizes at graphitic paste electrodes resulted in enhanced electrochemical responses, due to faster HET kinetics. This chapter infers that the observed improvement is related to the "edge plane" content from the different lateral flake sizes. The flake graphite electrode was highly sensitive to some inner-sphere redox probe due to the presence of oxygenated species (and ligands), having some interactions that might perturb the overall trend of the results.

8.4 Experimental information

The tested solutions were: 1 mM RuHex (in 0.1 M KCl), dopamine, uric acid, ascorbic acid, acetaminophen and p-benzoquinone in phosphate buffer solution (PBS) pH 7. Working paste electrodes were in-house fabricated using a piston-driven polymeric-composite electrode shell with an inner diameter of 4.5 mm (0.159 cm^2 of area) and graphite and graphene powders from Graphene Supermarket (Reading, MA, USA) as shown in Figure 62. The graphite powders are as follows: 'High Crystalline Natural graphite (HCNG)' and 'Nanostructured graphite – 250 (G250)' which comprised of an average lateral flake size of 0.7-2 mm, >150 μm, 12.2 (± 0.7) μm and 0.5 (± 0.1) μm respectively. The graphene powders are as follows: 'AO1', 'AO3', 'AO4', 'AO2' and 'C1' which comprised of an average lateral flake size of 9.4 (± 0.7) μm, 5.0 (± 0.3) μm, 4.0 (± 0.3) μm, 2.3 (± 0.5) μm and 1.3 (± 0.1) μm respectively. Average lateral flake sizes and oxygen average percentages are extracted from Ref 171.

Figure 62 shows the fabrication process of graphite and graphene paste electrodes, that was the result of using a mixture of 60 % graphitic materials with 40 % mineral oil (Nujol), and were used without any modification but polishing the surface of the electrode. A platinum wire counter/auxiliary electrode and a silver/silver chloride electrode (Ag/AgCl) reference electrode completed the circuit.

All samples were degassed vigorously prior to electrochemical analysis with high purity, oxygen free nitrogen in order to remove any trace of oxygen, which could affect the analyte's voltammetric current (analytical signal).

The HET rate constants, k^0_{obs}, were calculated using the near ideal outer-sphere redox probe $[Ru(NH_3)_6]^{3+/2+}$ (in 0.1 M KCl) using the well-known[190] and utilised

Nicholson method[8], for electrochemical reactions *via* the equation 1.25 and 1.26[9] described in Chapter 1.

The electroactive area of the electrode, A_{real}, is calculated using the Randles-Ševćik equations 1.22 to 1.24) [1, 5-7] at non-standard conditions as described in Chapter 1 and 3.

Following the calculation of A_{real}, the percentage of the geometrical area was calculated using the following: $\%Real = (A_{real} / A_{geo}) \times 100$.

Limit of Detection (LOD) were calculated as 3 times the standard deviation of the blank (σ) divided by the slope of the calibration plot (M).

8.5 Supporting information

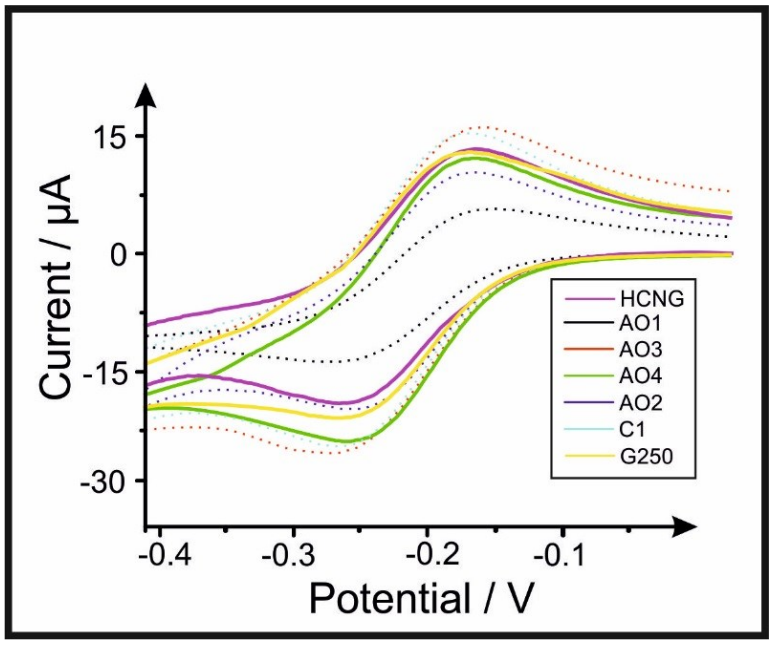

Figure 58. 1 mM RuHex in 0.1 M KCl voltammetric profiles using the range of graphite and graphene paste electrodes (Scan rate: 15 mV s^{-1}; *vs.* Ag/AgCl).

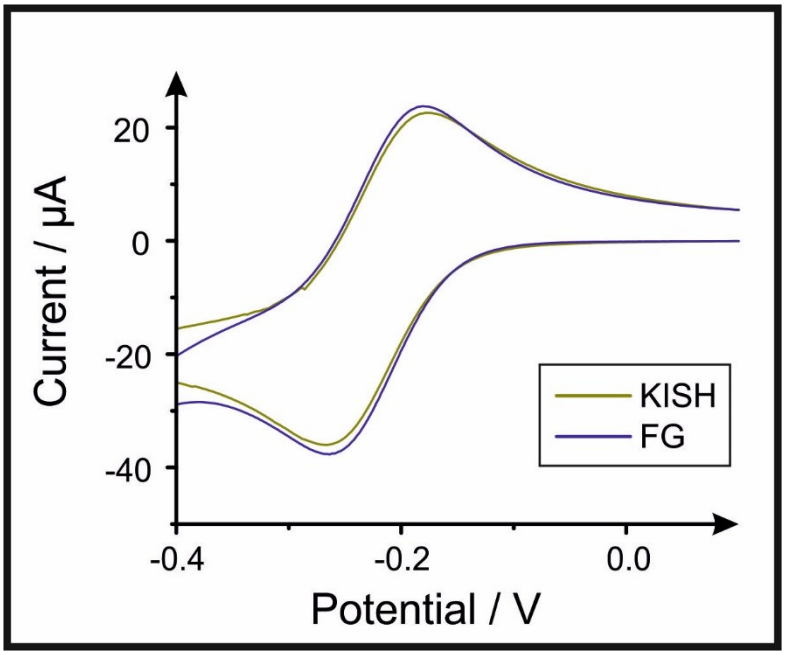

Figure 59. 1 mM RuHex in 0.1 M KCl voltammetric profiles using the range of FG and KISH paste electrodes (Scan rate: 15 mV s^{-1}; *vs.* Ag/AgCl).

		Size / µm (*N* = 20)	*Oxygen average / %*	*Avg.* k^0 / cm s^{-1}	*ΔEp* (at 15 mV/s)	*Avg.* A_{real} / cm^{-2}	*%Real*$_{area}$
GRAPHITE	KISH	1389.9 (± 148)	10.62	1.06×10^{-3}	0.076	0.156	98.22
GRAPHITE	FG	608.0 (± 40)	3.45	1.15×10^{-3}	0.073	0.135	84.81

Table 12. Electrochemical characterisation of FG and KISH graphite paste electrodes determined from cyclic voltammetry using 1 mM RuHex probe in 0.1 M KCl ($N = 3$) (k^0 values are the calculated averages of measurements carried out at 15, 50, 100 and 500 mV s^{-1}).

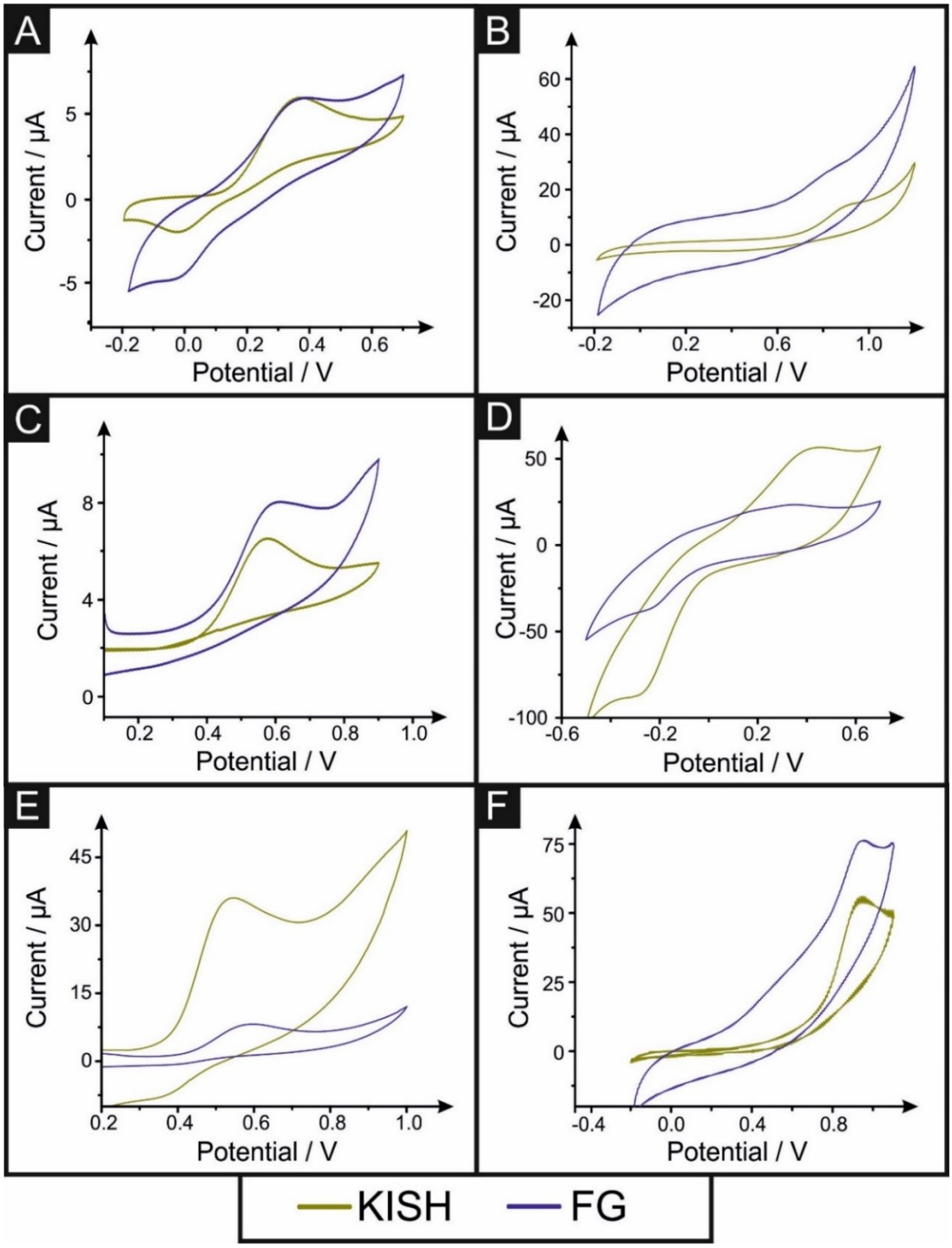

Figure 60. Voltammetric profiles of 100 µM of dopamine (A), uric acid (B), ascorbic acid (C), NADH (D), acetaminophen (E) and p-Benzoquinone (F) in PBS pH 7 using FG and KISH graphite paste electrodes (Scan rate 50 mV s^{-1}; *vs.* Ag/AgCl).

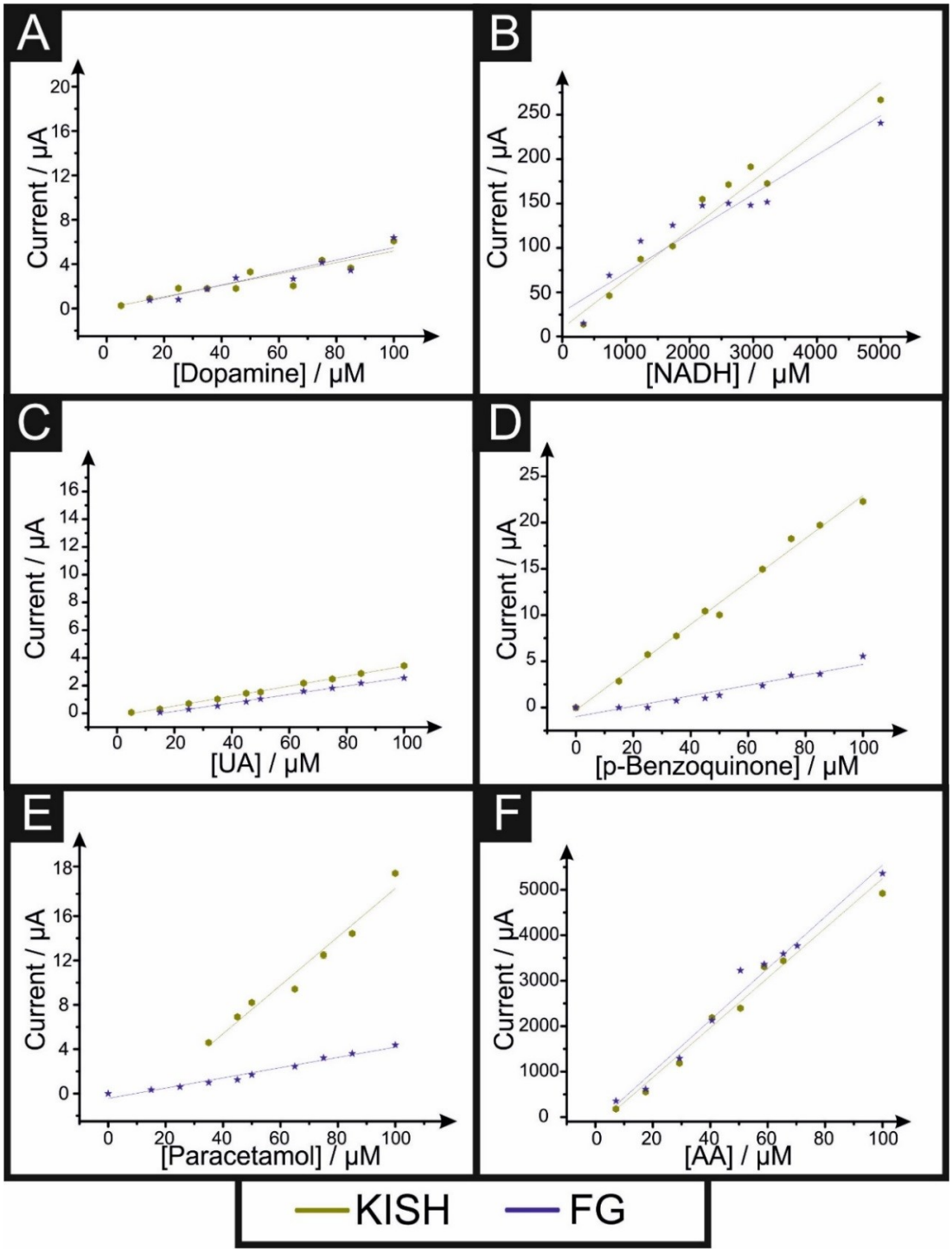

Figure 61. Calibration plots of dopamine (A), uric acid (B), ascorbic acid (C), NADH (D), acetaminophen (E) and p-Benzoquinone (F) in PBS pH 7 using the FG and KISH graphite paste electrodes (Scan rate 50 mV s^{-1}; *vs.* Ag/AgCl).

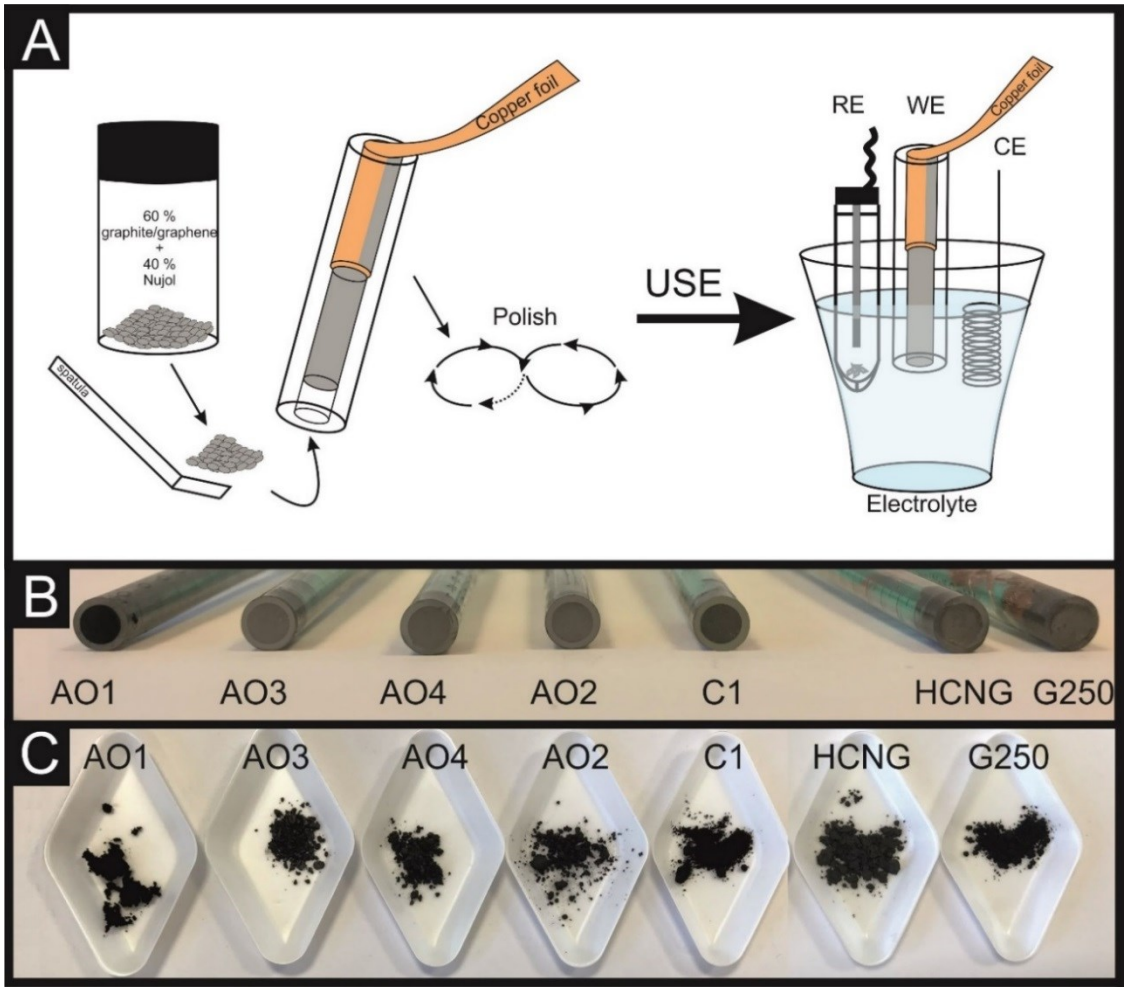

Figure 62. A schematic shows that the graphite/graphene pastes are mixed with Nujol (60-40 % ratio respectively), are then inserted into a polymeric-composite electrode shell with an inner diameter of 4.5 mm. Electrode material is in contact with copper foil as electrode connector. After polishing treatment, electrodes are ready to be used in conjunction with reference (RE) and counter (CE) electrodes in a three-electrode cell configuration. B Depicts the different working electrodes used in this manuscript. C Shows the different graphene (AO1, AO3, AO4, AO2 and C1) and graphite (HCNG and G250) powders used as electrode material in this manuscript.

Chapter 9: Tailorable Graphene/Polylactic(acid) thin films, printable filaments and 3D Printable electrodes for electrochemical applications

This chapter investigates the electrochemical performance of in-house manufactured graphene/PLA thin films, 3D printable filaments and 3D printed electrodes, where the graphene content can be readily tailored and controlled over the range 5-40 % *wt*.. This chapter reports the physicochemical and electrochemical characterisation, allowing for optimisation of the graphene content to allow control over the 3D printability. Graphene/PLA polymeric materials are characterised and benchmarked as electrochemical systems against the inner-sphere redox probes dopamine, ascorbic acid, β-nicotinamide adenine dinucleotide (NADH) and $Fe^{2+/3+}$, and against the near ideal outer-sphere redox probe RuHex. This chapter enhances the field of 3D printed graphene-based electrodes for future sensing and energy applications, and emphasises the importance of having accessible edge plane like-sites/defects in graphene composites.

9.1 Introduction

Additive manufacturing (AM)/3D printing technologies create three-dimensional objects from a digital design, allowing the fabrication of any shape and form in a single-step process, being able to tailor the printed material according to the desired final properties[326]. The most used 3D printing methods at the moment are fused deposition modelling (FDM), selective laser sintering (SLS) and stereolithography (SLA)[327-329]. 3D printing has developed as a prominent manufacturing practise for a wide range of applications, being tailorable to the needs of each application. In extrusion-based 3D printing, such as FDM, material properties are highly dependent on material preparation, composition and structural design[330]. FMD uses a continuous filament of a thermoplastic material, which is heated and

placed on the horizontal plane (or layer), once a layer is finished the heated bed is moved vertically to begin a new layer. There are many thermoplastic polymeric materials used in FDM, with Polylactic acid (PLA) being considered the green alternative to petroleum based plastics, due to being biodegradable, bio-absorbable and from natural sources[331, 332]. PLA is already being applied in the pharmaceutical, textile, chemical, automotive and biomedical industries[333, 334]. The mechanical, electron- and heat-transfer properties of PLA-based 3D printed devices have been reported to be enhanced with the use of nanofillers[335], due to their unique enhanced/beneficial properties, such as thermal conductivity, resistance at low and high pH levels, improvements in band gap and electron transfer properties[336].

The understanding and application of nanomaterials has generally been focusing upon their utilisation as 2D printed devices, such as screen-printed electrodes, nonetheless research has now fixed the attention to the incorporation of these nanomaterials into the 3D world, by AM/3D printing, attracting great interest within the field of electrochemistry. Recently, the performance of these 3D nanomaterials-based structures has outperformed their 2D counterparts[326, 337, 338]. There is also a need to understand fundamentally how these 2D materials behave as electrodes in electrochemical systems[339] and also develop these 2D materials into useful 3D structures, *e.g.* as biosensors[340], energy storage systems (ESS)[341, 342]. One of the great advantages of utilising 2D materials in 3D structures is that they have higher surface areas and high absorption capacity over planar geometries which are traditionally used which will give benefits when used as the basis of a sensor[343]. As a result of the capability of 3D printing graphene structures, the architecture of ESS and sensing devices will give significant advantages from improved surface areas, electrical properties and hierarchical pore structures/porous channels. Through

developing and incorporating graphene powders with enhanced properties to create novel 3D structures for applications in electroanalytical devices, there is the possibility of improving the limit of detection (LODs), sensitivity and specificity in sensor devices. In energy applications it could increase the charge storage of batteries to meet possible future demands; next generation batteries with enhanced performance (e.g. improved cycle stability, specific energy, power density etc.).

Currently, graphene oxide (GO)-based aerogels are the most common 3D printed graphene in the literature[344, 345], where the self-assembly of the GO suspension takes place *via* hydrothermal[346] or chemical reduction[347], or direct cross-linking of GO sheets[348]; other common processing method is freeze-casting[349]; however the structure of these systems is extremely arbitrary, with limited mass transport and reduced mechanical properties[350].

In this chapter, the fabrication *via* FDM and application of AM/3D printed graphene electrodes is reported, where the graphene content can be readily tailored and controlled over the range 5–40 *% wt.*. Physicochemical and electrochemical characterisation is performed allowing for optimisation of the graphene content to allow control over the 3D printability, conductivity and electrochemical activity of 3D printed electrodes (3DEs); this approach allows an easy and tailorable manufacture of low cost and disposable electrodes for energy and sensing applications.

9.2. Results and discussion

Herein it is reported the fabrication, characterisation (SEM, Raman spectroscopy and Thermogravimetric analysis (TGA) and electrochemical properties of graphene thin films, graphene 3D printable filaments and graphene additive manufacture (AM)/3D printed electrodes at different ratios *via* a facile fused deposition modelling technique. The graphene thin films, filaments and 3D printed electrodes evaluated were fabricated in-house by mixing varying graphene powders with a biopolymer (PolyLactic Acid, PLA), which acts as a binder different ratios.

9.2.1 Development and Optimisation of the graphene/PLA polymers

Graphene/polylactic acid (PLA) composites were fabricated by pre-mixing the graphene powder and PLA utilising a facile solution based mixing step (see experimental methods for further details). They consisted in a range of graphene nano-platelets loaded into the composite containing 5, 10, 15, 20 and 40 *% wt.* graphitic powder, validated by thermogravimetric analysis (TGA), with their respective Scanning Electron Microscopy (SEM) images as depicted in Figure 63.

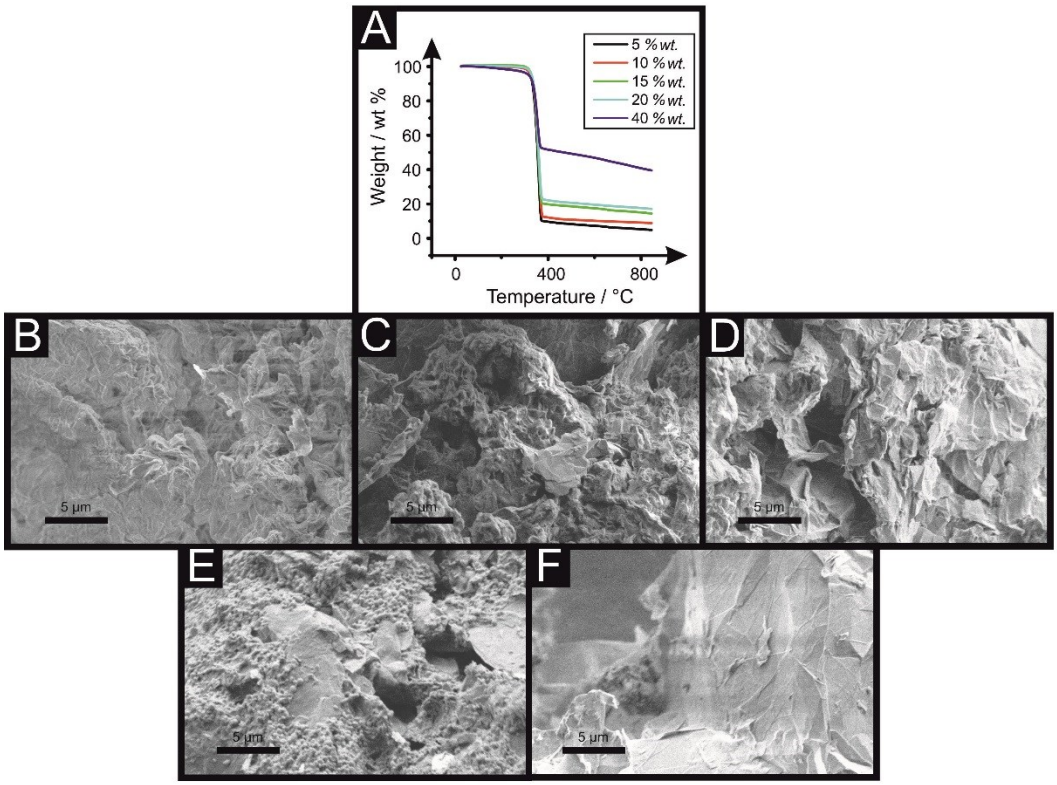

Figure 63. Thermogravimetric analysis and SEM images of 5-40 *% wt.* graphene/PLA material. A shows the thermogravimetric analysis (TGA) of 5, 10, 15, 20 and 40 *% wt.* graphene/PLA material. B to F show the SEM images of the 5, 10, 15, 20 and 40 *% wt.* graphene thin films respectively.

First, the resulting graphene/PLA powder mix was made into a thin film using a hot press (see experimental methods for further details), 2 x 3 mm rectangular piece of the thin film then were characterised and benchmarked as electrochemical systems against the near-ideal outer sphere redox probe hexaammineruthenium (III) chloride (RuHex) in order to calculate the Heterogeneous Electron Transfer (HET) rate constant (k^0) values, for the different graphene thin film electrodes as described in the Experimental section as shown in Table 13 (see voltammetric profiles in Figure 64).

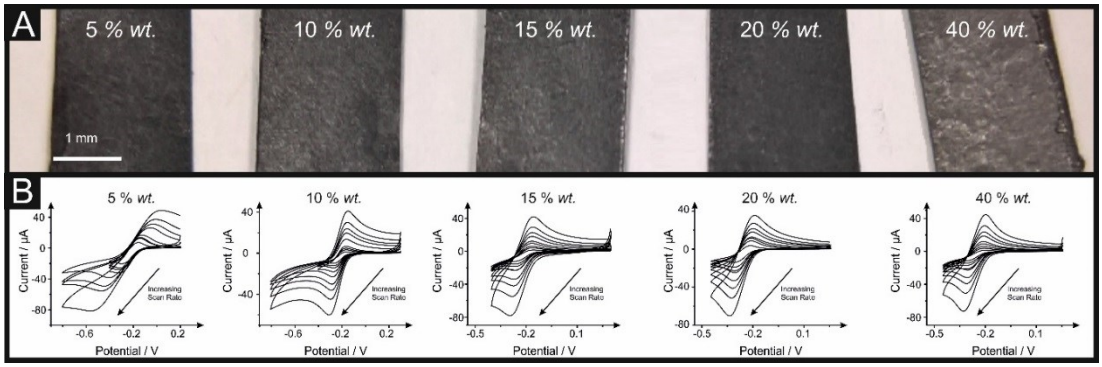

Figure 64. Optical and RuHex scan rates studies for 5 to 40 *% wt.* graphene/PLA thin films. A shows the optical images of the graphene/PLA thin films with loading varying from 5 to 40 *% wt.* respectively. B depicts the respective scan rates studies of 1 mM RuHex from 5 to 500 mV s^{-1} (*vs.* Ag/AgCl).

k^0 / cm s^{-1} (at mV s^{-1})	k^0 / cm s^{-1} (at 15 mV s^{-1})	k^0 / cm s^{-1} (at 25 mV s^{-1})	k^0 / cm s^{-1} (at 50 mV s^{-1})	k^0 / cm s^{-1} (at 100 mV s^{-1})	k^0 / cm s^{-1} (at 150 mV s^{-1})	k^0 / cm s^{-1} (at 250 mV s^{-1})	k^0 / cm s^{-1} (at 500 mV s^{-1})	Averag
30 x 10^{-4}	1.04 x 10^{-3}	1.27 x 10^{-3}	3.01 x 10^{-4}	2.72 x 10^{-4}	2.47 x 10^{-4}	2.37 x 10^{-4}	2.14 x 10^{-4}	5.3
91 x 10^{-4}	1.62 x 10^{-3}	2.09 x 10^{-3}	2.31 x 10^{-3}	3.11 x 10^{-3}	3.62 x 10^{-4}	4.23 x 10^{-3}	4.91 x 10^{-4}	2.8
84 x 10^{-4}	1.70 x 10^{-3}	2.09 x 10^{-3}	2.82 x 10^{-3}	3.61 x 10^{-3}	4.20 x 10^{-3}	5.16 x 10^{-3}	5.98 x 10^{-3}	3.3
16 x 10^{-3}	1.88 x 10^{-3}	2.20 x 10^{-3}	3.11 x 10^{-3}	3.79 x 10^{-3}	4.42 x 10^{-3}	5.70 x 10^{-3}	6.61 x 10^{-3}	4.1
96 x 10^{-3}	1.79 x 10^{-3}	2.31 x 10^{-3}	3.11 x 10^{-3}	4.40 x 10^{-3}	4.64 x 10^{-3}	5.99 x 10^{-3}	6.61 x 10^{-3}	4.1

Table 13. Electrochemical characterisation of graphene/PLA thin film electrodes determined from cyclic voltammetry using 1 mM RuHex probe in 0.1 M KCl ($N = 7$; *vs.* Ag/AgCl).

The k^0 values indicate a trend that, as the higher amount of active material (graphene) is added to the polymer, the electrochemical process becomes faster due to the higher availability of active edge plane like- sites (see Table 13). Resultantly, it was electrochemically estimated that the 5 % *wt*. thin film, with a *ΔEp* of 310 mV (at 50 mV s^{-1}), has an averaged HET value of 5.39 x 10^{-4} cm s^{-1}, the 10 % *wt*. thin film, with a *ΔEp* of 105 mV (at 50 mV s^{-1}), has an averaged HET value of 2.85 x 10^{-3} cm s^{-1}, the 15 % *wt*. thin film, with a *ΔEp* of 87 mV (at 50 mV s^{-1}), has an averaged HET value of 3.32 x 10^{-3} cm s^{-1}, the 20 % *wt*. thin film, with a *ΔEp* of 75 mV (at 50 mV/s), has an averaged HET value of 4.16 x 10^{-3} cm s^{-1} and lastly, the 40 % *wt*. thin film, with a *ΔEp* of 75 mV (at 50 mV s^{-1}), has an averaged HET value of 4.10 x 10^{-3} cm s^{-1}. Overall, the above results indicate that the reversibility of the electrochemical reaction increases (and therefore its HET), as the ratio of the active material (graphene) is increased within the electrode, increasing the amount of available electrochemically reactive edge sites[34, 313].

Considering these results, it is time to explore the electrochemical performance of these graphene thin film electrodes towards the electrochemical detection of relevant biological analytes such as dopamine, ascorbic acid, β-nicotinamide adenine dinucleotide (NADH), RuHex and $Fe^{2+/3+}$ sulphate respectively, as depicted in Figure 65 and shown in Table 14. Table 14 shows a general trend of higher current response at lower potentials when higher percentages of graphene are incorporated into the thin films. It is important to note that some data does not follow this trend, which could be due to crack/rifts in the thin film, resulting in a higher surface area in contact with the

electrolyte solution at cases where the loading of the filler is lower than the rest of the comparison.

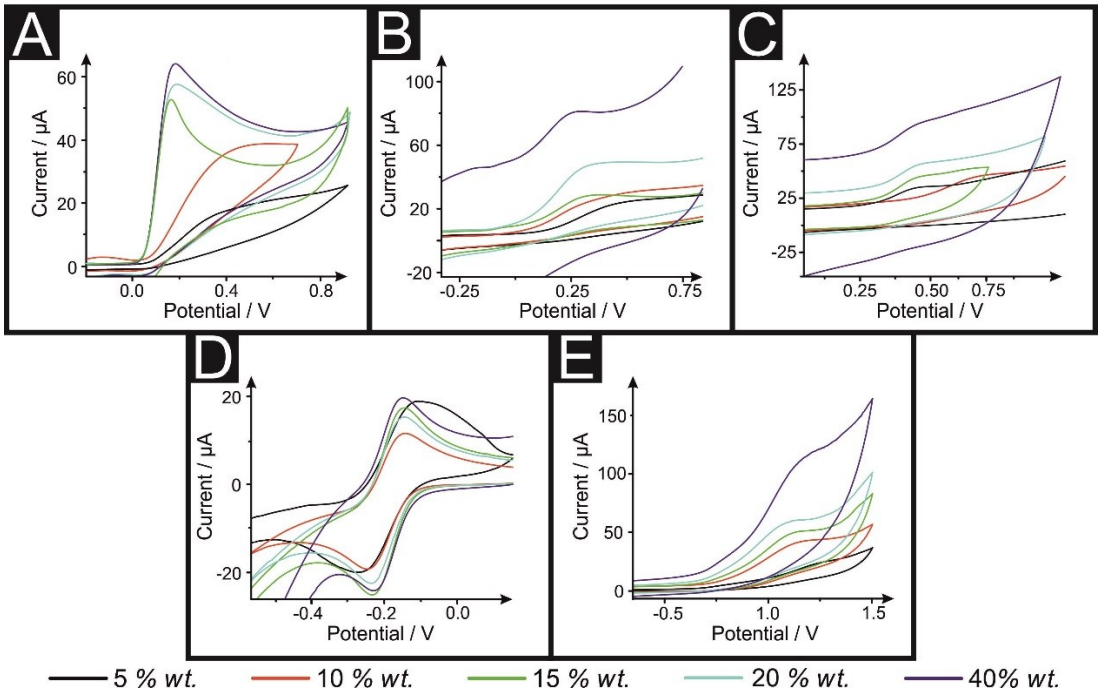

Figure 65. Voltammetric profiles of 1 mM dopamine (A), ascorbic acid (B), β-nicotinamide adenine dinucleotide (NADH) (C), RuHex (D) and $Fe^{2+/3+}$ (F) when using the graphene thin film electrodes (Scan rate 50 mV s^{-1}; *vs.* Ag/AgCl).

% wt. GRAPHENE	***DA***		***AA***		***NADH***		***RuHex***		**$Fe^{2+/3+}$**	
	Ip / μA	*Ep / V*	*Ip / μA*	*Ep / V*	*Ip / μA*	*Ep / V*	*Ip / μA*	*Ep / V*	*Ip / μA*	*Ep / V*
5%	14.33	0.37	7.77	0.46	7.26	0.66	-24.91	-0.39	10.29	1.12
10%	7.21	0.37	8.41	0.41	5.57	0.44	-15.84	-0.27	1.433	1.26
15%	26.16	0.18	10.37	0.31	8.86	0.46	-11.36	-0.25	11.85	1.06
20%	33.19	0.17	20.30	0.32	8.45	0.46	-15.71	-0.26	10.11	1.10
40%	57.75	0.36	13.13	0.24	5.71	0.45	-12.77	-0.25	17.96	1.12

Table 14. Comparison of the analytical voltammetric profiles obtained at the various graphene/PLA thin films electrodes towards the detection of 1 mM dopamine (DA),

ascorbic acid (AA), NADH, RuHex and $Fe^{2+/3+}$ determined from cyclic voltammetry (Scan rate 50 mV s^{-1} *vs.* Ag/AgCl).

9.2.2 Development and Optimisation of the graphene/PLA 3D printed electrodes

Next, attention is turned to build a 3D printable filament by extruding the polymers (see experimental methods for further details), obtaining a 1.75 mm diameter filament. The graphene/PLA filaments were subjected to electrochemical characterisation utilising the near-ideal outer-sphere redox probe 1 mM RuHex/0.1 M KCl, which is commonly utilised redox probe in the academic literature.

Finally, such graphene/PLA 3D printable filaments are printed as 3D printed electrodes (3 mm radius and 1 mm thickness; see experimental methods for further details). The fabrication of graphene/PLA 3D printed electrodes containing percentages over 20 % *wt.* is extremely brittle and unreproducible in terms of homogeneity, printability and structural integrity. It is found out that the 15 – 20 % are the optimal % *wt.* when one is considering graphene, as those filaments are the ones that are still printable and contain the higher amount of active material (and are more electroactive), creating a conductive network throughout the graphene/PLA filament, and still able to successfully 3D print useful electrochemical geometries. After optimisation of the graphene content, the 20 % graphene filaments were 3D printed producing working electrodes as shown in Figure 66.

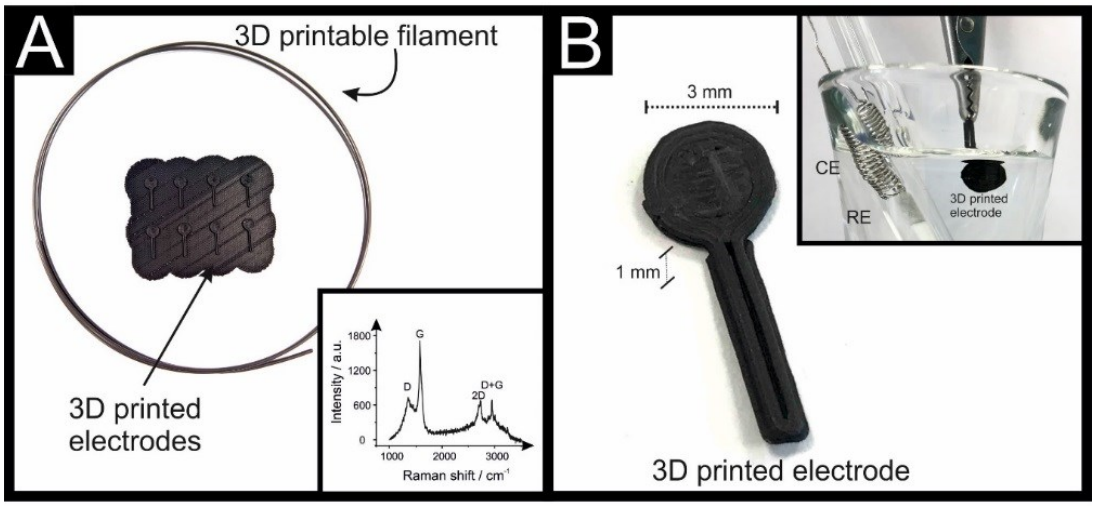

Figure 66. Optical images of the 20 *% wt.* graphene/PLA 3D printable filament and 3D printed electrodes (A) with a Raman inset showing the characteristic peaks of graphitic materials. Zoomed in section 20 *% wt.* 3D printed electrode with its measurements, including an inset showing the 3D printed working electrode, counter and reference electrodes (CE and RE respectively) in the electrolyte.

Next, the 20 *% wt.* graphene/PLA 3D printed electrodes were characterised and benchmarked against the near-ideal outer sphere redox probe RuHex as shown in Figure 67, where it can be compared to the scan rate studies of RuHex using 20 *% wt.* graphene thin film (Figure 67A) and the 20 *% wt.* graphene 3D printable filament in bulk (Figure 67B).

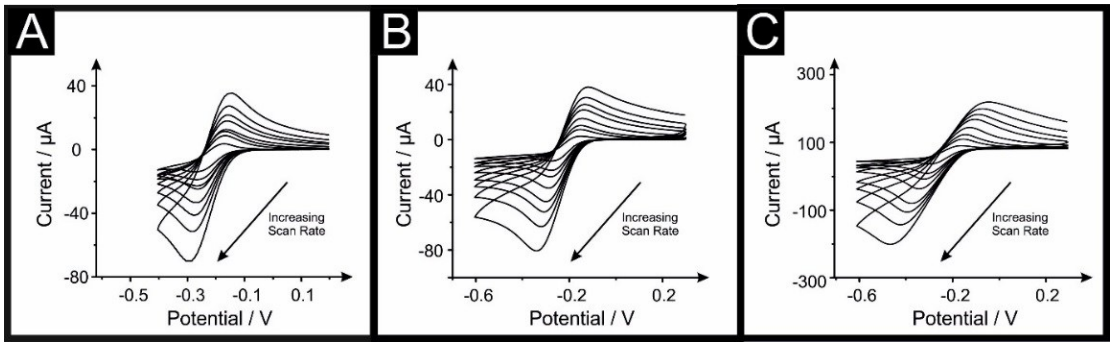

Figure 67. Scan rate studies of 1 mM RuHex using the 20 *% wt.* graphene electrodes in the following forms: thin film (A), 3D printable filament (B) and 3D printed electrode (C) respectively (Scan rate studies from 5 to 500 mV s^{-1}; *vs.* Ag/AgCl).

As shown in Table 15, the 20 *% wt*. graphene thin film electrode as it was electrochemically estimated that with a *ΔEp* of 87 mV (at 50 mV s^{-1}), has an averaged HET value of 3.32 x 10^{-3} cm s^{-1}. The 20 *% wt*. graphene 3D printable filament has a *ΔEp* of 130 mV (at 50 mV s^{-1}), has an averaged HET value of 1.90 x 10^{-3} cm s^{-1} and the 20 *% wt*. graphene 3D printed electrode has a *ΔEp* of 220 mV (at 50 mV s^{-1}), with an averaged HET value of 6.56 x 10^{-4} cm s^{-1}.

k^0 / cm s^{-1} (at 5 mV s^{-1})	k^0 / cm s^{-1} (at 15 mV s^{-1})	k^0 / cm s^{-1} (at 25 mV s^{-1})	k^0 / cm s^{-1} (at 50 mV s^{-1})	k^0 / cm s^{-1} (at 100 mV s^{-1})	k^0 / cm s^{-1} (at 150 mV s^{-1})	k^0 / cm s^{-1} (at 250 mV s^{-1})	k^0 / cm s^{-1} (at 500 mVs^{-1})	Average k^0 / cm s^{-1}
9.84×10^{-4}	1.70×10^{-3}	2.09×10^{-3}	2.82×10^{-3}	3.61×10^{-3}	4.20×10^{-3}	5.16×10^{-3}	5.98×10^{-3}	3.32×10^{-3}
7.67×10^{-4}	1.20×10^{-3}	1.48×10^{-3}	1.80×10^{-3}	2.09×10^{-3}	2.31×10^{-3}	2.57×10^{-3}	2.98×10^{-3}	1.90×10^{-3}
5.46×10^{-4}	8.51×10^{-4}	8.14×10^{-4}	7.36×10^{-4}	6.38×10^{-4}	6.09×10^{-4}	4.75×10^{-4}	3.85×10^{-4}	6.32×10^{-4}
5.42×10^{-4}	9.86×10^{-4}	1.21×10^{-3}	$1.48\ 10^{-3}$	$1.80\ 10^{-3}$	$1.99\ 10^{-3}$	2.22×10^{-3}	2.33×10^{-3}	1.57×10^{-3}

Table 15. Comparison of the heterogeneous electron transfer (HET; k^0) values obtained at the various graphene/PLA electrodes from 1 mM RuHex scan rate studies ($N = 7$; *vs*. Ag/AgCl).

As per the aforementioned results, is clearly evident that at the same 20 *% wt*. graphene, the thin film electrodes are the ones with faster heterogeneous electron transfer kinetics (HET; k^0), with an averaged HET value of 3.32 x 10^{-3} cm s^{-1}. The 20 *% wt*. graphene 3D printable filaments in comparison reported an averaged HET value of 1.90 x 10^{-3} cm s^{-1} and the 3D printed electrodes showed the slowest of them with an averaged HET value of 6.32 x 10^{-4} cm s^{-1}. The HET kinetics value for the 3D printed electrodes was the slowest, which could be due to a not sufficient percolation due to the multiple extrusion process that creates an enriched outer layer of PLA in the filament and 3D printed electrode. In order to overcome this limitation, a polishing method on the surface of the electrode is tested, in order to reduce the presence of the thermoplastic upon the surface of the electrode, allowing more electrolyte to react with the 3D printed electrode, resulting in an averaged k^0 value of 1.57 x 10^{-3} cm s^{-1} similar but not as fast as the one measured in the graphene bulk filament.

The effect of the polishing treatment on the surface of the electrode was also studied towards the voltammetric profiles of dopamine, ascorbic acid, β-nicotinamide adenine dinucleotide (NADH), RuHex and $Fe^{2+/3+}$ respectively, as depicted in Figure 68 and shown in Table 16, where it can be clearly seen that there is an improved current response recorded, due to a higher electroactive surface area of the electrode.

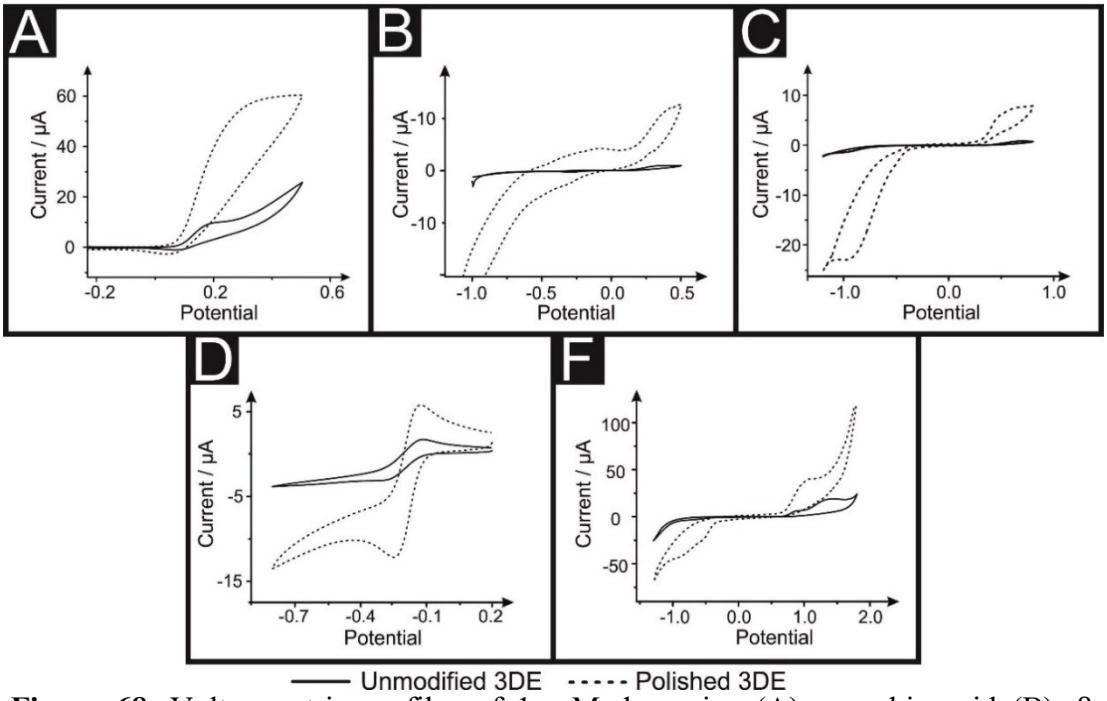

Figure 68. Voltammetric profiles of 1 mM dopamine (A), ascorbic acid (B), β-nicotinamide adenine dinucleotide (NADH) (C), RuHex (D) and $Fe^{2+/3+}$ (F) when using the 20 *% wt.* graphene 3D printed electrodes unmodified and polished respectively (Scan rate 50 mV s^{-1}; *vs.* Ag/AgCl).

20 % wt. Graphene	**DA**		**AA**		**NADH**		**RuHex**		**$Fe^{2+/3+}$**	
	Ip / µA	*Ep / V*	*Ip / µA*	*Ep / V*	*Ip / µA*	*Ep / V*	*Ip / µA*	*Ep / V*	*Ip / µA*	*Ep / V*
Unmodified	3.18	0.18	0.29	0.35	0.24	0.69	-3.10	-0.29	4.99	1.40
Polished	20.92	0.32	1.38	0.35	2.31	0.57	-12.10	-0.51	12.40	1.03

Table 16. Comparison of the analytical voltammetric profiles obtained at the unmodified and polished 20 *% wt.* 3D printed Graphene/PLA electrode towards the detection of 1 mM dopamine (DA), ascorbic acid (AA), NADH, RuHex and $Fe^{2+/3+}$ determined from cyclic voltammetry (Scan rate 50 mV s^{-1} *vs.* Ag/AgCl).

Seen the results above, it is suggested that the graphene incorporated into 3D printable filaments and then printed into fully 3D printed electrodes is a suitable electrochemical platform, although can be enhanced *via* physical pre-treatment in order to increase the surface area of the graphene nano-platelets within the composite

material to increase the exposure and coverage of edge plane like-sites/defects and increase the contact with electrolytes. Further research needs to explore different methods of surface activation/exposure of filler material within the prints, such as chemical, physical or electrochemical pre-treatments. The results presented herein enhances the field of additive manufacturing/3D printed graphene-based electrochemical devices with the utilisation of a tailorable graphene/PLA filament.

9.3 Conclusions

For the first time, it is reported the fabrication of additive manufacturing/3D printed graphene/PLA 3D printed electrode using a solution based mixing step. The 3D printable graphene/PLA filament can be tailored and controlled (5-40 % *wt.*). It is found that the optimal graphene content is 20 % *wt.* in order to provide effective conductivity and 3D printability. The initial specific electrochemical sensing properties of these graphene 3D printed electrodes is poor, however there is a need of investigating further methods to increase the surface area or the porosity of such electrodes depending on the desired applications. These results presented herein enhance the field of additive manufacturing/3D printed graphene electrochemical devices demonstrating that useful 3D printable electrode can be manufactured.

9.4 Experimental Section

The tested solutions were: 1 mM dopamine in pH 7 phosphate buffer solution(PBS)/0.1 M KCl; 1 mM ascorbic acid in pH 7 PBS/0.1 M KCl; 1 mM β-nicotinamide adenine dinucleotide (NADH) in pH 7 PBS/0.1 M KCl; 1 mM hexaammineruthenium (III) chloride (RuHex) in 0.1 M KCl; 1 mM $Fe^{2+/3+}$/0.2 M $HClO_4$. Raman Spectroscopic analysis was performed using a Thermo Scientific DXR Raman Microscope fitted with a 532 nm excitation laser at a low power of 6 mW to avoid any heating effects. Spectra were recorded using a 3 seconds exposure time for 3 accumulations in each point. To collect a Raman profile between the region of 1000 and 3500 cm^{-1}. Scanning electron microscope (SEM) images were obtained using a JSM-5600LV (JEOL, Japan) model. Thermogravimetric analysis (TGA) was conducted utilising a PerkinElmer TGA 4000. The PLA samples were subject to a gradual temperature increase of 10 °C per minute, over a range between 25–800 °C, under a flow of nitrogen (40 ml/min).

The graphene/polylactic acid (PLA) composites were made by dispersing the graphene nanoplatelets within xylene and heated (under reflux) at 160 °C for 3 hours, the PLA was then added to the mixture and left for a further 3 hours. The resulting homogenous (solution phase) mixture then was then recrystallized within methanol, and left to dry (at 50 °C within a fan oven) until the xylene had evaporated, obtaining the final graphene/PLA powder mix. Thin films were made by using an industrial press, first under 180 °C and 15 ton of pressure for 180 seconds to make sure the homogeneous distribution of the heat and then left to cool down and pressed again at 15 ton of pressure at room temperature for another 180 seconds. The 3D printable filaments were extruded placing the graphene loaded PLA powder mix into a MiniCTW twin-screw extruder (ThermoScientific) at a temperature of 200 °C and a

screw speed of 30 rpm, obtaining a 1.75 mm diameter filament (see Figure 66A). The 3D printed designs were fabricated using a ZMorph® printer (Warsaw, Poland) with a direct drive extruder at a temperature of 190 °C. The 3D printed designs were drawn *via* Solidworks, to create a circular disc electrode with a diameter of 3mm and a thickness of 1 mm (see Figure 66A).

The HET rate constants, k_{obs}^{0}, were calculated using the near ideal outer-sphere redox probe $Ru(NH_3)_6^{3+/2+}$ (in 0.1 M KCl) using the well-known[190] and utilised Nicholson method[8], for electrochemical reactions *via* the equation 1.25 and 1.26[9] described in Chapter 1.

Chapter 10: Conclusions and future work

10.1 Overall conclusions

This thesis has significantly contributed to the fundamental understanding of pristine graphene (mono-layer) electrochemistry and its application as electrode material. First, exploring the most recommended method to estimate the real electroactive area of graphene (polymer-free CVD mono-layer graphene). It is also shown that mono- and few-layer CVD graphene are not suitable platforms for energy applications that generate gas bubbles and/or need high positive and negative potentials. It is also demonstrated herein that 2D-hBN needs to be further studied in order to understand its fundamentals electrochemical properties. In addition, it is proven in this work that smaller lateral size graphitic powder have enhances electrochemical properties than the bigger ones, which could lead to easily improve current devices. Finally, it is also reported herein the fabrication and application of 3D printed graphene/PLA electrodes with tailored filler loadings as additive manufacturing/3D printed electrochemical platforms.

10.2 Suggestions for future work

Future work continuing this thesis is as follows:

1. Future work should study in-situ the structural integrity of true monolayer graphene towards other electrochemical applications such as supercapacitors, fuel cells etc. to evaluate their usefulness and to compare the response obtained to other 2D materials.

2. Since the electrochemical properties of CVD graphene arise from its edge plane like-sites/defects, different modifications (boron and nitrogen doping) and structural disposition of graphene (PVD CVD graphene and vertically aligned graphene, with different ratios of edge plane coverage) and other 2D nanomaterials (such as 2D-hBN, MoS_2, $MoSe_2$ etc.) as electrode materials should be explored in order to tailor the different electrochemical properties of those electrodes.

3. Polymer-free 2D-hBN true electrochemical properties should be explored at the edge plane like- sites/defects in order to elucidate the origin of the newly-seen electrochemical capabilities. In-situ physicochemical and electrochemical characterisation of both 2D-hBN and substrate (SiO_2, CVD Graphene or others) could discern the true origin of the electrochemical response, differentiating if the arise from the doping of 2D-hBN or others.

4. Smaller lateral flake sizes of graphitic powders should be explored to enhance current screen-printed and 3D printed electrodes/devices towards sensing and energy applications in order to bring these devices into a new range of capabilities.

Publications arising from this Thesis

Published:

1. **Determination of the Electrochemical Area of Screen-Printed Electrochemical Sensing Platforms**, A. García-Miranda Ferrari, Christopher W. Foster, Peter J. Kelly, Dale A. C. Brownson and Craig E. Banks, Biosensors (Basel). 2018 Jun; 8(2): 53.

   Contributions: Electrochemical measurements, data analysis and writing of peer-review article.

2. **Exploring the reactivity of distinct electron transfer sites at CVD grown monolayer graphene through the selective electrodeposition of MoO_2 nanowires**, A. García-Miranda Ferrari, Christopher W. Foster, Dale A. C. Brownson, Kathryn A. Whitehead and Craig E. Banks, Scientific Reports, 2019, 9: 12814.

   Contributions: Graphene growth and transfer, electrochemical measurements, physicochemical characterisation, data analysis and writing of peer-review article.

3. **Investigating the Integrity of Graphene towards the Electrochemical Hydrogen Evolution Reaction (HER),** A. García-Miranda Ferrari, Dale A. C. Brownson and Craig E. Banks, Scientific Reports, 2019, 9: 15961.

   Contributions: Electrochemical measurements, physicochemical characterisation, data analysis and writing of peer-review article.

4. **Investigating the Integrity of Graphene towards the Oxygen Evolution Reaction (OER)**, A. García-Miranda Ferrari, Dale A. C. Brownson and Craig E. Banks, ChemElectroChem, 2019, 6, 5446.

   Contributions: Electrochemical measurements, physicochemical characterisation, data analysis and writing of peer-review article.

5. **Tailoring the electrochemical properties of 2D-hBN *via* physical linear defects: physicochemical, computational and electrochemical characterisation,** A. García-Miranda Ferrari, Ahmed S. Abo Dena, Christopher W. Foster, Samuel J. Rowley-Neale, Dale A. C. Brownson and Craig E. Banks, Nanoscale Advances, 2019 (10.1039/C9NA00530G).

   Contributions: Electrochemical measurements, data analysis and writing of peer-review article.

6. **Next-Generation Additive Manufacturing: Tailorable Graphene/Polylactic(acid) Filaments Allow the Fabrication of 3D Printable Porous Anodes for Utilisation within Lithium-ion Batteries**, Christopher W. Foster, Guo-Qiang Zou, Yunling Jiang, Michael P. Down, Christopher M. Liauw, Alejandro Garcia-Miranda Ferrari, Xiaobo Ji, Graham C. Smith, Peter J. Kelly and Prof. Craig E. Banks, Batteries & Supercaps. 2019, 2, 448–453.
   Contributions: Manufacture of graphene/PLA composites, electrochemical measurements, data analysis and writing of peer-review article.

Under peer-review:

7. **An investigation into the influence of lateral flake size on the electroanalytical performance of Graphene/Graphite paste electrodes,** A. García-Miranda Ferrari, Valentine Silva, Dale A. C. Brownson and Craig E. Banks, Under peer-review (Analytical Chemistry).
   Contributions: Electrochemical measurements, data analysis and writing of peer-review article.

In preparation:

8. **Determination of the Electrochemical Area of polymer-free CVD Grown Mono-layer Graphene Electrodes**, A. García-Miranda Ferrari, Christopher W. Foster, Dale A. C. Brownson and Craig E. Banks.
   Contributions: Graphene growth and transfer, electrochemical measurements, data analysis and writing of peer-review article.

References

1. A. Bard and L. Faulkner, *Electrochemical Methods: Fundamentals and Applications*, John Wiley & Sons, Inc, 2001.
2. J. Wang, *Analytical electrochemistry / Joseph Wang*, 2019.
3. R. G. Compton and C. E. Banks, *Understanding Voltammetry*, Imperial College Press, 2nd edn., 2010.
4. A. Fick, *Annalen der Physik*, 1855, 170, 59-86.
5. J. E. B. Randles, *Transactions of the Faraday Society*, 1948, 44, 327-338.
6. A. Ševčík, *Collect. Czech. Chem. Commun.*, 1948, 13, 349-377.
7. D. A. C. Brownson and C. E. Banks, *The Handbook of Graphene Electrochemistry*, 2014.
8. R. S. Nicholson, *Analytical Chemistry*, 1965, 37, 1351-1355.
9. S. J. Rowley-Neale, D. A. C. Brownson and C. E. Banks, *Nanoscale*, 2016, 8, 15241-15251.
10. D. Brownson and C. E. Banks, *The Handbook of Graphene Electrochemistry*, 2014.
11. F. C. Anson, *Analytical Chemistry*, 1966, 38, 54-57.
12. *Advances in Electrochemical Science and Engineering*, Wiley.
13. D. A. C. Brownson, D. K. Kampouris and C. E. Banks, *Journal of Power Sources*, 2011, 196, 4873-4885.
14. D. A. C. Brownson and C. E. Banks, *Analyst*, 2010, 135, 2768-2778.
15. M. Pumera, *The Chemical Record*, 2009, 9, 211-223.
16. D. A. C. Brownson, P. J. Kelly and C. E. Banks, *RSC Advances*, 2015, 5, 37281-37286.
17. K. Zeng and D. Zhang, *Progress in Energy and Combustion Science*, 2010, 36, 307-326.
18. W. M. Singh, T. Baine, S. Kudo, S. Tian, X. A. N. Ma, H. Zhou, N. J. DeYonker, T. C. Pham, J. C. Bollinger, D. L. Baker, B. Yan, C. E. Webster and X. Zhao, *Angewandte Chemie International Edition*, 2012, 51, 5941-5944.
19. S. Srinivasan and F. J. Salzano, *International Journal of Hydrogen Energy*, 1977, 2, 53-59.
20. R. L. McCreery, *Chemical Reviews*, 2008, 108, 2646-2687.
21. J. O. Besenhard and H. P. Fritz, *Angewandte Chemie International Edition in English*, 1983, 22, 950-975.
22. Z. Kominkova, V. Vales, M. C. Hersam and M. Kalbac, *Carbon*, 2014, 78, 366-373.
23. Z. Kominkova and M. Kalbac, *RSC Advances*, 2014, 4, 11311-11316.
24. C. T. J. Low, F. C. Walsh, M. H. Chakrabarti, M. A. Hashim and M. A. Hussain, *Carbon*, 2013, 54, 1-21.
25. K. S. Novoselov, A. K. Geim, S. V. Morozov, D. Jiang, Y. Zhang, S. V. Dubonos, I. V. Grigorieva and A. A. Firsov, *Science*, 2004, 306, 666-669.
26. Y. R. Kim, S. Bong, Y. J. Kang, Y. Yang, R. K. Mahajan, J. S. Kim and H. Kim, *Biosens Bioelectron*, 2010, 25, 2366-2369.
27. X. Kang, J. Wang, H. Wu, I. A. Aksay, J. Liu and Y. Lin, *Biosens Bioelectron*, 2009, 25, 901-905.
28. Y. Wang, Y. Wan and D. Zhang, *Electrochemistry Communications*, 2010, 12, 187-190.
29. J.-F. Wu, M.-Q. Xu and G.-C. Zhao, *Electrochemistry Communications*, 2010, 12, 175-177.
30. W.-J. Lin, C.-S. Liao, J.-H. Jhang and Y.-C. Tsai, *Electrochemistry Communications*, 2009, 11, 2153-2156.
31. D. A. C. Brownson, M. Gomez-Mingot and C. E. Banks, *Physical Chemistry Chemical Physics*, 2011, 13, 20284-20288.
32. X. Kang, J. Wang, H. Wu, J. Liu, I. A. Aksay and Y. Lin, *Talanta*, 2010, 81, 754-759.
33. D. Brownson and C. Banks, *Analyst*, 2010, 135, 2768-2778.

34. D. A. C. Brownson, S. A. Varey, F. Hussain, S. J. Haigh and C. E. Banks, *Nanoscale*, 2014, 6, 1607-1621.
35. W. Lu, A. Adriano and P. Martin, *Angewandte Chemie International Edition*, 2013, 52, 13818-13821.
36. L. C. S. Figueiredo-Filho, D. A. C. Brownson, O. Fatibello-Filho and C. E. Banks, *Analyst*, 2013, 138, 4436-4442.
37. D. A. C. Brownson, G. C. Smith and C. E. Banks, *Royal Society Open Science*, 2017, 4.
38. D. A. C. Brownson, J. P. Metters, D. K. Kampouris and C. E. Banks, *Electroanalysis*, 2011, 23, 894-899.
39. J. M. Tour, *Chemistry of Materials*, 2014, 26, 163-171.
40. Z. Yan, J. Lin, Z. Peng, Z. Sun, Y. Zhu, L. Li, C. Xiang, E. L. Samuel, C. Kittrell and J. M. Tour, *ACS Nano*, 2012, 6, 9110-9117.
41. X. Li, C. W. Magnuson, A. Venugopal, J. An, J. W. Suk, B. Han, M. Borysiak, W. Cai, A. Velamakanni, Y. Zhu, L. Fu, E. M. Vogel, E. Voelkl, L. Colombo and R. S. Ruoff, *Nano Letters*, 2010, 10, 4328-4334.
42. S. Bae, H. Kim, Y. Lee, X. Xu, J.-S. Park, Y. Zheng, J. Balakrishnan, T. Lei, H. Ri Kim, Y. I. Song, Y.-J. Kim, K. S. Kim, B. Ozyilmaz, J.-H. Ahn, B. H. Hong and S. Iijima, *Nat Nano*, 2010, 5, 574-578.
43. K. S. Kim, Y. Zhao, H. Jang, S. Y. Lee, J. M. Kim, K. S. Kim, J.-H. Ahn, P. Kim, J.-Y. Choi and B. H. Hong, *Nature*, 2009, 457, 706-710.
44. A. Reina, X. Jia, J. Ho, D. Nezich, H. Son, V. Bulovic, M. S. Dresselhaus and J. Kong, *Nano Letters*, 2009, 9, 30-35.
45. C. Mattevi, H. Kim and M. Chhowalla, *Journal of Materials Chemistry*, 2011, 21, 3324-3334.
46. R. Muñoz and C. Gómez-Aleixandre, *Chemical Vapor Deposition*, 2013, 19, 297-322.
47. X. Li, W. Cai, J. An, S. Kim, J. Nah, D. Yang, R. Piner, A. Velamakanni, I. Jung, E. Tutuc, S. K. Banerjee, L. Colombo and R. S. Ruoff, *Science*, 2009, 324, 1312-1314.
48. J. W. Suk, A. Kitt, C. W. Magnuson, Y. Hao, S. Ahmed, J. An, A. K. Swan, B. B. Goldberg and R. S. Ruoff, *ACS Nano*, 2011, 5, 6916-6924.
49. D.-Y. Wang, I.-S. Huang, P.-H. Ho, S.-S. Li, Y.-C. Yeh, D.-W. Wang, W.-L. Chen, Y.-Y. Lee, Y.-M. Chang, C.-C. Chen, C.-T. Liang and C.-W. Chen, *Advanced Materials*, 2013, 25, 4521-4526.
50. J. Kang, D. Shin, S. Bae and B. H. Hong, *Nanoscale*, 2012, 4, 5527-5537.
51. A. Pirkle, J. Chan, A. Venugopal, D. Hinojos, C. W. Magnuson, S. McDonnell, L. Colombo, E. M. Vogel, R. S. Ruoff and R. M. Wallace, *Applied Physics Letters*, 2011, 99, 122108.
52. J. R. Vig, *Journal of Vacuum Science & Technology A*, 1985, 3, 1027-1034.
53. G. Lupina, J. Kitzmann, I. Costina, M. Lukosius, C. Wenger, A. Wolff, S. Vaziri, M. Östling, I. Pasternak, A. Krajewska, W. Strupinski, S. Kataria, A. Gahoi, M. C. Lemme, G. Ruhl, G. Zoth, O. Luxenhofer and W. Mehr, *ACS Nano*, 2015, 9, 4776-4785.
54. H. Van Ngoc, Y. Qian, S. K. Han and D. J. Kang, *Scientific Reports*, 2016, 6, 33096.
55. G. Lene, M. C. José, C. Alberto, M. A. M. David, H. P. Dirch, J. B. Timothy and B. Peter, *2D Materials*, 2014, 1, 035005.
56. A. Yulaev, G. Cheng, A. R. Hight Walker, I. V. Vlassiouk, A. Myers, M. S. Leite and A. Kolmakov, *RSC Advances*, 2016, 6, 83954-83962.
57. B. J. Tyler, B. Brennan, H. Stec, T. Patel, L. Hao, I. S. Gilmore and A. J. Pollard, *The Journal of Physical Chemistry C*, 2015, 119, 17836-17841.
58. Y. Zhu, S. Murali, M. D. Stoller, K. J. Ganesh, W. Cai, P. J. Ferreira, A. Pirkle, R. M. Wallace, K. A. Cychosz, M. Thommes, D. Su, E. A. Stach and R. S. Ruoff, *Science*, 2011, 332, 1537-1541.

59. Y. Wang, Z. Shi, Y. Huang, Y. Ma, C. Wang, M. Chen and Y. Chen, *The Journal of Physical Chemistry C*, 2009, 113, 13103-13107.
60. C. Liu, Z. Yu, D. Neff, A. Zhamu and B. Z. Jang, *Nano Letters*, 2010, 10, 4863-4868.
61. L. L. Zhang, R. Zhou and X. S. Zhao, *Journal of Materials Chemistry*, 2010, 20, 5983-5992.
62. X. Wang, L. Zhi and K. Müllen, *Nano Letters*, 2008, 8, 323-327.
63. K. Cui, T. Chiba, X. Chen, S. Chiashi and S. Maruyama, *Journal of Nanoscience and Nanotechnology*, 2015, 15, 3107-3110.
64. M. Zhong, D. Xu, X. Yu, K. Huang, X. Liu, Y. Qu, Y. Xu and D. Yang, *Nano Energy*, 2016, 28, 12-18.
65. X. Miao, S. Tongay, M. K. Petterson, K. Berke, A. G. Rinzler, B. R. Appleton and A. F. Hebard, *Nano Letters*, 2012, 12, 2745-2750.
66. A. Marinoiu, M. Raceanu, E. Carcadea, M. Varlam and I. Stefanescu, *Applied Surface Science*, 2017, 424, 93-100.
67. L. Zhang and Z. Xia, *The Journal of Physical Chemistry C*, 2011, 115, 11170-11176.
68. F. Bonaccorso, L. Colombo, G. Yu, M. Stoller, V. Tozzini, A. C. Ferrari, R. S. Ruoff and V. Pellegrini, *Science*, 2015, 347.
69. G. Xie, K. Zhang, B. Guo, Q. Liu, L. Fang and J. R. Gong, *Advanced Materials*, 2013, 25, 3820-3839.
70. D. Golberg, Y. Bando, Y. Huang, T. Terao, M. Mitome, C. Tang and C. Zhi, *ACS Nano*, 2010, 4, 2979-2993.
71. M. Xu, T. Liang, M. Shi and H. Chen, *Chemical Reviews*, 2013, 113, 3766-3798.
72. W. H. Balmain, *Journal für Praktische Chemie*, 1842, 27, 422-430.
73. W. H. Balmain, *The London, Edinburgh, and Dublin Philosophical Magazine and Journal of Science*, 1842, 21, 270-277.
74. C. Y. Zhi, Y. Bando, C. C. Tang, Q. Huang and D. Golberg, *Journal of Materials Chemistry*, 2008, 18, 3900-3908.
75. Y. Kimura, T. Wakabayashi, K. Okada, T. Wada and H. Nishikawa, *Wear*, 1999, 232, 199-206.
76. O. N. Çelik, N. Ay and Y. Göncü, *Particulate Science and Technology*, 2013, 31, 501-506.
77. M. Mosleh, N. D. Atnafu, J. H. Belk and O. M. Nobles, *Wear*, 2009, 267, 1220-1225.
78. D. Lee, S. H. Song, J. Hwang, S. H. Jin, K. H. Park, B. H. Kim, S. H. Hong and S. Jeon, *Small*, 2013, 9, 2602-2610.
79. C. Zhi, Y. Bando, C. Tang, H. Kuwahara and D. Golberg, *Advanced Materials*, 2009, 21, 2889-2893.
80. W. Zhou, J. Zuo, X. Zhang and A. Zhou, *Journal of Composite Materials*, 2014, 48, 2517-2526.
81. Y. Shi, C. Hamsen, X. Jia, K. K. Kim, A. Reina, M. Hofmann, A. L. Hsu, K. Zhang, H. Li, Z.-Y. Juang, M. S. Dresselhaus, L.-J. Li and J. Kong, *Nano Letters*, 2010, 10, 4134-4139.
82. J. G. Kho, K. T. Moon, J. H. Kim and D. P. Kim, *Journal of the American Ceramic Society*, 2000, 83, 2681-2683.
83. J. N. Coleman, M. Lotya, A. O'Neill, S. D. Bergin, P. J. King, U. Khan, K. Young, A. Gaucher, S. De, R. J. Smith, I. V. Shvets, S. K. Arora, G. Stanton, H. Y. Kim, K. Lee, G. T. Kim, G. S. Duesberg, T. Hallam, J. J. Boland, J. J. Wang, J. F. Donegan, J. C. Grunlan, G. Moriarty, A. Shmeliov, R. J. Nicholls, J. M. Perkins, E. M. Grieveson, K. Theuwissen, D. W. McComb, P. D. Nellist and V. Nicolosi, *Science*, 2011, 331, 568-571.
84. B. Sachs, T. O. Wehling, M. I. Katsnelson and A. I. Lichtenstein, *Physical Review B*, 2016, 94, 224105.
85. Y. Kubota, K. Watanabe, O. Tsuda and T. Taniguchi, *Science*, 2007, 317, 932-934.

86. C. R. Dean, A. F. Young, I. Meric, C. Lee, L. Wang, S. Sorgenfrei, K. Watanabe, T. Taniguchi, P. Kim, K. L. Shepard and J. Hone, *Nature Nanotechnology*, 2010, 5, 722.
87. I. M. Felix and L. F. C. Pereira, *Scientific Reports*, 2018, 8, 2737.
88. D. Golla, A. Brasington, B. J. LeRoy and A. Sandhu, *APL Materials*, 2017, 5, 056101.
89. A. Kumar, T. Low, K. H. Fung, P. Avouris and N. X. Fang, *Nano Letters*, 2015, 15, 3172-3180.
90. M. P. Levendorf, C.-J. Kim, L. Brown, P. Y. Huang, R. W. Havener, D. A. Muller and J. Park, *Nature*, 2012, 488, 627.
91. M. Liu, Y. Li, P. Chen, J. Sun, D. Ma, Q. Li, T. Gao, Y. Gao, Z. Cheng, X. Qiu, Y. Fang, Y. Zhang and Z. Liu, *Nano Letters*, 2014, 14, 6342-6347.
92. L. Ci, L. Song, C. Jin, D. Jariwala, D. Wu, Y. Li, A. Srivastava, Z. F. Wang, K. Storr, L. Balicas, F. Liu and P. M. Ajayan, *Nature Materials*, 2010, 9, 430.
93. Z. Liu, L. Ma, G. Shi, W. Zhou, Y. Gong, S. Lei, X. Yang, J. Zhang, J. Yu, K. P. Hackenberg, A. Babakhani, J.-C. Idrobo, R. Vajtai, J. Lou and P. M. Ajayan, *Nature Nanotechnology*, 2013, 8, 119.
94. Z. Liu, L. Song, S. Zhao, J. Huang, L. Ma, J. Zhang, J. Lou and P. M. Ajayan, *Nano Letters*, 2011, 11, 2032-2037.
95. M. Gurram, S. Omar, S. Zihlmann, P. Makk, Q. C. Li, Y. F. Zhang, C. Schönenberger and B. J. van Wees, *Physical Review B*, 2018, 97, 045411.
96. X. Wang, X. Li, L. Zhang, Y. Yoon, P. K. Weber, H. Wang, J. Guo and H. Dai, *Science*, 2009, 324, 768-771.
97. T. B. Martins, R. H. Miwa, A. J. R. da Silva and A. Fazzio, *Physical Review Letters*, 2007, 98, 196803.
98. D. Albert and K. Mahfuza, *Journal of Physics D: Applied Physics*, 2019, 52, 025301.
99. R. Mukherjee and S. Bhowmick, *Journal of Chemical Theory and Computation*, 2011, 7, 720-724.
100. C.-H. Park and S. G. Louie, *Nano Letters*, 2008, 8, 2200-2203.
101. A. F. Khan, M. P. Down, G. C. Smith, C. W. Foster and C. E. Banks, *Journal of Materials Chemistry A*, 2017, 5, 4103-4113.
102. A. F. Khan, E. P. Randviir, D. A. C. Brownson, X. Ji, G. C. Smith and C. E. Banks, *Electroanalysis*, 2017, 29, 622-634.
103. *Light Scattering in Solids*, Springer, 1975.
104. L. G. Cançado, M. A. Pimenta, B. R. A. Neves, G. Medeiros-Ribeiro, T. Enoki, Y. Kobayashi, K. Takai, K.-i. Fukui, M. S. Dresselhaus, R. Saito and A. Jorio, *Physical Review Letters*, 2004, 93, 047403.
105. G. Dresselhaus and S. Riichiro, *Physical properties of carbon nanotubes*, World scientific, 1998.
106. R. J. Nemanich and S. A. Solin, *Solid State Communications*, 1977, 23, 417-420.
107. R. J. Nemanich and S. A. Solin, *Physical Review B*, 1979, 20, 392-401.
108. M. S. Dresselhaus, G. Dresselhaus, K. Sugihara, I. L. Spain and H. A. Goldberg, *Graphite fibers and filaments*, Springer Science & Business Media, 2013.
109. A. C. Ferrari, J. C. Meyer, V. Scardaci, C. Casiraghi, M. Lazzeri, F. Mauri, S. Piscanec, D. Jiang, K. S. Novoselov, S. Roth and A. K. Geim, *Physical Review Letters*, 2006, 97, 187401.
110. A. C. Ferrari, *Solid State Communications*, 2007, 143, 47-57.
111. L. M. Malard, M. A. Pimenta, G. Dresselhaus and M. S. Dresselhaus, *Physics Reports*, 2009, 473, 51-87.
112. E. Blanco, C. W. Foster, L. R. Cumba, D. R. do Carmo and C. E. Banks, *Analyst*, 2016, 141, 2783-2790.
113. L. R. Cumba, C. W. Foster, D. A. C. Brownson, J. P. Smith, J. Iniesta, B. Thakur, D. R. do Carmo and C. E. Banks, *Analyst*, 2016, 141, 2791-2799.

114. Kemet, https://www.kemet.co.uk/products/diamond-products/kemet-diamond-spray, Accessed 20/04/2019.
115. K. K. Kim, A. Hsu, X. Jia, S. M. Kim, Y. Shi, M. Hofmann, D. Nezich, J. F. Rodriguez-Nieva, M. Dresselhaus, T. Palacios and J. Kong, *Nano Letters*, 2012, 12, 161-166.
116. Graphene Supermarket, http://www.graphene-supermarket.com.
117. D. A. C. Brownson and C. E. Banks, *Phys Chem Chem Phys*, 2012, 14, 8264-8281.
118. X. Li, Y. Zhu, W. Cai, M. Borysiak, B. Han, D. Chen, R. D. Piner, L. Colombo and R. S. Ruoff, *Nano Letters*, 2009, 9, 4359-4363.
119. X. Liang, B. A. Sperling, I. Calizo, G. Cheng, C. A. Hacker, Q. Zhang, Y. Obeng, K. Yan, H. Peng, Q. Li, X. Zhu, H. Yuan, A. R. Walker, Z. Liu, L. M. Peng and C. A. Richter, *ACS Nano*, 2011, 5, 9144-9153.
120. T. H. Bointon, M. D. Barnes, S. Russo and M. F. Craciun, *Advanced Materials*, 2015, 27, 4200-4206.
121. M. Hu, Z. Yao and X. Wang, *AIMS Materials Science*, 2017, 4, 755-788.
122. A. C. Ferrari and J. Robertson, *Physical Review B*, 2000, 61, 14095-14107.
123. F. Tuinstra and J. L. Koenig, *The Journal of Chemical Physics*, 1970, 53, 1126-1130.
124. F. Negri, E. d. Donato, M. Tommasini, C. Castiglioni, G. Zerbi and K. Müllen, *The Journal of Chemical Physics*, 2004, 120, 11889-11900.
125. G. Zhang, A. G. Güell, P. M. Kirkman, R. A. Lazenby, T. S. Miller and P. R. Unwin, *ACS Applied Materials & Interfaces*, 2016, 8, 8008-8016.
126. J. P. Metters, R. O. Kadara and C. E. Banks, *Analyst*, 2011, 136, 1067-1076.
127. M. Li, Y. T. Li, D. W. Li and Y. T. Long, *Anal Chim Acta*, 2012, 734, 31-44.
128. R. O. Kadara, N. Jenkinson and C. E. Banks, *Electroanalysis*, 2009, 21, 2410-2414.
129. C. W. Foster, A. P. de Souza, J. P. Metters, M. Bertotti and C. E. Banks, *Analyst*, 2015, 140, 7598-7612.
130. N. Hernández-Ibáñez, L. García-Cruz, V. Montiel, C. W. Foster, C. E. Banks and J. Iniesta, *Biosensors and Bioelectronics*, 2016, 77, 1168-1174.
131. N. Hernández-Ibáñez, I. Sanjuán, M. Á. Montiel, C. W. Foster, C. E. Banks and J. Iniesta, *Journal of Electroanalytical Chemistry*, 2016, 780, 303-310.
132. J. Lee, G. Hussain, C. E. Banks and D. S. Silvester, *Sensors (Basel, Switzerland)*, 2017, 17, 2734.
133. A. Morata, J. P. Viricelle, A. Tarancón, G. Dezanneau, C. Pijolat, F. Peiro and J. R. Morante, *Sensors and Actuators B: Chemical*, 2008, 130, 561-566.
134. M. Maczuga, A. Economou, A. Bobrowski and M. Prodromidis, *Electrochimica Acta*, 2013, 114, 758.
135. E. P. Randviir, J. P. Metters, J. Stainton and C. E. Banks, *Analyst*, 2013, 138, 2970-2981.
136. K. Ngamchuea, P. Hurst, C. Batchelor-McAuley and R. G. Compton, *Sensors and Actuators B: Chemical*, 2016, 232, 138-142.
137. G. Jarzabek and Z. Borkowska, *Electrochimica Acta*, 1997, 42, 2915-2918.
138. M. Łukaszewski, M. Soszko and A. Czerwiński, *Electrochemical Methods of Real Surface Area Determination of Noble Metal Electrodes – an Overview*, 2016.
139. V. Fragkou, Y. Ge, G. Steiner, D. Freeman, N. Bartetzko and A. P. F. Turner, *Int. J. Electrochem. Sci.*, 2012, 7, 6214-6220.
140. N. S. K. Gowthaman, M. A. Raj and S. A. John, *ACS Sustainable Chemistry & Engineering*, 2017, 5, 1648-1658.
141. A. Purwidyantri, C.-H. Chen, L.-Y. Chen, C.-C. Chen, J.-D. Luo, C.-C. Chiou, Y.-C. Tian, C.-Y. Lin, C.-M. Yang, H.-C. Lai and C.-S. Lai, *Speckled ZnO Nanograss Electrochemical Sensor for Staphylococcus epidermidis Detection*, 2017.
142. M. A. Ali, P. R. Solanki, S. Srivastava, S. Singh, V. V. Agrawal, R. John and B. D. Malhotra, *ACS Appl Mater Interfaces*, 2015, 7, 5837-5846.

143. S. E. Jeena and T. Selvaraju, *Journal of Chemical Sciences*, 2016, 128, 357-363.
144. T. Sagarica and H. Saha, *Current Science*, 2015, 109, 1427.
145. E. Tamburri, M. C. Cassani, B. Ballarin, M. Tomellini, C. Femoni, A. Mignani, M. L. Terranova and S. Orlanducci, *ChemSusChem*, 2016, 9, 1153-1165.
146. K. Ngamchuea, S. Eloul, K. Tschulik and R. G. Compton, *Journal of Solid State Electrochemistry*, 2014, 18, 3251-3257.
147. A. García-Miranda Ferrari, C. W. Foster, D. A. C. Brownson, K. A. Whitehead and C. E. Banks, unpublished work.
148. R. G. Compton and C. E. Banks, *Understanding voltammetry, 2nd edition*, 2010.
149. T. J. Davies, R. R. Moore, C. E. Banks and R. G. Compton, *Journal of Electroanalytical Chemistry*, 2004, 574, 123-152.
150. C. R. Wilke and P. Chang, *AIChE Journal*, 1955, 1, 264-270.
151. R. Sitaraman, S. H. Ibrahim and N. R. Kuloor, *Journal of Chemical & Engineering Data*, 1963, 8, 198-201.
152. X. Jiao, C. Batchelor-McAuley, E. Kätelhön, J. Ellison, K. Tschulik and R. G. Compton, *The Journal of Physical Chemistry C*, 2015, 119, 9402-9410.
153. E. Peltola, S. Sainio, K. B. Holt, T. Palomäki, J. Koskinen and T. Laurila, *Analytical Chemistry*, 2018, 90, 1408-1416.
154. S. H. DuVall and R. L. McCreery, *Journal of the American Chemical Society*, 2000, 122, 6759-6764.
155. G. Ziyatdinova, E. Ziganshina, A. Shamsevalieva and H. Budnikov, *Arabian Journal of Chemistry*, 2017, DOI: https://doi.org/10.1016/j.arabjc.2017.12.019.
156. C. Jian, Q. Cai, W. Hong, J. Li and W. Liu, *Small*, 2018, 14, 1703798.
157. R. Kachoosangi, G. G Wildgoose and R. G Compton, *Carbon Nanotube-Based Electrochemical Sensors for Quantifying the 'heat' of Chilli Peppers: The Adsorptive Stripping Voltammetric Determination of Capsaicin*, 2008.
158. M. Březina, J. Koryta, T. Loučka, D. Maršíková and J. Pradáč, *Journal of Electroanalytical Chemistry and Interfacial Electrochemistry*, 1972, 40, 13-17.
159. C. Zanardi, E. Ferrari, L. Pigani, F. Arduini and R. Seeber, *Chemosensors*, 2015, 3, 118.
160. R. C. Alkire, P. N. Barlett and J. Lipkowski, *Electrochemistry of Carbon Electrodes*, Wiley, 2016.
161. A. K. Geim and K. S. Novoselov, *Nat Mater*, 2007, 6, 183-191.
162. A. K. Geim, *Science*, 2009, 324, 1530-1534.
163. K. S. Novoselov, A. K. Geim, S. V. Morozov, D. Jiang, M. I. Katsnelson, I. V. Grigorieva, S. V. Dubonos and A. A. Firsov, *Nature*, 2005, 438, 197-200.
164. S. V. Morozov, K. S. Novoselov, M. I. Katsnelson, F. Schedin, D. C. Elias, J. A. Jaszczak and A. K. Geim, *Physical Review Letters*, 2008, 100, 016602.
165. J.-H. Chen, C. Jang, S. Xiao, M. Ishigami and M. S. Fuhrer, 2008, 3, 206.
166. Y. H. Kwak, D. S. Choi, Y. N. Kim, H. Kim, D. H. Yoon, S.-S. Ahn, J.-W. Yang, W. S. Yang and S. Seo, *Biosensors and Bioelectronics*, 2012, 37, 82-87.
167. R. K. Joshi, H. Gomez, F. Alvi and A. Kumar, *The Journal of Physical Chemistry C*, 2010, 114, 6610-6613.
168. T.-Y. Chen, P. T. K. Loan, C.-L. Hsu, Y.-H. Lee, J. Tse-Wei Wang, K.-H. Wei, C.-T. Lin and L.-J. Li, *Biosensors and Bioelectronics*, 2013, 41, 103-109.
169. W. Yuan, Y. Zhou, Y. Li, C. Li, H. Peng, J. Zhang, Z. Liu, L. Dai and G. Shi, *Sci Rep*, 2013, 3, 2248.
170. E. P. Randviir, D. A. C. Brownson and C. E. Banks, *Materials Today*, 2014, 17, 426-432.
171. A. J. Slate, D. A. C. Brownson, A. S. Abo Dena, G. C. Smith, K. A. Whitehead and C. E. Banks, *Physical Chemistry Chemical Physics*, 2018, DOI: 10.1039/C8CP02196A.
172. H. Hou, C. E. Banks, M. Jing, Y. Zhang and X. Ji, *Advanced Materials*, 2015, 27, 7861-7866.

173. J. Cao, P. He, M. A. Mohammed, X. Zhao, R. J. Young, B. Derby, I. A. Kinloch and R. A. W. Dryfe, *J Am Chem Soc*, 2017, 139, 17446-17456.
174. W. Li, C. Tan, M. A. Lowe, H. D. Abruña and D. C. Ralph, *ACS Nano*, 2011, 5, 2264-2270.
175. D. A. C. Brownson, D. K. Kampouris and C. E. Banks, *Chem Soc Rev*, 2012, 41, 6944-6976.
176. S. J. Rowley-Neale and C. E. Banks, *Encyclopedia of Interfacial Chemistry: Electrocatalytic Properties of Carbon Electrode Surfaces*, Elsevier, Oxford, 2018.
177. A. T. Valota, I. A. Kinloch, K. S. Novoselov, C. Casiraghi, A. Eckmann, E. W. Hill and R. A. W. Dryfe, *ACS Nano*, 2011, 5, 8809-8815.
178. M. A. Edwards, P. Bertoncello and P. R. Unwin, *The Journal of Physical Chemistry C*, 2009, 113, 9218-9223.
179. D. A. C. Brownson, L. J. Munro, D. K. Kampouris and C. E. Banks, *RSC Advances*, 2011, 1, 978-988.
180. X. Ji, C. E. Banks, W. Xi, S. J. Wilkins and R. G. Compton, *The Journal of Physical Chemistry B*, 2006, 110, 22306-22309.
181. M. P. Zach, K. Inazu, K. H. Ng, J. C. Hemminger and R. M. Penner, *Chemistry of Materials*, 2002, 14, 3206-3216.
182. M. P. Zach, K. H. Ng and R. M. Penner, *Science*, 2000, 290, 2120-2123.
183. E. C. Walter, M. P. Zach, F. Favier, B. J. Murray, K. Inazu, J. C. Hemminger and R. M. Penner, *ChemPhysChem*, 2003, 4, 131-138.
184. M. E. Hyde, T. J. Davies and R. G. Compton, *Angew Chem*, 2005, 44, 6491-6496.
185. T. J. Davies, M. E. Hyde and R. G. Compton, *Angew Chem*, 2005, 44, 5121-5126.
186. R. E. G. Smith, T. J. Davies, N. B. Baynes and R. J. Nichols, *Journal of Electroanalytical Chemistry*.
187. M. A. Camacho-López, L. Escobar-Alarcón, M. Picquart, R. Arroyo, G. Córdoba and E. Haro-Poniatowski, *Optical Materials*, 2011, 33, 480-484.
188. P. R. Unwin, A. G. Güell and G. Zhang, *Accounts of Chemical Research*, 2016, 49, 2041-2048.
189. A. G. Güell, A. S. Cuharuc, Y.-R. Kim, G. Zhang, S.-y. Tan, N. Ebejer and P. R. Unwin, *ACS Nano*, 2015, 9, 3558-3571.
190. A. García-Miranda Ferrari, C. W. Foster, P. Kelly, D. C. Brownson and C. E. Banks, *Biosensors*, 2018, 8.
191. M. G. Walter, E. L. Warren, J. R. McKone, S. W. Boettcher, Q. Mi, E. A. Santori and N. S. Lewis, *Chem Rev*, 2010, 110, 6446-6473.
192. M. S. Dresselhaus and I. L. Thomas, *Nature*, 2001, 414, 332-337.
193. J. Xu, T. Liu, J. Li, Y. Liu, B. Zhang, D. Xiong, I. Amorim, W. Li and L. Liu, *Energy & Environmental Science*, 2018, DOI: 10.1039/C7EE03603E.
194. J. Yang, D. Wang, H. Han and C. Li, *Accounts of Chemical Research*, 2013, 46, 1900-1909.
195. B. Hinnemann, P. G. Moses, J. Bonde, K. P. Jørgensen, J. H. Nielsen, S. Horch, I. Chorkendorff and J. K. Nørskov, *Journal of the American Chemical Society*, 2005, 127, 5308-5309.
196. N. M. Marković and P. N. Ross, *Surface Science Reports*, 2002, 45, 117-229.
197. Y. Yan, B. Xia, Z. Xu and X. Wang, *ACS Catalysis*, 2014, 4, 1693-1705.
198. K. Ravindra, L. Bencs and R. Van Grieken, *Sci Total Environ*, 2004, 318, 1-43.
199. K. S. Novoselov, D. Jiang, F. Schedin, T. J. Booth, V. V. Khotkevich, S. V. Morozov and A. K. Geim, *Proceedings of the National Academy of Sciences of the United States of America*, 2005, 102, 10451-10453.
200. J. Xia, F. Chen, J. Li and N. Tao, *Nat Nano*, 2009, 4, 505-509.

201. T. J. Booth, P. Blake, R. R. Nair, D. Jiang, E. W. Hill, U. Bangert, A. Bleloch, M. Gass, K. S. Novoselov, M. I. Katsnelson and A. K. Geim, *Nano Letters*, 2008, 8, 2442-2446.
202. C. Lee, X. Wei, J. W. Kysar and J. Hone, *Science*, 2008, 321, 385-388.
203. Y. Jiao, Y. Zheng, M. Jaroniec and S. Z. Qiao, *Journal of the American Chemical Society*, 2014, 136, 4394-4403.
204. Y. Ito, W. Cong, T. Fujita, Z. Tang and M. Chen, *Angewandte Chemie International Edition*, 2015, 54, 2131-2136.
205. L. Yu, X. Pan, X. Cao, P. Hu and X. Bao, *Journal of Catalysis*, 2011, 282, 183-190.
206. Y. Dong, Z.-S. Wu, W. Ren, H.-M. Cheng and X. Bao, *Science Bulletin*.
207. L. Dai, D. W. Chang, J.-B. Baek and W. Lu, *Small*, 2012, 8, 1130-1166.
208. J. Li, Z. Zhao, Y. Ma and Y. Qu, *ChemCatChem*, 2017, 9, 1554-1568.
209. A. Xie, N. Xuan, K. Ba and Z. Sun, *ACS Applied Materials & Interfaces*, 2017, 9, 4643-4648.
210. M. T. Koper, *Nat Chem*, 2013, 5, 255-256.
211. X. Liu and L. M. Dai, *Nature Reviews Materials*, 2016, 1.
212. Y. Liang, Y. Li, H. Wang and H. Dai, *J Am Chem Soc*, 2013, 135, 2013-2036.
213. Y. Jiao, Y. Zheng, K. Davey and S. Z. Qiao, *Nature Energy*, 2016, 1, 9.
214. Y. Zheng, Y. Jiao, Y. Zhu, L. H. Li, Y. Han, Y. Chen, A. Du, M. Jaroniec and S. Z. Qiao, *Nature Communications*, 2014, 5, 3783.
215. H. Wang and H. Dai, *Chem Soc Rev*, 2013, 42, 3088-3113.
216. Y. Zheng, Y. Jiao, L. H. Li, T. Xing, Y. Chen, M. Jaroniec and S. Z. Qiao, *ACS Nano*, 2014, 8, 5290-5296.
217. J. Deng, P. Ren, D. Deng and X. Bao, *Angewandte Chemie International Edition*, 2015, 54, 2100-2104.
218. T. F. Jaramillo, K. P. Jorgensen, J. Bonde, J. H. Nielsen, S. Horch and I. Chorkendorff, *Science*, 2007, 317, 100-102.
219. D. Kong, H. Wang, J. J. Cha, M. Pasta, K. J. Koski, J. Yao and Y. Cui, *Nano Lett*, 2013, 13, 1341-1347.
220. S. J. Rowley-Neale, C. W. Foster, G. C. Smith, D. A. C. Brownson and C. E. Banks, *Sustainable Energy & Fuels*, 2017, 1, 74-83.
221. R. J. Rice and R. L. McCreery, *Analytical Chemistry*, 1989, 61, 1637-1641.
222. H. Ji, X. Zhao, Z. Qiao, J. Jung, Y. Zhu, Y. Lu, L. L. Zhang, A. H. MacDonald and R. S. Ruoff, *Nat Commun*, 2014, 5, 3317.
223. A. N. Patel, M. G. Collignon, M. A. O'Connell, W. O. Y. Hung, K. McKelvey, J. V. Macpherson and P. R. Unwin, *Journal of the American Chemical Society*, 2012, 134, 20117-20130.
224. D. A. C. Brownson, L. C. S. Figueiredo-Filho, X. Ji, M. Gomez-Mingot, J. Iniesta, O. Fatibello-Filho, D. K. Kampouris and C. E. Banks, *Journal of Materials Chemistry A*, 2013, 1, 5962-5972.
225. R. Raj, S. C. Maroo and E. N. Wang, *Nano Letters*, 2013, 13, 1509-1515.
226. D. A. C. Brownson and C. E. Banks, *Physical Chemistry Chemical Physics*, 2012, 14, 8264-8281.
227. GrapheneSupermarket, http://www.graphene-supermarket.com.
228. D. Graf, F. Molitor, K. Ensslin, C. Stampfer, A. Jungen, C. Hierold and L. Wirtz, *Nano Lett*, 2007, 7, 238-242.
229. M. Ding, Q. He, G. Wang, H.-C. Cheng, Y. Huang and X. Duan, *Nature Communications*, 2015, 6, 7867.
230. P. Wang, M. Yan, J. Meng, G. Jiang, L. Qu, X. Pan, J. Z. Liu and L. Mai, *Nature Communications*, 2017, 8, 645.
231. Y. Jiao, Y. Zheng, M. Jaroniec and S. Z. Qiao, *Chemical Society Reviews*, 2015, 44, 2060-2086.

232. S. Trasatti, *Electrochimica Acta*, 1984, 29, 1503-1512.
233. Y. Matsumoto and E. Sato, *Materials Chemistry and Physics*, 1986, 14, 397-426.
234. J. Rossmeisl, Z. W. Qu, H. Zhu, G. J. Kroes and J. K. Nørskov, *Journal of Electroanalytical Chemistry*, 2007, 607, 83-89.
235. I. C. Man, H.-Y. Su, F. Calle-Vallejo, H. A. Hansen, J. I. Martínez, N. G. Inoglu, J. Kitchin, T. F. Jaramillo, J. K. Nørskov and J. Rossmeisl, *ChemCatChem*, 2011, 3, 1159-1165.
236. C. C. L. McCrory, S. Jung, I. M. Ferrer, S. M. Chatman, J. C. Peters and T. F. Jaramillo, *Journal of the American Chemical Society*, 2015, 137, 4347-4357.
237. L. C. Seitz, T. J. P. Hersbach, D. Nordlund and T. F. Jaramillo, *The Journal of Physical Chemistry Letters*, 2015, 6, 4178-4183.
238. J. Chang, Q. Lv, G. Li, J. Ge, C. Liu and W. Xing, *Core-shell structured Ni12P5/Ni3(PO4)2 hollow spheres as difunctional and efficient electrocatalysts for overall water electrolysis*, 2016.
239. G. Wu, A. Santandreu, W. Kellogg, S. Gupta, O. Ogoke, H. Zhang, H.-L. Wang and L. Dai, *Nano Energy*, 2016, 29, 83-110.
240. D. Chen, C. Chen, Z. M. Baiyee, Z. Shao and F. Ciucci, *Chemical Reviews*, 2015, 115, 9869-9921.
241. J. Zhang, Z. Zhao, Z. Xia and L. Dai, *Nature Nanotechnology*, 2015, 10, 444.
242. L. Zhang, J. Xiao, H. Wang and M. Shao, *ACS Catalysis*, 2017, 7, 7855-7865.
243. X. Li, P. Cui, W. Zhong, J. Li, X. Wang, Z. Wang and J. Jiang, *Chemical Communications*, 2016, 52, 13233-13236.
244. F. Calle-Vallejo, J. Tymoczko, V. Colic, Q. H. Vu, M. D. Pohl, K. Morgenstern, D. Loffreda, P. Sautet, W. Schuhmann and A. S. Bandarenka, *Science*, 2015, 350, 185-189.
245. K. Ding, A. Gulec, A. M. Johnson, N. M. Schweitzer, G. D. Stucky, L. D. Marks and P. C. Stair, *Science*, 2015, 350, 189-192.
246. G. Gao, Y. Jiao, E. R. Waclawik and A. Du, *Journal of the American Chemical Society*, 2016, 138, 6292-6297.
247. X. Li, W. Zhong, P. Cui, J. Li and J. Jiang, *The Journal of Physical Chemistry Letters*, 2016, 7, 1750-1755.
248. J. Deng, L. Yu, D. Deng, X. Chen, F. Yang and X. Bao, *Journal of Materials Chemistry A*, 2013, 1, 14868-14873.
249. J. Deng, P. Ren, D. Deng, L. Yu, F. Yang and X. Bao, *Energy & Environmental Science*, 2014, 7, 1919-1923.
250. V. S. Sapner, B. B. Mulik, Renuka V. Digraskar, S. S. Narwade and B. R. Sathe, *RSC Advances*, 2019, 9, 6444-6451.
251. T. Y. Ma, S. Dai, M. Jaroniec and S. Z. Qiao, *Angewandte Chemie (International ed. in English)*, 2014, 53, 7281-7285.
252. J. P. Paraknowitsch and A. Thomas, *Energy & Environmental Science*, 2013, 6, 2839-2855.
253. C. C. L. McCrory, S. Jung, J. C. Peters and T. F. Jaramillo, *Journal of the American Chemical Society*, 2013, 135, 16977-16987.
254. S. Bhattacharya, A. R. Riahi and A. T. Alpas, *MRS Proceedings*, 2012, 1388, mrsf11-1388-f1312-1311.
255. S. Bhattacharya and A. T. Alpas, *Carbon*, 2012, 50, 5359-5371.
256. E. Markervich, G. Salitra, M. D. Levi and D. Aurbach, *Journal of Power Sources*, 2005, 146, 146-150.
257. D. B. Shinde and V. K. Pillai, *Chemistry – A European Journal*, 2012, 18, 12522-12528.
258. H. Cheng, Y. Zhao, Y. Fan, X. Xie, L. Qu and G. Shi, *ACS Nano*, 2012, 6, 2237-2244.
259. J. Lee, K. Kim, W. I. Park, B.-H. Kim, J. H. Park, T.-H. Kim, S. Bong, C.-H. Kim, G. Chae, M. Jun, Y. Hwang, Y. S. Jung and S. Jeon, *Nano Letters*, 2012, 12, 6078-6083.

260. L. Fan, M. Zhu, X. Lee, R. Zhang, K. Wang, J. Wei, M. Zhong, D. Wu and H. Zhu, *Particle & Particle Systems Characterization*, 2013, 30, 764-769.
261. J.-B. Wu, M.-L. Lin, X. Cong, H.-N. Liu and P.-H. Tan, *Chemical Society Reviews*, 2018, 47, 1822-1873.
262. M. Bodik, A. Zahoranova, M. Micusik, N. Bugarova, Z. Spitalsky, M. Omastova, E. Majkova, M. Jergel and P. Siffalovic, *Nanotechnology*, 2017, 28, 145601.
263. A. Taqieddin, R. Nazari, L. Rajic and A. Alshawabkeh, *Journal of The Electrochemical Society*, 2017, 164, E448-E459.
264. C. A. C. Sequeira, D. M. F. Santos, B. Šljukić and L. Amaral, *Brazilian Journal of Physics*, 2013, 43, 199-208.
265. H. Vogt and K. Stephan, *Electrochimica Acta*, 2015, 155, 348-356.
266. C. W. M. P. Sillen, DOI: 10.6100/IR40592, Eindhoven 1983.
267. C. E. Banks and R. G. Compton, *ChemPhysChem*, 2003, 4, 169-178.
268. A. García-Miranda Ferrari, D. A. C. Brownson and C. E. Banks, *Communications Chemistry*, 2019, Under review.
269. H. Zeng, C. Zhi, Z. Zhang, X. Wei, X. Wang, W. Guo, Y. Bando and D. Golberg, *Nano Letters*, 2010, 10, 5049-5055.
270. W. Chen, Y. Li, G. Yu, C.-Z. Li, S. B. Zhang, Z. Zhou and Z. Chen, *J. Am. Chem. Soc.*, 2010, 132, 1699-1705.
271. R. Koitz, J. K. Norskov and F. Studt, *Physical Chemistry Chemical Physics*, 2015, 17, 12722-12727.
272. K. Uosaki, G. Elumalai, H. Noguchi, T. Masuda, A. Lyalin, A. Nakayama and T. Taketsugu, *Journal of the American Chemical Society*, 2014, 136, 6542-6545.
273. Q. Li, C. Huo, K. Yi, L. Zhou, L. Su and X. Hou, *Sens. Actuator B-Chem.*, 2018, 260, 346-356.
274. A. F. Khan, D. A. C. Brownson, E. P. Randviir, G. C. Smith and C. E. Banks, *Anal. Chem.*, 2016, 88, 9729-9737.
275. l. Song, L. Ci, H. Lu, P. B. Sorokin, C. Jin, J. Ni, A. G. Kvashnin, D. G. Kvashnin, J. Lou, B. I. Yakobson and P. M. Ajayan, *Nano Lett.*, 2010, 10, 3209-3215.
276. P. Swift, *Surf. Interface Anal.*, 1982, 4, 47-51.
277. A. Reina, H. Son, L. Jiao, B. Fan, M. S. Dresselhaus, Z. Liu and J. Kong, *The Journal of Physical Chemistry C*, 2008, 112, 17741-17744.
278. E. Gracia-Espino, G. Hu, A. Shchukarev and T. Wågberg, *J. Am. Chem. Soc.*, 2014, 136, 6626-6633.
279. C. Fettkenhauer, X. Wang, K. Kailasam, M. Antonietti and D. Dontsova, *J. Mater. Chem. A*, 2015, 3, 21227-21232.
280. S. Hu, M. Lozada-Hidalgo, F. C. Wang, A. Mishchenko, F. Schedin, R. R. Nair, E. W. Hill, D. W. Boukhvalov, M. I. Katsnelson, R. A. W. Dryfe, I. V. Grigorieva, H. A. Wu and A. K. Geim, *Nature*, 2014, 516, 227.
281. S. M. Holmes, P. Balakrishnan, V. S. Kalangi, X. Zhang, M. Lozada-Hidalgo, P. M. Ajayan and R. R. Nair, *Advanced Energy Materials*, 2017, 7, 1601216.
282. K.-H. Oh, D. Lee, M.-J. Choo, K. H. Park, S. Jeon, S. H. Hong, J.-K. Park and J. W. Choi, *ACS Applied Materials & Interfaces*, 2014, 6, 7751-7758.
283. R. V. Gorbachev, I. Riaz, R. R. Nair, R. Jalil, L. Britnell, B. D. Belle, E. W. Hill, K. S. Novoselov, K. Watanabe, T. Taniguchi, A. K. Geim and P. Blake, *Small*, 2011, 7, 465-468.
284. Q. Cai, D. Scullion, A. Falin, K. Watanabe, T. Taniguchi, Y. Chen, E. J. G. Santos and L. H. Li, *Nanoscale*, 2017, 9, 3059-3067.
285. A. Eckmann, J. Park, H. Yang, D. Elias, A. S. Mayorov, G. Yu, R. Jalil, K. S. Novoselov, R. V. Gorbachev, M. Lazzeri, A. K. Geim and C. Casiraghi, *Nano Letters*, 2013, 13, 5242-5246.

286. I. Stenger, L. Schué, M. Boukhicha, B. Berini, B. Plaçais, A. Loiseau and J. Barjon, *2D Materials*, 2017, 4, 031003.
287. A. García-Miranda Ferrari, D. A. C. Brownson and C. E. Banks, *CHEM SCI.*, 2019, Under review.
288. S. A. Solin and A. K. Ramdas, *Physical Review B*, 1970, 1, 1687-1698.
289. A. K. Geim and I. V. Grigorieva, *Nature*, 2013, 499, 419-425.
290. S. J. Rowley-Neale, M. Ratova, L. T. N. Fugita, G. C. Smith, A. Gaffar, J. Kulczyk-Malecka, P. J. Kelly and C. E. Banks, *ACS Omega*, 2018, 3, 7235-7242.
291. A. Ambrosi, Z. Sofer and M. Pumera, *Angewandte Chemie*, 2017, 129, 10579-10581.
292. E. Martínez-Periñán, M. P. Down, C. Gibaja, E. Lorenzo, F. Zamora and C. E. Banks, *Advanced Energy Materials*, 2018, 8, 1702606.
293. M. Pumera, A. Ambrosi, A. Bonanni, E. L. K. Chng and H. L. Poh, *TrAC Trends in Analytical Chemistry*, 2010, 29, 954-965.
294. M. Liang and L. Zhi, *Journal of Materials Chemistry*, 2009, 19, 5871-5878.
295. S. Yuyan, W. Jun, W. Hong, L. Jun, A. I. A. and L. Yuehe, *Electroanalysis*, 2010, 22, 1027-1036.
296. D. Chen, L. Tang and J. Li, *Chemical Society Reviews*, 2010, 39, 3157-3180.
297. W. Yang, K. Ratinac, S. Ringer, P. Thordarson, J. Gooding and F. Braet, *Angewandte Chemie International Edition*, 2010, 49, 2114-2138.
298. T. Gould, S. Lebègue, T. Björkman and J. F. Dobson, *2D Materials*, Elsevier Science, 2016.
299. V. V. Yanilkin, V. P. Gubskaya, V. I. Morozov, N. V. Nastapova, V. V. Zverev, E. A. Berdnikov and I. A. Nuretdinov, *Russian Journal of Electrochemistry*, 2003, 39, 1147-1165.
300. Y. Chen, H. Liu, T. Ye, J. Kim and C. Mao, *Journal of the American Chemical Society*, 2007, 129, 8696-8697.
301. Z. Liu, X. Li, S. M. Tabakman, K. Jiang, S. Fan and H. Dai, *Journal of the American Chemical Society*, 2008, 130, 13540-13541.
302. L. Cao, X. Wang, M. J. Meziani, F. Lu, H. Wang, P. G. Luo, Y. Lin, B. A. Harruff, L. M. Veca, D. Murray, S.-Y. Xie and Y.-P. Sun, *Journal of the American Chemical Society*, 2007, 129, 11318-11319.
303. C.-C. Fu, H.-Y. Lee, K. Chen, T.-S. Lim, H.-Y. Wu, P.-K. Lin, P.-K. Wei, P.-H. Tsao, H.-C. Chang and W. Fann, *Proceedings of the National Academy of Sciences*, 2007, 104, 727-732.
304. C. Hao, L. Ding, X. Zhang and H. Ju, *Analytical Chemistry*, 2007, 79, 4442-4447.
305. T. N. Narayanan, P. M. Ajayan, S. Viswanathan, G. Manickam and V. Renugopalakrishnan, *MRS Proceedings*, 2015, 1725, mrsf14-1725-i1708-1705.
306. P. Suvarnaphaet and S. Pechprasarn, *Sensors (Basel, Switzerland)*, 2017, 17, 2161.
307. B. Yu, H. Yuan, Y.-Y. Yang, H.-L. Cong, T.-Z. Hao, X.-D. Xu, X.-L. Zhang, S.-J. Yang and L.-X. Zhang, *Chinese Chemical Letters*, 2014, 25, 523-528.
308. M. J. Allen, V. C. Tung and R. B. Kaner, *Chem Rev*, 2010, 110, 132-145.
309. I. Švancara, K. Vytřas, K. Kalcher, A. Walcarius and J. Wang, *Electroanalysis*, 2009, 21, 7-28.
310. B. Uslu and S. A. Ozkan, *Analytical Letters*, 2007, 40, 817-853.
311. I. Švancara, K. Vytřas, J. Barek and J. Zima, *Critical Reviews in Analytical Chemistry*, 2001, 31, 311-345.
312. Š. Ivan, V. Karel, K. Kurt, W. Alain and W. Joseph, *Electroanalysis*, 2009, 21, 7-28.
313. L. C. S. Figueiredo-Filho, D. A. C. Brownson, M. Gómez-Mingot, J. Iniesta, O. Fatibello-Filho and C. E. Banks, *Analyst*, 2013, 138, 6354-6364.
314. D. A. Brownson, S. A. Varey, F. Hussain, S. J. Haigh and C. E. Banks, *Nanoscale*, 2014, 6, 1607-1621.

315. A. D. Clegg, N. V. Rees, O. V. Klymenko, B. A. Coles and R. G. Compton, *Journal of the American Chemical Society*, 2004, 126, 6185-6192.
316. Y. Wang, Y. Li, L. Tang, J. Lu and J. Li, *Electrochemistry Communications*, 2009, 11, 889-892.
317. J. Du, R. Yue, Z. Yao, F. Jiang, Y. Du, P. Yang and C. Wang, *Colloids and Surfaces A: Physicochemical and Engineering Aspects*, 2013, 419, 94-99.
318. O. Arrigoni and M. C. De Tullio, *Biochimica et Biophysica Acta (BBA) - General Subjects*, 2002, 1569, 1-9.
319. G.-C. Yen, P.-D. Duh and H.-L. Tsai, *Food Chemistry*, 2002, 79, 307-313.
320. J. Zhu, X. Chen and W. Yang, *Sensors and Actuators B: Chemical*, 2010, 150, 564-568.
321. M. E. Bosch, A. J. R. Sánchez, F. S. Rojas and C. B. Ojeda, *Journal of Pharmaceutical and Biomedical Analysis*, 2006, 42, 291-321.
322. R. Snyder, *Critical Reviews in Toxicology*, 2002, 32, 155-210.
323. E. S. Johnson, S. Langård and Y.-S. Lin, *Science of The Total Environment*, 2007, 374, 183-198.
324. R. Snyder, *J Toxicol Environ Health A*, 2000, 61, 339-346.
325. Y. S. Lin, W. McKelvey, S. Waidyanatha and S. M. Rappaport, *Biomarkers*, 2006, 11, 14-27.
326. V. G. Rocha, E. García-Tuñón, C. Botas, F. Markoulidis, E. Feilden, E. D'Elia, N. Ni, M. Shaffer and E. Saiz, *ACS Applied Materials & Interfaces*, 2017, 9, 37136-37145.
327. B. Derby, *Science*, 2012, 338, 921-926.
328. I. Gibson, D. Rosen and B. Stucker, *Additive Manufacturing Technologies – Rapid Prototyping to Direct Digital Manufacturing*, 2010.
329. J. R. Tumbleston, D. Shirvanyants, N. Ermoshkin, R. Janusziewicz, A. R. Johnson, D. Kelly, K. Chen, R. Pinschmidt, J. P. Rolland, A. Ermoshkin, E. T. Samulski and J. M. DeSimone, *Science*, 2015, 347, 1349-1352.
330. K. Fu, Y. Wang, C. Yan, Y. Yao, Y. Chen, J. Dai, S. Lacey, Y. Wang, J. Wan, T. Li, Z. Wang, Y. Xu and L. Hu, *Advanced Materials*, 2016, 28, 2587-2594.
331. X. Wang, M. Jiang, Z. Zhou, J. Gou and D. Hui, *Composites Part B: Engineering*, 2017, 110, 442-458.
332. A. E. Ongaro, I. Keraite, A. Liga, G. Conoscenti, S. Coles, H. Schulze, T. T. Bachmann, K. Parvez, C. Casiraghi, N. Howarth, V. La Carubba and M. Kersaudy-Kerhoas, *ACS Sustainable Chemistry & Engineering*, 2018, 6, 4899-4908.
333. A. J. R. Lasprilla, G. A. R. Martinez, B. H. Lunelli, A. L. Jardini and R. M. Filho, *Biotechnology Advances*, 2012, 30, 321-328.
334. C. Gonçalves, I. C. Gonçalves, F. D. Magalhães and A. M. Pinto, *Polymers*, 2017, 9, 269.
335. E. Ivanov, R. Kotsilkova, H. Xia, Y. Chen, R. K. Donato, K. Donato, A. P. Godoy, R. Di Maio, C. Silvestre, S. Cimmino and V. Angelov, *Applied Sciences*, 2019, 9, 1209.
336. Y. Li, J. Yang and J. Song, *Renewable and Sustainable Energy Reviews*, 2017, 652–663.
337. P. C. Sherrell and C. Mattevi, *Materials Today*, 2016, 19, 428-436.
338. E. García-Tuñon, S. Barg, J. Franco, R. Bell, S. Eslava, E. D'Elia, R. C. Maher, F. Guitian and E. Saiz, *Advanced Materials*, 2015, 27, 1688-1693.
339. A. Ambrosi and M. Pumera, *Chemical Society Reviews*, 2016, 45, 2740-2755.
340. R. M. Cardoso, D. M. H. Mendonça, W. P. Silva, M. N. T. Silva, E. Nossol, R. A. B. da Silva, E. M. Richter and R. A. A. Muñoz, *Analytica Chimica Acta*, 2018, 1033, 49-57.
341. C. W. Foster, M. P. Down, Y. Zhang, X. Ji, S. J. Rowley-Neale, G. C. Smith, P. J. Kelly and C. E. Banks, *Scientific Reports*, 2017, 7, 42233.
342. P. Chang, H. Mei, S. Zhou, K. G. Dassios and L. Cheng, *Journal of Materials Chemistry A*, 2019, 7, 4230-4258.
343. A. Gupta, T. Sakthivel and S. Seal, *Progress in Materials Science*, 2015, 44–126.

344. X. Zhang, Z. Sui, B. Xu, S. Yue, Y. Luo, W. Zhan and B. Liu, *Journal of Materials Chemistry*, 2011, 21, 6494-6497.
345. Y. Xu, K. Sheng, C. Li and G. Shi, *ACS Nano*, 2010, 4, 4324-4330.
346. J. Zhao, W. Ren and H.-M. Cheng, *Journal of Materials Chemistry*, 2012, 22, 20197-20202.
347. W. Chen and L. Yan, *Nanoscale*, 2011, 3, 3132-3137.
348. M. Worsley, T. Olson, J. R. I. Lee, T. Willey, M. H. Nielsen, S. Roberts, P. J. Pauzauskie, J. Biener, J. H. Satcher and T. F. Baumann, *High Surface Area, sp(2)-Cross-Linked Three-Dimensional Graphene Monoliths*, 2011.
349. S. Barg, F. M. Perez, N. Ni, P. do Vale Pereira, R. C. Maher, E. Garcia-Tuñon, S. Eslava, S. Agnoli, C. Mattevi and E. Saiz, *Nature Communications*, 2014, 5, 4328.
350. C. Zhu, T. Liu, F. Qian, T. Y.-J. Han, E. B. Duoss, J. D. Kuntz, C. M. Spadaccini, M. A. Worsley and Y. Li, *Nano Letters*, 2016, 16, 3448-3456.